Progress in Materials Science 139 (2023) 101166

Contents lists available at ScienceDirect

Progress in Materials Science

journal homepage: www.elsevier.com/locate/pmatsci

Doped MXenes—A new paradigm in 2D systems: Synthesis, properties and applications

Avishek Dey [a,b,1,*], Silvia Varagnolo [a,1], Nicholas P Power [c], Naresh Vangapally [d], Yuval Elias [d], Lois Damptey [a], Bright N. Jaato [e], Saianand Gopalan [f], Zahra Golrokhi [a], Prashant Sonar [g,h], Vimalnath Selvaraj [e], Doron Aurbach [d,*], Satheesh Krishnamurthy [a,i,*]

[a] School of Engineering & Innovation, The Open University, Walton Hall, Milton Keynes MK7 6AA, UK
[b] Department of Chemistry, University College London, WC1H 0AJ, UK
[c] School of Life, Health & Chemical Sciences, The Open University, Walton Hall, Milton Keynes MK7 6AA, UK
[d] Department of Chemistry and Institute of Nanotechnology & Advanced Materials (BINA), Bar-Ilan University, Ramat-Gan 5290002, Israel
[e] Department of Materials Science & Metallurgy, University of Cambridge, Cambridge CB3 0FS, UK
[f] Global Centre for Environmental Remediation (GCER), College of Engineering, Science and Environment, The University of Newcastle, Callaghan 2308, New South Wales, Australia
[g] Centre for Materials Science, School of Chemistry and Physics, Queensland University of Technology, 2 George Street, QLD 4000, Australia
[h] Centre for Clean Energy and Practices, School of Chemistry and Physics, Queensland University of Technology, 2 George Street, QLD 4000, Australia
[i] Surrey Ion Beam Centre, Advanced Technology Institute, University of Surrey, Guildford Surrey GU2 7XH, United Kingdom

A B S T R A C T

Since 2011, 2D transition metal carbides, carbonitrides and nitrides known as MXenes have gained huge attention due to their attractive chemical and electronic properties. The diverse functionalities of MXenes make them a promising candidate for multitude of applications. Recently, doping MXene with metallic and non-metallic elements has emerged as an exciting new approach to endow new properties to this 2D systems, opening a new paradigm of theoretical and experimental studies. In this review, we present a comprehensive overview on the recent progress in this emerging field of doped MXenes. We compare the different doping strategies; techniques used for their characterization and discuss the enhanced properties. The distinct advantages of doping in applications such as electrocatalysis, energy storage, photovoltaics, electronics, photonics, environmental remediation, sensors, and biomedical applications is elaborated. Additionally, theoretical developments in the field of electrocatalysis, energy storage, photovoltaics, and electronics are explored to provide key specific advantages of doping along with the underlying mechanisms. Lastly, we present the advantages and challenges of doped MXenes to take this thriving field forward.

1. Introduction

Since the discovery of graphene, 2D materials have aroused immense interest due to their promising physical and chemical properties and many potential practical applications. Alongside graphene are h-BN, SiC, Si_2BN and phosphorene transition metal dichalcogenides with a general formula of MX_2 and an X-M-X sandwiched structure where M = Mo, Ta, W, etc. and X = S, Se, Te. Layered metal oxides (MoO_3, WO_3, Ga_2O_3, V_2O_5) and the ultrathin group-IV allotropes silicene (Si), germanene (Ge) and stanene (Sn)

* Corresponding authors.
E-mail addresses: A.Dey@ucl.ac.uk (A. Dey), Doron.Aurbach@biu.ac.il (D. Aurbach), satheesh.krishnamurthy@open.ac.uk (S. Krishnamurthy).
[1] These authors contributed equally to this work.

https://doi.org/10.1016/j.pmatsci.2023.101166
Received 3 January 2023; Received in revised form 22 June 2023; Accepted 21 July 2023
Available online 22 July 2023

are other extensively researched 2D systems [1–7].

MXenes are among the recent addition to this 2D variety. They comprise transition metal carbides, nitrides, and carbonitrides and have been at the forefront of scientific research and innovation since their discovery in 2011.[8] The name MXenes stems from their general formula $M_{n+1}X_nT_x$ ($n = 1$, 2 or 3), where M, X, and T_x, represent an early *d*-block transition metal (e.g., Sc, Ti, Zr, Hf, V, Nb, Ta, Cr or Mo), carbon and/or nitrogen, and surface termination (fluorine, hydroxyl and/or oxygen) respectively. MXenes are derived from selective etching of the single A layer and exfoliation of its precursor MAX phases.[9] This sequential etching and exfoliation results in the introduction of an abundance of surface functional groups (O, OH, F, Cl) making MXenes hydrophilic in nature. These MAX phases correspond to a broad group of ternary carbides and nitrides with formula $M_{n+1}AX_n$ where A represents an element from group 13 or 14 (formerly IIIA or IVA) such as Al or Si.[10] Due to the difference in strength and chemical activity between M−X and M−A bonds, the relatively active A layer can be selectively etched using wet chemical routes. Hydrofluoric acid (HF) or HF forming chemicals such as hydrochloric acid (HCl) and lithium fluoride (LiF) are commonly used as etchants for this purpose.[11] Alkali treatment and electrochemical etching were also applied to synthesize high-purity MXenes.[12,13] Naguib *et al.* were the first to make Ti_3C_2 MXenes by exfoliation of Ti_3AlC_2 [14]. This spurred research interests towards the discovery of new MXene compositions both theoretically and experimentally. Over 70 MAX phases were reported, and >30 MXene compositions were successfully synthesized.[15] Owing to their inherent desirable properties including large specific surface area, good hydrophilicity, excellent thermal/electrical conductivity, high chemical stability, and environmental friendly nature, MXenes hold promise for a broad range of applications. They were successfully employed for energy storage (rechargeable batteries, supercapacitors) and generation (photo/electrocatalysis, solar cells), environmental remediation (water treatment, adsorption of oil and heavy metals), sensors, hydrogen storage, electromagnetic shielding, composite materials, microelectronics, and biomedical applications [11,12,16–20]. In spite of the enormous promise, MXenes are highly susceptible to performance degradation. Some of the major challenges with MXene research are restacking of the layers, prone to oxidation, low flexibility, large contact resistance, biocompatibility, and cytotoxicity [21–24]. Like other layered and 2D systems, doping MXene has proven to be a successful strategy to tackle these challenges. Doping MXene has not only improved its properties, but has unlocked its potential in new frontiers e.g., catalysis, sensors, and many more.

The introduction of foreign elements into 2D materials, known as “doping”, is an effective way to tune their physical and chemical properties. Controlled doping of graphene and its derivatives with heteroatoms significantly broadened their applications [25–27]. In general, doping can be achieved in two different ways: by surface functionalization with molecules that donate or withdraw electrons or by substitution/introduction of heteroatoms in the lattice. The success of doping strategies in erstwhile 2D systems influenced the design of new MXene based systems, offering a new paradigm for theoretical and experimental studies. Table 1 highlights the advantages of doping MXenes and the improved properties for various applications. Which is discussed in detail in the next sections. Numerous reviews are dedicated to the progress of MXenes in a multitude of applications.[8,10–13,16,17,19,28–33] Nevertheless, research on doped MXene systems is rapidly progressing, adding new avenues to the far-reaching possibilities of these extraordinary materials. A review highlighting the recent progress in doped MXenes seems therefore both necessary and timely. Whilst many reviews consider the benefits of surface functionalization, the focus here is on doping by heteroatoms in the lattice. After describing synthesis and characterization techniques, experimental applications of various doped MXene systems are surveyed in several key areas: electrocatalysis, energy storage, photovoltaics, electronics, photonics, sensors, environmental applications, and biomedical

Table 1
Positive impacts of doping MXene for various applications.

Application	Superior properties of Doped MXenes
Electro and Photo Catalysis	• Higher electrocatalytic activity and stability. Improved kinetics and thermodynamics of water dissociation. Lower Gibbs free energy for adsorption of reaction intermediates. Increase in catalytic active sites. Improved precious metal anchoring through charge redistribution and coordination. Improved Faradaic efficiency for N_2 reduction and CO_2 reduction reactions.
Energy storage (batteries and supercapacitors)	• Ability to tune interlayer structure and surface area. Increase in electrochemical stability and performance. Significant reduction in charge transfer resistance. Increase in electrode conductivity. Decrease in electrode/electrolyte interfacial impedance. Improved Li^+ / Na^+ ion diffusion.
Photovoltaics	• Tunable band gap to match the one required for photon-electron conversion. Improved conductivity and charge transfer leading to higher efficiency of the photovoltaic device.Tunable work function to have the choice of using the doped MXene electrode either as a hole or an electron transport layer.In perovskite solar cells, improved perovskite crystallization leading to higher efficiency.
Electronics	• Tunable band gap to induce semiconductor or conductor behaviour as required.Tunable band gap to improve the performance of nano electronic devices.Tunable work function that allows to improve the performance of field-effect transistors.
Photonics	• Smaller lateral size. Enhanced photoluminescence quantum yield.Increased lifetime.Tunable peak of the photoluminescence emission through different doping. Consequently, quantum dots emitting light of different colours can be combined to produce white light emitting diodes or lasers. • Metallic conductivity with intrinsic functional groups.Spacious matrix for nanoparticles loading.Adequate sites for biomolecule binding led to rapid transduction of signals.

applications (Fig. 1). Furthermore, theoretical developments in electrocatalysis, energy storage, photovoltaics and electronics are covered to provide insight into the specific advantages of doping, along with underlying mechanisms. In conclusion, benefits and limitations of doped MXenes are highlighted along with future prospects of this exciting new domain.

2. Mxene doping

Both theoretical and experimental approaches have been explored for the design, engineering and functionalisation of doped MXenes. Accordingly, doping has been investigated for M, X or T components of MXenes either during MAX phase or post exfoliation, and have been classified as (a) M-doped, (b) X-doped or (c) T-substituted.[34] Heteroatoms such as N, P, S or O can be placed in all three positions (M, X, T), halides can substitute for T elements, whilst transition metals (Mo, Cr, Ru, etc.) may be introduced to replace either or both M and X positions in the doped MXenes [9,15,35,36] With such broad availability of diversity in elemental composition and stoichiometry within their structural configuration, doped MXenes offer incredible opportunities to exploit their promising physical and chemical properties in a diverse array of applications. Doping strategies (in situ and ex situ), mechanisms, properties, and the respective challenges for doping MXenes are reviewed herein.

2.1. Synthetic strategies for heteroatom doping of MXenes

Through compositional engineering of 2D MXenes, doping can be achieved via two synthetic pathways: (i) *in-situ* (bottom-up) and (ii) *ex-situ* (top-down) strategies (Fig. 2). *In-situ* (e.g., by sintering) involves inclusion of the dopant for the 3D MAX phase (MXene precursor) synthesis followed by selective etching and exfoliation to reveal the doped MXenes.[15] The implications for this approach are primarily substitutions at M and X, dependent on the respective transition metal and heteroatom dopant used. The *ex-situ* strategy has typically involved post-synthesis modifications (e.g., by hydro/solvo-thermal or heat treatment or plasma) which allows for doping or substitution at either/both X and T, depending on the heteroatom and conditions pursued. A more recent *ex-situ* strategy involves etching of the 3D MAX phase via molten salts whilst simultaneously provisioning readily modifiable termination groups (T) that allows for substitution doping of the MXenes at T with ease. All of these are discussed in the following sections.

Density functional theory (DFT) approaches in atomistic simulations of doped MXenes as well as other computational approaches have been exploited to design, analyse and predict properties of the 2D materials molecular compositional framework, surface composition and interactions, electronic and mechanical properties, along with modelling applications (catalysis, energy storage) of MXenes using first principles (ab initio) methods. It has proven to be a powerful and useful tool helping to optimise approaches for strategic introduction of dopants in design, synthesis, and elucidation of mechanisms of formation, predicting and optimising intrinsic properties, as well as in the analysis and rationalisation of experimental and characterisation data of MXenes. DFT modelling of

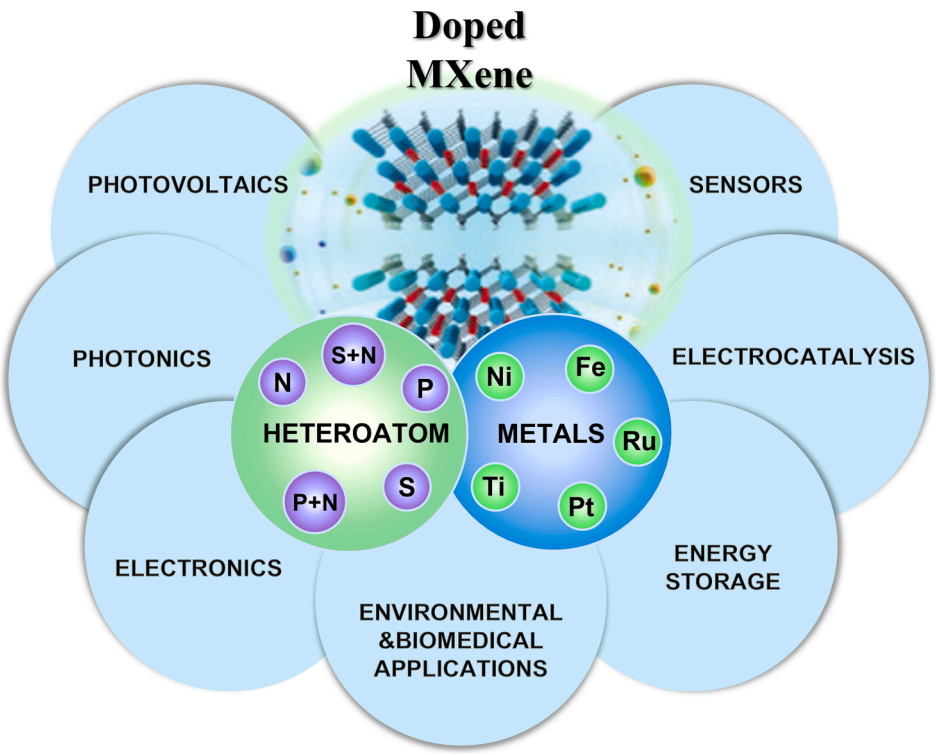

Fig. 1. Doping of MXenes by metals and heteroatoms and prospective applications.

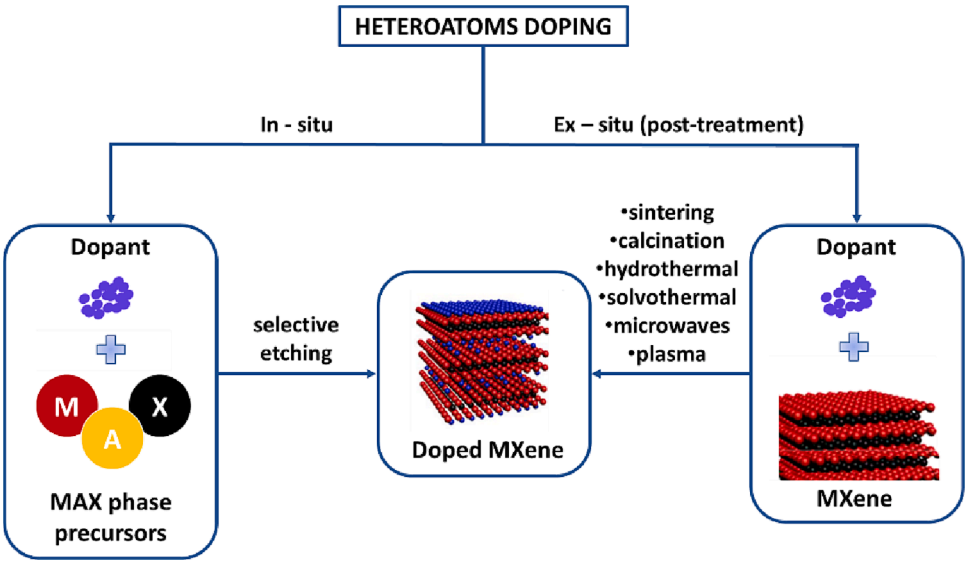

Fig. 2. The two approaches to doping of MXenes (images adapted from [37] with permission from American Chemical Society).

transition metal doping (M) reflects the introduction of alternative *d* orbital properties that impact the MXenes intrinsic properties such as band gap and magnetic properties, changes in lattice parameters and layer thickness, and mechanical properties. [38] DFT analysis on X substitution (B, N, Si, S, for C) in MXenes reflect the respective changes in M−X interatomic distance for the dopant and its impact on the corresponding layer thickness and lattice values, and electronic properties of the 2D materials. First-principles calculations have also been used in prediction of formation and electronic properties for functionalized surfaces (T = F, OH, O, S, and Cl) for a variety of MXenes (M = Sc, Ti, V, Cr, Zr, Nb, Ta) in prediction and analysis of the geometric and electronic properties of single layers and multilayer systems. What follows within this section will present the diversity of methodologies available to introduce dopants (N, S, P, O, halides, and metals) strategically and successfully into the desired positions of MXenes (M, X, T), indicating the rational for the approaches taken, vignettes of characterisation and success of the prepared doped MXenes, and their significance in the materials development, from the recent literature.

2.2. Non-metal doping

2.2.1. Nitrogen doping (N doping)

Nitrogen is a popular dopant (5-valent dopant) for a host of carbon-based nanostructures due to its comparable atomic radius with that of carbon. Its use as a dopant has been explored in materials such as carbon quantum dots [39], carbon nanotubes [40], carbon nanosheets [41], and graphene [42], in addition to MXenes. It is well known that N doping may introduce oxygen vacancies and or interstitials that not only alters the electronic and optical properties, but also enigneers the bandgap [43,44]. The first *in-situ* synthesis for the preparation of N doped MXene was exemplified by Naguib *et al.* (2012) by including dopant N atoms into the preparative mix for formation of the MAX phase precursor . This involved treating a 3:1:1 ratio mixture of Ti, AlN, and graphite at 1500 °C for 2 h to give Ti_3AlCN . Selective HF etching of aluminum from Ti_3AlCN provided the N doped MXene, Ti_3CNT_X. [9] Other approaches for etching include use of LiF-HCl solutions; Cai et al. sought to prepare a high-performance microwave absorbing hybrid composite using Ti_3CNT_X MXene in conjunction with Co-ZIF nanoparticles.[45] The LiF-HCl etching of the Ti_3AlCN precursor, followed by ultra-sonication exfoliation in deionized water allowed fabrication of few-layered Ti_3CNT_x. The etched removal of Al atomic layer was confirmed by XRD. As hoped, the N-doping introduced improved electromagnetic parameters in multilayer Ti_3CNT_X than that for multilayer $Ti_3C_2T_X$ as reflected by values representative of storage and dissipative capabilities of electric energy. More recently, Lu *et al.* exploited DFT simulation analysis of Ti_3C_2Tx (T = F, OH, and O) for N-doping. [46] By assessing all plausible arrangements of N within MXene along with experimental corroboration, they identified three nitrogen species as energetically favorable sites. The N-doping within the MXene was constituted as either carbon lattice substitution (LS), –OH function substitution (FS), or -O termination surface absorption (SA) (Fig. 3), each with formation energies of −1.31, −4.71, and −2.87 eV, respectively. The authors targeted preparation of the corresponding N-doped Ti_3C_2 MXenes allowed nitrogen to be preferentially/predominantly allocated at the DFT identified sites via three nitrogen doping strategies. These were (i) in-situ etching of the MAX phase Ti_3AlCN, (ii) hydrothermal processing of Ti_3C_2 MXene with urea, and (iii) cold plasma treatment with pure nitrogen gas of Ti_3C_2 MXene, to provide N-doped MXenes that the authors referred to as Ti_3CN, HND (hydrothermal N-doping), and PND (plasma N-doping), respectively. The respective X-ray photoelectron spectroscopy (XPS) high-resolution spectra for the targeted as-synthesized MXenes revealed N 1 s peaks of 396.0, 399.7, and 401.9 eV, that were correspondingly attributed to N-Ti (Ti_3CN) within the lattice site, N- function substitution (pyrrolic nitrogen) via HND, and N- surface absorption (quaternary nitrogen) via PND, by strategies (i), (ii), and (iii) respectively.

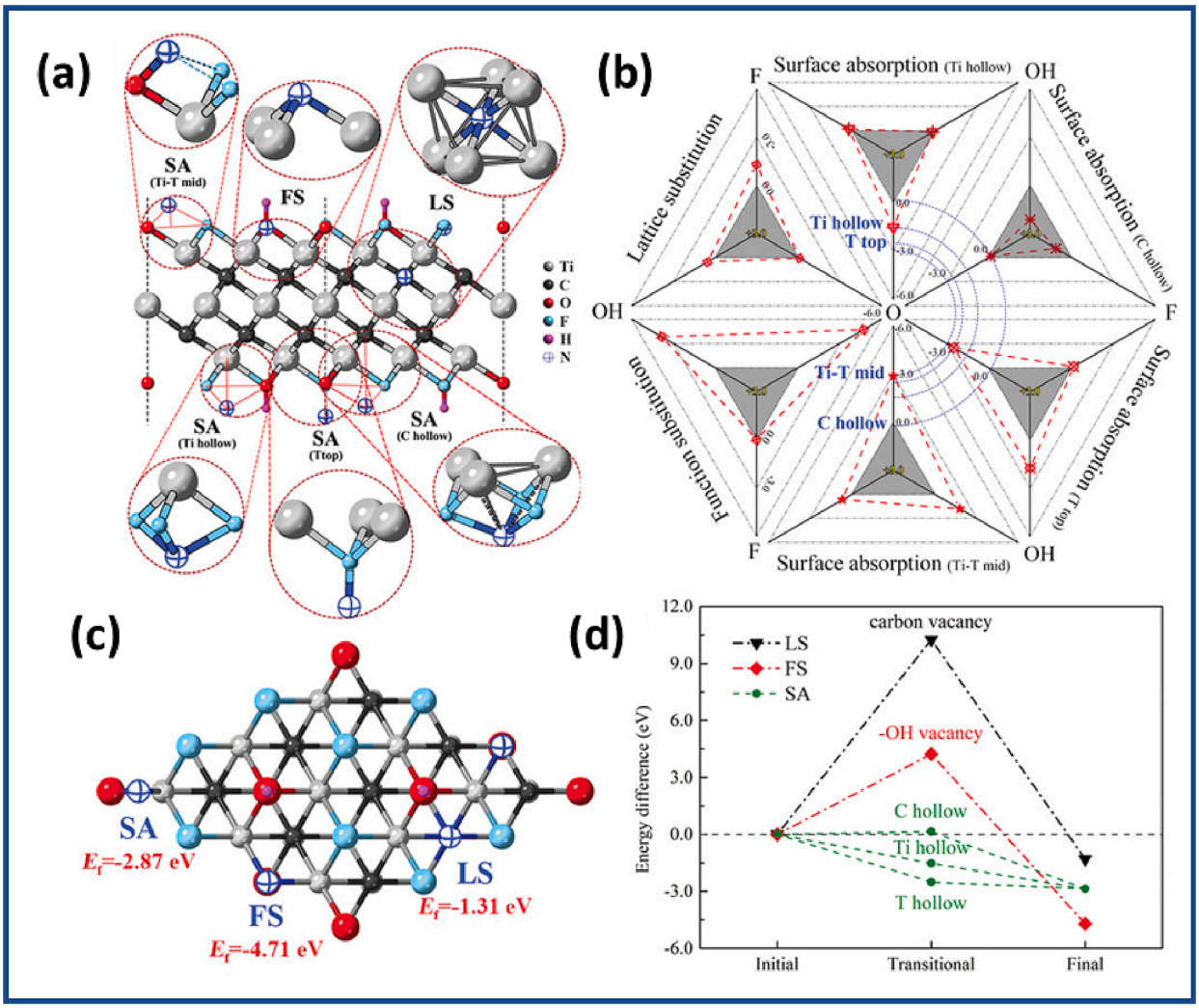

Fig. 3. Simulation of nitrogen dopants in Ti_3C_2: a) atomic scheme of $Ti_3C_2T_x$ with all possible sites for nitrogen dopants; b) formation energy calculation results (shaded part for positive values); c) atomic scheme (top view) of Ti_3C_2 supercell with nitrogen atoms at the most energetically favorable sites; d) transition state energy calculation results. Reproduced from [46] with permission from Willey.

Comparison of electrochemical data for electrodes for all three prepared N-doped MXenes (84.6, 92.2, and 98.6 F/g for HND, PND, and Ti_3CN respectively) showed improved specific capacitance over the neat Ti_3C_2 electrode (76.1 F/g) at scan rates of 5 mV s^{-1}.[46] This computational model approach for elemental doping can be applied to other MXene 2D materials as described for their targeted approach to nitrogen doping mechanisms for Ti_3C_2 MXene: thus, providing useful theoretical guidelines for consideration in synthetic strategies of MXenes for energy storage or alternative applications. Prior to this study by Lu *et al.,* Tang *et al.* took the *ex-situ* approach (Fig. 2) for the preparation of N-doped Ti_3C_2 for applications in enhancing the electrochemical performance of supercapacitors. The N-doped Ti_3C_2 was prepared via an autoclave in a facile hydrothermal reaction of Ti_3C_2 MXene with urea as the nitrogen dopant at 180 °C for 12 h (Fig. 4aii). X-ray photoelectron spectroscopy (XPS) characterization revealed the diversity of nitride peaks assigned as N-Ti, pyrrolic N, and quaternary N, at 396.1 eV, 399.3 eV, and 401.0 eV respectively, for the as-synthesized N-Ti_3C_2. With superior electrochemical performance and exceptional cycling stability for specific capacitance over that of most carbon-based materials cited, the as-synthesized N-Ti_3C_2 performance was attributed to the pyrrolic N and quaternary N functional groups that facilitated redox reactions and charge transfer, respectively, thus synergistically enhancing the pseudo capacitance of N-Ti_3C_2.[47] The electrochemical enhancements are discussed further in more depth in the sections dealing with Electrocatalysis (4.1.2) and Energy Storage (4.2).

In Wen *et al.*'s preparation of N-doped (N-$Ti_3C_2T_x$) MXene for electrodes for supercapacitors, they explored the ex-situ heteroatom doping strategy to prepare N-doped MXenes (Ti_3C_2Tx). [48] Synthesis proceeded via facile annealing of Ti_3C_2Tx MXenes (etched from Ti_3AlC_2 with HF, washed with de-ionised water (DI), and dried under vacuum) placed in a tube furnace under an ammonia atmosphere (100 ml min^{-1}) over a temperature range of 200 °C to 700 °C. [44] The nitrogen surface concentration was shown by XPS to have increased with increasing temperature of the ammonia treatment (1.7 – 20.7 N at%). The as prepared N-doped (N-$Ti_3C_2T_x$) MXene

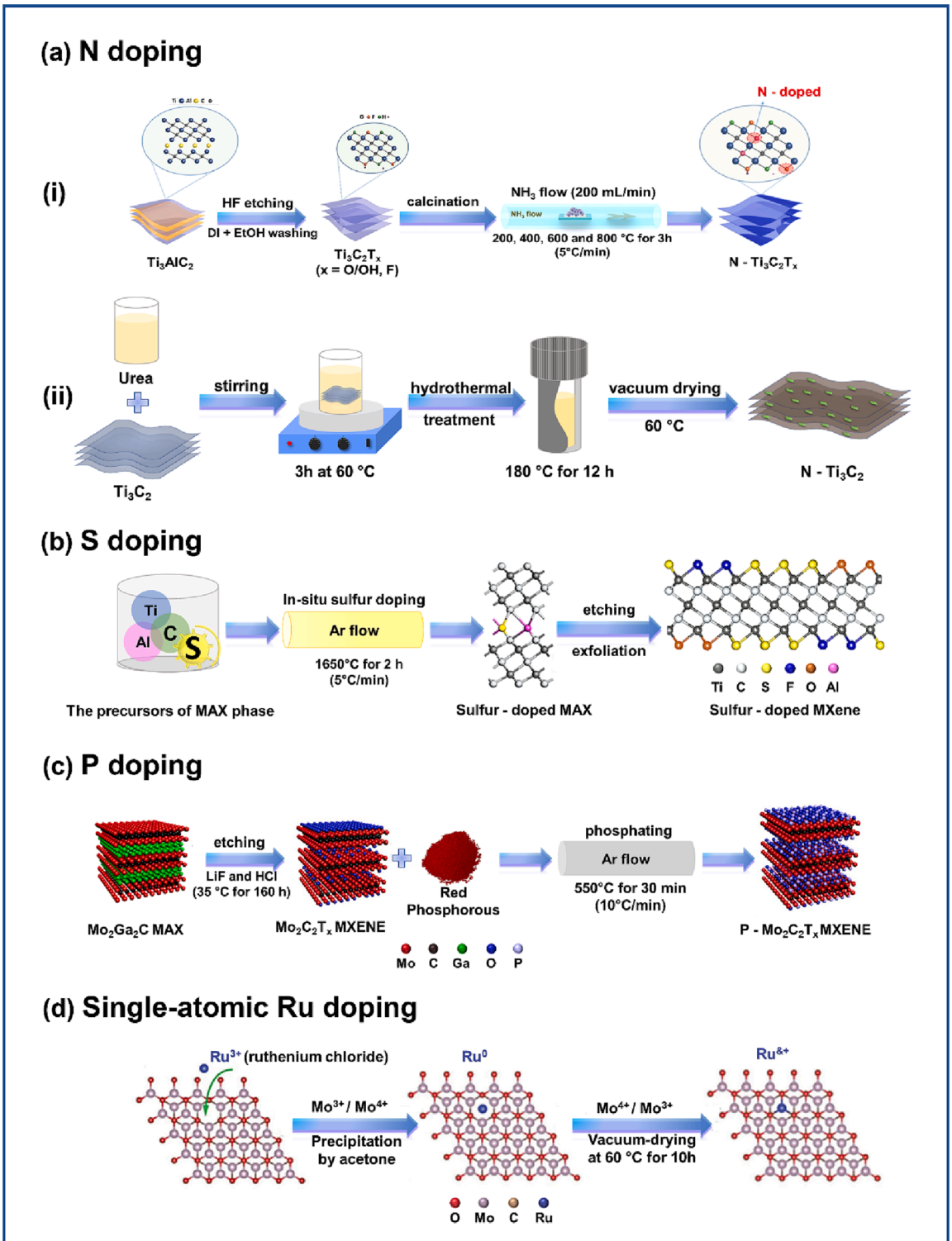

Fig. 4. Schematic illustration showing the structures during in-situ (from parent molecules) and ex situ (post-synthetic) doping approaches. Reproduced from [37,44,47,58] with permission from American Chemical Society and The Electrochemical Society.

(200 °C preparation) exhibited superior specific capacitance performance (192 F g^{-1} and 82 F g^{-1} in 1 M H_2SO_4 and 1 M $MgSO_4$ electrolytes respectively) with retention of 67% of initial capacitance (scan rates from 1 to 200 mV s^{-1}) over that of pristine $Ti_3C_2T_x$ MXene (34 F g^{-1} and 52 F g^{-1} in the respective electrolytes). Le *et al.*'s preparation of N-$Ti_3C_2T_x$ MXenes were made in a similar fashion (Fig. 4 a(i)) for applications in enhanced Hydrogen Evolution Reaction (HER). [44] Energy dispersive X-ray (EDX) and XPS probed the surface properties reflected the altered chemical compostion and commensurate increase in nitrogen uptake with increasing preparative temperatures for the heat treated MXene samples, with optimal HER enhancement exhibited by the 600 °C N-doped prepared samples. The aforesaid optimal N-doped $Ti_3C_2T_x$ Mxenes demonstrated HER performances (low onset potential of −30 mV, overpotential of 198 mV @ 10 mA cm^{-2}, and Tafel slope of 92 mV dec^{-1}) that exceeded that of pristine $Ti_3C_2T_x$ Mxene (high onset potential, overpotential of 531 mV @ 10 mA cm^{-2}, and Tafel slope of 268 mV dec^{-1}).

Jiang *et al.*'s interest in developing enhanced electrochemiluminescence (ECL) aptasensor lead to an approach involving ultrasonication of an aqueous solution of N-dopant, glycine, with $Zn(NO_3)_2{\cdot}6H_2O$ and Ti_3C_2 MXene nanosheets (1 h), followed by the resulting precursor solution undergoing thermal annealing in an argon-atmosphere tube furnace (500 °C at 5 °C/min) to support nucleation and growth of ZnO QDs on a N-Ti_3C_2 nano sheet matrix. [49] Electrochemical measurements revealed N-doping of Ti_3C_2 MXene significantly improved ECL performance (2.8-fold ECL enhancement) with an ECL onset potential positive increase of 250 mV for ZnO QDs/N-Ti_3C_2 (5.43 wt% N) over the non-doped equivalent, ZnO QDs/Ti_3C_2 MXene. This change in the onset potential exemplified the facilitation of N-doping of MXenes in reducing the barrier to ZnO QDs reduction on the nanosheets. An *ex-situ* approach was also taken by Bao *et al.*, a strategy for defined porous structure, high surface area, and large pore volume, by preparing crumpled nitrogen-doped mxene nanosheets for Li–S batteries development. [50] They prepared a colloidal suspension of etched-$Ti_3C_2T_X$ with an acidified solution of melamine (nitrogen source and spacer) allowing the protonated melamine to intercalate to self-assemble into the hydrophilic negatively charged (owing to the predominant MXene surface functionality of –OH, –O, and –F) thin layered structure of $Ti_3C_2T_X$ MXene. The intercalated material was thermally annealed (550 °C, 4 h), providing the N-$Ti_3C_2T_X$ nanosheets. Data from an XPS survey of the as-prepared crumpled N-$Ti_3C_2T_X$ nanosheets revealed three significant N 1 s peaks at 397, 398.3, 399.8 eV, corresponding to formation of Ti–N (27.70%), pyridinic N (34.18%), and pyrrolic N (38.12%), and a peak at 281.6 eV for C-Ti-N. The elemental nitrogen content was confirmed as 8.41 at%. Similar approaches have been engaged using other sources of N, such as cyanamide [51], ammonium chloride [52], and ammonium citrate [53], in preparation of N-doped $Ti_3C_2T_X$ Mxenes, among other commonly available amine derivative N dopants .[34,54].

OER and HER interests by Chen *et al.*, instigated *ex-situ* preparation of N-doped $Ti_3C_2T_X$ MXene using an NH_3/Ar plasma process with tuneable control of structural properties and nitrogen content by volume ratio adjustment of ammonia and argon (6:1 being optimal).[55] Etched $Ti_3C_2T_X$ MXene was stirred overnight in saturated ammonium bicarbonate solution, facilitating intercalation of NH_4HCO_3 into the $Ti_3C_2T_X$ interlaminar spaces. The NH_4HCO_3 /$Ti_3C_2T_X$ mixture was freeze dried, placed into a quartz, and treated with a plasma NH_3/Ar gas via a DBD plasma reactor (50 V × 2 A AC input power for 10 min) to give few layered delaminated N-doped $Ti_3C_2T_X$ MXene. The plasma treatment decomposed NH_4HCO_3 into NH_3, CO_2, and H_2O vapour. The XPS spectral data confirmed successful N-doping (with an optimal 5 at.%) with a N 1 s peak (400 eV), and a presence in three forms: lattice substitution (LS), functional substitution (FS), and surface absorption (SA) with optimal N-doping content at 8.26, 27.4, and 64.3 % respectively. This correlated with the respective DFT calculated formation energies for FS, SA, and LS, of −4.71 eV, −2.87 eV and −1.31 eV. The optimal weight fraction of N-doped $Ti_3C_2T_x$ exhibited the lowest HER potential (119.17 mV @ 10 mA cm^{-2}) compared to pristine $Ti_3C_2T_X$ MXene (192.95 mV @ 10 mA cm^{-2}) along with faster reaction kinetics (Tafel slope of 61.81 mV dec^{-1}) indicating more rapid HER activity. OER analysis reflected similar improvements over pristine $Ti_3C_2T_X$ MXene (overpotential of 2.01 V @ 100 mA cm^{-2}) for optimal N-doped $Ti_3C_2T_x$ (overpotential of 1.74 V @ 100 mA cm^{-2}).

In Alli *et al.*'s pursuance of a binder-free Li-ion battery anode, they prepared N-doped Ti_2C MXene/TiO_2 composites using supercritical conditions via a continuous hydrothermal flow synthesis (350 °C or 450 °C, P = 22.4 MPa) where tuned product formation can be controlled and maintained from continuous converging streams in the reactor of supercritical water and aqueous solutions of delaminated MXene and 0.5 M ammonia at prescribed temperatures and pressure. [56] Their doping strategy involved the oxidation of some MXene lattice Ti to TiO_2 nanoparticles, located between N-doped MXene sheets forming the N-Ti_2C MXene/TiO_2 composite material , as confirmed by HRTEM. Whilst high-resolution XPS confirmed N 1s two peaks at 400.8 eV and 399.1 eV for protonated pyridinic nitrogen and pyrrolic nitrogen respectively, a Ti-N peak (395.6 eV) was only apparent within the MXene lattice structure for samples prepared above temperatures of 400 °C. Elemental analysis of N-Ti_2C MXene/TiO_2 composites reflected increased nitrogen uptake (1.60 % to 2.14 %) with corresponding reaction temperature increase and concomitant decrease in F-surface terminations. Analysis for both (350 °C and 450 °C) prepared N-Ti_2C MXene/TiO_2 electrodes indicated an initial activation process to provide eventual specific energy capacities of 355 and 369 $mAhg^{-1}$ respectively (100 cycles at 0.1 C charge rate) with Coulombic efficiencies up to 99.7%. In comparison, undoped Ti_2C MXene/TiO_2 electrodes provided specific energy capacity of 252 $mAhg^{-1}$ with capacity fade to 140 $mAhg^{-1}$ under similar test conditions.

An interest in low cost electrocatalyst development for HER by Han *et al.*, explored an ex-situ approach optimizing an ultrasonic temperature method to produce N-Ti_3C_2 Mxene for electrocatalytic HER applications.[57] Pristine Ti_3C_2 MXene powder was combined with ammonia (30 wt%) and $NaBH_4$ and ultrasonicated (200 W, 3 h) at various temperatures (5, 15, 35, 55 and 75 °C) using a bath-sonicator. It was anticipated that the ammonia would act thermodynamically and kinetically on defects at oxygen-containing functional groups forming C–NH_2, C–NH, and Ti–NH_2, with subsequent N–H dissociation to give C–N and Ti–N bonds. The successful N-doping of Ti_3C_2 MXenes was confirmed by XPS signals at 400 eV from N 1 s, and peaks at 398.8 eV, 400.1 eV, 401.4 eV, 403.3 eV and 396.5 eV corresponding to pyridinic-N, pyrrolic-N, graphitic-N, O–N–C, and Ti-N, respectively, with optimal N-doping (1.84 at.%) occurring at 35 °C, and Ti-N formation occurring at 15 °C and above. The optimal N-doped Ti_3C_2 Mxene provided superior HER activity with an overpotential (162 mV @ 10 mA cm^{-2}) 3.5 times lower than that for pristine MXene (578 mV @ 10 mA cm^{-2}), along with

faster reaction kinetics as exemplified by the lower Tafel slope (69 mV dec^{-1}), in comparison to pristine Ti_3C_2 MXene (150 mV dec^{-1}).

2.2.2. Sulphur (S) doping

Exploration of the interlayer spacing within the nanoflakes of MXenes is another area of limited exploitation using non-metal dopants such as the hypervalent S atom (Fig. 3b). Sulfur is ideal in this respect due to its large covalent radius that is anticipated to increase the interlayer distance of S-Ti_3C_2Tx MXenes, as well as influence change in the material's intrinsic properties. First-principle DFT calculations by Bao *et al.*'s studies into using MXenes for performance enhancement of Na–S Batteries, determined two possible doping sites for sulfur doping in the S–Ti_3AlC_2 Max phase; finding greater preference for positioning of the sulfur atoms in the Al layer sites (−5.372 eV), rather than at any C site (−5.122 eV).[58] They extended their DFT analysis to the S–$Ti_3C_2T_x$ MXene matrix and found their predictions to be consistent with experimental XPS binding energies for C–Ti–S bond (161.2 eV), terminal sulfur (163.5 eV), and bridging sulfur (S–S) bonds (164.5 eV), with S_{1s} peaks as the dominant oxidation state for their in-situ preparation of wrinkled S–$Ti_3C_2T_x$ MXene nanosheets from sulfur doped MAX phase precursor, $Ti_3AlC_2S_x$ (Fig. 2b). The dopant sulfur atoms had good uniformity in distribution throughout as evidenced by SEM energy-dispersive X-ray spectroscopy (EDS) of the MAX phase. Further DFT calculations on the adsorption capacity of S–Ti_3C_2Tx MXene nanosheets with representative sodium polysulfides, by the group, indicated preferential surface binding for S–$Ti_3C_2T_x$ rather than O–$Ti_3C_2T_x$ or F–$Ti_3C_2T_x$, which was backed up by their experimental data, again demonstrating the usefulness of theoretical computational approaches in MXene functional design. MAX phase synthesis was based on a 3:1.0:1.8:0.1 atomic ratio mixture of titanium, aluminum, graphite, and sulfur, sintered in a tube furnace at 1650 °C (5 °C/min for 2 h under argon). After milling and sieving (200-mesh), the MAX compound underwent etching with LiF-HCl solution, intercalation with chloroform under argon, exfoliation by sonication in an aqueous solution, and finally freeze dried to yield S–$Ti_3C_2T_x$ MXene nanosheets.

Battery technology is a significant driver in exploration of new MXene materials; in this regard An *et al.* developed a 3D protective layer composed of S-Ti_3C_2Tx MXene/ZnS for anodes, and a freestanding 3D S-Ti_3C_2Tx MXene@MnO_2 cathode for zinc-ion batteries. [59] The S-doping with 3D structure formation on MXene are concomitant with ZnS generation. Synthesis involved coating a uniform solution of sulfur and $Ti_3C_2T_x$ MXene on to a Zn foil and dried at 50 °C for 10 h. The obtained S@MXene@Zn was subjected to thermal annealing under vacuum at temperatures of 300 °C, 350 °C, and 400 °C, (5 °C min^{-1}, 2 h) in a tubular furnace to determine optimal S-doping conditions. Successful S-doping of the MXene-coated Zn foil led to S-MX@ZnS@Zn formation, confirmed by EDS elemental mapping along with the presence of the Ti–S bond by XPS. For synthesis of S-$Ti_3C_2T_x$ MXenes@MnO_2 cathode, MnO_2 nanotubes were mixed with $Ti_3C_2T_x$ MXene and sulfur into a homogeneous solution. The mixture was filtered, dried under vacuum (50 °C) to give S@MXene@MnO_2 which then underwent thermal treatment (350 °C, 2 h) to yield flexible S-$Ti_3C_2T_x$ MXene@MnO_2 product as confirmed by HR-XPS spectral survey exhibiting a series of peaks for S 2p, located at 160.8, 161.9, and 164.0 eV, corresponding to Ti–S, S $2p_{3/2}$, and S $2p_{1/2}$, respectively, and a Ti 2p peak at 454.9 eV attributable to Ti–S. In Shuvo *et al.*'s studies for room-temperature gas sensors for volatile organic compounds (VOC), they prepared S-doped Ti_2C_2Tx via an *ex-situ* strategy, which involves co-milling pristine $Ti_3C_2T_x$ with thiourea and heating at 500 °C for 3 h.[60] The heteroatom S-dopant was found to have enhanced the interlayer spacing of the S-$Ti_2C_2T_x$ MXene nanoflakes substantially by microstructural characterization techniques (TEM, HAADF-STEM, and HRTEM). In pursuance of enhanced anode performance via improved sodium storage capabilities for sodium-ion batteries, Li *et al.* were able to prepare multi-layered S-$Ti_3C_2T_x$ MXene with widened interlayer spacing along with the sought after enhanced electrical conductivity attributable to surface-induced capacitivity by S doping. *The ex-situ* synthesis of S-doped Ti_2C_2Tx involved placing $Ti_3C_2T_x$ (0.2 g) with S-dopant, thiourea (4 g), at two separate positions in a quartz boat with the thiourea upstream in a furnace in an argon atmosphere for 3 h. A range of samples were prepared at 200, 300, and 400 °C, at a heating rate of 2 °C min^{-1} to determine optimal preparative conditions. [61].

Myagmarsereejid *et al.* prepared S-$Ti_3C_2T_x$ MXene nanosheets as doping agents for ambient fabrication of Sb_2S_3 light absorbers for improved efficiency and stability for solar cells. [62] The S-doped $Ti_3C_2T_x$ MXene was prepared from a 1:10 ratio of pristine $Ti_3C_2T_x$ nanosheets mixed with thiourea (phenyl thiourea) in DI water, which was successively freeze-dried, and annealed at 500 °C for 3 h (3 °C min^{-1}) under an argon atmosphere. Characterization by energy-dispersive X-ray spectroscopy (EDX) and elemental mapping revealed successful S doping of 1.1 at%, and XPS data confirmed a decrease in F and Cl surface termination groups concomitantly replaced by O- (Ti-O) and S- (Ti-S) groups which was consistent with XRD data. DFT calculations using the garnered XPS data indicated that models with S-doping (S-$Ti_3C_2O_2$) exhibited a metallic character without a band gap; the S dopant introducing new electronic states around the Fermi level, suggesting greater electronic conductivity compared to the non-doped model ($Ti_3C_2O_2$). The group fabricated Sb_2S_3 solar cell devices with S-$Ti_3C_2T_x$ MXene nanosheet doping under inert (Ar) and air atmospheres, revealing that the best power conversion efficiency (PCE) performance was provided by the in-air preparation with an enhancement of 59.65% compared to the Ar-atmosphere prepared device; the enhanced performance considered to be due to the combination of O and p-type doping effects.

2.2.3. Phosphorus (P) doping

Doping MXenes with phosphorus is relatively unexplored as a single dopant and has been used more so as a co-dopant with nitrogen. Like sulfur in having a large covalent radius and hypervalency, it too is expected to increase the interlayer distance of MXenes as well as impacting the intrinsic properties of the material. Most of the reported P-doped MXene synthesis have involved *ex-situ* route processes (Fig. 4c). Wen *et al.*'s exploration of MXenes as electrode material for supercapacitors led to their synthesis of P-doped $Ti_3C_2T_x$ MXene. After a solution of sodium hypophosphite (300 mg) in N_2-saturated water (100 ml) was stirred with $Ti_3C_2T_x$ MXene (30 mg) under N_2 for 10 h at room temperature, the mixture was freeze-dried, and then annealed under argon flow over a range of test temperatures (300 °C, 500 °C, 700 °C) with optimal conditions at 500 °C (2 °Cmin.$^{-1}$, 2 h). [63] Removal of the phosphate salt by-

product required a week's dialysis under N_2 to finally yield P-$Ti_3C_2T_x$ MXene. DFT analysis was used to help elicit the P-doping mechanism in MXenes from the collected characterisation data for the observed reaction temperatures. Lower doping temperature (300 °C) observations indicated P atoms preference for bonding at surface terminals leading to P-O configurations; 500 °C indicated more lattice defects would be generated allowing more P-doping at the Ti vacancies although no P-Ti bond is formed in the P-$Ti_3C_2T_x$ due to its greater formation energy requirements. The DFT analysis complimented the XPS data which also confirmed optimal P-doping was at 500 °C (12.9P at%). Temperatures above 700 °C resulted in generation of an inactive phase, $NaTi_2(PO_4)_3$ resulting in poor capacitive properties. A significant increase in interlayer distance for P-$Ti_3C_2T_x$ MXene (1.51 nm) was also observed ($Ti_3C_2T_x$ MXene (1.05 nm)), as well as an enhanced specific capacitance of 320 Fg^{-1} at a current density of 0.5 Ag^{-1} reflecting a significantly improved electrochemical performance due to P doping in comparison to pristine $Ti_3C_2T_x$. [63].

To overcome the bottleneck of undesired titanium phosphate phase formation during P-doping of Ti_3C_2 MXenes, Gupta *et al.* exploited microwave (MW) assisted heating of homogeneous mixtures of reactants.[64] A prepared oxygen free aqueous solution of pristine $Ti_3C_2T_x$ with a selection of P-doping reagents of either phytic acid ($C_6H_{18}O_{24}P_6$), phosphoric acid (H_3PO_4), or sodium dihydrogen phosphate (NaH_2PO_4), ultrasonicated (26 kHz for 2 min intervals for 30 min) to ensure homogeneity, were microwaved at a range of power settings and times (500–1000 W, 30 sec to 5 min). A variety of weight ratios of $Ti_3C_2T_X$ and respective P-doping sources were also explored. Post MW irradiation work-up involved washing with DI water and ethanol, to adjust sample pH to 7, and drying under vacuum at 60 °C. A comparative set of samples were prepared by thermal annealing in a tubular furnace (250–900 °C, 1–4 hrs) under an inert N_2 flow. The thermal annealing studies were prone to form titanium phosphates, in contrast, the optimised MW reactions ($Ti_3C_2T_X$:Phytic acid (1:10), 700 W MW, 2 mins), 2 mins (P-Ti_3C_2-MW-PA@1:10)) delivered P-doped Ti_3C_2 MXenes without phosphates present. It was proposed that MW irradiation generates rapid localised heating (1200 ℃) initiating the decomposition/reduction of phosphate dopants into phosphate ions and carbonaceous residue, thus promoting rapid P-doping into the $Ti_3C_2T_x$ lattice site. The combination of the $Ti_3C_2T_x$ surface, phytic acid, and H_2O, creates a favourable matrix that enhances MW absorbance to generate heat through interfacial and/or dipolar polarization (TiO(H), Ti-F, P-O, and H-OH dipoles). The successful intercalation of phytic acid into the hydrophilic negatively charged $Ti_3C_2T_x$ MXene was not just electrostatically more favourable than for the other phosphate compounds, but also the role of H-bonding in the aqueous surface environment would be significant in enhancing the colloidal stability. XPS deconvolution of the Ti 2p spectrum revealed peaks for Ti-P bond ($2p_{1/2}$, 456 eV, and $2p_{3/2}$, 461.4 eV) ascribed to substitution of C atom by P in the $Ti_3C_2T_x$ lattice. The P 2p peaks were assigned to P-O-Ti (132.5 eV) and P-O (133.5 eV) indicating adsorption/substitution of the surface functional groups by the P dopant. A peak assigned as a P-C bond (131.3 eV) was suggested as P-doping of the exposed edges of $Ti_3C_2T_x$. The extent of optimal P-doping was assessed as 3.80 wt% by EDS, or 3.77P at%, by XPS. The microwave generated titanium phosphate free P-Ti_3C_2 MXene provided an increased interlayer spacing (1.18 nm) with a significantly improved surface area (6.7-fold) over that of $Ti_3C_2T_x$ (0.98 nm). This afforded a wealth of phosphorous redox-active sites and elevated electronic conductivity that remarkably enriched the MXenes pseudo capacitance capability. Optimal supercapacitor performance was realised for the titanium phosphate free P-Ti_3C_2-MW-PA@1:10 flexible supercapacitor devices with outstanding volumetric capacitance (~1201 F cm^{-3}), energy density (41.7 W h L^{-1}), and power density (712.5 W/L), that not only exceeded pristine $Ti_3C_2T_x$ based supercapacitor devices but also all other doped MXene devices.

Qu *et al.* successfully explored the introduction of phosphorus and oxygen as dopants for Mo_2CT_x MXenes as potential electrocatalysts for HER.[37] The Mo_2CT_x MXene was etched from a stirred Mo_2Ga_2C MAX phase and LiF/HCl solution mixture (35 °C, 160 h) to remove Ga layers. The work up involved washing in degassed DI water to a pH > 6, and centrifugation (3500 rpm, 1 h). The Mo_2CT_x collected from the supernatant was dried in vacuo. Preparation of the P-doped Mo_2CT_x MXenes, involved separate ceramic boat samples of red phosphorous (P) and Mo_2CT_x loaded into a tube furnace with P upstream in a furnace under Ar atmosphere (550 °C for 30 min, 10 °C min^{-1}, Ar flow (50 SCCM)). Energy-dispersive X-ray spectroscopy (EDS) mapping indicated P was distributed uniformly throughout the P– Mo_2CT_x MXene. XPS spectra revealed increased P and O atoms for P–Mo_2CT_x in comparison with pristine Mo_2CT_x, along with the deconvolution of the Mo 3d peak revealing Mo–P signals at 231.6 eV and 228.1 eV, and a P $2p_{3/2}$ peak at 129.4 eV ascribed to P–Mo bond.

2.2.4. Dual doping

Dual doping with two different heteroatoms (N and S, or N and P) into a material allows for versatility in the creation of more defects whilst also providing for more active sites, as well as influencing interlayer spacing of 2D materials. The introduction of such can also facilitate single metal atom coordination into the material, thus further enhancing the material's properties and diversifying their range of applications. Each of the processes for the heteroatom doping enacted by the various research groups achieved significant outcomes in respect to their aims, however, the nature of those processes were varied in their impact to the degree of heteroatom doping, the diversity of heteroatom bond formation or replacement (with resident Ti, C, or O) and location of heteroatom dopants (carbon lattice substitution (LS), –OH function substitution (FS), or -O termination surface absorption (SA). Bai *et al.* produced nitrogen, phosphorus-doped $Ti_3C_2T_x$ MXene quantum dots (MQDs) for colorimetric/fluorometric dual-modal sensors for nitrite assay.[65] They prepared an aqueous solution of $Ti_3C_2T_x$ MXene, H_3PO_4, and formamide, adjusted to pH 9.0 using ammonia, after which the reactants were subjected to MW irradiation (800 W, 120 ℃, 30 min). Work-up involved centrifugation (5000 rpm, 10 min), and membrane filtration (220 nm) of the supernatant, and drying under vacuum to give N, P- $Ti_3C_2T_x$ MQDs with consistent uniformity in size (3.11 ± 0.86 nm) and QY of 21.5%. XPS spectral survey displayed peaks at 401.3, 134, 192 eV confirming the presence of dopant elements for N 1 s, P 2p, and P 2 s, respectively in N, P- $Ti_3C_2T_x$ MQDs. Deconvolution of the N 1 s spectrum displayed peaks at 399.6, 400.4 and 401.9 eV, attributed to N–H, N–$(C)_3$ and N-N/N-P, respectively, whilst the P 2p peak deconvolution revealed peaks at 132.76 and133.7 eV, for P-O and P-C/ P-N. Other new peaks at 459.2 and 462.3 eV were attributed to Ti(2) $2p_{3/2}$, and Ti(3) $2p_{1/2}$, anticipated characteristic peaks for N, P-$Ti_3C_2T_x$ MQDs. Similar to that of Gupta *et al.*, there was no evidence of titanium phosphates having been

formed.[64] Xia et al. created N, P- doped MXene ribbons for electrochemical stripping analysis sensor for multiple heavy metal ions. [66] Pristine $Ti_3C_2T_x$ was cut into ribbons by stirring in a KOH solution under N_2 atmosphere at 25 ℃ for 108 h. The nanoribbons were washed and dried before combining with diammonium phosphate solution (N,P-dopant), and subjected to hydrothermal conditions (120 °C, 12 h), after which the product was filtered, washed, and dried to yield N,P-$Ti_3C_2T_x$ ribbons. XPS spectra confirmed successful N and P heteroatom doping of N,P-$Ti_3C_2T_x$ ribbons with characteristic peaks of N 1 s and P 2p. The N 1s peaks centred at 401.6, 399.8, and 397.5 eV, corresponded to graphitic-N (SA), pyrrolic-N (FS), and pyridinic-N (LS), respectively, whilst the P 2p spectrum was deconvoluted for P- bonds at 134.0, 133.3, 132.8 and 130.1 eV and assigned as the corresponding P-O, P-N, P-C, and P-Ti bonds. Interestingly, there was no indication of titanium phosphates being present in these materials, possibly a consequence of the morphology of the materials produced compared to that of the thermally annealed materials by Gupta *et al.*[64] With N,P co-doping, an enhancement of the electrochemical activity and conductivity was observed for the N,P-$Ti_3C_2T_x$ ribbons. The N,P-$Ti_3C_2T_x$ ribbons provided improved adsorption and reducing capabilities for Cu^{2+} and Hg^{2+} for advanced sensing performances with electrodeposition-free detection (LODs of 1.8 nM and 0.29 nM respectively), outperforming that of $Ti_3C_2T_x$R and other materials. Chen *et al.* explored application of N,S doped MXenes in the development of colorimetric and electrochemical coupling sensors for uric acid detection.[67] They proceeded with grinding thiourea with $Ti_3C_2T_x$ MXene before annealing the sample in a tubular furnace (500 °C, 3hrs) under argon atmosphere. The product was grounded and washed with DI water until a pH 7, and dried to yield N,S-$Ti_3C_2T_x$ MXene. Characterization by XPS spectral survey of N,S-$Ti_3C_2T_x$ MXene revealed within the C 1s region on deconvolution the presence of C–S–C and C–N–C bonds at 284.9 eV and 286.0 eV respectively. Within the N 1s spectrum, peaks could be attributed to pyridinic-N (398.2 eV), pyrrolic-N (399.6 eV), graphitic-N (401.5 eV) and oxidized-N (402.4 eV). Among the four characteristic S 2p peaks indexed to C–S (2p3/2), C–S(2p1/2), was C = S and C-SOX-C, along with the presence of C–S–C moiety reinforced with an assignment of S $2p_{3/2}$ and S $2p_{1/2}$ to peaks at 163.0 eV and 164.18 eV. Notably, among the Ti 2p data, none was observed for the existence of Ti–S or Ti–N species; it was speculated that the Ti atoms may have experienced replacement by the S atoms or N atoms rather than bonding with Ti. The N, S co-doping for formation of N,S-Ti_3C_2 allowed S to increase the interlayer distances of the MXene, improving catalytic site access, and for N to promote electron transport efficiency, properties that provided significantly greater performances for NS-Ti_3C_2 NSs-modified glassy carbon electrode (GCE) for the electrochemical redox of 3,3′,5,5′-tetramethylbenzidine (TMB) and H_2O_2 compared to Ti_3C_2 NSs/GCE.

Yang *et al.* studied the use of N and S heteroatoms for introducing defects in to MXenes to expand the interlayer spacing for increased ion transfer in the charge/discharge process for energy storage systems.[53] They proceeded by stirring $Ti_3C_2T_x$ MXene powder in an aqueous ammonium citrate solution for 4 h, where the ammonium citrate had a dual role as an intercalant to facilitate interlayer access for sulfur, as well as a N-dopant on degradation in the thermal annealing process. The intercalated sample was dried and placed in a ceramic boat. A separate ceramic boat contained sulfur and both were loaded into a tube furnace with sulfur upstream in a furnace under Ar atmosphere at the desired temperatures (200 °C, 400 °C and 600 °C for 2 h, 5 °C min^{-1}, Ar flow (0.1 L min^{-1}): the optimal temperature found was 400 °C. High resolution XPS spectra of the N,S-$Ti_3C_2T_x$ MXene for the deconvoluted S signal presented just two peaks at 163.5 and 164.7 eV, attributed to the S2p3/2 and S2p1/2 for Ti–O–S. This reflected a surprising lack of diversity of sulphur present in the material, particularly when considered against that achieved by Chen *et al.*. [67] The spectral survey revealed three peaks within the N1s spectra at 396.0, 399, and 401.7 eV, assigned to lattice substitution, functional group substitution and surface absorption, respectively. However, the degree of heteroatomic doping revealed by XPS (1.3 at% sulfur and 1.4 at% nitrogen) was significant in the as prepared N,S-$Ti_3C_2T_x$ MXenes. The introduction of the dual dopants, N and S, expanded the MXenes' interlayer spacing thus allowing for more active sites and facilitating increased intercalation, whilst also inducing changes in the electronic structure that improved ion transfer kinetics for charging/discharging processes. The optimal N, S co-doped $Ti_3C_2T_x$ MXene exhibited excellent gravimetric capacitance (495 F g^{-1} at 1 A g^{-1}, compared to pristine $Ti_3C_2T_x$ (321 F g^{-1} at 1 A g^{-1})), rate capability (180 F g^{-1} at 10 A g^{-1}) and cycle stability (98% retention over 6000 charge/discharge cycles).

Zhang *et al.* sought to mitigate difficulties encountered in ion transport within electrodes for lithium-ion batteries (LIBs) by application of N, S co-doped V_2CT_X MXenes for anodes. [68] Preparation of V_2CT_X MXene was processed by HF etching of V_2AlC MAX phase (40% conc., 35 °C, 5 days). After centrifugation, washing (pH 7), and freeze-drying (24 h), the V_2CT_X MXene was mixed to uniformity with thiourea, and underwent thermal annealing at a desired series of temperatures (500 °C, 600 °C and 700 °C, 3 h, 2 °C min^{-1}, N_2 atmosphere) to yield under optimal conditions (600 °C) the N, S co-doped V_2CT_X MXene. A range of new peaks in the XPS survey presented for the co-doped N,S-V_2CT_X MXenes that were not present in the pristine V_2CT_X MXenes along with a reduction/disappearance of other peaks. The S 2p XPS spectrum showed two peaks at 163.2 and 167.8 eV attributed to the S 2p3/2 and S 2p1/2 peaks respectively for the C-S-C bond. This was complimented by the XPS spectra of C 1s assigned for a strong C-S bond at 285.4 eV. The deconvoluted N 1s spectrum showed peaks at 396.8, 398.6, and 400.1 eV that were respectively assigned as V-N, pyridinic N, and pyrrolic N. XPS analysis revealed quite a remarkable degree of heteroatomic doping of 8.3 at% for sulfur and 20.3 at% for nitrogen for the as prepared co-doped N,S- V_2CT_X MXenes at 600 °C. The effective N and S co-doping significantly improved electrochemical reactivity and charge transfer ability, increased interlayer spacing, and promoted effective diffusion of ions and electrons. The optimal performing samples, N,S-V_2CT_X, demonstrated greater reversible capacity (590 mAh g^{-1} at 0.1 A g^{-1} after 100 cycles), and rate capability (347 mAh g^{-1} at 1 A g^{-1} and 171 mAh g^{-1} at 5 A g^{-1}) with long-term cycling stability (298 mAh g^{-1} after 300 cycles at 2 A g^{-1}), than other reported V_2CT_x-based anode materials (*ibid.* 15 & 16). Tan group explored N,S-co-doping of $Ti_3C_2T_x$ MXene for facilitating single-metal sites for HER electrocatalysis with an Ir atom. A condensed colloidal solution of melamine hydrochloride with pristine $Ti_3C_2T_x$ was mixed with thiourea and H_2IrCl_6, then freeze dried for 72 h, and pyrolyzed in Ar (550 ℃, 2 h, 5 ℃ min^{-1}) to yield porous N,S-co-doped $Ti_3C_2T_x$ MXene [69]. High-resolution XPS analysis confirmed a peak for N 1s, which deconvoluted revealed four peaks attributed to Ti–N (396.3 eV), pyridinic-N (397.5 eV), N–Ti–O (398.6 eV), and pyrrolic-N (399.5 eV), for NS-$Ti_3C_2T_x$. The S 2p spectrum was deconvoluted into six components: S–Ti (160.5 eV), chemisorbed S (161.7 eV), Ir–S (162.4 eV), S–C (163.3 and 165.0

eV), and sulfate species (168.0 eV), and a Ti 2p peak at 455.7 eV attributed to Ti–N bonds confirming successful formation of N,S-co-doped $Ti_3C_2T_x$ MXene. Both Ir–N bonds and Ir–S bonds were also identified by high-resolution XPS data confirming Ir coordination within the porous heteroatom in Ir-N,S-$Ti_3C_2T_x$ MXenes. The effectiveness of the doping for HER electrocatalysis is discussed later in 4.1.1, Hydrogen evolution reaction (HER).

2.2.5. Halide (F, Cl, Br, I) doping: Opening new avenues

Fluoride doping in MXenes is well established by default since the very first preparation of MXenes by Naquib *et al.* due to the ubiquitous etching process via either HF acid solution or LiF/HCl solutions. [14] Because of the very nature of the etching solutions, there is also concomitant oxidation, hydroxylation, and possible chlorination of the surface terminations of MXenes with limited control. Whilst the surface termination groups of etched MXenes can be eliminated or exchanged using various energetic methodologies such as hydrothermal, solvothermal, or calcination; the hazardous fluoride etching route of the MAX phase is still relatively restrictive and limiting. The resultant MXene T_x surface groups composed of M−F and M−O bonds are far stronger than for example either M−Cl or M−Br, thus making it challenging for controlled and tunable covalent surface modifications post MXene synthesis for tailoring to desired applications. However, a safer more recent fluoride free approach has been developed that opens a plethora of opportunities in advancing MXene preparation allowing for the introduction of more modifiable surface metal halide terminations. Using molten salts for etching MAX phase allows for the transformation of MXenes with excellent uniformity in termination groups that are readily modifiable to the desired MXene composition of choice. [70] This has allowed halides other than just fluorine to be easily introduced, such as chlorine, bromine, or iodine, with up to 100% coverage as termination groups, i.e., elimination of unwanted oxidation and hydrolysis. Whilst fluoride termination bonds are very stable, chlorides and bromides on the other hand are more labile and provide opportunities to readily substitute with group 6 elements (oxygen, sulfur, selenium, tellurium) or –NH groups, to the desired degree, or alternatively the labile halide can be readily removed to create vacancy sites. Significantly, this not only allows researchers to by-pass the hazardous HF etching process but offers a possibly greener chemistry process with far more access to tailoring the surface chemistry of MXenes, and excitingly, an unprecedented scalable approach to commercial production of MXenes.

The gateway to this ex-situ molten salt approach was first opened by Huang and co-workers introducing the late transition element, Zn, into the A site (Al) for a range of MAX phases (Ti_3AlC_2, Ti_2AlC, Ti_2AlN, and V_2AlC) by combining the respective materials with molten $ZnCl_2$ to yield new MAX phase materials (Ti_3ZnC_2, Ti_2ZnC, Ti_2ZnN, and V_2ZnC), and successively Cl-MXenes ($Ti_3C_2Cl_2$ and Ti_2CCl_2) with pure Cl termination thus eliminating unwanted oxidation and hydrolysis.[70] Based on their understanding of molten transition-metal halides ability to act as Lewis acids that can react thermodynamically with the A element of the MAX phases, and the liquid environment simultaneously allowing diffusion through the MAX phases 2D plane thus facilitating bonding with layer elements, they explored a range of variables (Al-MAX/$ZnCl_2$ molar ratio (1:1 to 1:6) and time (0.5 h to 5 h)) required to bring about changes. Their phase change studies identified that a molar ratio of 1:1.5 of the Al-MAX/$ZnCl_2$ powders (mixed and ground under N_2 and annealed at 550 °C for 5 h under Ar) was best for Zn-MAX formation, whilst a molar ratio of 1:6 for 5 h under similar treatment was best for Cl-MXene ($Ti_3C_2Cl_2$ and Ti_2CCl_2) formation. However, MXenes Ti_2NCl_2 and V_2CCl_2 were not formed due to anticipated higher M−A bonding energies within the respective Zn-MAX phases. The as-synthesised material was washed with 5 wt% HCl and DI water to remove any by-products of Zn before filtration. Based on their timeline study observations and analysis for the $Ti_3C_2Cl_2$ formation, they identified that this occurred via a two-step process with initial formation of Ti_3ZnC_2 followed by etching of the same by the excess molten $ZnCl_2$ to form $Ti_3C_2Cl_2$ via a proposed reaction mechanism involving a low valence Zn_2^{2+} cation as follows in equations 1 to 7:

$$Ti_3AlC_2 + 1.5ZnCl_2 = Ti_3ZnC_2 + 0.5Zn + AlCl_3\uparrow \quad (1)$$

$$Ti_3AlC_2 + 1.5ZnCl_2 = Ti_3C_2 + 1.5Zn + AlCl_3\uparrow \quad (2)$$

$$Ti_3C_2 + Zn = Ti_3ZnC_2 \quad (3)$$

$$Ti_3ZnC_2 + ZnCl_2 = Ti_3C_2Cl_2 + 2Zn \quad (4)$$

$$Ti_3ZnC_2 + Zn^{2+} = Ti_3C_2 + Zn_2^{2+} \quad (5)$$

$$Ti_3C_2 + 2Cl^- = Ti_3C_2Cl_2 + 2e^- \quad (6)$$

$$Zn_2^{2+} + 2e^- = 2Zn \quad (7)$$

XPS confirmed peaks for Ti–C (I) ($2p_{3/2}$), Ti–C (II) ($2p_{3/2}$), Ti–C (I) ($2p_{1/2}$), Ti–C (II) ($2p_{1/2}$) bonds (454.4 eV, 455.7 eV, 460.3 eV, 461.8 and 464.1 eV, respectively) as well as peaks for Ti–Cl ($2p_{3/2}$) and Ti–Cl ($2p_{1/2}$) bonds (458.1 and 464.1 eV). Interestingly, the XRD recorded *c* lattice parameters (22.24 Å) for $Ti_3C_2Cl_2$ are not only in good agreement with DFT calculated values (22.34 Å) but significantly larger than those prepared by HF etching for $Ti_3C_2T_x$ ($Ti_3C_2(OH)_2$ (19.49 Å) and $Ti_3C_2F_2$ (21.541 Å)). [14] Huang and co-workers have since proposed a generalized and systematic approach for molten salt etching in the preparation of MXenes for their interests in enhancing development of negative-electrode materials for electrochemical energy storage. [71] Their approach in planning the respective syntheses was to predict via a Gibbs free energy map based on thermodynamic calculations (@700 °C) of the relevant electrochemical redox potentials for the MAX phase A-site elements and chloride Lewis acid molten salt cations. This allowed them to strategically choose the most effective combinations that would allow etching based on the Lewis acid molten salt having a higher redox potential. Using this strategy, they successfully exfoliated eight MAX phases (Ti_2AlC, Ti_3AlC_2, Ti_3AlCN, Nb_2AlC, Ta_2AlC, Ti_2ZnC and Ti_3ZnC_2) into seven corresponding MXenes (Ti_2CT_x, $Ti_3C_2T_x$, Ti_3CNT_x, Nb_2CT_x, Ta_2CT_x, Ti_2CT_x, $Ti_3C_2T_x$) through the suitably chosen molten chloride salts ($CdCl_2$, $FeCl_2$, $CoCl_2$, $CuCl_2$, AgCl, $NiCl_2$).

The Highlighting Ti_3SiC_2 MAX precursor as an example for etching, $Ti_3C_2Cl_2$ MXene was prepared from an eutectic preparation of Ti_3SiC_2:$ZnCl_2$:NaCl:KCl (molar ratio of 1:3:2:2) at 750 °C (4 °C min^{-1}, 24 h) molten mix under argon, and on cooling, washed with DI water to remove salts but leaving Cu metal behind, so denoted $Ti_3C_2Cl_2$-Cu MXene. The authors proposed that the weakly bonded Si is readily oxidized to Si^{4+} (Si^{4+}/Si redox potential of −1.38 V) with concomitant reduction of Cu^{2+} to Cu (Cl_2/Cl^- redox potential of −0.43 V for $CuCl_2$ molten salt), with the excess Cu^{2+} also partially oxidising layered Ti, thus allowing charge compensation by Cl^- anions to form the product $Ti_3C_2Cl_2$ MXene, along with by-products Cu metal and volatile $SiCl_4$ (equations 8 and 9). The authors have drawn an analogy with the etching process for Ti_3AlC_2 in HF solution where Cu^{2+} and Cl^- act as H^+ and F^-, respectively.

$$Ti_3SiC_2 + 2CuCl_2 = Ti_3C_2 + SiCl_4\uparrow + 2Cu \quad (8)$$

$$Ti_3C_2 + CuCl_2 = Ti_3C_2Cl_2 + Cu \quad (9)$$

To remove the Cu metal by-product, the as-synthesised $Ti_3C_2Cl_2$-Cu MXene was washed with ammonium persulfate ($(NH_4)_2S_2O_8$) solution, a strong oxidising agent. This resulted in the introduction of O as a surface termination group. The new material was referred to as MS-$Ti_3C_2T_x$ MXene, where T_x represents both O and Cl termination groups, and MS referring to its molten salt origin. The oxidation demonstrated the ease with which the Cl termination groups can be replaced allowing for the introduction of terminal dopants. Oxidation can be avoided using a 0.1 M aqueous solution of $FeCl_3$ to remove copper. CHNO combustion elemental analysis revealed circa 12 wt% and 14 wt% for the O- and Cl-termination-groups respectively in MS-$Ti_3C_2T_x$ MXene, indicating elemental composition of $Ti_3C_{1.94}Cl_{0.77}O_{1.71}$. The authors also introduced Ga as an A-site element in preparation of Ti_2GaC MAX-phase via this strategy (Ti_3SiC_2: $GaCl_2$ (molar ratio of 1:1.5), as well as having prepared Br-MXene and I-MXene from Ti_3AlC_2 with $CuBr_2$ and CuI molten salts respectively. The groups analysis of MS-$Ti_3C_2T_x$ MXene for electrochemical performance demonstrated the highest capacitance values reported for any Ti_3C_2 MXenes in non-aqueous electrolytes.

Kamysbayev *et al.* investigated the influence of tailored surface modifications on structural and electronic properties of MXenes using molten inorganic salts (eutectic melts). [72] They prepared MXenes, $Ti_3C_2Cl_2$, Ti_2CCl_2, and Nb_2CCl_2, from MAX phase Ti_3AlC_2 with $CdCl_2$ molten salt, as well as $Ti_3C_2Br_2$ and Ti_2CBr_2 from the same MAX phase but with CdBr molten salt. They were also able to demonstrate the ease of substitution of Cl- and Br-terminated MXenes for other atoms and functional groups in contrast to O- and F-terminations. Examples provided included Ti_3C_2Te and Ti_3C_2S from $Ti_3C_2Br_2$ MXene in a eutectic solution of CsBr-KBr-LiBr with Li_2Te and Li_2S, respectively. Introduction of telluride terminations showed significant in-plane lattice expansion (>18%). Other examples of substitution were Ti_3C_2Se, Ti_3C_2O, and $Ti_3C_2(NH)$ MXenes from reactions of $Ti_3C_2Cl_2$ and $Ti_3C_2Br_2$ with Li_2Se, Li_2O, and $NaNH_2$, respectively.

Treatment of the multilayered $Ti_3C_2T_n$ MXenes (T = Cl, S, NH) with n-butyl lithium introduced a negative surface charge thereby allowing intercalation of Li^+ between the layers. This facilitated easy dispersion of the MXenes in polar organic solvent (N-methyl formamide) providing a stable colloidal solutions of single layer flakes. The authors were also able to achieve the highlighted surface modifications for Ti_2CCl_2, Ti_2CBr_2, and Nb_2CCl_2. Through reductive elimination of $Ti_3C_2Br_2$ and Ti_2CBr_2 with LiH at 300 °C, bare $Ti_3C_2\square_2$ and $Ti_2C\square_2$ MXenes (□ = vacancy site) were also created. HAADF analysis confirmed the vacancy sites by revealing the center-to-center distance between the Ti_3C_2 sheets was 7.59 Å, as opposed to a theoretical predicted value of 8.26 Å for $Ti_3C_2H_2$ and a predicted smallest spacing value of 7.23 Å. They also demonstrated that surface modifications for Nb_2CT_n MXenes (T = S, Se, NH) influenced control in superconductivity.

Sarfraz *et al.* developed Cl-doped MXene ($Ti_3C_2Cl_2$) electrodes for electrocatalytic water splitting (OER and HER) in alkaline media. [73] Preparation involved grinding MAX phase powder (Ti_3AlC_2) with copper chloride ($CuCl_2$) in a 1:6 M ratio, that was then subjected to 550 °C under an argon atmosphere for 5 h in a tube furnace. After cooling, the work up involved 5% HCl treatment for 2 h to remove any residual copper contaminants, followed by centrifugation (4000 rpm for 5 min), washing with deionized water and then drying at 60 °C. XPS data analysis revealed peaks for Cl 2p at 198.5 and 200 eV confirming the Ti-Cl bonds of $2p_{1/2}$ and $2p_{3/2}$, respectively. Peaks for Ti-C $2p_{3/2}$ and Ti-C $2p_{1/2}$ bonds were also determined at 456.7 and 461.89 eV, respectively. The prepared $Ti_3C_2Cl_2$ MXene electrodes exhibited good electrocatalytic activity for HER and OER in 1 M KOH with an overpotential of 259 mV and Tafel slope of 92 mV dec^{-1} (at 10 mA cm^{-2} current density) and 330 mV and 48 mV dec^{-1} (30 mA cm^{-2} current density) respectively. This was superior to electrodes prepared from HF etched MXene, $Ti_3C_2T_x$, for HER (overpotential of 444 mV, Tafel slope of 311 mV dec^{-1}) and OER (overpotential of 390 mV and Tafel slope of 136 mV dec^{-1}). The improved performances were attributed to the increased interlayer spacing and greater stability due to structural enhancement afforded by uniform Cl terminations over that of the mixed F and O terminated MXenes.

An interest in chloride-ion batteries (CIBs) led to Zhu *et al.*'s preparation of Cl-terminated MXene ($Ti_3C_2Cl_2$) as a cathode material that allowed for high Cl^- capacity with low Cl^- diffusion barrier for chloride-ion hybrid capacitors (CHCs).[74] Mixing a stoichiometric molar ratio (1:3) of MAX Phase Ti_3AlC_2 and $CuCl_2$ with NaCl and KCl as a Lewis-acidic-melt (700 °C, argon, 24 hrs) yielded the $Ti_3C_2Cl_2$ MXene after $NH_3{\cdot}H_2O/NH_4Cl$ solution work up. High-resolution XPS analysis confirmed Ti 2p peaks at 463.0/456.7 and 464.3/458.4 eV bonds for the Ti–Cl and Ti–O bonds, respectively, and the presence of Ti–Cl bond further confirmed with respective Cl $2p_{3/2}$ and $2p_{1/2}$ peaks at 198.7 and 200.4 eV. The presence of Ti–O bond was attributed to oxidation in the work up wash, however, the XPS assessed atomic ratio of Ti to Cl as 3:1.59 in the $Ti_3C_2Cl_2$ MXene, indicating close to complete Cl-termination of the MXene. The $Ti_3C_2Cl_2$ based electrode demonstrated a gravimetric capacity of 536 mAh·g^{-1} with impressive Coulombic efficiency (>99.5% after 1000 cycles at a current density of 0.2 A·g^{-1}) whilst the $Ti_3C_2Cl_2$ Mxene's rate capability of 181 mAh·g^{-1} (at 0.2 A·g^{-1}), was superior to that of HF prepared $Ti_3C_2T_x$ (96 mAh·g^{-1}) for CHCs.

Gong *et al.* recognizing that regulating the surface terminations of MXenes was a major challenge for enhancing the electrochemical performance in pseudocapacitor performance. [75] They set about by-passing the typical resultant deleterious surface terminations (F,

OH, and O) obtained in MXenes by HF etching of the MAX phase material, by instead taking a top-down (ex-situ) approach in introducing iodine terminations via a facile Lewis-acidic-melt etching method using CuI with the MAX phase to form the I-doped $Ti_3C_2T_x$ MXene. The MAX phase, Ti_3AlC_2 (0.5 g), was mixed and ground with CuI (3 g) under Ar, and placed in an alumina crucible and calcinated at 700 °C (4 ℃/min) for 9 h under Ar. On cooling, the mixture was washed with $NH_4Cl/NH_3{\cdot}H_2O$ solution, then DI water, and freeze dried to yield I-Ti_3C_2 MXene. XRD data of the as synthesised I-Ti_3C_2 MXene revealed that the characteristic peaks of Ti_3AlC_2 had disappear. XPS analysis revealed peaks for Ti 2*p*, confirming the presence of Ti–I and Ti–O bonds, due to –I and –O surface terminations, as well as Ti–C bonds. In addition, the Ti–I bond was further confirmed by the presence of I 3*d* peaks in the spectral analysis of I-Ti_3C_2 MXene. The successful introduction of iodine terminations of I-Ti_3C_2 MXene demonstrated remarkably higher specific capacitance than for pristine $Ti_3C_2T_x$ MXene with incredible long-term cyclic performance at high current density (50 A/g) and 91% specific capacitance retention after 100,000 cycles, with average specific capacitance loss of only 0.00009% per cycle.

Taking the more traditional approach with HF etching, I-doped $Ti_3C_2T_x$ MXenes were prepared by Yu *et al.* as a catalytic layer in Li–S batteries for trapping of lithium polysulfides (LiPS) and suppression of the shuttle effect thus, reportedly, enhancing the electrochemical performance of Li–S batteries tested. [76] They ground together potassium iodide (500 mg), with few-layered $Ti_3C_2T_x$ MXene(200 mg), and then transferred the mixture to a quartz porcelain boat for calcination in a tubular furnace at 500 °C (5 °C min^{-1}) for 12 h under Ar gas. On cooling, the sample was washed with acetone and vacuum dried overnight to yield I-$Ti_3C_2T_x$ MXene powder. High-resolution XPS survey of I-$Ti_3C_2T_x$ MXene displayed $3d_{5/2}$ and $3d_{3/2}$ peaks, at 618.5 and 630.0 eV, corresponding to the Ti–I bond and atomic iodine (I^-), respectively, thus confirming chemical bonding of the atomic iodine with MXene. XRD confirmed an enhanced interlayer distance for the as synthesised I-$Ti_3C_2T_x$ MXene due to iodine-doping. A DFT computational study investigated structural arrangements and binding energy between I-MXene and polysulfides. Data calculated based on the optimized structure of $Ti_3C_2T_x$ and as tested for various surface functional groups, revealed that $Ti_3C_2I_2$ had the lowest band gap, a value near 0 eV, of those studied ($Ti_3C_2(OH)_2$, $Ti_3C_2F_2$, $Ti_3C_2O_2$, $Ti_3C_2Cl_2$), implying iodine-doping can enhance electronic conductivity.

2.2.6. Oxygen doping

The ubiquitous functionalization with a non-uniform mixture of OH, F, Cl, and O, as terminal groups that comes with the HF etching process of MXenes reflects the persistent challenge in functionally tuning MXenes. Among the terminal atoms of interest in the tuning of MXenes is oxygen,[77] which based on extensive theoretical/computational (DFT) studies suggest favorable enhancements for electrochemical energy storage [78], semi conduction [79], hydrogen evolution reaction [80], photocatalysis [81], piezoelectricity [82], topological insulator [83], sensors [84], and superior mechanical strength [85]. However, controlled oxidation of MXene surfaces is not trivial where non-selective or over oxidation leads to structural issues in phase stability or oxide formation, respectively, a significant detrimental risk in preparation.[86] Given oxygens' greater electronegativity (O (3.44), C (2.55), S (2.58), N (3.04)), its impact as a dopant is expected to reflect significant modulation of the electron distribution and cloud density of doped MXenes, particularly as a surface termination group, impacting on the intrinsic surface chemistry. As a global surface termination group, oxygen would also be expected to increase electrostatic repulsion between the MXene 2D nanosheets deterring agglomeration.

Exclusive termination with O of MXenes ($M_{n+1}X_nO_2$) had proved elusive till Persson *et al.* explored the limitations of tuning and tailoring of $Ti_3C_2T_x$ MXene surface.[77] Their preparation involved drop-casting 0.1 μL colloidal suspension of $Ti_3C_2T_x$ singe-flakes (20 × 20 μm) (prepared from LiF– HCl solution) on a DENS solutions Wildfire nanoreactor chip for HRTEM image acquisition and EELS. In-situ data collection was procured in high vacuum with sequential 2 mbar O_2 exposures for single sheets for temperatures ranging from RT to 450 °C. The HRTEM and EELS analysis confirmed exclusive O termination on MXene surfaces ($Ti_3C_2O_2$) over a temperature range of 100 – 250 °C. Temperatures above this up to 400 °C led to supersaturation ($x \approx 3.5$) whilst still maintaining a stable MXene sheet structure. However, extended O_2 exposure at 450 °C resulted in destabilization of the MXene structure with C loss and TiO_2 formation.

Jiang *et al.* explored the removal of the detrimental fluorine for oxygen terminations from MXenes for the hydrogen evolution reaction, citing that a previously published DFT study indicated that oxygen terminations would favourably lower ΔG_{H^*} (0.00283 eV) suggesting the changes would make the MXene an ideal electrocatalyst for HER activity.[80] Pristine $Ti_3C_2T_x$ nanosheets etched from Max Phase Ti_3AlC_2 (HF solution, DMSO-intercalation, isolated via centrifugation) were subjected to 10 wt% KOH solution (4hr, RT) to remove F terminal groups for OH groups to form $Ti_3C_2(OH)_x$ MXenes. Both the pristine $Ti_3C_2T_x$ nanosheets and as prepared $Ti_3C_2(OH)_x$ were calcined (450 °C, 3hr, Ar), dehydrating the MXene surfaces forming O terminal groups from the OH groups, denoted $Ti_3C_2T_x$-450 and $Ti_3C_2O_x$, respectively. The high-resolution XPS survey for pristine $Ti_3C_2T_x$ displayed peaks for F 1s and O 1s orbitals attributed to Ti–F terminations, and Ti–OH (532.3 eV) and Ti–O (530.4 eV) terminations, respectively. The base treated MXenes ($Ti_3C_2(OH)_x$) displayed almost complete removal of the Ti–F peak, but with significant concomitant increase in peak intensity for Ti–OH bond. XPS of the calcinated $Ti_3C_2(OH)_x$, revealed <5 % Ti–OH was left on the as prepared $Ti_3C_2O_x$, surface. These results combined with HRTEM and XRD data confirmed calcination as an effective approach for $Ti_3C_2O_x$ MXene preparation without detriment to morphology and structure. The $Ti_3C_2O_x$ MXene exhibited superior HER activity (190 mV overpotential at 10 mA cm^{-2} and Tafel slope of 60.7 mV Dec^{-1}) in acidic media (in 0.5 m H_2SO_4) with long-term stability over that of its as prepared analogues, $Ti_3C_2T_x$-450 and $Ti_3C_2(OH)_x$ (266 and 217 mV at a current density of 10 mA cm^{-2} and Tafel slopes of 109.8 and 88.5 mV Dec^{-1} respectively). Confirmation that the O terminations rather than the OH terminations on the basal plane of Ti_3C_2 that provide active catalytic sites large with surface area and high conductivity for the superior HER performance.

In pursuance of non-noble-metal heterogeneous catalysts for dehydrogenation of HCOOH, Hou *et al.* explored modifying the terminal groups Ti_3C_2Tx MXenes with O terminations. [87] Pristine Ti_3C_2Tx MXene samples were heated in a muffle furnace under air at 150, 250, and 350 °C for 1 hr. Each of the treated samples exhibited under HAADF-STEM analysis nanosheet morphology resembling that of the pristine Ti_3C_2Tx MXene. The 250 °C sample had lattice spacing of 2.6 Å, consistent with the (0110) crystal plane for the

pristine Ti_3C_2Tx MXene. XPS survey analysis was performed for each of the treated Ti_3C_2Tx MXene samples, and identified were four O 1s peaks at 533.7, 532.2, 531.7, and 529.7 eV attributed to the surface-adsorbed O, O-Ti bond, Ti-OH bond, and lattice oxygen in TiO_2, respectively. Peaks attributed to O-Ti grew for each sample with increasing temperature such that the percentages of O-Ti bonds were estimated as 3.4, 7.3, and 26.5% for the pristine Ti_3C_2Tx MXene, and Ti_3C_2Tx samples treated at 150, and 250 °C, respectively. The TiO_2 at 529.7 eV was the dominant peak for the 250 °C sample. Further XPS analysis confirmed Ti 2*p* peaks at 461.1/455.3 eV, 464.4/458.8 eV, and 461.9/457.8 eV corresponding to Ti-C, Ti-O, and Ti-F, respectively. A progressive decrease in the Ti-F peak was also observed with the associated increased sample preparation temperature, along with the Ti-O peak being most prominent for the 250 °C treated sample. The 350 °C sample showed deterioration of the MXene where Ti-O peak was dominant but peaks for Ti-C and Ti-F were negligible. This was reflective of the experience discussed earlier by Persson *et al.*. [77] The $Ti_3C_2T_x$ prepared at 250 °C exhibited a mass activity of 365 mmol $g^{-1}h^{-1}$ with 100% of selectivity for H_2, twice that of commercially available Pd/C or Pt/C. This performance was attributed to the lowered reaction barrier energy for conversion of HCOO* to CO_2* and the role of the increased oxygen surface coverage of $Ti_3C_2T_x$ MXenes in weakening the adsorption energy for CO_2 and H_2.

Hart *et al.* investigated increased O functionalization for MXenes (Ti_2CT_x and $Mo_2TiC_2T_x$) through iterative vacuum annealing and Ar + O_2 low-power plasma annealing, in preparation of MXene for thin films. [88] This was in recognition of the prevailing challenges that remain in tuning the MXene surface termination groups and the promise predicted by previously mentioned DFT studies. The process was followed with in-situ monitoring using electron diffraction, electron spectroscopy, and resistance versus temperature (R *vs* T) analysis. The Mo_2TiC_2Tx was etched from Mo_2TiAlC_2 MAX powder (2 g, circa. 50% HF soln. (40 ml), 50 °C, 48 hr). Post etchant work up involved delamination (2.5 wt% tetramethylammonium hydroxide (TMAOH) solution (10 ml, 12 hr), repeated washing and centrifugation (pH of 7–8, 3 × (3500 rpm, 15 min)), where the final sedimentation was dispersed in 30 ml of DI water and centrifuged (3500 rpm, 30 min) for isolation of single- to few-layer MXene flakes in the supernatant. Single to a few layered flakes of the respective prepared MXenes (pristine Ti_2CT_x or Mo_2TiC_2Tx) were spin-coated (2000 rpm for 2 min, followed by 5000 rpm for 45 s) onto transmission TEM chip and treated in situ with Ar + O_2 plasma (100–300 °C, 1 °C /s, 80 % Ar and 20 % O_2, ~1 mbar, 18 W., 1 min). Vacuum annealing (~10^{-7} torr, 400–800 °C, 5 min) was used prior to plasma treatment to remove the non O termination groups (OH and F) and residual intercalants (H_2O, Li^+, and TMA^+). Alterations of the surface terminations for the respective MXenes ($Mo_2TiC_2O_x$ and Ti_2CT_x) was confirmed by electron energy loss spectroscopy (EELS) and rotationally averaged electron diffraction (RAED) data. These demonstrated that $Mo_2TiC_2O_x$ could undergo pure O functionalization with added value of being able to undergo reversible O addition and removal from the $Mo_2TiC_2O_x$ MXene surface. Global O termination for Ti_2CT_x, however, remained challenging due to residual F termination and limited thermal stability for Ti_2CT_x due to strong Ti–T bonds under the conditions explored. None the less the authors did achieve a degree of success with the preparation of $Ti_2CO_{1.8}F_{0.3}$ with fully saturated Ti surface sites whilst maintaining the intact Ti_2C structure. R *vs* T data revealed that increasing O termination increased electrical resistance, and both MXenes ($Mo_2TiC_2O_{2.1}$ and $Ti_2CO_{2.0}F_{0.3}$) were found to be metallic, with Ti_2CT_x approaching temperature independent resistance with increasing O termination. The authors also commented that the increased O termination for the MXenes studied reduced the surface M−site d orbital occupancy, which should afford insights into how surface termination alters MXene chemistry, properties relevant to many of its diverse applications.

Most of the reported O-doped MXene syntheses have been primarily ex-situ route processes. In their pursuit of developing MXene based supercapacitor electrodes, Tian *et al.* employed experimental and density-functional theory (DFT) to explore an in situ approach to oxygen doped MXenes via introduction of the O-dopant, aluminum oxide, in preparation of $Ti_3AlC_{2-\delta}O_\delta$ MAX phases. [78] Varying molar ratios of Ti metal powder, aluminium metal powder, titanium carbide powder, and aluminium oxide powder ((1 + δ): (1.2–1.5δ): (2-δ): δ (where δ was 0, 0.03, 0.05, 0.08 and 0.10, respectively) were milled and sintered (1350 ℃, 2 hr, Ar). XRD analysis of the microstructural properties for the doped material confirmed changes reflecting reduction of the interplanar spacing in the c-axis direction due to presence of shorter Ti-O bonds, and a shift in the (0 0 2) peak (9.44° to 9.50°) with increased O doping content, with maximum doping observed for the O-Ti_3AlC_2-0.08 sample. XPS analysis confirmed peaks for Al-Ti-O (530.3 eV) in the pristine Ti_3AlC_2, O-Ti_3AlC_2-0.05, and O-Ti_3AlC_2-0.10 with the Al-Ti-O bond content increasing 33.2%, 33.9%, and 35.5%, respectively, reflecting the increase in the doped oxygen content as well as confirming carbon atom substitution in the Ti octahedron. Flexible O-doped $Ti_3C_{2-\delta}O_\delta T_x$ MXenes were etched (LiF and HCl solution) from the respective $Ti_3AlC_{2-\delta}O_\delta$ MAX phases. High-resolution XPS survey revealed O1s spectra for the $Ti_3C_{2-\delta}O_\delta T_x$ MXenes, consisting of C-Ti-O bond, O-Ti-O bond, C-Ti-OH bond. It also revealed that the C-Ti-O, O-Ti-O, and C-Ti-OH bonds shifted to lower binding energies with the partial substitution of carbon atoms with oxygen dopant, confirming electron cloud density enhancement for the respective O-doped MXene samples. The significant increase in O-Ti-O bonds also reflected the conversion of –OH to -O termination in the $Ti_3C_{2-\delta}O_\delta T_x$ nanosheets which complimented observed increases in the interlayer spacing for the $Ti_3C_{2-\delta}O_\delta T_x$ MXenes due to O and -O repulsion. The increased partial substitution of carbon atoms (C-Ti-C bond to the O-Ti-C) was also supported by the observed peak shift for the Ti-C bond from 455.1 eV to 454.8 eV atom. The changes to the titanium octahedron through oxygen substitution was also supported by DFT. Electrochemical performances for the O-doped $Ti_3C_{2-\delta}O_\delta T_x$ MXene sample, O-$Ti_3C_2T_x$-0.05 film electrode, demonstrated a superior capacity of 306.0 C g^{-1} over that of the pristine $Ti_3C_2T_x$ electrode, 216.8 C g^{-1}. The improved capacitance capability being attributed to the higher Ti metal active centres, enhanced quantum capacitance, and higher adsorption energy, all contributing to improved diffusion-controlled capacitance and interface capacitance.

2.3. Doping by metallic elements

Doping by metal ions offers many other opportunities for manipulating the intrinsic properties of materials like MXenes. Introduction of metal ions into host materials (crystalline, amorphous, polymeric, composite) is employed in numerous applications. In the field of energy storage and conversion, metal ions intercalation processes into transition metal oxides, sulphides, phosphates are

significant and important. Many electrodes in batteries including graphite anodes, transition metal oxides, and phosphate cathodes, exhibit their redox activity via intercalation/deintercalation processes of metal ions (Li^+, Na^+, Mg^{2+}) accompanied by parallel changes in the transition metals oxidation states. It is important to distinguish between intercalation processes and that of doping host materials with metallic elements. Intercalation processes are massive, change drastically the hosts' stoichiometry, usually reversible, and thereby induce reversible structural and valence changes in the host materials. Doping by metallic ions is typically aimed at inducing irreversible structural changes that also change (positively) materials intrinsic properties. As an example in modulating intrinsic properties of MXenes, Peng *et al.*'s interest in electrocatalytic nitrogen reduction reaction (NRR) led to their preparation of NRR catalysts based on single-atomic Ru dopant in Mo_2CT_X MXene nanosheets (SA Ru-Mo_2CT_X) for nitrogen fixation at ambient conditions. [89] The Ru element within the Mo_2CT_X MXene nanosheets behaves as an active site for catalysis promoting N_2 activation and hydrogenation of the absorbed N_2. The effectiveness of the doping for NRR catalysis is discussed later in 4.1.3 Nitrogen reduction reaction (NRR).

After a lengthy *ex-situ* preparatory process was involved in initial prepping of the MAX phase Mo_2Ga_2C, the material was etched in a Li-HCl solution, centrifuged, and washed successively (1 M HCl, 1 M LiCl, and DI water to a pH 6). This yielded (post ultrasonication and centrifugation) single or few-layered Mo_2CT_X nanosheets. Preparation of SA Ru-Mo_2CT_X involved stirring combined aqueous solutions of Mo_2CT_X (10 ml, 0.1 mg ml^{-1}) and $RuCl_3$ (50 ml, 0.1 mg ml^{-1}) at room temperature for 10 h, product precipitation with acetone, centrifugation, and vacuum-dried (60 °C, 10 h). The authors considered that the introduction of Ru^{3+} ions would be readily facilitated by the observed Mo single vacancies or vacancy cluster defects created in the etching process of the exfoliated Mo_2CT_X nanosheets by high-angle annular dark-field scanning transmission electron microscopy (HAADF-STEM). Aided by the electrostatic nature of the terminal functional groups (O^{2-}, OH^-) the Ru^{3+} ions were readily absorbed from solution and positioned on the Mo_2CT_x

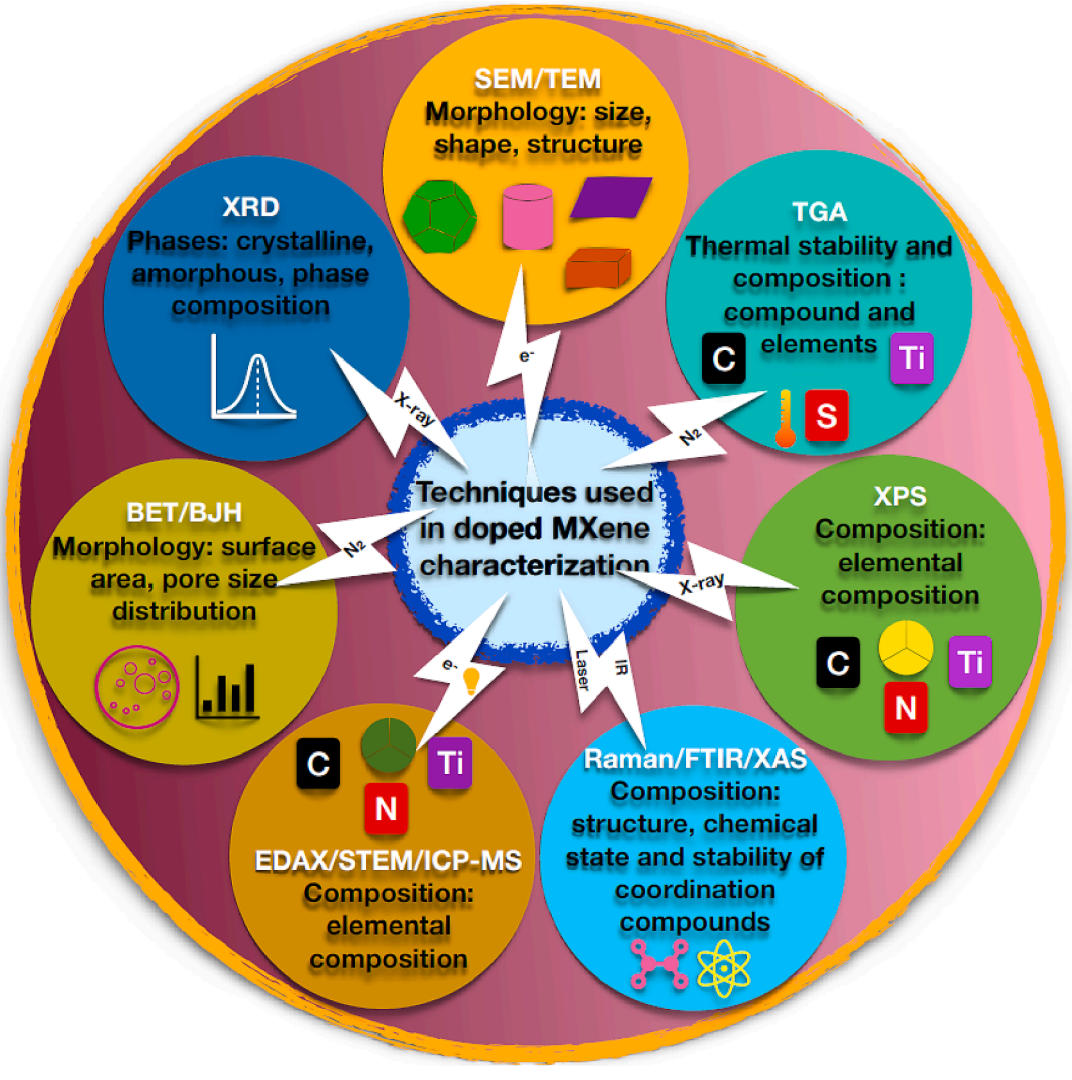

Fig. 5. Overview of techniques used for characterizing doped MXenes.

nanosheets: the Mo vacancies reduced the dopant Ru^{3+} ions into the more stable Ru doped Mo_2CT_X nanosheets. The mixed valences observed by XPS for Mo (Mo (III) ($3d_{3/2}$ at 231.5 eV and $3d_{5/2}$ at 228.2 eV) and Mo (IV) ($3d_{3/2}$ at 232.1 eV and $3d_{5/2}$ at 228.8 eV) confirmed suitability of the pristine Mo_2CT_x nanosheets for redox catalysis. EDX spectroscopy elemental analysis confirmed uniformity in the homogenous distribution of single-atomic Ru on Mo_2CT_X (SA Ru-Mo_2CT_X) nanosheets, and significantly, no Ru-based crystalline phases were observed. Furthermore, XPS data for the SA Ru-Mo_2CT_X revealed binding energies for Ru $3p_{3/2}$ and Ru $3p_{1/2}$ (463.2 and 485.7 eV respectively) were between those expected for Ru (IV) and Ru (0) indicating a partial positive charge for the Ru dopant atoms ($Ru^{\delta+}$) reflecting strong electronic interaction between single Ru atoms and Mo_2CT_X nanosheets. This attribution was complimented by XPS data showing a higher energy shift for Mo 3d peaks for the SA Ru-Mo_2CT_X compared to pristine Mo_2CT_X reflecting a higher oxidation state for Mo, along with a positive shift in binding energy for the C-Mo bond due to a possible overlapping effect of the C-Ru and C-Mo bonds. The SA Ru-Mo_2CT_X catalyst exhibited a high and stable NRR performance with large Faradaic efficiency and excellent electrochemical stability.

An approach by Tan and co-workers for a universal strategy in engineering single-metal sites for HER electrocatalysis targeted the formation of single-metal sites on 3D porous N, P-co-doped $Ti_3C_2T_X$ MXenes (denoted as M_1 SA-PNPM, M1 = Pt, Ir, Ru, Pd, and Au).

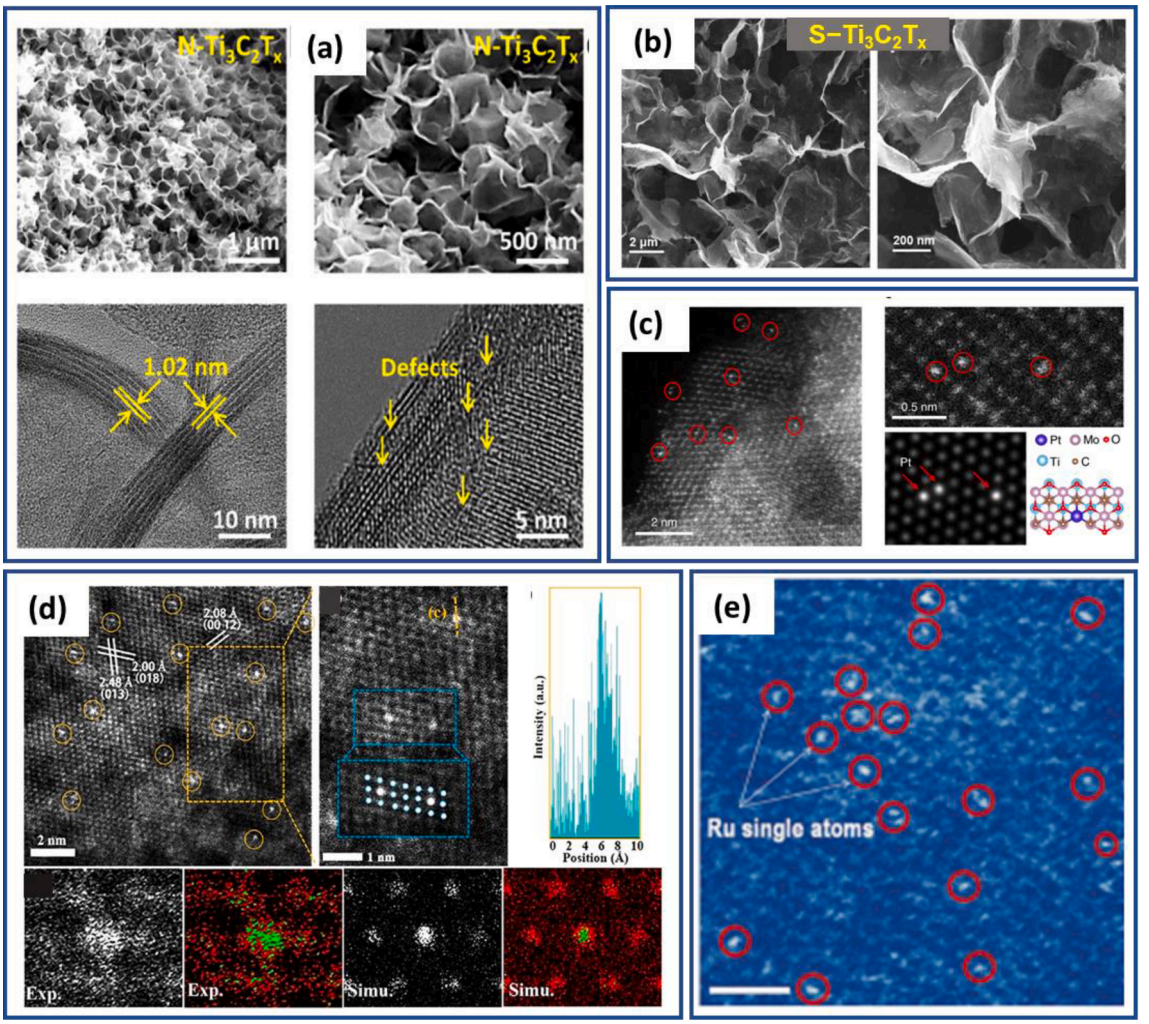

Fig. 6. Scanning/transmission electron microscopy (SEM/TEM) technique for characterizing doped MXene structures: (a) SEM images of N-$Ti_3C_2T_x$ presenting a highly uniform and well-defined porous framework,HRTEM image of N- $Ti_3C_2T_x$ showing expanded interlayer spacing of ~1.02 nm. [93] (b) SEM image of wrinkled S–$Ti_3C_2T_x$ MXene architecture. [58] (c) HAADF–STEM image of Mo_2TiC_2Tx–Pt_{SA}. Magnified HAADF–STEM image of Mo_2TiC_2Tx–Pt_{SA} and its corresponding simulated image, and illustration of the structure of Mo_2TiC_2Tx–Pt_{SA}, showing the isolated Pt atoms (circles)[95] (d) HAADF–STEM image of Pt/$Ti_{3-x}C_2T_y$. and Magnified HAADF image of the area in the yellow box. Schematic columns of atoms are overlaid on the experimental images. Experimental raw and falsely coloured HAADF–STEM images and the simulated HAADF–STEM images using a model with a Pt atom replacing one of the surface Ti atoms. [96] (e) HAADF-STEM image of Ru_{SA}-N-S-$Ti_3C_2T_x$ (bright dots marked with red circles indicate the Ru_{SA} on the $Ti_3C_2T_x$ MXene support). Scale bar, 2 nm. [97] Reproduced from [93,58,95,96,97] with permission from American Chemical Society, Nature Portfolio, Wiley. (For interpretation of the references to color in this figure legend, the reader is referred to the web version of this article.)

[90] A prepared colloidal coagulation of melamine hydrochloride and delaminated pristine $Ti_3C_2T_X$ was stirred with a *tert*-butanol solution of triphenylphosphine and respective metal complex (e.g., H_2PtCl_6, H_2IrCl_6, $RuCl_3$, K_2PdCl_6, and $HAuCl_4$,), freeze-dried, then annealed at 500 °C (2 h, 5 °C/min, Ar (50 sccm) flow) to yield M_1 SA-PNPM. The melamine pyrolysis and triphenylphosphine decomposition provided the N and P doping on $Ti_3C_2T_X$ MXene and immobilized single metal atoms with good uniformity and dispersion on 3D porous N, P co-doped $Ti_3C_2T_X$ MXene. The Pt SA-PNPM high resolution XPS spectral survey confirmed N 1s peaks at 396.6, 398.2, 400.1, 401.5, and 398.4 eV, assigned to Ti–N, pyridinic-N, pyrrolic-N, graphitic-N, and Pt–N bonds, respectively, with the pyridinic-N coordinating Pt. Also confirmed, were peaks for P 2p that were deconvoluted as two sets of dual peaks for P–O (133.5 and 134.6 eV) and P–Ti/P-Pt (129.2 and 130.2 eV), thus verifying that both N and P atoms were coordinated with Ti and Pt in Pt_{SA}-PNPM. The optimal prepared Pt_{SA}-PNPM catalyst displayed greater electrochemical HER activity (~20-fold) than commercially available HER Pt/C catalysts.

3. Dopants characterization

After introduction of dopants in the structure, it is important to understand the physical and chemical interactions between the dopant atoms and the MXene hosts. Characterization using multiple techniques illuminates the mechanisms underlying the improved performance (Fig. 5). Doped MXenes are typically characterized by combining several different techniques, principally electron microscopy (scanning/transmission), X-ray diffraction (XRD), vibrational spectroscopy including Raman, Fourier-transform infrared (FTIR) and X-rays based spectroscopy. Secondary techniques include energy-dispersive X-ray analysis (EDAX), scanning transmission electron microscopy (STEM), Brunauer–Emmett–Teller (BET), Barrett-Joyner-Halenda (BJH) and thermogravimetric analysis (TGA).

3.1. Characterization by electron microscopy

Scanning/transmission electron microscopy (SEM/TEM) has been the commonly used technique for characterizing doped MXene structures (Fig. 6). One of the major advantages of electron microscopy is the exceptional spatial resolution, ~1 nm in SEM and ~ 1 Å in TEM. [91] It can provide information about morphology, crystal structure, atomic arrangement, elemental composition, and chemical state. In contrast to other techniques, electron microscopy has become quintessential for investigations of MXene based 2D systems. This section highlights the findings from electron microscopy, which play a significant role towards successful integration of foreign elements into the MXene matrix.

Different morphologies of doped MXenes were uncovered depending on the experimental methods. For instance, Wen *et al.* characterized as-synthesized MAX Ti_3AlC_2 and $Ti_3C_2T_x$ and N-$Ti_3C_2T_x$ MXenes using SEM and revealed the Al layers etched by HF from the Ti_3AlC_2 phase directed for generating well stacked nanosheets in the multi-layered $Ti_3C_2T_x$. SEM also uncovered the perfectly stacked nanosheets of N-doped MXenes.[48] In another study, Yan *et al.* used SEM and TEM and exposed an accordion-like architecture with layered Ti_3C_2 structure changing to thin lamellas of Ti_3C_2 layers after delamination by the intercalants, when Ti_3C_2 was prepared by etching Ti_3AlC_2 in the presence of HF at ambient temperature for removing Al. Nitrogen doping of Ti_3C_2 derived from a restacked layered structure lead to generation of small nanosheets on the thin Ti_3C_2 providing nicely nanoscale lamellas and rough carbonized lamellas.[92] Based on the SEM images of synthesized Ti_3C_2 and N-Ti_3C_2 samples, Tang *et al.* showed N-doped MXene holding perfectly layered nanosheets comprising a small amount of rod-like TiO_2 nanoparticles. The nanosheets were evidently separated from each layer compared to unreacted Ti_3AlC_2 particles. Retaining a 2D multi layered structure in N-Ti_3C_2 provides added advantage for intercalation and diffusion of electrolyte ions. [47] fan *et al.* [93] investigated the morphological features of fabricated N-$Ti_3C_2T_x$ using SEM, low magnification TEM, and high-resolution TEM (HRTEM). The SEM and low magnification TEM images show N-$Ti_3C_2T_x$ comprising a highly uniform and well-defined porous framework with the inner voids maintained by outer shells composed of thin nanosheets. HRTEM examination of N-$Ti_3C_2T_x$ uncovered a few layers of wrappings with expanded interlayer spacing of around 1.02 nm, which facilitate enhanced uptake/release of sodium ions.[93] A similar wrinkled structure of sulfur doped $Ti_3C_2T_x$ was observed by Bao *et al.* [58]SEM images reveal an enlarged gap between the exfoliated layers, producing a larger surface area. The observed morphology of sulfur-doped MXene (S–$Ti_3C_2T_x$) nanosheets led to a high areal sulfur loading of up to 4.5 mg/cm^2 for MXene/sulfur electrode.

Understanding the coordination environment of single atom noble metal catalysts (Pt, Pd, Au, Rh) is particularly important for stabilizing the atomic dispersion on MXene substrates. The coordination environment strongly contributes to the electronic structure and in turn influences the catalytic performance. HRTEM images can reveal the atomic structure of the dopant. During synthesis, the aggressive etching of the MAX phase using HF leads to metal atom vacancies or vacancy clusters. These highly unstable vacancy sites are ideal for supporting single metal atoms.[94] For example, single Pt atoms can be stabilized on Mo vacancy sites by formation of covalent Pt–C bonds with the surrounding C atoms of $Mo_2TiC_2T_x$ MXene.[95] High-angle annular dark-field scanning transmission electron microscopy (HAADF- STEM) images of $Mo_2TiC_2T_x$-Pt_{SA} (Fig. 6d) show that isolated Pt atoms are immobilized exactly at the Mo (vacancy) positions on $Mo_2TiC_2T_x$. As highlighted in Fig. 6d and Fig. 6e isolated single Pt atoms appear as bright dots within the regular MXene crystal lattice fringes. Interestingly, the atoms were found to be located at the lattice plane walls of the Ti columns rather than in the spacings between them, indicating that the single Pt atoms were stabilized in the Ti vacancies by substitution rather than interstitial doping.[96] A similar uniform dispersion of isolated Ru single atoms on the $Ti_3C_2T_x$ support was also observed from the HAADF-STEM images.[97] Hence, TEM techniques have been pivotal to fundamental understanding towards superiority of MXenes as support for single atom catalysts.

3.2. Characterization by X-ray diffraction

X-ray diffraction (XRD) is a non-destructive characterization technique which does not require sophisticated sample preparation for analysis. In XRD, a cathode ray tube produces monochromatic radiation (incident rays) to bombard a sample. XRD is used to determine crystal structure (orientation and stacking order of 2D layers, as well as interlayer spacing and crystal symmetry), identify different phases including secondary phases or impurities from a few atoms thickness, and determine structural changes due to external physical and chemical perturbations. XRD is a commonly used technique to determine the phases of MXenes (Fig. 7). [48,98,99] The (0 0 2) diffraction peak is used as an indicator for changes in the lattice parameter.[9] Studies using XRD for characterizing doped MXenes consistently reveal a peak shift corresponding to (0 0 2) from higher to lower angle confirming doping.[47,48,92,93] The successful preparation of $Ti_3C_2T_x$ from Ti_3AlC_2 can be confirmed from the XRD data itself. Upon removal of the Al layer, the corresponding Ti_3AlC_2 diffraction peak (1 0 4) at $2\theta = 39.08^\circ$ disappears making the (0 0 2) peak the prominent feature in the diffractogram.[48] Upon doping this characteristic (0 0 2) diffraction peak was found to show a clear shift towards lower degrees for both metallic and non-metallic dopants.[37,100–103] This shift in the (0 0 2) peak represents a change in c-lattice parameter (c-LP) and indicates an increase in interlayer spacing. Wen *et al.* observed that the (0 0 2) diffraction peak for $Ti_3C_2T_x$ shifted from 9.20° to 7.18° after nitrogen doping (N-$Ti_3C_2T_x$) which corresponds to c-LP of 1.92 nm (0.96 nm d-spacing) and 2.46 nm (1.23 nm d-spacing) respectively.[48] In the study by Yan *et al.*, after urea assisted nitrogen doping the (0 0 2) peak of Ti_3C_2 shifts from 8.8° to 6.9° corresponding to an increase in d-spacing from 1.01 to 1.27 nm, as shown in Fig. 7(a).[92] Furthermore, the increase in c-LP and (0 0 2) peak intensity confirms nitrogen doping in the Ti_3C_2 lattice along with an organized crystal structure of N-Ti_3C_2. Yoon *et al.* observed a temperature dependent structural evolution of phosphorus doped V_2CT_x MXene.[100] Pristine V_2CT_x showed a broad (0 0 2) peak at 9.14°. After P-doping at 300 °C (P1-V_2CT_x), 400 °C (P2-V_2CT_x) and 500 °C (P3-V_2CT_x) the diffraction peak shifted to 8.06° (c-LP = 21.92 Å), 8.28° (21.34 Å)

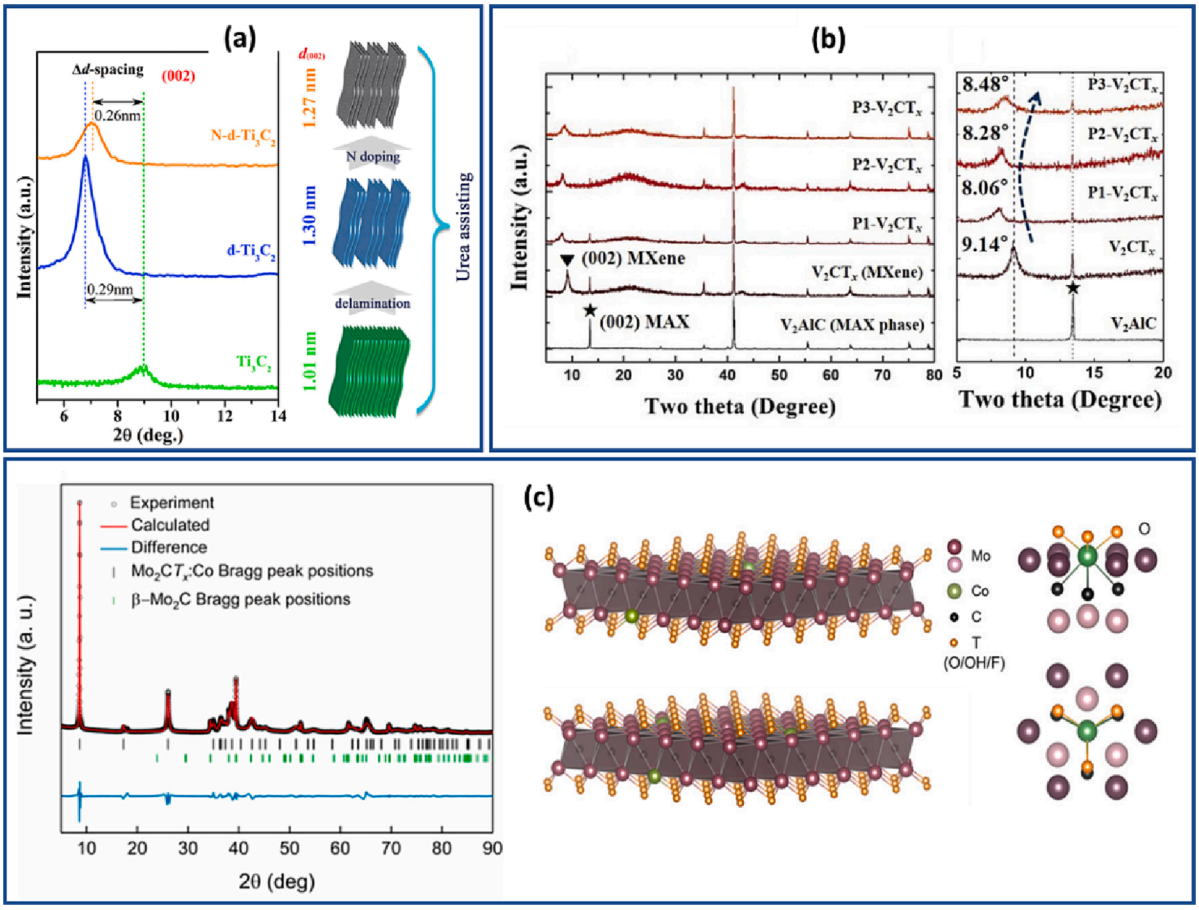

Fig. 7. X-ray diffraction (XRD) technique to determine the phases of MXenes: (a) XRD patterns showing a shift in the (0 0 2) peak of Ti_3C_2 after urea assisted delamination (d-Ti_3C_2) and nitrogen doping (N-d-Ti_3C_2) and schematics of the Ti_3C_2 layers with corresponding d-spacing. [92] (b) XRD patterns showing temperature-dependent structural transition of phosphorus doped V_2CT_x and variation of the interlayer distance (c-LP) from the shift in the (0 0 2) peak position. [100] (c) Le Bail fitting of the XRD data for Mo_2CT_x:Co material revealing that all reflections are assigned to Mo_2CT_x and β-Mo_2C phases along with schematic representation of the Mo_2CT_x:Co structure and two projections of the coordination environment of cobalt. The model structure substitutes a Mo atom by Co in the parent Mo_2CT_x assuming that the surface is fully terminated by oxygen groups. [102] Reproduced from [92,100,102] with permission from Elsevier, Wiley and American Chemical Society.

and 8.48° (20.84 Å), respectively (Fig. 7(a)). This variation is attributed to gasification of the dopant source triphenylphosphine at higher temperature (350 °C). On the other hand doping with larger ions, e.g Ce^{3+} did not result in the inter lattice insertion but resulted in the formation of surface oxides. [104].

Crystallographic modelling of doped MXene systems is quite challenging due to the nano crystallinity of MXene sheets, the short-range order of the surface structure, and the stacking disorder between adjacent single layers. Structural analysis using a pair distribution function showed that MXene adopts the same $P6_3/mmc$ space group structure as the MAX phase. Kuznetsov *et al.*[102] were able to find the lattice parameter for Co-doped Mo_2CT_x by fitting their experimentally acquired XRD patterns with $P6_3/mmc$ space group (Fig. 7(c)). The carbon atoms occupy octahedral positions, forming close packed Mo_2C sheets terminated by T_x groups bound to Mo atoms.[102] This section highlights the importance of XRD in identifying the crystal phases of various doped MXene structures and how it helps to unfold the structural evolution of multi-layered, delaminated, and porous structures.

3.3. X-ray spectroscopy

X-ray spectroscopy is a powerful tool for probing the characteristics of doped MXene systems. It is often carried out in the soft (0.1–2 keV) and hard (2–35 keV) regimes. Soft X-rays are highly sensitive to surface chemistries and electronic states, while hard X-rays penetrate much deeper into the sample and are more bulk sensitive. Among the many techniques, X-ray photoelectron spectroscopy (XPS) and X-ray absorption spectroscopy (XAS) are the most widely used. XPS and XAS include primarily photon-in-electron-out and photon in photon processes. XPS uses a single photon source and can be carried out at lab scale, while XAS requires synchrotron facilities for photons with variable energy and high brilliance.[105].

In many applications, knowledge of the surface chemistry is critical. X-ray photoelectron spectroscopy (XPS) is a powerful surface sensitive tool to understand the electronic properties of systems with a sampling depth about 1–5 nm. This is primarily used to determine chemical bonding, ionic state, charge transfer characteristics, core level characteristics of elements, hybridisation of different orbitals (in valence band). Another important information related to the surface layer, any contaminants or adsorbates, oxidation state of transition metals, bonding configuration of functional groups on the surface, surface sensitivity/reactivity of the 2D layers, interface between the layers and other materials, stoichiometric quantity of elemental composition, and density and

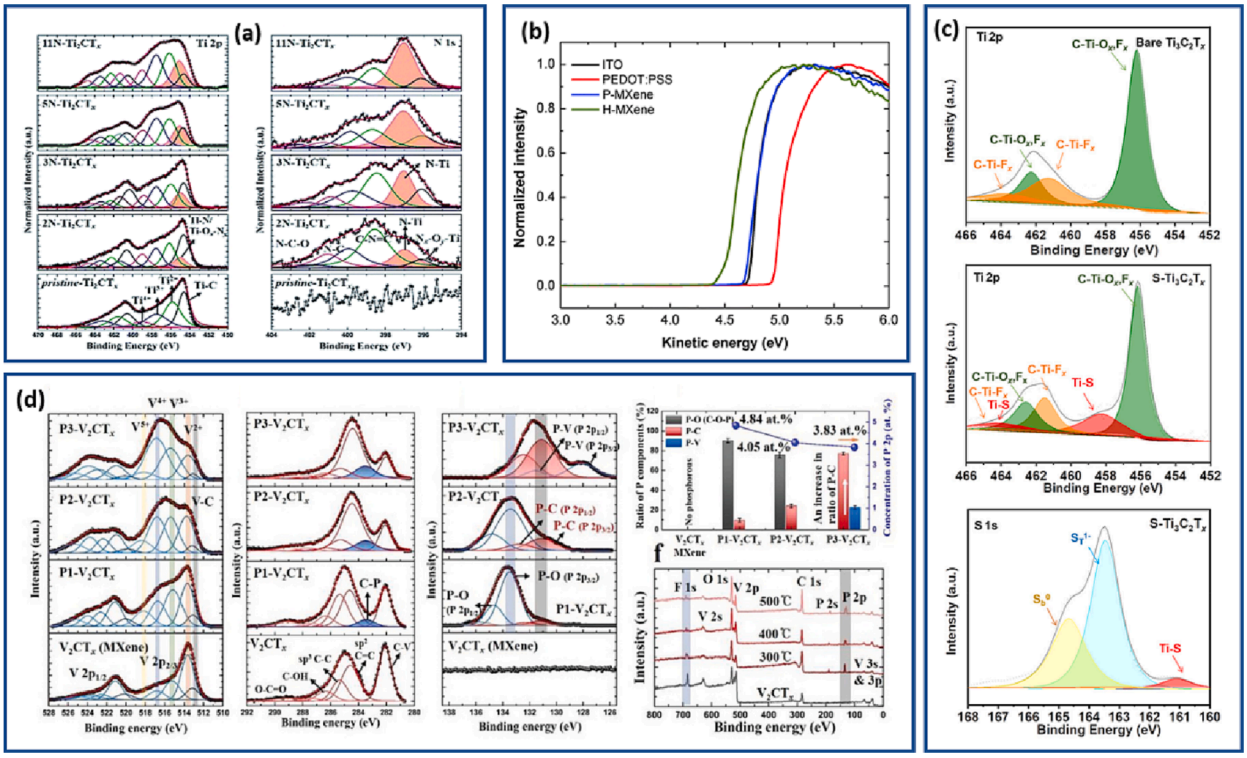

Fig. 8. X-ray photoelectron spectroscopy to probe the surface chemistry of doped MXene systems. (a) High resolution Ti 2p and N 1s core level XPS spectra showing changes in the chemical composition after nitridation of Ti2CTx MXene. [101] (b) Valence band spectra of bare ITO, PEDOT:PSS and nitrogen doped Ti3C2Tx MXene to measure corresponding work function values. [111] (c) Ti 2p and S 1s core level XPS spectra showing changes in surface chemistry after sulfur doping of Ti3C2Tx. [58] (d) V 2p, C 1s and P 2p core level spectra of triphenyl phosphine treated vanadium carbide MXene and variation in P composition in P 2p core level spectra as a function of reaction temperature, survey spectra of pristine-V2CTx and all synthesized products after heat treatment.[100] Reproduced from [101,111,58,100], with permission from Royal Society of Chemistry, American Chemical Society and Wiley.

distribution of surface functional groups. All these pieces of information's are critically important to understand the chemical behaviour of 2D systems as they have different functional groups with differing bonding nature, influence of dopant might alter the electronic structure and hence the properties of materials.[106–109].

XPS can be used to determine dopant concentration and elemental oxidation states at the surface of the material. XPS allows to calculate the concentration of nitrogen dopant in N-$Ti_3C_2T_x$. Wen *et al.* evidenced that the concentration of nitrogen increased with respect to the temperature of the ammonia treatment. Also, the XPS result revealed the complete removal of F introduced during HF etching.[48] The nitrogen spectra showed that the bonding environment varied with temperature. At higher temperature (>500 °C) nitrogen was predominantly bonded to Ti, while at lower temperature Ti-O-N and surface adsorbed nitrogen was observed. Yan *et al.* used XPS as a confirmatory technique to ascertain the successful incorporation of nitrogen in the nanosheets of d-Ti_3C_2 through the presence of an additional strong N 1s peak in N-d-Ti_3C_2.[92].

In another study [47] XPS data revealed the presence of Ti 2*p*, C 1s, O 1s, N 1s and F 1s elements and an additional peak of N 1*s*

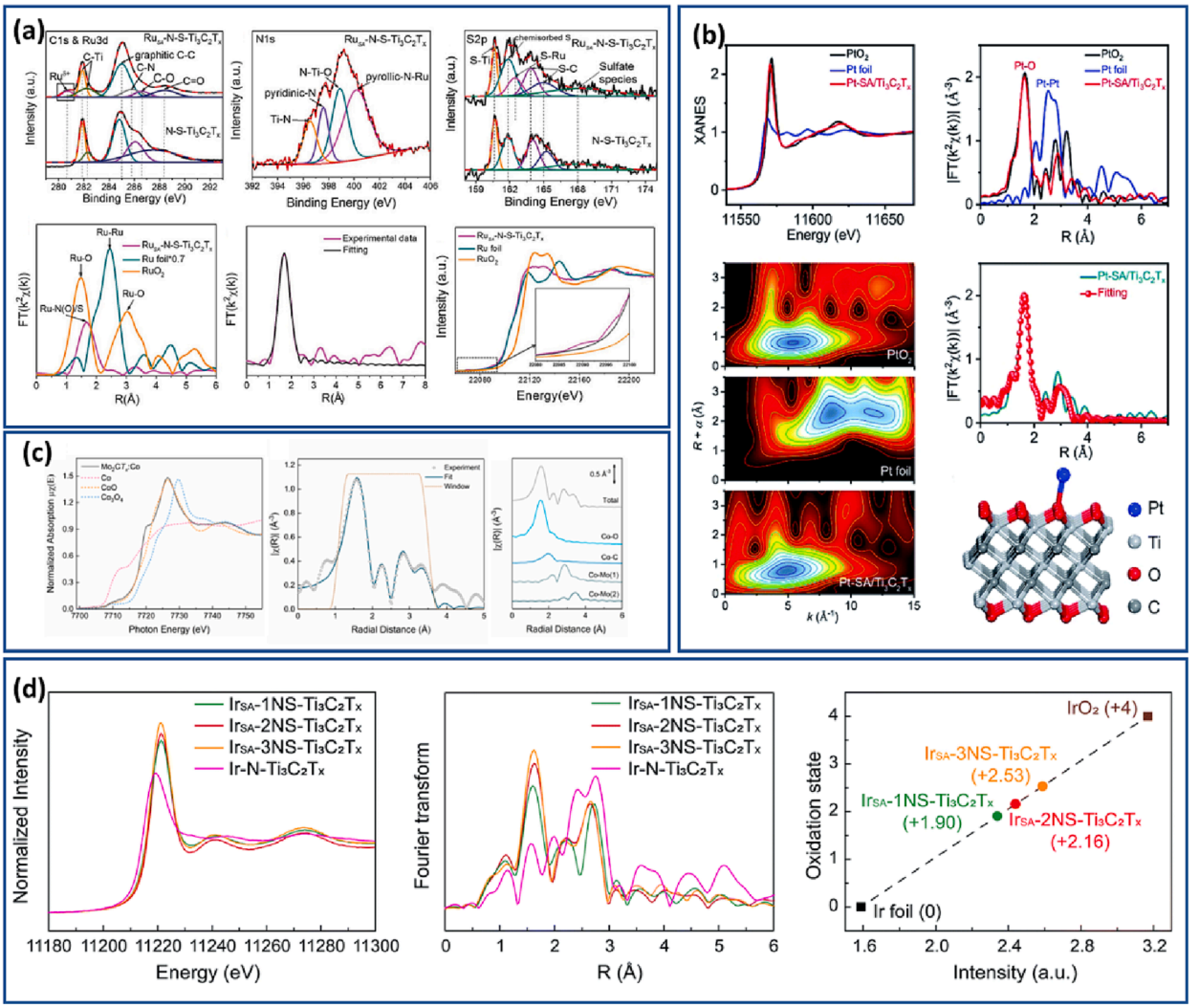

Fig. 9. Hard/High energy X-ray absorption spectroscopy of Doped MXenes. (a) Chemical state and coordination environment of Ru single atoms in the RuSA-N-S- $Ti_3C_2T_x$ catalyst. High-resolution C 1s, Ru 3d and N 1s XPS spectra of N-S- $Ti_3C_2T_x$ and RuSA-N-S- $Ti_3C_2T_x$. FT-EXAFS spectra of Ru foil, RuO2 and RuSA-N-S- $Ti_3C_2T_x$. Quantitative EXAFS curve fitting in r-space for RuSA-N-S- $Ti_3C_2T_x$, and normalized Ru K-edge XANES spectra of Ru foil, RuO_2, and RuSA-N-S- $Ti_3C_2T_x$. [97] (b) XANES and EXAFS characterization of PtSA/ $Ti_3C_2T_x$. XANES spectra at the Pt L_3-edge of PtO_2 and Pt foil and Pt-SA/ $Ti_3C_2T_x$ with corresponding FT-EXAFS spectra. WT-EXAFS plots in which k and (R + a) represent the electron wave vector and interatomic distance without phase correction, respectively. Fitted FT-EXAFS curve and atomic-structure model of PtSA/ $Ti_3C_2T_x$.[112] (c) Normalized Co K-edge XANES spectra of Mo_2CT_x:Co with Co, CoO and Co_3O_4. Phase-uncorrected Fourier-transform of Co K-edge EXAFS function for Mo_2CT_x:Co and its fit, and single scattering paths used in the EXAFS fit.[86] (d) Normalized Ir L_3-edge XANES spectra of single atoms (IrSA) on N-doped and N,S co-doped Ti3C2Tx, corresponding Fourier transform of the EXAFS spectra of Ir–N– $Ti_3C_2T_x$, IrSA and N,S co-doped $Ti_3C_2T_x$, and fitted average oxidation state of Ir spectra obtained from XANES.[69] Reproduced from [97,112,102,69] with permission from Wiley, Royal Society of Chemistry and American Chemical Society.

suggestive of incorporation of nitrogen in the nanosheets of N-Ti_3C_2. In this case, the chemical structure of N-Ti_3C_2 was evaluated using fitting of three XPS peaks at 396.1, 399.3 and 401.0 eV assigned to nitride N (N-Ti), pyrrolic N (N-5) and quaternary N (N-Q) respectively.[47] In the study by Fan *et al.*,[93] the chemical compositions of synthesized N-$Ti_3C_2T_x$ were explored using XPS. The quantified surface atomic ratios indicate a nitrogen content that is amplified with respect to melamine formaldehyde (MF) dosage. The XPS spectrum depicts the high-resolution N 1s signal of porous N-$Ti_3C_2T_x$ with three deconvoluted peaks at 397, 398.3 and 399.8 eV corresponding to Ti–N, pyridinic N and pyrrolic N, respectively. The bonding of Ti–C, Ti–N, and Ti–OH is revealed in the high-resolution Ti 2*p* spectrum with peaks at 455.2, 456.0 and 458.7 eV, and the appearance of a signal at 457.2 eV suggests partial oxidation of $Ti_3C_2T_x$ upon sample synthesis.[93] Yoon *et al.* used the Ti 2*p* and N 1*s* core level spectra of Ti_2CT_x MXene to quantify the chemical nitridation after annealing in $NaNH_2$ (Fig. 8(a)).[101] They identified multiple bonding environments corresponding to Ti–C, Ti^{2+}, Ti^{3+} and Ti^{4+} in the Ti 2*p* spectra and the N–Ti, N–O–Ti bond, C–N = C, pyridinic N–C, graphitic N–C, and pyridinic-N oxide (O^-–N^+–C) from N 1*s*. Quantitative analysis of these Ti 2*p* and N 1*s* spectra revealed that $NaNH_2$ not only prevents surface oxidation but also leads to nitridation of Ti_2CT_x.

Ultraviolet photoelectron spectroscopy (UPS) is a widely used method to understand the valence band electronic properties, UPS is key technique to determine the work function of materials. By exposing a material to ultraviolet radiation and measuring the energy of the emitted electrons, UPS provides valuable information about the material's electronic structure, hybridisation, total density of states at the valence band edge (close to Fermi Level) (sampling depth of He-II excitation about 0.5–0.8 nm). This technique is highly surface sensitive, making it ideal for analysing the electronic properties of thin films, and interfaces. It reveals the occupied electronic state and density of the valence region or conduction bands, binding orbitals between adsorbates or surfaces functional groups and surface atoms. With a polarised UV irradiation, UPS can be used to study adsorbate orientations relative to the surface. It is particularly useful for analysing materials used in electronic and optoelectronic devices, such as 2D semiconductors and organic materials. By providing insights into the energy levels and electronic transitions occurring within these materials, UPS can help improve their performance.[106,110] Yu et al. reported tuning of the work function of MXenes by mapping the valence band using ultraviolet photoelectron spectroscopy (UPS) shown in Fig. 8(b).[111] In UPS the excitation is carried out by an ultraviolet source, providing a higher cross section and resolution at the valence band. UPS provides one of the most effective ways to measure the work function of materials, which has particular importance for solar cell and optoelectronic devices. From XPS analysis Bao et al. inferred the binding energy of S doping at the Al and C sites, −5.372 eV and −5.122 eV, respectively. Accordingly, S is more prone to doping in the Al layer (Fig. 8(c)).[58] Typically it is observed doping of a MXene happens via the substitution of the surface terminated oxygen groups. However, the Yoon et al. found that at elevated temperatures the heteroatom can substitute a metal centre favouring bonding with carbon. For phosphorus doped V2CTx, the calculated free energies for P bonded to carbon is much smaller than P bonded to oxygen or P bonded to vanadium. [100] XPS analysis on the P doped V2CTx confirmed these theoretical findings. As shown in C1s spectra of Fig. 8(d), the formation of carbon-phosphorus bonds started at 300 °C and gradually increased up to 500 °C. Also, by comparing the V 2p and P 2p spectra, it could be confirmed that such heteroatom can be doped or substituted at the V defect sites, along with the surface terminated oxygen. In this case XPS provided vital information on the chemical evolution of the doped MXene with varying temperature.

Hard X-ray absorption spectroscopy is particularly suited for single atom supported catalysts where long-range order is absent but there exists a well-defined coordination around the single atom catalytic sites. For example, for ruthenium single atom catalyst supported on nitrogen (N) and sulfur (S) co-doped (Ti3C2Tx) MXene, the successful coordination of ruthenium single atom with the N and S species can only be probed using hard X-ray absorption spectroscopy.[97] The high-resolution N 1s and S 2p core level spectra of the system identified the Ru-N and Ru-S bond, confirmed by quantitative EXAFS fitting of Ru k-edge spectra shown in Fig. 9(a). The well dispersed and stable single Pt atom on $Ti_3C_2T_x$ is formed by Pt-O coordination on the surface-adsorbed oxygen. Zhao *et al.* used density functional theory calculations and X-ray absorption spectroscopy to validate that the single-atom Pt sites are captured by surface oxygen-containing groups rather than Ti vacancy sites.[112] Here Fourier transform (FT) and wavelet transform (WT) of Pt L_3-edge EXAFS oscillations were employed due to their powerful resolution in both k and R spaces to understand the atomic dispersion of Pt on the $Ti_3C_2T_x$ matrix (Fig. 9(b)).

Kuznetsov *et al.* confirmed the single site Co substitution in Mo_2CT_x by comparing EXAFS data of Mo_2CT_x:Co in R-space with Co, CoO and Co_3O_4 references. The local structure of cobalt in Mo_2CT_x:Co differs significantly from the reference materials (Fig. 9 (c)). By fitting the EXAFS data, they observed that Co-Co scattering was missing, while two non-equivalent Co–Mo shells indicate partial substitution of Mo in Mo_2CT_x by Co, in excellent agreement with experiment. Some of the results presented in this section highlight that X-ray spectroscopy is the most suitable technique for obtaining direct insights into the surface chemistry, electronic structure, and local atomic environment of doped MXene systems used in a range of energy generation and storage applications. Lin et al. were also able to observe a similar electronic metal–support interaction due to formation of new chemical bonds and rearrangement of molecular energy levels inducing orbital rehybridization and charge transfer across the iridium metal and Ti3C2Tx support.[69] Fig. 9(d) shows the X-ray absorption spectra of iridium single atoms on nitrogen and nitrogen, sulfur co-doped $Ti_3C_2T_x$ MXene (IrSA-NS-Ti3C2Tx). Comparing the Ir L_3-edge XANES spectra with those of IrO2 and metallic iridium, they found that the number of unoccupied states in the 5*d* orbitals of iridium in IrSA-2NS- $Ti_3C_2T_x$ is between those of IrO_2 and metallic Ir. Increasing dopant concentration, a linear increase in intensity was observed. Fourier analysis of the spectra revealed that the average iridium oxidation state originates from the increase in Ir–N ligands and is independent of the Ir–S and Ir–Ti scattering interactions. Supported by DFT calculations, these highly coordinated Ir–N interactions result in charge redistribution in the interfacial region of the $Ti_3C_2T_x$ support, improving the overall catalytic activity toward hydrogen evolution.

3.4. Vibrational spectroscopy: Raman and infrared spectroscopy

Vibrational spectroscopy is extensively used to characterize 2D materials. Both Raman and Fourier transform infrared spectroscopy can successfully determine the structure and obtain a molecular fingerprint. Raman spectroscopy has been the most widely used technique for various 2D systems due to its speed, non-invasive nature, and high structural sensitivity. Analogous to other cases, the Raman spectra of MXenes consist of A1g and Eg vibrational modes corresponding to out of plane and in plane vibrations, respectively, and depend on phonon dispersion relations.[113] However, according to the M, X and T constituents, the vibration modes can shift to different wavenumbers.[11] MXene falls in the P63/mmc space group, however the structure is highly distorted due to the surface terminal groups, leading to broadened vibrational bands, referred to as "pseudo-P63/mmc".[114] For Ti3C2 the vibration modes can be represented as 4Eg + 2A1g + 4Eu + 2A2u. Among these vibrations, Eg and A1g are the Raman-active modes, whereas Eu and A2u are IR-active. Fig. 10(a) shows the Raman spectrum of Ti3C2Tx. Sarycheva et al. analyzed this complex spectrum by separating it into several regions including a flake region consisting of Eg(Ti, C, O) and A1g(Ti, C, O) modes, in-plane (Eg) vibrations of surface groups attached to titanium atoms, and carbon vibrations (both Eg and A1g).[113] In addition, there are two peaks located between 1200 and 1800 cm^{-1}, which are characteristic for the D and G-modes of graphitic carbon. Like graphite and its derivatives, these two peaks have been the descriptor of any doping induced structural changes for doped MXene systems. In several instances, after doping no changes could be observed in the Raman spectra at wavenumbers below 1000 cm-1 (Fig. 10(b)).[46,95,115–117] Almost identical Raman fingerprints were observed for Mo2TiC2Tx–PtSA *vs.* Mo2TiC2Tx and V-Ti3C2Tx *vs.* Ti3C2Tx.[95,115] However, the increased ratio between the intensities of D and G bands (ID/IG) can be ascribed to disorder and defects upon doping. This can be seen from the calculated ID/IG of 0.89 for Ti3C2, 0.98 for Ti3C1.8 N0.2, and 1.06 for Ti3C1.6 N0.4 (Fig. 10(c)). Lu et al. used ID/IG to study the defects induced during synthesis of nitrogen doped MXene.[46] They compared between Ti3CN prepared by in-situ etching from Ti3AlCN, hydrothermally prepared N-Ti3C2 (labelled as HND) and cold plasma induced N-Ti3C2 (labelled as PND). ID/IG ratios for Ti3C2 and Ti3CN, HND and PND MXenes were found to be 0.59, 0.60, 0.86 and 0.97 respectively (Fig. 10(d)). These values indicate that hydrothermal and cold plasma treatment promote formation of thinner nanosheets and defects, eventually affecting the electrochemical properties. The Raman spectra of Ti3C2, d-Ti3C2 and N-d-Ti3C2 reveal that delamination and carbonization promote the formation of thinner nanosheets with large structural defect.[92] Furthermore, in the study by Tang et al.[47] the Raman spectra illustrate characteristic broad peaks around 1350 and 1590 cm^{-1} corresponding to the D (amorphous carbon deformation vibrations of a hexagonal ring) and G modes (stacking of the hexagonal network plane) of graphitic carbon. Possession of larger graphitic domains

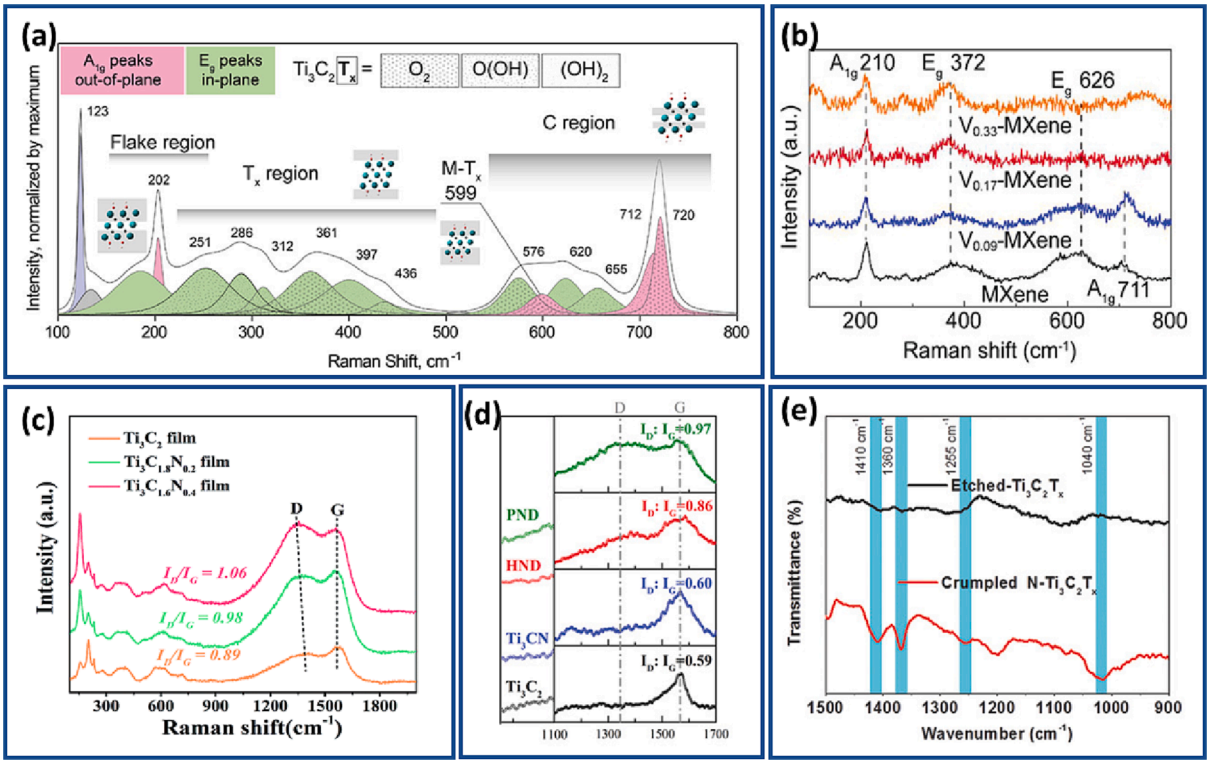

Fig. 10. Raman spectroscopy of doped MXenes to show the structural changes and obtain a molecular fingerprint (a) Deconvoluted Raman spectrum of Ti3C2Tx film excited with a 785 nm laser.[113] (b) Identical Raman spectra of pristine and vanadium doped Ti3C2Tx between 100 and 800 cm^{-1}. [95,115] (c) Increase in ID/IG ratio for N-doped compared to pristine Ti3C2Tx. [46,95,115–117] (d) ID/IG ratio of pristine MXene *vs.* material doped in three different ways showing the corresponding induced disorder.[46] (e) FTIR spectra of N-Ti3C2Tx nanosheets and etched Ti3C2Tx.[119] Reproduced from [113,95,115,46,119] with permission from American Chemical Society, Wiley-VCH and Wiley.

or more carbonaceous defects and partial substitution of carbon with nitrogen in N-Ti3C2 due to the hydrothermal treatment in the presence of urea was confirmed by the higher ID/IG ratio.[47].

On the other hand, IR spectroscopy which is more sensitive to functional groups is complementary to Raman spectroscopy. The presence of trapped water molecules can sometimes prove disadvantageous, hence careful sample preparation is important for reliable FTIR data. FTIR spectra provide information about the bonding environment of the dopant. After nitrogen incorporation the spectra of Ti3C2Tx MXene show four additional peaks around 1410, 1360, 1255 and 1040 cm^{-1} attributed to N-Ti vibrations (Fig. 10(e)). Similarly, incorporation of N and S into Nb2C MXene quantum dots is evident from peaks at 3470.4, 1638.8, 1105, 992 and 832.6 cm-1 attributed to –OH and –NH groups, C = O stretching vibration, C–S bonds, C-F bonds, and Nb-O bonds, respectively. The good water solubility and stability of N–S functionalized nanomaterials revealed by FTIR of S,N co-doped-Nb2C MXene quantum dots promoted surface modification of nanomaterials with hydroxyl and carbonyl groups.[118].

3.5. Other techniques

3.5.1. EDAX/STEM

Apart from XPS, EDAX/STEM is also used for elemental analysis of doped MXenes. In the fields of materials science and chemistry, EDAX is a technique used to analyse the elemental composition of a sample. Typically, EDAX is paired with scanning electron microscopy (SEM) to examine the sample's surface and identify its chemical composition. During the EDAX process, a high-energy electron beam is directed towards the sample's surface, causing the atoms in the sample to emit X-rays. The X-rays have a distinct energy level corresponding to the emitting element and helps in determining the sample's elemental composition. An X-ray detector is used to measure the energy and the intensity of the emitted X-rays. EDAX can analyse both conductive and non-conductive samples without causing damage, making it particularly useful for analysing small particles, thin films, and surface layers at a scale of micrometers or even nanometers [118] Moreover, EDAX can map out the spatial distribution of elements across a sample. Furthermore, it is a non-destructive technique that does not alter or damage the sample. EDAX is fast and easy to use, making it a valuable tool for routine characterisation.[119,120] EDAX can be used to identify the elements present in a MXene sample. STEM is a cutting-edge imaging technique that uses a focused electron beam to produce high-resolution images of materials at the nanoscale. STEM works by scanning across the sample with a tiny electron beam and detects the electrons emitted from sample. STEM instrument is made up of an electron source, electromagnetic lenses, and a detector for collecting the transmitted electrons. The detector can be positioned at different angles to capture various signals, like bright-field (BF) and dark-field (DF) images, high-angle annular dark-field (HAADF) images, and energy-dispersive X-ray spectroscopy (EDX) spectra. [121,122] STEM can also be used for elemental mapping and chemical analysis. The high spatial resolution of the STEM technology can enable the examination of individual atoms and their arrangements in MXene materials. In addition, STEM can provide 3D imaging of MXene materials allowing for the visualisation of their structure stability and morphology. STEM can also be used to study MXene materials under different conditions in real time, providing insights into their behaviour and properties. Importantly, this technique is non-destructive, meaning that MXene materials can be analysed without any changes to their structure or properties. [123,124] EDAX confirmed the presence of nitrogen in the interlayers of N-d-Ti_3C_2 nanosheets and the composition of elements, namely Ti, C and N. Furthermore, it showed that the decrease in F content led to an increase in C, N, O content resulting in a significant improvement in the specific capacitance.[92] EDAX mapping performed to determine the element distribution of the N-Ti_3C_2 nanosheets uncovered evenly distributed Ti, C and homogeneously doped 9.97% of N in the matrix of N-Ti_3C_2 sheet.[47] Scanning TEM (STEM) elemental mapping analysis discovered not only the presence of Ti, C and N, but also a uniform distribution of N within the porous network indicating the successful incorporation of nitrogen doping in N-$Ti_3C_2T_x$.[93].

3.5.2. BET/BJH

BET technique, or Brunauer-Emmett-Teller, is widely used in materials science and engineering to measure the specific surface area of porous materials like catalysts, adsorbents, and powders. This technique involves adsorbing gas molecules onto the material's surface, measuring the gas adsorption at different pressures and fitting the data to the isotherm model to calculate the total surface area. The theoretical assumption is that gas molecules form a uniform monolayer on the material surface and measuring this layer's thickness allows for surface area calculation. Surface area is a vital parameter affecting catalyst's activity and selectivity in many applications. This quantitative measurement can allow precise comparisons of different doped MXene materials and to optimise the doping process. Additionally, the BET method is non-destructive, making it possible to reuse the material after the measurement is taken. This is particularly useful when the doped MXene material is expensive or difficult to synthesise. The BET method is highly sensitive and can detect even small changes in surface area due to the doping process). [125,126].

The BJH analysis method, also known as Barrett-Joyner-Halenda, is used to study pore size distribution of porous materials like zeolites, activated carbons, MXene and metal–organic frameworks, including micropores and mesopores. The method relies on the adsorption and desorption isotherms obtained from BET analysis. It uses the Kelvin equation to translate relative pressure values into pore diameters and then employs the BJH equation to calculate the pore size distribution [127,128]When MXene is doped, it changes the way it absorbs and releases substances due to changes in its surface and pore structure. Hence, BJH can be used for doped MXene characterization. Studies showed that the SSA of Ti_3C_2 (5.1 m^2/g) increases dramatically to 23.5 m^2/g in N-d-Ti_3C_2 after delamination and carbonization; this area is smaller compared to d-Ti_3C_2 (27.9 m^2/g) due to restacking of Ti_3C_2 nanolayers.[92] Ti_3C_2, d-Ti_3C_2 and N-d-Ti_3C_2 samples subjected to BJH follow type IV isotherms with type H3 hysteresis and relative pressure between 0.45 and 1.0, indicating mesoporosity and slit-shaped pores with size of 4–70 nm.[92] N_2 adsorption/desorption isotherms of synthesized N-$Ti_3C_2T_x$ uncovered a much higher surface area of 173 m^2/g.[93] Karthikeyan et al. used the BET and BJH models to analyse the MXenes,

focusing on their specific surface area, pore diameter and total pore volume of 11.21 m^2/g, 21.2 nm, and 0.04 cm^3/g respectively, through nitrogen adsorption–desorption isotherm.[129] Based on the isotherm classification, the authors observed a type IV isotherm, which suggests a sheet-like structure and organized mesoporous nature. The authors concluded that a high specific surface area is crucial for effectively removing toxic anions. In another study by Gul et al. erbium adsorption increased the surface area of MXene from 1.68 m^2/g to 5.48 m^2/g. [130] The higher surface area improves electrochemical sensing due to increased ion diffusion and easier access to active sites for reactions. The surface area and pore volume of samples tested were in the range of 2.68 to 5.48 m^2/g and 0.311 to 0.34 cm^3/g respectively. The results showed that the incorporation of erbium forms erbium oxide, which contributes to the larger surface area. Tahir *et al.* (2022) measured the surface area, pore volumes, and pore-size distribution of pure VO, the composite GVO, and the GVO-MXene composite using the BET and BJH methods. [131] The results showed that GVO-MXene had the largest surface area of 23.69 m^2/g, while VO and GVO had surface areas of 4.32 and 20.46 m^2/g, respectively. The pore volumes were 0.019 cm^3/g for VO, 0.027 cm^3/g for GVO, and 0.038 cm^3/g for GVO-MXene. The isotherm of all samples showed type IV behavior, indicating that they were mesoporous. Gd^{+3} doped VO showed an increase in surface area.

3.5.3. TGA

Thermogravimetric analysis (TGA) is a method used to examine how materials react to heat and can provide valuable information about a material's thermal stability, composition, and purity. It is commonly used in fields like polymer science, materials science, and chemistry. During TGA, a small material sample is heated at a steady pace under controlled conditions and its weight is continuously monitored. As the temperature increases, the sample undergoes different thermal events like evaporation, decomposition, oxidation or reduction, which changes in the sample weight can detect. Information obtained from TGA can be used to calculate various properties, such as the mass loss rate, decomposition temperature, and activation energy. In addition, TGA analyses doped MXene materials by measuring their weight changes during heating. This helps to determine their thermal stability, composition, and decomposition behaviour. [125,132,133].

Bao *et al.* studied the thermal stability and composition of S–$Ti_3C_2T_x$/S using thermogravimetric analysis (TGA) with nitrogen and determined the sulfur content in the as-prepared S–$Ti_3C_2T_x$/S. The mass loss observed at 250–310 °C in the TGA curve indicates evaporation of elemental sulfur. The final S content was found to be 72.38 wt%, and the MXene structure decomposed at higher temperatures. $Ti_3C_2T_x$/S showed only 58.75 wt% of sulfur.[58] The effect of MXene on the thermal decomposition of poly (vinyl alcohol) (PVA) was studied by Pan *et al.* using TGA to determine the thermal stabilities of PVA and PVA-MXene. [134] The results showed that MXene enhances the thermal stability of PVA, improving its char residue and lowering its weight loss rates during degradation. PVA-MXene composites showed a 20 °C improvement in T–5% compared to pure PVA. Karthikeyan et al. (2021) investigated thermal behavior of MXenes using TGA. [135] The authors found that the MXenes were thermally stable and as the heating rate increased, degradation occurred in three stages. The first stage (30 and 220 °C) was due to the evaporation of sorbed water molecules. The second stage (220 and 360 °C) was caused by the degradation of interlayer ions. The third stage (360 and 800 °C) occurred due to the dehydroxylation of brucite-like layers and the collapse of the layered arrangement. A recent study by Zhang et al. (2022) used TGA to analyze how PS and PS-O-Ti3C2 nanocomposites behave during thermal decomposition. The results showed that the PS-O-Ti_3C_2 nanocomposites, which contained 2D layered Ti3C2 and, delayed T5% by an average of 60 °C. [136] This was because of the MXene nanosheets acting as a physical barrier with thermal stability and prevented early degradation of the PS molecular chain. These findings suggest that incorporating layered MXene nanosheets can significantly enhance thermal stability and delay the degradation of PS.

4. Applications

4.1. Electrocatalysis

Electrocatalysis has grown to become one of most important branches in electrochemistry. Regulations and concerns regarding sustainability are the driving force behind the developments. Electrocatalysis holds the promise to generate greener energy and conversion of greenhouse emissions. In a typical electrocatalysis, redox reactions occur on the surface of electrodes. However, the promise of electrocatalytic processes is severely challenged by the large overpotentials and unsatisfactory selectivity. To lower the overpotential of specific electrochemical reactions, catalysts are introduced at either electrode. Hence, material discovery is the key to achieve higher electrocatalytic efficiency. In this section we discuss the developments in doped MXene based catalysts for water splitting (hydrogen and oxygen evolution), nitrogen reduction reaction, and carbon fixation, while Table 3 highlights the best performing electrocatalysts along with the doping strategies.

4.1.1. Hydrogen evolution reaction (HER)

Rising concerns for global warming and excessive dependence on fossil fuels led to a paradigm shift towards cleaner and carbon free sources of energy. Using hydrogen as energy source is considered the clean and sustainable solution for a carbon neutral economy. A wide range of techniques can be used to produce hydrogen including biomass conversion, water gas shift reaction, formic acid decomposition, reforming hydrocarbons, and water splitting.[16] Among these, electrocatalytic splitting of water is the most desirable method. Electrocatalytic water splitting is not only clean, safe, and cheap, but can employ renewable energy as well. In a typical electrocatalytic water splitting, hydrogen is evolved at the cathode upon a bias applied between two electrodes. Platinum is considered the ideal material for the hydrogen evolution reaction (HER) due to its low Gibbs free energy for hydrogen adsorption (ΔG_H^*). According to the Brønsted–Evans–Polanyi relationship, the hydrogen adsorption energy is the rate determining step as it is linearly

correlated to the HER activation.[120] However, the high cost and rarity of Pt makes it practically impossible for industrial applications. Hence, for a material to be an ideal alternative to Pt it is essential that the hydrogen adsorption energy is near zero. Both theoretical and experimental studies show that MXenes may be promising materials for HER catalysis. Unlike other 2D systems such as 2H-MoS_2, where HER catalytic activity is restricted to the edge sites, the basal planes of MXenes have demonstrated a significant density of catalytic sites per particle.[121–123] Gao *et al.* were among the first to predict the surface oxygen atoms on the top and bottom layers of 2D MXenes as the catalytic active sites for the HER.[123] Most importantly, MXenes are stable under acidic electrolytes.[121] Although several reports predict and demonstrate the HER-activity of bare 2D-MXenes, their key catalytic performance is far from ideal.[11,16,120].

Multiple strategies were implemented to improve the HER activity of MXenes, such as modifying the surface terminal groups, structural engineering, coupling with other active materials, and doping.[33] Among these, doping is the most viable due to the ability to intrinsically optimize the electronic structure for improved HER activity. Studies on Mo_2C nanosheets showed that doping with nitrogen and sulfur can significantly enhance efficiency.[124,125] Although these systems are not derived from MAX phases, results indicate the potential of doping MXenes to improve their HER activity. Previous reviews showed that nitrogen doping is an effective way to tailor the properties of 2D materials for potential use in HER.[25,26] Among all MXenes, 2D titanium carbides Ti_2CT_x and $Ti_3C_2T_x$ are the most extensively studied and were demonstrated for a multiple applications.[126] However, the HER catalytic activity of Ti_2CT_x can be termed poor, requiring an overpotential of > 600 mV to achieve a current density of 10 mA/cm^2 and low cycling stability.[121] Yoon *et al.* were able to significantly reduce the overpotential to 215 mV *vs.* normal hydrogen electrode (NHE) for HER at 10 mA/cm^2 through nitrogen doping of Ti_2CT_x. In addition, after nitrogen doping Ti_2CT_x showed excellent durability under acidic conditions (0.5 M H_2SO_4).[101] Nitrogen-terminated or substituted N-Ti_2CT_x with HER active Ti–N_x motifs resulted in higher electrocatalytic activity and stability in comparison to oxygen-terminated Ti_2CT_x. The higher HER activity originates from these Ti-N_x motifs, which provide efficient pathways for transferring electrons by spin polarization. DFT calculations show that N substitution lowers the Fermi level of Ti_2CT_x to 0.972 eV and ΔG_H^* to −0.347 eV.

Le and co-workers achieved better performance with nitrogen doped $Ti_3C_2T_x$ MXene.[44] N-$Ti_3C_2T_x$ shows an onset potential of 30

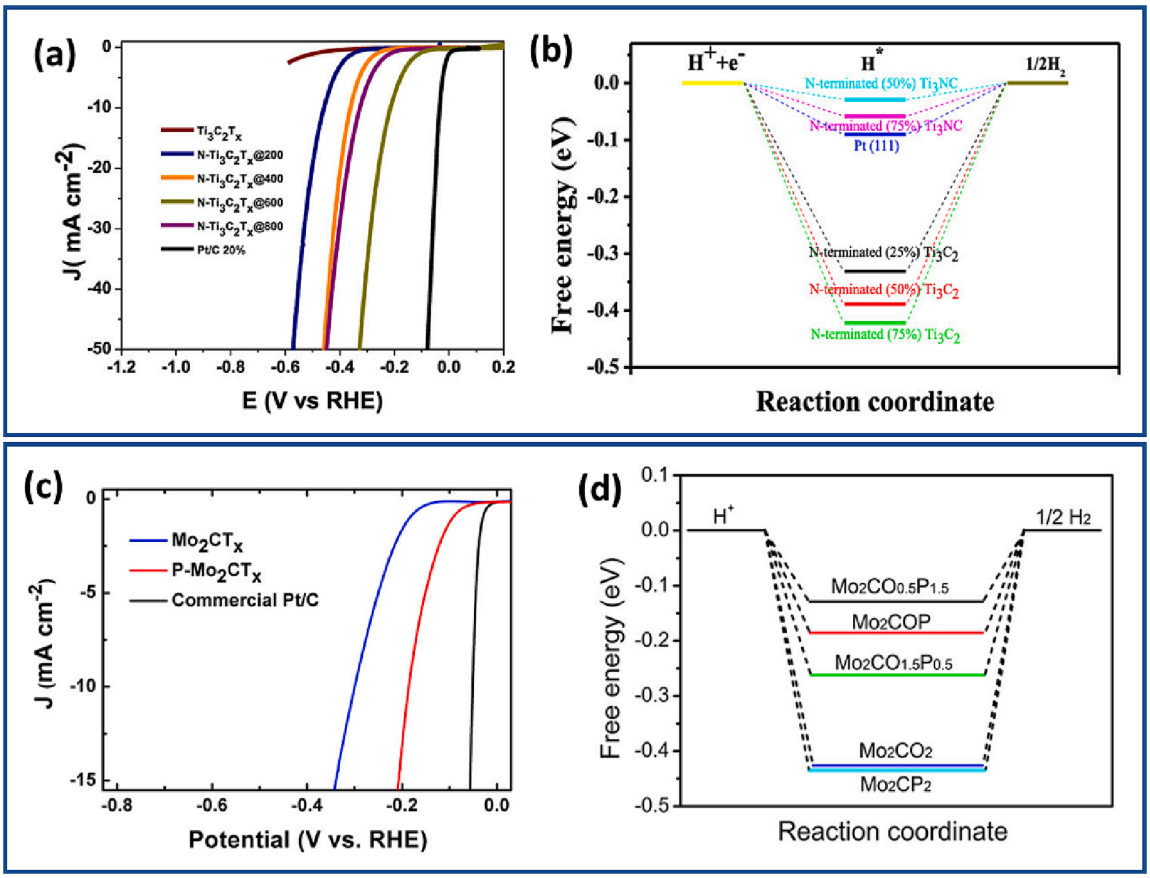

Fig. 11. Electrochemical HER performance of doped MXenes. (a) polarization curves of different N-doped $Ti_3C_2T_x$ catalysts, (b) ΔG_H^* diagram of different H adsorption states corresponding to H coverage of 3/8 on N-terminated (50%) Ti_3NC, 4/8 on N-terminated (75%) Ti_3NC, 2/8 on N-terminated (25%) Ti_3C_2, 3/8 on N-terminated (50%) Ti_3C_2, and 4/8 on N-terminated Ti_3C_2. [44]; (c) Electrocatalytic performance for HER of P doped Mo_2CT_x MXenes, (d) calculated free-energy diagram of the HER on $Mo_2CO_{2-x}P_x$ catalysts. [37] Reproduced from [44,37] with permission from American Chemical Society.

mV and an overpotential as low as 198 mV at 10 mA/cm^2 as well as a much smaller Tafel slope of 92 mV/dec (Fig. 11(a)). Their studies revealed that all nitrogen related species (e.g., N–H, O–Ti–N) contribute to HER enhancement rather than only Ti-N_x motifs as stated by Yoon *et al.*[101] (Fig. 11(b)). Also, heavy doping of nitrogen resulted in poor HER activity and partial transformation of titanium carbide to titanium nitride. A similar improvement in catalytic activity of $Ti_3C_2T_x$ MXene upon nitridation was reported by Han *et al.*

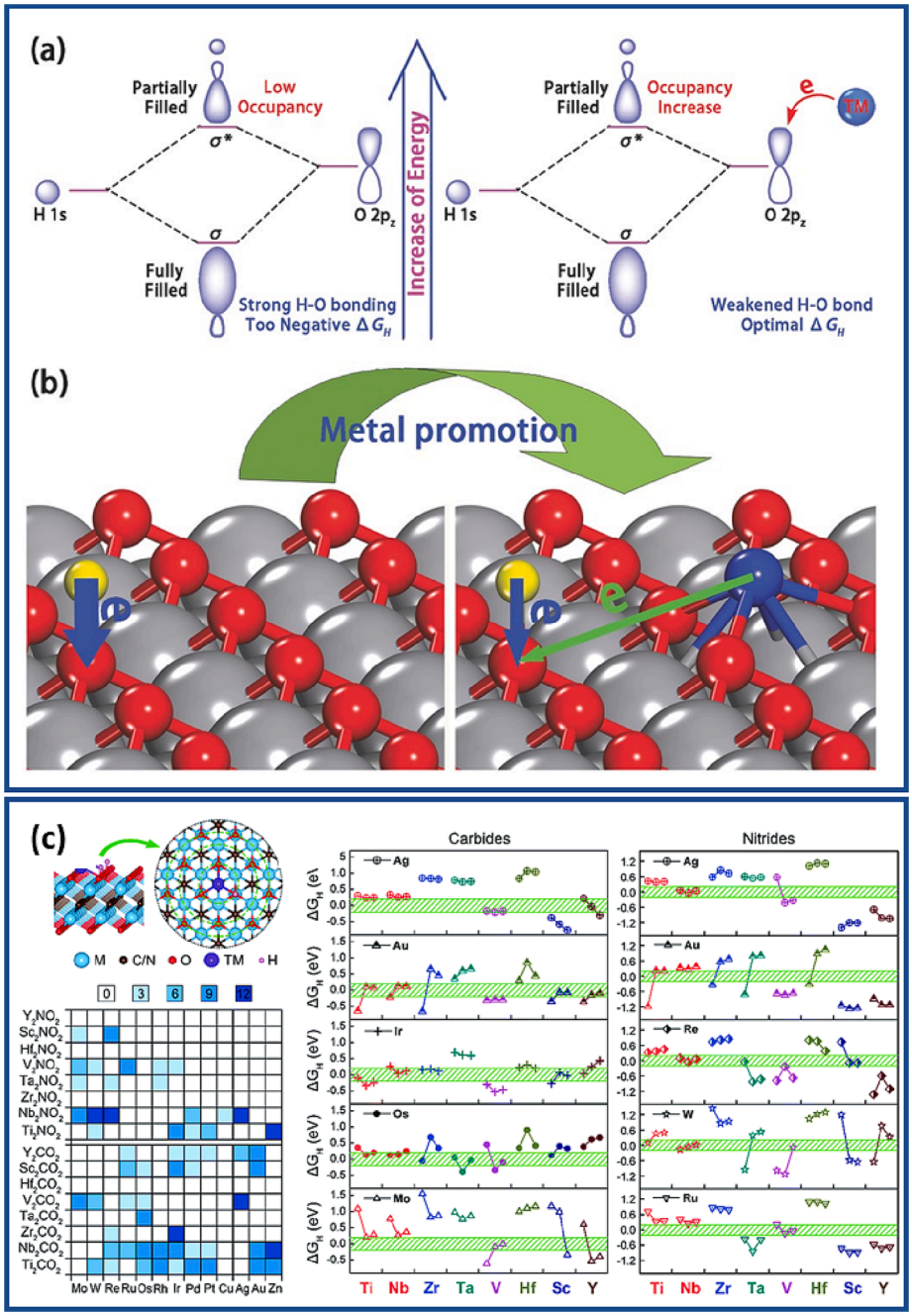

Fig. 12. Scheme of modulating the HER performance of V_2CO_2 by introducing a transition metal onto the surface. (a) The combination of H 1s orbital and O 2p_z orbital forms a fully filled bonding orbital and a partially filled anti-bonding orbital in which the occupancy of the latter determines the strength of the H-O bond. (b) Charge transfer from H to O will occur when H adsorbs on O; by introducing a TM atom onto the surface, O will gain extra electrons from the TM, leading to less charge transfer from H to O and a higher occupancy of the anti-bonding orbital when forming the H-O bond. [129] (c) The structure of H atom adsorbed on the modified surface. Color-coded active site number: the more active sites, the darker the shade. White means no active site. The ΔG_H* of TM-modified carbide and nitride MXenes. The green shaded region marks the HER active energy windows with ΔG_H* from −0.2 to 0.2 eV. [131] Reproduced from [129,131] with permission from Royal Society of Chemistry and Wiley-VCH. (For interpretation of the references to color in this figure legend, the reader is referred to the web version of this article.)

[57] where nitrogen doping was achieved at a lower temperature (35 °C) by ultrasonication in ammonia solution. The best performing catalyst in their case achieved 10 mA/cm^2 at overpotentials around 160 mV in N_2-saturated 0.5 M H_2SO_4 electrolyte solution. In addition to nitrogen, the influence of other heteroatom doping (X = N, B, P, S) on the HER activity of M_2C MXenes (M = Ti, Mo) with or without oxygen functional groups was investigated by Ding *et al.* using density functional calculations.[127] By calculating the Gibbs free energies of hydrogen adsorption (ΔG_H*) they found that N-doped Ti_2CO_2 can exhibit higher electrocatalytic activity than Pt(1 1 1), although pristine Ti_2C is not good for HER catalysis. After heteroatom doping MXenes becomes more metallic in nature, and the electronegative dopants (N, P, S) were able to cause a favourable shift in the Fermi level. Nitrogen as a dopant improves the HER catalytic performance up to a certain threshold concentration above which the catalytic activity is adversely affected. For Ti_2CO_2 8.8 atom% was found to be the optimal N-doping [128] with the lowest ΔG_H* and highest conductivity. It was also predicted that this 8.8% dopant concentration will be thermodynamically most favoured when NH_3 is used as doping agent. [128] Studies by Qu *et al.* and Yoon *et al.* revealed that phosphorization can also be an effective route to enhance the HER activity of MXenes.[37,100] Qu *et al.* synthesized phosphorus doped P–Mo_2CT_x by annealing Mo_2CT_x MXenes in phosphorus/argon atmosphere.[37] As can be seen in Fig. 11 (c), the HER overpotential dropped by 114 mV at 10 mA/cm^2. The improved conductivity of P–Mo_2CT_x facilitates electron transport, improving HER kinetics. Yoon *et al.* doped vanadium carbide MXene with phosphorus by heat treatment at different temperatures (300, 400, 500 °C) with triphenyl phosphine (TPP).[100] The catalyst prepared at 500 °C showed the smallest overpotential of −163 mV at 10 mA/cm in 0.5 m H_2SO_4. Combining computational and experimental results they showed that P-C bonds in P-V_2CT_x are the active sites with the lowest ΔG_H*, which promote HER kinetics through electron transfer into the antibonding orbitals of V-H and/or O–H bonds. (Fig. 11 (d)).

Transition metals (TMs) have long been engineered in various ways to compete with the benchmark Pt catalyst for HER. Incorporating TMs into MXene is a key development towards improving HER performance. Ling *et al.* were among the first to theoretically predict the extremely high catalytic activity after introduction of TM (Fe, Co, Ni) atoms onto the surface of fully terminated vanadium carbides (V_2CO_2).[129] Using first-principle calculations they were able to show that under optimal conditions, introduction of TMs can reduce ΔG_H* to 0, better than Pt(1 1 1). This enhanced activity stems from the strong charge transfer between the metal atom and surface O atoms of V_2CO_2 (Fig. 12 (a,b)). They also discovered that the catalytic activity of TM modified V_2CO_2 can be further modulated by applying tensile strain. It should be noted that under alkaline conditions MXenes are inert toward HER, mainly due to the oxygen terminal groups. These terminal groups obstruct the adsorption and dissociation of water molecules, thereby increasing the

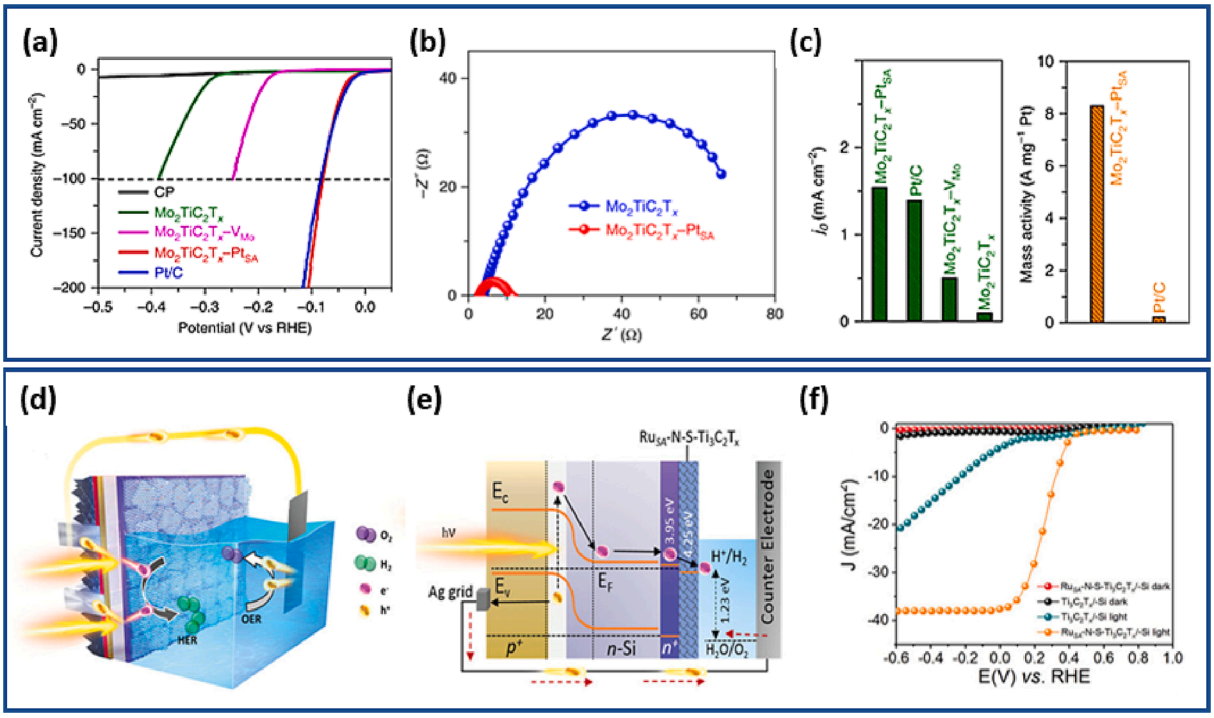

Fig. 13. Enhanced activities of precious metal atom immobilized MXene. (a) HER polarization curves of carbon paper (CP), $Mo_2TiC_2T_x$, $Mo_2TiC_2T_x$–V_{Mo}, $Mo_2TiC_2T_x$–Pt_{SA} and Pt/C (40%) acquired using graphite rod as the counter electrode in 0.5 M H_2SO_4 electrolyte. (b) EIS Nyquist plots of $Mo_2TiC_2T_x$–Pt and $Mo_2TiC_2T_x$ catalysts. (c) Exchange current densities of the catalysts, and mass activity of state-of-the-art Pt/C and $Mo_2TiC_2T_x$–Pt_{SA}. [95] (d) Device structure for PEC H_2 production performance of the Ru-N-S-$Ti_3C_2T_x$ catalyst integrated with n^+np^+-Si photocathode. (e) Band structure diagram of the Ru-N-S-$Ti_3C_2T_x$/n^+np^+-Si photocathode. (f) Current density–voltage (J-V) characteristic curves of $Ti_3C_2T_x$ and Ru-N-S-$Ti_3C_2T_x$ integrated on the n^+np^+-Si photocathode. [97] Reproduced from [95,97] with permission from Nature Portfolio and Wiley.

energy barrier for the first steps of the reaction. However, anchoring transition metals on the MXene vacancy sites can remarkably improve the kinetics and thermodynamics of water dissociation.

Tahini *et al.* recommended Mn anchored on Ti_2CO_2 and V_2CO_2, Fe on V_2CO_2, and Ir on Nb_2CO_2 as promising candidates as TM single atom MXene catalysts for alkaline HER.[130] Similar findings were reported by Li *et al.* for M_2XO_2 type MXenes modified with different TM adatoms. [131] They systematically measure the ΔG_H* values for a combination of 16 different types of M_2XO_2 with 13 types of TM adatoms and identified Os-Ta_2CO_2, Ir-Sc_2CO_2, Ag-Nb_2NO_2, Re-Nb_2NO_2, W-Nb_2NO_2 with ΔG_H* very close to the ideal value of 0 eV (Fig. 12 (c)). The TM adatoms can change the preferential reaction mechanism from Volmer–Heyrovsky to Volmer–Tafel via TM induced electron redistribution on the surface of the MXene. All recent reports on simulated HER activities of TM doped MXenes mention the suitable tuning of ΔG_H* after TM incorporation.[132–134] The main advantages of TM dopants are that they change the conductivity of MXenes, turn nearby sites active for catalysing HER, and transfer charge to the surface O terminal groups, resulting in increased occupancy, thereby weakening O–H bonds.

One effective way to overcome the restrictions of precious metal catalysts is to significantly reduce the metal loading through single atom immobilization. Zhang *et al.* were among the first to practically realize single atom immobilized MXene for HER.[95] In their work, they synthesized Pt atoms immobilized onto double TM MXene nanosheets $Mo_2TiC_2T_x$. Through electrochemical exfoliation they prepared $Mo_2TiC_2T_x$ nanosheets with abundant Mo vacancies which acted as anchoring sites for single Pt atoms. These Pt atoms were stabilized by the formation of covalent Pt–C bonds with the surrounding C atoms on the MXene sheets. Most importantly, this $Mo_2TiC_2T_x$-Pt catalyst demonstrated HER activity equivalent to Pt and even surpassed the commercial Pt/C catalyst. Overpotentials of 30 and 77 mV were recorded to achieve 10 and 100 mA/cm^2 HER current densities and a mass activity about 40 times greater than the commercial platinum-on-carbon catalyst shown in Fig. 13(a-c). The superior activity was due to the extremely low H^+ adsorption energy of single Pt atom on MXene with ΔG_H* of about −0.08 eV, below the commercial catalyst (-0.10 eV).

Jing *et al.* also explored the electrocatalytic performance of Pt doped $Mo_2TiC_2O_2$ monolayer using first principles calculations.[135] However, they used a different approach, placing Pt atoms at the oxygen vacancy sites. After measuring the ΔG_H* values for all intrinsic and extrinsic defects sites, Pt–O defect sites were found to remarkably enhance HER activity. Similar increase in HER activity was observed for Pt loaded V_2CT_x and $Ti_3C_2T_x$ MXenes. [136,137] For both systems the activity was comparable to the commercial catalyst. Pt–V_2CT_x exhibited 10 mA/cm^2 at a low overpotential of ~ 27 mV in 0.5 M H_2SO_4, while Pt-$Ti_3C_2T_x$ electrocatalysts exhibited a much lower overpotential of 12 mV under similar conditions. The presence of vacancies is critical for successfully immobilizing the Pt atoms. Also, the oxygen terminal groups mediate the electron transfer from Pt to surrounding atoms thereby reducing the hydrogen adsorption energy. These results suggest that the immobilized Pt atoms primarily contribute to the hydrogen adsorption and the overall catalytic activity. A plausible way to increase the involvement of MXenes support during catalysis is to tune its electronic properties by heteroatom doping along with single atom immobilization.

Ramalingam *et al.* used this strategy to further enhance the HER activity of single atom immobilized MXenes.[97] They studied the coordination interaction between ruthenium single atoms and 2D titanium carbide ($Ti_3C_2T_x$) MXene support with nitrogen and sulfur heteroatom dopants. In this case the Ru atoms were stabilized via formation of Ru-N and Ru-S bonds. The heteroatom mediated Ru-$Ti_3C_2T_x$ showed superior HER kinetics in comparison to the bare Ru-$Ti_3C_2T_x$ catalyst. Ru-N-S-$Ti_3C_2T_x$ exhibited nearly zero onset potential and the smallest overpotentials of 76 and 237 mV to attain 10 and 100 mA/cm^2 (0.5 M H_2SO_4) in comparison to Ru-$Ti_3C_2T_x$, requiring 215 mV to reach 10 mA/cm^2. The catalyst showed excellent activity in alkaline and neutral electrolytes as well. The HER kinetics for Ru-N-S-$Ti_3C_2T_x$ followed the Volmer–Heyrovsky mechanism which includes a fast initial Volmer reaction step of $H_3O^+ + e^- \rightarrow H_{ads} + H_2O$ followed by a slow Heyrovsky reaction step of $H_{ads} + H_3O^+ + e^- \rightarrow H_{ads} + H_2O$. For practical implementation, they integrated the electrocatalysts with n^+np^+-Si photocathode and evaluated their PEC H_2 production performance; the device structure is shown in Fig. 13 (d-e). A photocurrent density of 37.6 mA/cm^2 was achieved with Ru-N-S-$Ti_3C_2T_x$, 10 times higher than $Ti_3C_2T_x$/n^+np^+-Si photocathode (Fig. 13 (f)). Similarly, for Ir single atoms confined on N, S co-doped $Ti_3C_2T_x$, the highly coordinated Ir–N and Ir–S bonds improve the charge redistribution in the interfacial region of the $Ti_3C_2T_x$ support, resulting in improved HER activity. Recently, Huang *et al.* used Nitrogen-Doped Nb_2CT_x as the support matrix to host Ni nanoparticles for HER in 1 M $HClO_4$.[138] As an electrocatalyst Ni/N-Nb_2CT_x demonstrated Pt-like onset potentials and could achieve 500 mA cm^{-2} at overpotentials of only 383 mV. Moreover, the catalysts remained stable for at least 24 h at high HER current density of 300 mA cm^{-2}. Though this study establishes the performance of Ni/N-Nb_2CT_x as a catalyst, the influence of nitrogen as dopant has not been discussed.

Dual doped Ir-2NS-$Ti_3C_2T_x$ (nitrogen twice than sulfur) showed much improved catalytic properties compared to single atom doped Ir–N–$Ti_3C_2T_x$. This indicates that the coordination of Ir with N and S is important for achieving improved intrinsic activity.[69] Notably, the overpotential at a current density of 10 mA/cm^2 is much smaller for Ir-2NS-$Ti_3C_2T_x$ (57.7 mV) compared to the Ru-N-S-$Ti_3C_2T_x$ catalyst (76 mV). This leaves us with new opportunities to optimize the coordination of precious metals with N, S co-dopants. In another article published almost at the same time, Liu *et al.* present a similar work of single-atom ruthenium (Ru_{SA}) supported on nitrogen (N)-doped $Ti_3C_2T_x$ MXene.[97,139] Their catalyst also showed superior electrocatalytic activity and durability compared with commercial Pt/C catalysts toward HER in different pH conditions. They also mention that ruthenium single atoms are stabilized on MXene species via formation of Ru–N bonds. Consequently, the Ru–N-$Ti_3C_2T_x$ catalyst demonstrated outstanding catalytic performance towards HER with overpotential values of 23, 27 and 81 mV to achieve 10 mA/cm^2 current density in 0.5 M H_2SO_4, 1 M KOH, and 1 M phosphate-buffered saline (PBS) electrolytes, respectively.

Apart from nitrogen and sulfur, boron was successfully used as an alternative heteroatom dopant for $Ti_3C_2T_x$ MXene. Ru nanoparticles supported on B-doped $Ti_3C_2T_x$ MXene were demonstrated as a promising electrocatalyst for HER under acidic conditions. [140] This catalyst achieved 10 mA/cm^2 at a relatively low overpotential of 62.9 mV. From DFT calculations the ΔG_{H^*} value for Ru@B–MXene was found to be much lower than the established HER catalysts, namely $\Delta G_{H^*} = 0.002$ eV compared with Pt (-0.09 eV), MoS_2 (0.08 eV) and WS_2 (0.22 eV). Most importantly the study also reveals that the outstanding catalytic performance is due not only

to Ru anchoring on the MXene, but also to the effect of B-doping that provides abundant catalytically active sites. All works highlighted here demonstrate the advantage of engineering noble metal-MXene interaction with heteroatoms for higher HER activity. Although the activities are excellent under acidic conditions, they are not admirable under alkaline or neutral conditions.

Other transition metals such as cobalt and niobium doping were also reported to improve the HER catalytic properties of MXenes. Kuznetsov *et al.* designed Co doped Mo_2CT_x as hydrogen evolution catalyst in acidic conditions.[102] They developed a methodology that uses a bulk β-Mo_2C phase for incorporation of cobalt atoms that are retained in the final solid solution of Mo_2CT_x:C. After Co doping, the average $|\Delta G_H^*|$ value calculated for the adsorption of six H atoms in the vicinity of the Co site was 0.40 eV, significantly lower than 0.61 eV for the unsubstituted Mo_2CO_2. Du *et al.* demonstrated that Nb-doping of $Ti_3C_2T_x$ MXene is crucial for achieving higher HER activity for the Ni/Co(alloy)-MXene composite catalyst.[141] The influence of Nb doping could be seen from the over-potential values of 55.5 versus 255.5 mV at j_{Cdl} of 1000 mA/F for undoped MXene.

It has been established that HER is favoured in acidic conditions due to the abundance of H^+. Most of the studies discussed above have been performed in 0.5 M H_2SO_4. The abundance OH^- significantly hinders the HER kinetics in alkaline conditions. Notable, very few 2D materials have succeeded in achieving benchmark performance under alkaline conditions. Zou *et al.* addressed this research gap using ruthenium single-atom modulated $Ti_3C_2T_x$ MXene. [142] The $Ru_{SA}@Ti_3C_2T_x$ achieved ampere-level HER current densities in 1 M KOH, which is remarkable considering the strong basic conditions. $Ru_{SA}@Ti_3C_2T_x$ could readily attain high current densities of 1 and 1.5 A cm^{-2} at over potentials of 425.7 and 464.6 mV (*vs* RHE), respectively. Compared to $Ru_{SA}@Ti_3C_2T_x$, $Ti_3C_2T_x$ demonstrated significantly inferior HER activity over the entire potential range. Notably, the $Ru_{SA}@Ti_3C_2T_x$ outperformed even the commercial Pt/C catalyst. To understand the mechanism of improved performance, they performed in-situ spectroelectrochemical Raman spectroscopy. Here they used the out-of-plane vibrations of C atoms in $Ti_3C_2T_x$ (A_{1g} mode at 728 cm^{-1}) as the key descriptor for the protonation of -O into –OH. The in-situ studies showed that during the cathodic bias of 0 V to −0.3 V the A_{1g} peak of $Ru_{SA}@Ti_3C_2T_x$ is red-shifted less (728 to 725 cm^{-1}) compared to $Ti_3C_2T_x$ (728 to 721 cm^{-1}). They interpreted this findings as the low coverage of protonated –OH on $Ru_{SA}@Ti_3C_2T_x$, resulting in improved HER kinetics. They mentioned that the Ru_{SA} modulate the surface protonation/deprotonation of $Ti_3C_2T_x$, significantly reducing the Gibbs free energy for hydrogen adsorption from −0.33 eV to −0.07 eV and hence the improved HER activity. Another challenge in the field of electrocatalysis in the dissociation of water under mild or neutral conditions, which bypasses the corrosive conditions. By dispersing Ru clusters on Mo_2CT_x, the catalytic activity of Mo_2CT_x can be significantly improved in 1.0 M phosphate buffer (pH 7.0).[143] Though the Ru/Mo_2CT_x couldn't surpass the commercial Pt/C, their performances were similar. Ru/Mo_2CT_x required overpotential of 73 mV while Pt/C required 52 mV at −10 mA cm^{-2} and Mo_2CT_x 376 mV at−10 mA cm^{-2}. Moreover, Ru/Mo_2CT_x exhibited stable HER activity for 1000 cycles and at a constant cathodic of−20 mA cm^{-2} for 30 h. These findings are critical in developing doped MXenes as electrocatalysts for water splitting in greener electrolytes.

4.1.2. Oxygen evolution reaction (OER) and oxygen reduction reaction (ORR)

During electrochemical splitting of water, hydrogen evolution occurs at the cathode while the oxygen evolution happens at the anode under an applied bias. Water gets reduced at the cathode, to hydrogen gas and hydroxide ions., while at the anode, water gets oxidized to oxygen gas and hydrogen ions. The efficiency of this redox process is dependent on the local pH at the electrode. HER is favored in acidic media while OER is thermodynamically more favorable under basic conditions. Under acidic condition two water molecules (H_2O) are oxidized into four protons (H^+) and one oxygen molecule (O_2), while in basic conditions hydroxyl radicals (OH^-) are oxidized into H_2O and O_2 as shown below:

$$4OH^- \leftrightarrow 2\ H_2O(l) + O_2(g) + 4\ e^-\ \text{(alkaline electrolyte)}$$

$$2\ H_2O(l) \leftrightarrow 4H+ + O_2(g) + 4\ e\text{-}\ \text{(acidic electrolyte)}$$

Compared to HER, the oxygen evolution reaction (OER) is kinetically more sluggish and requires energy beyond the theoretical potential of 1.23 V. [144] The oxygen reduction reaction (ORR) is another fundamental reaction in electrochemistry, which is critically important in fuel cells, metal-air batteries, and life processes such as respiration.[145] Unlike electrolysis, in proton exchange membrane fuel cells (PEM) hydrogen and oxygen are made to react at the catalyst surface producing water and electricity. In a PEM fuel cell hydrogen is catalytically split into protons and electrons at the anode while at the cathode oxygen molecules react with the protons and electrons forming water. This reduction of oxygen to water is known as oxygen reduction reaction. The oxygen reduction half cell reaction can be represented as:

$$O_2(g) + 4H^+ + 4\ e^- \leftrightarrow 2\ H_2O$$

Both OER and ORR reactions suffer from the need of inherent 4-electron transfer. For OER, precious metal-based catalysts such as IrO_2 and RuO_2 are often considered as benchmark materials. Similar to Pt, the large-scale applications of these materials are restricted due to high cost and scarcity. Although the superior properties of MXenes such as high conductivity can ensure fast electron transport during electrochemical reactions, pure MXenes show very limited OER activity.[146] Tang *et al.* improved the OER activity of $Ti_3C_2T_x$ by nitrogen doping,[117] which created more active sites, accelerated charge transfer, and improved the wettability. The onset potential for OER dropped from about 449 mV for fresh Ti_3C_2 to ~ 246 mV for the nitrogen doped electrocatalyst ($Ti_3C_{1.6}N_{0.4}$). For ORR, improved performance was demonstrated by Parse *et al.* using a composite structure of TiO_2 and nitrogen sulphur co-doped Ti_3C_2 MXene. The optimized catalyst showed an onset potential of 0.98 V versus RHE and a substantial ORR current of 3.5 mA/cm^2.

As mentioned in the previous section, several theoretical studies demonstrated the usefulness of single atoms supported MXene based catalysts for enhanced HER activities. Influenced by these findings, single atom doped MXenes were also searched and applied

for oxygen evolution/reduction through electrocatalysis. Cheng *et al.* investigated the OER activity of a series of TM atoms (Ti, V, Cr, Mn, Fe, Co, Ni, Cu, Zn) supported by M_2NO_2 (M = Ti, V, Cr) MXenes using DFT calculations. Among these, Cu anchored on Ti_2NO_2 demonstrated the potential to be the best OER electrocatalyst with an overpotential of 0.24 V. For ORR, Peng *et al.* proposed Ti_2CO_2-supported Cu as a potential candidate based on first-principles calculations.[147] They screened a range of 3*d*, 4*d* and 5*d* TM single atoms anchored on the surface of Ti_2CO_2, $Ti_3C_2O_2$ and Ti_3CNO_2 MXenes. Cu-Ti_2CO_2 exhibited a much lower overpotential of 0.25 V in comparison to commercial Pt/C catalyst (0.4 V) and could thus be an ideal cathode material for a proton exchange membrane fuel cell due to its ultralow overpotential, high $4e^-$ ORR selectivity, and acid stability as shown in Fig. 14 (a). Peng *et al.* also defined a composition descriptor, which can provide important guidance for experimental design of MXene based catalysts. It is often mentioned that the presence of various terminal functionalities (−O, −F, −OH) makes MXenes interesting candidates for various applications. However, the effect of these terminal groups has not been fully investigated for electrochemical applications. Liu *et al.* investigated the influence of surface terminations on the ORR activity of $Ti_{n+1}C_nT_x$ and Pt-decorated Pt/V-$Ti_{n+1}C_nT_x$ (n = 1–3, T = O and/or F) surfaces by first-principles calculations.[148] For the Pt-decorated catalyst, F-terminated surfaces were predicted to show better ORR performance than O-terminated surfaces. However, the F terminations were found to be less stable than O terminations. As already

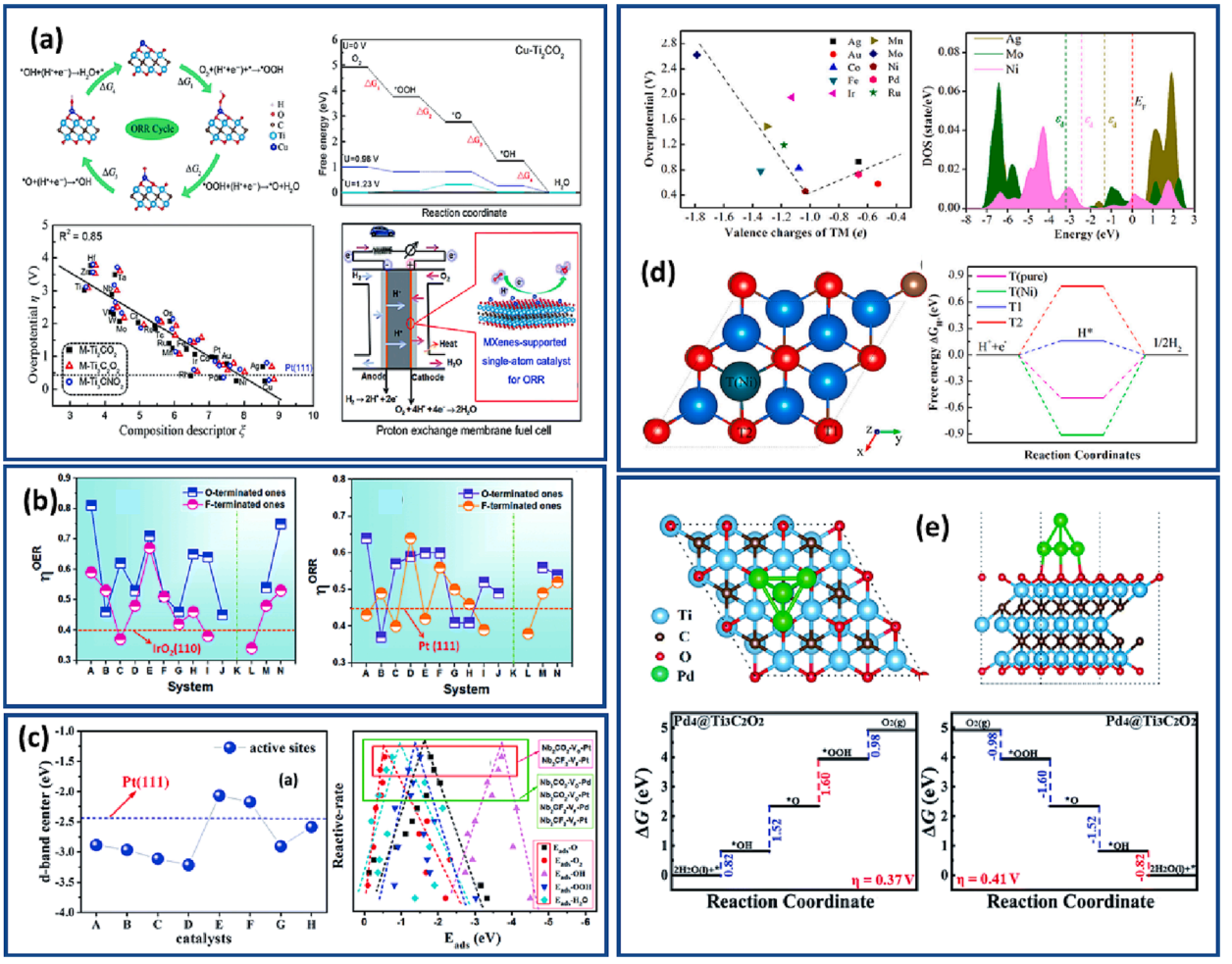

Fig. 14. Theoretical studies on doped MXenes as catalyst for OER and ORR.(a) Schematic $4e^-$ ORR associative mechanism. Free energy profile of ORR proceeding on Cu–Ti_2CO_2, overpotential versus composition descriptor ξ, where atoms anchored on Ti_2CO_2 are marked with element symbols to guide the eye and the horizontal dotted line indicates the overpotential (0.43 V) of Pt(1 1 1) and schematic of MXene supported single atom ORR catalysts at the cathode of a proton exchange membrane fuel cell.[147] (b) Catalytic activities described with h_{ORR} and h_{OER} where A–N represent Ti_2CT_2-V_T-Pt, V_2CT_2-V_T-Pt, Nb_2CT_2-V_T-Pt, Mo_2CT_2-V_T-Pt, $Ti_3C_2T_2$-V_T-Pt, $Zr_3C_2T_2$- V_T-Pt, $Ti_3(C,N)_2$-CT_2-V_T-Pt, $Ti_3(C,N)_2$-NT_2-V_T-Pt, $Nb_4C_3T_2$-V_T-Pt, $Ta_4C_3T_2$-V_T-Pt, $Ti_4N_3T_2$-V_T-Pt, $Cr_2TiC_2F_2$-V_F-Pt, $Mo_2TiC_2T_2$-V_T-Pt and $Mo_2Ti_2C_3T_2$-V_T-Pt (T = O; F).[159] (c) The d-band center on the surface of the recombinant catalysts, A to H represent Nb_2CO_2–Pd, Nb_2CO_2–Pt, Nb_2CF_2–Pd, Nb_2CF_2–Pt, Nb_2CO_2–VO–Pd, Nb_2CO_2–VO–Pt, Nb_2CF_2–VF–Pd and Nb_2CF_2–VF–Pt, and volcano plots of these catalysts, which describe the relationship between activity and adsorption energy for intermediates. [160] (d) Relationship of overpotential with TM valence charge, density of states of TM in TM/Cr_2CO_2 and corresponding ε_d, schematic of active sites of Ni/Cr_2CO_2 for HER, and ΔG_H* of Ni/Cr_2CO_2 at different sites. [161] (e) Top and side views of Pd_4@$Ti_3C_2O_2$ morphology. Free energy diagrams for the OER and ORR of Pd_4@$Ti_3C_2O_2$ at electrode potential U = 0.[164] Reproduced from [147,159,160,161,164] with permission from Royal Society of Chemistry and American Chemical Society.

mentioned earlier, Pt atoms immobilized onto MXenes were considered as an alternative to bulk Pt. One way to further reduce Pt loading is by alloying with a transition metal. Zhang *et al.* found that replacing Pt atoms with Au/Pt alloy on defective Ti_2CO_2 can be considered as a potential approach to reduce Pt loading while maintaining high ORR activity.[149] The ORR activity was shown to be $Pt_3Au/V\text{-}Ti_2CO_2 > Pt_3/V\text{-}Ti_2CO_2 > Pt_4/V\text{-}Ti_2CO_2 > Pt/V\text{-}Ti_2CO_2$.

Janus MXenes ($M_1M_2C_2T_x$) with two TM centers show promising electrochemical properties and HER activity. [36,150,151] Recently, Ma *et al.* explored the OER/ORR catalytic performance of Pt doped Ti_2CNL (N = O/S/Se; L = F/Cl/Br/I) using first-principles calculations.[152] They screened 31 combinations for ORR/OER bifunctional catalytic activity. Interestingly, all combinations showed affinity towards ORR rather than HER. Most importantly, the electronegativity of the Pt doping site controlled the absorption of reaction intermediates. A low electronegativity leads to high overpotential and low catalytic activity. The catalytic properties improve further when Pt is doped on the side of Janus-MXenes with two empty orbital atoms (O, S and Se). There are reports that demonstrate that controlled use of strain can improve the activity of a catalyst. [153–156] Therefore, by applying a controlled amount of strain on these single-doped MXene catalysts, their electronic and catalytic properties can be enhanced further.[157,158] For example, a 6% tensile strain on Pt-doped Ti_2CO_2 can enhance its efficiency as a bifunctional ORR/OER catalyst.[157] Similarly, Pt doped Ti_2CF_2 under a compressive strain of 14% and tensile strain of 4% showed the highest ORR/OER catalytic performance with overpotential of 0.45/0.43 V.[158].

Strain was predicted to reduce the bonding strength of OH on Pt doped Ti_2CF_2 and increase the d-band center. Under compressive strain the center could be moved to a higher energy level, influenced by the F atoms. Furthermore, strain can also be used to tune the work function of the catalyst. The work function of Pt doped Ti_2CF_2 of 4.62 eV increased to 5.18 and 4.84 eV under −14% and 10% strain, respectively. By adjusting the work function, the adsorption and desorption of OH* on the catalytic surface can be regulated. [159] It is noteworthy to mention that the same phenomena are observed for a range of "strained" Pt doped MXenes including Ti_2CNL (N = O/S/Se, L = F/Cl/Br/I), Ti_2CF_2 and Ti_2CO_2. These results encourage to investigate the influence of strain on other single atom doped MXene catalysts.

In fuel cells and metal-air batteries the ORR occurs during discharge, while the OER takes place during charge. Catalyst materials that can perform both processes with high efficiency are best suited for these applications. The search for an MXene based bifunctional catalysts consisted mostly of theoretical calculations and simulations. Kan *et al.* screened 26 different MXenes decorated with single Pt atoms for the best performing bifunctional catalyst.[159] The list includes O and F terminated monometal carbide MXenes (Ti_2C, V_2C, Nb_2C, Mo_2C, Ti_3C_2, Zr_3C_2, Nb_4C_3, Ta_4C_3), ordered bimetal carbide MXenes (Cr_2TiC_2, Mo_2TiC_2, $Mo_2Ti_2C_3$), a nitride MXene (Ti_4N_3), and a carbonitride MXene ($Ti_3(CN)_2$). The resultant adsorption energies and Bader charge are summarized in Table 2. Based on first-principles calculations, $Ti_2CF_2\text{-}V_F\text{-}Pt$, $Ti_3C_2F_2\text{-}V_F\text{-}Pt$, $V_2CO_2\text{-}V_O\text{-}Pt$, $Nb_2CF_2\text{-}V_F\text{-}Pt$, $Nb_4C_3F_2\text{-}V_F\text{-}Pt$, $Cr_2TiC_2F_2\text{-}V_F\text{-}Pt$, $Ti_3(C,N)_2\text{-}CO_2\text{-}V_O\text{-}Pt$ and $Ti_3(C,N)_2\text{-}NO_2\text{-}V_O\text{-}Pt$ are promising ORR catalysts, while $Nb_2CF_2\text{-}V_F\text{-}Pt$, $Nb_4C_3F_2\text{-}V_F\text{-}Pt$ and $Cr_2TiC_2F_2\text{-}V_F\text{-}Pt$ are effective bifunctional ORR/OER catalysts. For the screening, all adsorption energies were compared against the benchmark Pt(1 1 1) ($\mathbf{E_{ads}\text{-}O_2}$ = 0.69 eV and $\mathbf{E_{ads}\text{-}H_2O}$ = 0.34 eV) and IrO_2 ($\mathbf{E_{ads}\text{-}O_2}$ = 0.22 eV and $\mathbf{E_{ads}\text{-}H_2O}$ = 0.57 eV) catalysts and shown in Fig. 14 (b). Kan *et al.* proposed Pt/Pd-doped Nb_2CT_2 MXenes as promising bifunctional catalysts.[160] Using detailed DFT calculations they shortlisted eight Pd/Pt-supported systems (Nb_2C–Pd/Pt, Nb_2CO_2–Pd/Pt, Nb_2CF_2–Pd/Pt and $Nb_2C(OH)_2$–Pd/Pt) and four Pd/Pt-doped systems (Nb_2CO_2–V_O–Pd/Pt and Nb_2CF_2–V_F–Pd/Pt) as stable bifunctional catalysts. Among these, Pt doped systems showed the best activity,

Table 2
Adsorption properties of reaction intermediates on various Pt immobilized MXene systems. $E_{ads}\text{-}O_2$, $E_{ads}\text{-}O$, and $E_{ads}\text{-}H_2O$ represent the adsorption energies of O_2, O and H_2O molecules, and $Q\text{-}O_2$ and $Q\text{-}H_2O$ are the charge numbers of the adsorbates gained from the catalysts. Reprinted with permission from Kan et al.[159].

System	$E_{ads}\text{-}O_2$ (eV)	$E_{ads}\text{-}O$ (eV)	$E_{ads}\text{-}H_2O$ (eV)	$Q\text{-}O_2$ (e)	$Q\text{-}H_2O$ (e)
$Ti_2CO_2\text{-}V_O\text{-}Pt$	−0.38	−0.41	−0.26	0.51	0.38
$Ti_2CF_2\text{-}V_F\text{-}Pt$	−0.65	−0.48	−0.33	0.60	0.44
$V_2CO_2\text{-}V_O\text{-}Pt$	−0.36	−0.43	−0.22	0.49	0.21
$V_2CF_2\text{-}V_F\text{-}Pt$	−0.57	−0.66	−0.37	0.53	0.19
$Nb_2CO_2\text{-}V_O\text{-}Pt$	−0.66	−0.48	−0.72	0.69	0.63
$Nb_2CF_2\text{-}V_F\text{-}Pt$	−0.55	−0.50	−0.45	0.65	0.33
$Mo_2CO_2\text{-}V_O\text{-}Pt$	−0.22	−0.23	−0.33	0.22	0.28
$Mo_2CF_2\text{-}V_F\text{-}Pt$	−0.35	−0.28	−0.43	0.34	0.32
$Ti_3C_2O_2\text{-}V_O\text{-}Pt$	−0.40	−0.43	−0.28	0.52	0.38
$Ti_3C_2F_2\text{-}V_F\text{-}Pt$	−0.68	−0.50	−0.36	0.61	0.42
$Ti_3(C,N)_2\text{-}CO_2\text{-}V_O\text{-}Pt$	−0.87	−0.45	−0.32	0.66	0.28
$Ti_3(C,N)_2\text{-}CF_2\text{-}V_F\text{-}Pt$	−0.32	−0.69	−0.76	0.32	0.57
$Ti_3(C,N)_2\text{-}NO_2\text{-}V_O\text{-}Pt$	−0.94	−0.64	−0.50	0.72	0.31
$Zr_3C_2O_2\text{-}V_O\text{-}Pt$	−1.13	−0.86	−1.24	0.82	0.76
$Zr_3C_2F_2\text{-}V_F\text{-}Pt$	−1.48	−0.95	−1.05	0.90	0.83
$Nb_4C_3O_2\text{-}V_O\text{-}Pt$	−0.68	−0.46	−0.77	0.69	0.63
$Nb_4C_3F_2\text{-}V_F\text{-}Pt$	−0.57	−0.52	−0.49	0.65	0.33
$Ta_4C_3O_2\text{-}V_O\text{-}Pt$	−0.31	−0.79	−0.36	0.27	0.31
$Cr_2TiC_2F_2\text{-}V_F\text{-}Pt$	−0.52	−0.54	−0.48	0.66	0.37
$Mo_2TiC_2O_2\text{-}V_O\text{-}Pt$	−0.22	−0.32	−0.27	0.39	0.21
$Mo_2TiC_2F_2\text{-}V_F\text{-}Pt$	−0.76	−0.21	−0.83	0.47	0.29
$Mo_2Ti_2C_3O_2\text{-}V_O\text{-}Pt$	−0.27	−0.29	−0.30	0.42	0.28
$Mo_2Ti_2C_3F_2\text{-}V_F\text{-}Pt$	−0.77	−0.33	−0.81	0.45	0.30

and Nb_2CF_2–V_F–Pt even outperformed the benchmark Pt(1 1 1) and IrO_2(1 1 0) catalysts and can be seen form the corresponding d-band centre energies in Fig. 14 (c).

For water electrolyser applications, the bifunctional catalysts need to be proficient for both HER and OER. Cheng *et al.* proposed single atom Ni anchored on Cr_2CO_2 MXene as an ideal bifunctional catalyst.[161] Ten TMs (Mn, Fe, Co, Ni, Mo, Ru, Pd, Ag, Ir and Au) anchored on Cr_2CO_2 were considered. Ni-Cr_2CO_2 can perform HER and OER at low (theoretical) overpotential of 0.16 and 0.46 V, respectively, and a synthetic route to prepare it was proposed. Fig. 14 (d) shows the variation in overpotential values of these transition metal doped Cr_2CO_2 catalysts. In addition to bifunctional properties, Fu *et al.* reported trifunctional (OER, ORR, HER) properties of a single Pd atom supported on $Ti_3C_2O_2$ MXene. This catalyst was selected from 12 candidates, namely Fe, Co, Ni, Cu, Ru, Rh, Pd, Ag, Os, Ir, Pt and Au. The simulated activity showed that Pd supported on $Ti_3C_2O_2$ can initiate all three reactions at low overpotential of 0.22, 0.31 and 0.34 V for HER, OER and ORR, respectively, making it an excellent trifunctional electrocatalyst suited for overall water splitting and rechargeable air-based batteries. It is important to note that for all *3d*, *4d* and *5d* TMs studied as a single atom MXene-supported catalyst, the *d* orbital electrons are those that perturb the electronic state, enhancing the overall catalytic activity. Recently, Shabana *et al.* demonstrated Pt/Nb_2CT_x as an efficient bi-functional catalyst for HER and ORR. [162] The HER activity was investigated in 0.5 M $HClO_4$, and the ORR activity was tested in N_2 or O_2 saturated 0.1 M KOH. A substantial increase in electrocatalytic performance was observed after Pt loading. Though the reported activities are inferior to the commercial Pt/C for both HER and ORR, the Pt

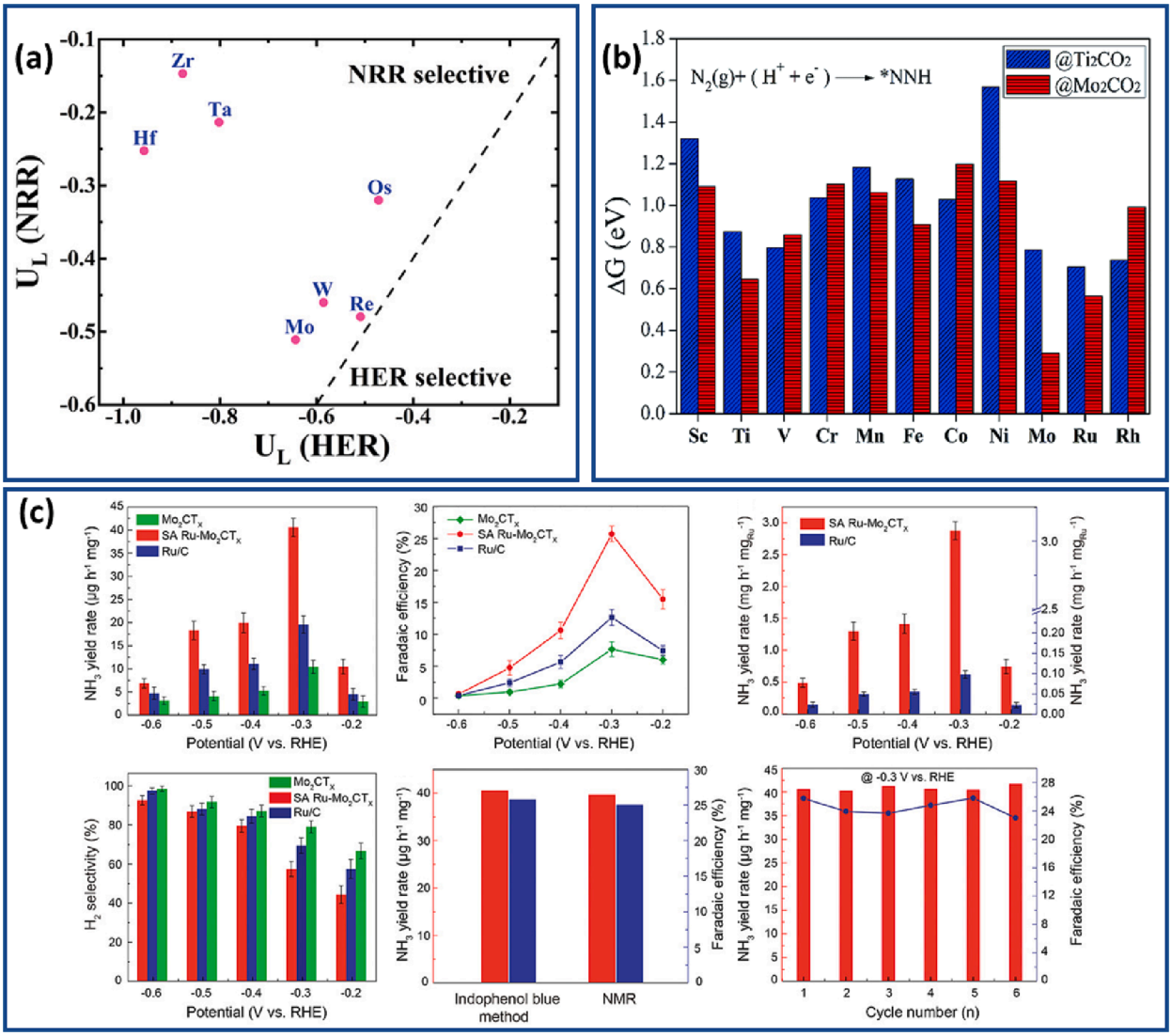

Fig. 15. Theoretical and experimental studies on the NRR activity of doped MXene catalysts.(a) Calculated limiting potentials for HER (U_L(HER)) and NRR (U_L(NRR)) on the surfaces of various single atoms supported onto $Mo_2TiC_2O_2$ defective layers. When U_L(NRR) < U_L(HER), the electrocatalysts are selective for NRR.[172] (b) Reaction free energies for *N_2 to *NNH on various single atom transition metal supported Ti_2CO_2 and Mo_2CO_2 nanosheets.[173] (c) NRR performance of Mo_2CT_x, single atom Ru-Mo_2CT_x and commercial Ru/C. [89] Reproduced from [172,173,89] with permission from Wiley and Royal Society of Chemistry.

mass activity of Pt/Nb_2CT_x was found to be 5 times higher than Pt/C for HER and 10 times higher than Pt/C for ORR. Having Ag nanoparticles dispersed on $Ti_3C_2T_x$ can also improve the bifunctional activity of $Ti_3C_2T_x$ towards HER and OER. [163] By optimizing the Ag loading, the catalyst could achieve current density of 10 mA cm^{-2} at overpotential of 0.117 V and 0.25 V for HER and OER, respectively in 0.5 M H_2SO_4, which are lower compared to commercial counterparts. Most importantly, these works demonstrated the viability of Single Atom Catalyst (SAC)-MXene as bifunctional catalyst. Using theoretical investigations and rational design techniques, SAC-MXenes can become a suitable alternative to rare earth catalysts.

A plethora of studies relate MXenes to OER/ORR, but experimental realization is rare. In most cases, MXenes are synthesized by HF etching of the MAX phase. Pang *et al.* devised a safer electrochemical etching (E-etching) technique to exfoliate and prepare Ti_2CT_x, Cr_2CT_x and V_2CT_x MXenes from the corresponding MAX phases.[164] These E-etched MXenes were then decorated with Co^{3+} ions to obtain a full water splitting catalyst. An initial improvement in HER performance was observed after Co^{3+} incorporation, and the measured overpotentials were in the order Co^{3+}-Cr_2CT_x, 404 mV > Co^{3+}-Ti_2CT_x, 458 mV > Co^{3+}-V_2CT_x, 460 mV. However, no difference in OER activity was observed, indicating that this activity was independent of the MXenes and occurred through the OER-active Co species. Kan *et al.* already stipulated the superior OER/ORR activities of Pt-MXenes in their first principles study. [159,160] The practical realization was carried out by Zhang *et al.* using Pt/$Ti_3C_2T_x$ as ORR catalyst.[165] The catalyst was tested in both alkaline and acidic electrolytes and demonstrated superior activity with respect to commercial 20% Pt/C. The catalytic activity of Pt/$Ti_3C_2T_x$ was found to be higher in alkaline (0.1 M KOH) than acidic conditions (0.5 M H_2SO_4). Though the isolated single atoms on MXene are the best candidates for electrocatalytic applications. However, during practical applications these isolated metal atoms tend to aggregate into clusters due to the high surface free energy. Fu *et al.* investigated the effect of metal clusters on the OER and ORR properties of $Ti_3C_2O_2$ supported Pd catalysts. [164] They found even if these catalysts aggregate to form small clusters, the overpotential for OER and ORR increases negligibly. Using the smallest stereo-cluster of Pd (Pd_4 cluster), as shown in as shown in Fig. 14(e) they calculated the corresponding overpotentials for OER and ORR. Compared with Pd_1@$Ti_3C_2O_2$ (single atom), the OER and ORR overpotentials increased by only 0.06 V and 0.07 V, for Pd_4@$Ti_3C_2O_2$.

Hence, even with small atomic clusters the excellent OER and ORR activities could be maintained. This section highlights the emerging role of MXenes that can be integrated with other materials and engineered at the atomic scale to yield hybrid heterostructures with multifunctional catalytic activities.

4.1.3. Nitrogen reduction reaction (NRR)

Ammonia (NH_3) is the key ingredient for production of nitrogen-containing chemicals and is used heavily in the pharmaceutical and fertilizer industries. Due to its huge demand, developing new synthetic strategies for ammonia has been of interest for decades. Ammonia is produced mostly using Haber–Bosch methods. Conventionally, the Haber–Bosch process is conducted at high temperature (400–500 °C) and pressure (10–30 MPa) and is highly energy demanding, requiring 1–2% of the global energy consumption, and bears a heavy carbon footprint (300 million metric tons of CO_2 annually).[166] Electrochemical reduction of nitrogen (ENRR) has attracted interest as a green and efficient way to synthesize ammonia. Thermodynamically, ENRR is 20% more energy efficient than traditional Haber–Bosch process.[167] However, the significant amount of energy required to break the nonpolar N_2 triple bond makes ENRR extremely challenging to carry out. The major challenge is the inherent selectivity for the HER due to its lower theoretical potential. As an emerging catalyst, MXenes have also been used for the conversion of N_2 to NH_3. So far, various reports predicted and highlighted the potential of MXenes as promising NRR electrocatalysts.[168–171] It is notable that bare MXenes are likely to be unstable under NRR operating conditions, and it is important to introduce foreign elements to overcome the parasitic effect of the HER.

Computational studies based on DFT calculations are crucial for understanding the mechanisms involved in the NRR. Li *et al.* simulated the performance of single TM incorporated MXenes as NRR catalysts.[172] They used DFT calculations to systematically study the NRR performance of $Mo_2TiC_2O_2$ nanosheets with single 3*d*, 4*d*, and 5*d* TM atoms (except Tc, Hg and lanthanides) embedded at the vacancy sites. The studies reveal that defective $Mo_2TiC_2O_2$ nanosheets doped with Zr, Mo, Hf, Ta, W, Re or Os exhibit significantly higher NRR activity. Among all, Zr doped $Mo_2TiC_2O_2$ was found to be the most promising catalyst due to its extremely low limiting potential of −0.15 V and excellent NRR selectivity as shown in Fig. 15(a). Also, the formation energy of Zr doped $Mo_2TiC_2O_2$ was calculated to be much more negative than Pt doped $Mo_2TiC_2O_2$, indicating the feasibility of synthesizing the catalysts.

Huang *et al.* studied Ti_2CO_2 and Mo_2CO_2 MXene monolayers supported with a series of single atoms towards electrocatalytic NRR using well-defined first-principles calculations.[173] Fig. 15(b) summarizes the measured reaction free energies of *NNH formation for the single atom supported Ti_2CO_2 and Mo_2CO_2 MXene surfaces. Their calculations indicated that Ru and Mo anchored Mo_2CO_2 and Ti_2CO_2 MXene monolayers exhibit higher activity towards nitrogen reduction to ammonia. Among the four combinations, the limiting potential for NRR was found to be the lowest for Ru@Mo_2CO_2 (-0.46 V) due to the higher conductivity of Mo_2CO_2 with respect to Ti_2CO_2. Also, by comparing the Gibbs free energy for dinitrogen protonation and hydrogen adsorption on Mo@Mo_2CO_2 surfaces, they found N_2 reduction proceeds via a distal or hybrid mechanism with low overpotential of 0.16 and 0.19 V respectively. Through these findings they suggested that Mo@Mo_2CO_2 could be a robust catalyst for NRR.

Gao *et al.* studied the NRR activity of $Ti_3C_2O_2$ supported with various TMs (Sc, Ti, V, Cr, Mn, Fe, Co, Ni, Cu, Zn, Mo, Ru, Rh, Pd, Ag, Cd or Au) as single-atom catalysts using DFT calculations.[174] According to their measurements the NRR overpotentials of Fe/$Ti_3C_2O_2$, Co/$Ti_3C_2O_2$, Ru/$Ti_3C_2O_2$, and Rh/$Ti_3C_2O_2$ were 0.92, 0.89, 1.16, and 0.84 eV respectively. They also found that Fe/$Ti_3C_2O_2$ had the lowest Gibbs free energy (−0.75 eV) for N_2 adsorption and exhibited good N_2 activation performance. These studies efficiently predict the potential of TM-doped MXene nanosheets as electrocatalysts for achieving high-efficiency N_2 reduction under ambient conditions. On the other hand, Zheng *et al.* considered the non-metal boron with MXenes as substrate for electrochemical NRR.[175] Boron has an electronic structure mimicking the filled and empty *d* orbitals in transition metals and can activate the triple bond in N_2 molecules. Their calculations revealed that B-doped Mo_2CO_2 and W_2CO_2 MXenes were the most promising candidates for the NRR with

the lowest limiting potentials of−0.20 and−0.24 V, respectively, along with high catalytic activity and selectivity. Importantly, the nature of the main transition metal of the MXene substrate is critical to the overall catalytic activity of the B-MXene catalyst. The interplay between TM *d* orbitals and boron *p* orbitals govern the degree of B-to-adsorbate electron donation.

Practical implementation of single atoms immobilized on MXene as an electrocatalyst for NRR was realized rather recently. Liu *et al.* synthesized Au nanoparticles (NPs) anchored onto Ti_3C_2 surface using an ultrasound reduction approach.[176] The Au/Ti_3C_2 catalyst with ~0.94% Au loading exhibited the best performance with an average ammonia yield of 30.06 μg/h/mg and a high Faradaic efficiency (FE) of 18.34% at−0.2 V *vs.* RHE. According to them, the oxygen containing groups on the MXene surface acted as the nucleation sites for Au(III) ions. Combining X-ray spectroscopy and DFT calculations they were able to conclude that the large energy of N_2 adsorption at the interface of Au and Ti_3C_2 weakens the N≡N bonds, and the total activation energy barrier was lowered though stabilization of N_2* and destabilization of NH_2NH_2*. Liu and co-workers studied the activity of Ti_3C_2 MXene decorated with both precious and non-precious TM as NRR catalysts, i.e. Cu/Ti_3C_2, CuAg/Ti_3C_2 and Ru/Ti_3C_2.[177–179] All three catalysts showed moderate activity in 0.1 M KOH under ambient conditions. The corresponding ammonia production rate and faradaic efficiency for Cu/Ti_3C_2, CuAg/Ti_3C_2 and Ru/Ti_3C_2 are 3.04 μmol/h/cm^2 / 7.31% at 0.5 V *vs.* RHE, 4.12 μmol/h/cm^2 / 9.77% at −0.5 V *vs.* RHE and 2.3 μmol/h/cm^2 / 13.13% at−0.4 V *vs.* RHE, respectively. Among them, Ru/Ti_3C_2 proved to be the most stable, >24 h for 5 repeated cycles. It should be noted that the electronic state of Ti atoms in the $Ti_3C_2O_2$ MXene structure can influence the activation of surface adsorbed N_2.[180] Among Ti^{2+}/Ti^{3+}/Ti^{4+}, the paramagnetic Ti^{3+} (3d1, S = 1/2) sites serve as the active site for ENRR. This is due to the orbital symmetry that weakens the back electron transfer between the Ti^{4+} 3d (0) and N_2 π2p* (antibonding) orbitals. The ENRR activity is usually described using the electron donation/back-donation process between the 3*d* orbitals of the TM and the 2*p* orbitals of N_2.[181] Hence, a suitable combination of occupied and empty orbitals is considered advantageous. To facilitate formation of surface Ti^{3+} states, nitrogen doping was used on $Ti_3C_2T_y$ MXene.[182] DFT studies showed that with nitrogen doping the N_2 adsorption energy is remarkably enhanced, from−0.56 to−1.86 eV, while the NH_3 adsorption energy decreases. Redistribution of the electron density of Ti^{3+} is further confirmed from the shift of the valence electron cloud towards lower energy and increase in electron concentration filling the partial density of states of $Ti_3C_2T_y$ MXene. Interestingly, nitrogen exchange between the N dopant in the catalyst and the N_2 was observed during the ENRR, proving that the dopant nitrogen sites also act as steady active sites in addition to the Ti^{3+} sites. At the optimized Ti vacancy density and nitrogen dopant concentration, an FE (towards NH_3) of 9.87% was achieved for N-doped-Ti_V-$Ti_{3-x}C_2T_y$ MXene.[182].

As discussed above, introduction of single atoms can significantly improve the electrocatalytic activity and selectivity of MXenes. Peng *et al.* designed single-atomic ruthenium modified Mo_2CT_x MXene NRR catalysts to achieve an excellent ammonia production rate and FE of 40.57 μg/h/mg and 25.77% respectively at −0.3 V *vs.* RHE in 0.5 M K_2SO_4 electrolyte.[89] The NRR was measured for different atomic loading of Ru, and the best performance was achieved for 1.41% Ru loading. To demonstrate the enhanced ENRR activity, the catalyst was evaluated for ammonia yield and FE against commercial Ru/C and pristine Mo_2CT_x as shown in Fig. 15(c). Operando X-ray absorption spectroscopy studies along with DFT calculations were used to unveil the exceptional electrochemical activity of this catalyst. They reasoned that the single atoms of Ru in the Mo_2CT_x MXene nanosheets are the active sites and constitute the adsorption and electron back-donation centers. These Ru atomic sites effectively promote N_2 activation at the Mo sites and reduce the thermodynamic energy barrier of the first hydrogenation step, thereby synergistically facilitating the further hydrogenation of the adsorbed N_2. It is noteworthy to mention that the termination groups (O, F, OH, Cl, and Li) of the doped MXene play a synergistic role in defining the ENRR performance. Studies on iridium single atom decorated *v*-Mo_2CO_2 (*v* represents the surface termination vacancy) reveal that the surface O-terminations promote the first hydrogenation step in the ENRR process.[183] The energy barrier for transition from *N_2 to *NNH intermediates is lowered due to the contributions of the Ir atom as well as the closest O atom on the Ir@*v*-Mo_2CO_2 surface. Hence, adjusting the coordination environment of the single atoms based catalysts with surface terminal groups of MXene substrates is an effective strategy to improve the NRR activity.

This section highlighted the promise of elemental engineering of MXenes for NRR electrocatalysis. Although new doping strategies are explored, the FE is yet to compete with the best performing catalysts.[184] Importantly, MXenes provide an excellent support for the single atom catalytic sites. Although reports suggest that the dopant atoms are the active sites, the rich surface chemistry of MXenes offers a variety of reaction pathways and adsorption of reaction intermediates. It is the synergistic effect of these individual components that eventually cascades the reactions. Inspired by the computational predictions, as more doped MXene systems are experimentally developed, we foresee the unfolding of their enormous promise. However, the success of these doped MXene systems depends heavily on the computational investigations carried out to simulate their dynamic behaviour during catalysis and to predict the reaction mechanisms and intermediates.

4.1.4. Carbon fixation

The rising levels of CO_2 and CO in the atmosphere have been a major contributor towards global climate change and drop in air quality. Electrochemical conversion of CO_2 and CO is a viable way to mitigate the adverse effects of these carbonaceous gases. CO_2 reduction reaction (CO_2RR) and CO oxidation reaction are the relevant catalytic processes to achieve this objective. In CO_2RR, molecules of CO_2 are hydrogenated to value added products like formic acid (HCOOH), methanol (CH_3OH), methane (CH_4), ethylene (C_2H_4), and carbon monoxide (CO). Results have already shown that the surface terminal groups on MXene are an excellent platform for the catalytic reduction of CO_2. The electronegative elements, e.g. F, O, Cl on MXenes promote the adsorption of intermediate molecules.[185–187].

Research on electrochemical reduction of CO_2 using MXenes as catalysts is at its infancy, and most of the work involves computational studies. As mentioned in the previous sections, MXenes emerged as an ideal support for single atom catalysts such as Pt, Ru, Rh or Pd. The vacancy sites on the MXene layers stabilize the single atom catalysts, while the surface functionalities promote the

adsorption of reaction intermediates. Zhao *et al.* were able to synthesize electrocatalysts based on single atom Pt supported at the Ti vacancy sites of $Ti_{3-x}C_2T_y$ MXene nanosheets at room temperature.[96] They utilized the highly reductive capability of the ultrathin nanosheets to stabilize single-metal atoms at the Ti-vacancy sites by forming metal carbon bonds (Fig. 16(a)). DFT calculations reveal that, in comparison to Pt nanoparticles, single Pt atoms perturb the electronic structure of the MXene support, thereby significantly decreasing the adsorption and activation energies. The $Pt/Ti_{3-x}C_2T_y$ catalysts were found to be highly active toward CO_2 fixation in the presence of a diverse range of amines and silanes to yield value-added amides. These single atom catalysts exhibited excellent conversion and selectivity, exceeding Pt NPs. Traditionally CO_2RR is carried out in either inorganic salt solutions or ionic liquids. To make the process more cost effective and practical to operate, Qu *et al.* used seawater as the electrolyte, with doped Ti_3C_2 MXene as electrocatalyst. [188] They prepared N-doped nanosheets with abundant titanium vacancies via a facile NH_3-etching pyrolysis approach. These nanosheets demonstrated impressive CO_2RR performance in seawater with a remarkable FE of 92% (Fig. 16 (b)). N-Ti_3C_2 MXene achieved a current density (j) of−18.3 mA/cm^2 at a potential of−0.8 V *vs.* RHE, 5.3 times higher than pristine Ti_3C_2 (−3.4 mA/cm^2).

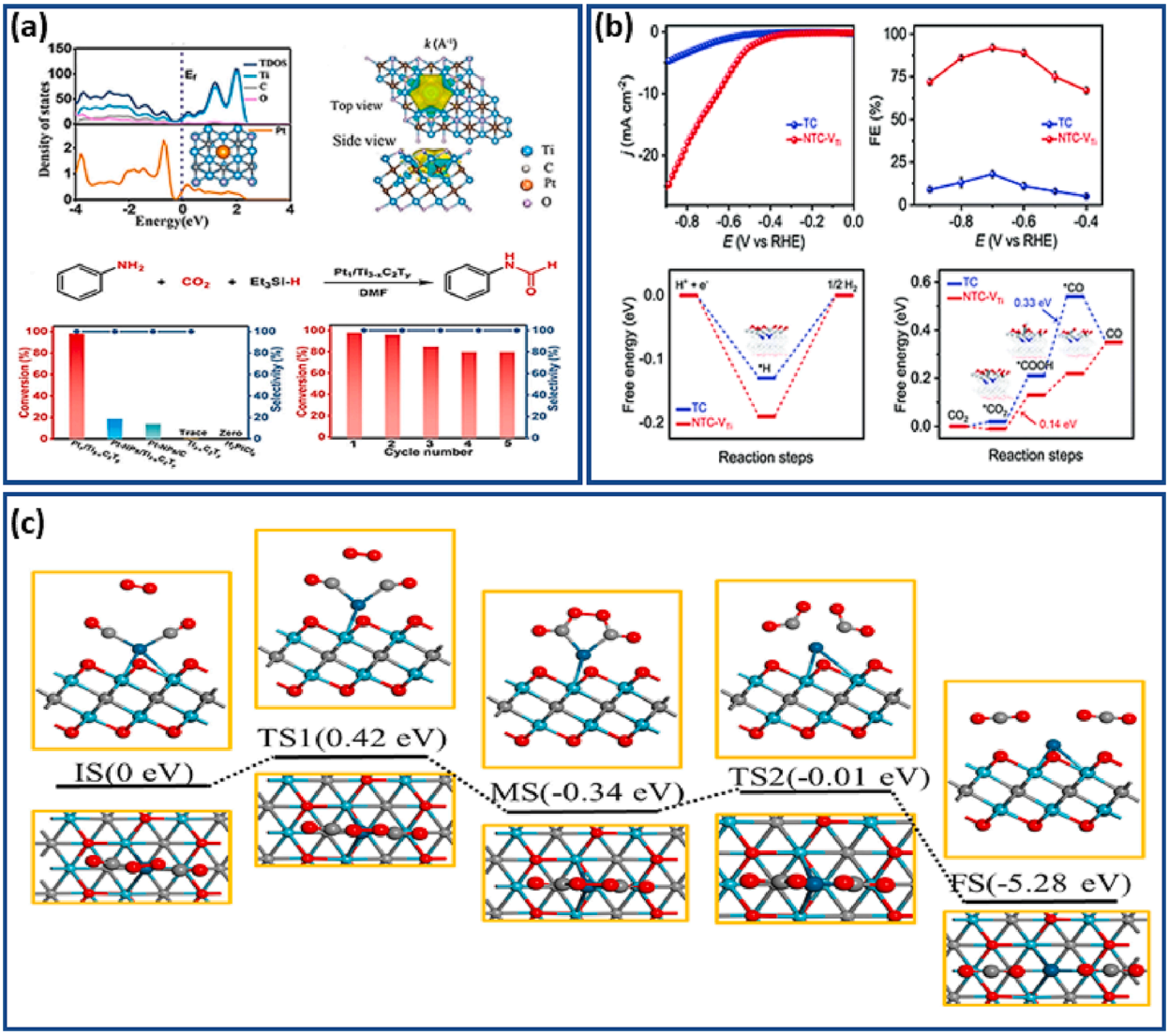

Fig. 16. Theoretical and experimental studies on doped MXene as catalyst for various carbon fixation reactions. (a) Charge density difference of $Pt/Ti_{3-x}C_2T_y$ with plain and side-on views. Yellow and cyan regions represent electron accumulation and depletion, respectively. Chemical equation for the N-formylation of aniline with CO_2 and Et_3SiH. Catalytic performance of the N-formylation of aniline using different catalysts. Recycling test of $Pt_1/Ti_{3-x}C_2T_y$ for the catalytic N-formylation of aniline.[96] (b) CO_2RR performance of N doped Ti_3C_2-V_{Ti} in seawater. Polarization curves of N-Ti_3C_2-V_{Ti} and Ti_3C_2, supported on carbon paper. Faradaic efficiencies at different applied potentials. Calculated free energy of hydrogen adsorption on N-Ti_3C_2-V_{Ti} and Ti_3C_2 and of CO_2RR on N-Ti_3C_2-V_{Ti} and Ti_3C_2. [188] (c) The tri-molecular Eley-Rideal (TER) mechanism reaction pathway of carbon monoxide oxidation on Pd/O_V–Nb_2CO_2.[198] Reproduced from [96,188,198] with permission from American Chemical Society, Royal Society of Chemistry and Elsevier. (For interpretation of the references to color in this figure legend, the reader is referred to the web version of this article.)

Using DFT calculations, they were able to establish that the co-existence of N dopants and titanium vacancies synergistically modulates the electronic structure of the active titanium site and reduces the free energy barriers for *COOH formation and *CO desorption, leading to improved CO_2RR activity. Among non-precious metal electrocatalysts, copper is highly promising for CO_2 electroreduction. The affinity of Cu towards CO* protonation to hydrocarbons and alcohols is superior to Pt, Rh, Pd, Ni, Au and Ag.[189] Compared to other carbon-based systems, $Ti_3C_2T_x$ MXene possesses superior physicochemical properties and is a promising support for Cu doping. [190,191] Cu doped $Ti_3C_2T_x$ shows a promising FE of 58.1% towards formic acid with a Cu loading of just 1.04 wt%. The presence of -O and-OH terminations results in dissimilar coordination on the Cu/$Ti_3C_2T_x$ surface with different intermediates including *COOH and *HCOOH. It was found that *COOH binds to the surface –O, while *HCOOH binds through the surface H atoms. These bound intermediates are further catalysed by the Cu dopants to form CH_3OH through the OCHO*. Further DFT studies reveal that the Cu dopant induces polarized sites with high electron density, favoring adsorption of reaction intermediates, especially *COOH and *HCOOH, although the adsorption of CO_2 on the catalyst surface remains unaffected.[191].

Zhao *et al.* demonstrated an efficient approach to synthesize single atom copper immobilized $Ti_3C_2Cl_x$ MXene for electrocatalytic CO_2 reduction to methanol via selective etching of the hybrid A layers (Al and Cu) from quaternary MAX phases ($Ti_3(Al_{1-x}Cu_x)C_2$). [192] Utilizing the difference in saturated vapor pressure of Al and Cu, they were able to selectively etch Al, while preserving and immobilizing the Cu atoms. This single atom Cu-$Ti_3C_2Cl_x$ catalyst exhibits a high FE of 59.1% towards electroreduction of CO_2 to CH_3OH with good electrocatalytic stability. The presence of single Cu atoms with unsaturated electronic structure ($Cu^{\delta+}$, $0 < \delta < 2$) lowered the energy barrier for conversion of HCOOH* to CHO* intermediate, in turn improving the CO_2 electroreduction efficiency. Studies on the CO_2RR properties beyond Ti based MXenes are scarce. This is mostly due to their inherent selectivity towards HER.[193] For example, pure Nb_2CO_2 MXene is not suitable as catalyst for CO_2 electroreduction. However, with metal or non-metal doping the Gibbs free energy is considerably reduced, making it active towards CO_2RR. Interestingly the reaction intermediates can vary between nonmetal and metal doped system. HCOOH is the favoured product for metal dopants. Vanadium was found to be most suitable, with the lowest free energy of−0.11 V for *HCOOH formation (calculated).[194] These findings are critical toward experimental design of alternative doped MXene catalysts.

CO oxidation is one of the best-known heterogeneous reactions often considered as the benchmark in heterogenous catalysis.[195] Electrocatalytic oxidation of CO to CO_2 using doped MXenes was investigated theoretically but is yet to be realized experimentally. A major concern with this process is the CO poisoning of the electrodes' surfaces. Cheng *et al.* evaluated the CO oxidation capability of Cu_3-cluster-doped monolayer Mo_2CO_2 MXene by first-principles calculations. [196] They compared the activities between Cu_3 doped pristine and defective Mo_2CO_2 nanosheets and suggested that Cu_3 doped on defective Mo_2CO_2 with oxygen vacancies has superior activity and stability than pristine Mo_2CO_2. Here, the dopant Cu_3 cluster functions as an electron reservoir controlling the electron release and collection, mediating the CO oxidation reaction. Cheng *et al.* next studied the low-temperature CO oxidation activity of Fe, Co, Ni, Cu, Zn, Ru, Rh, Ag, Ir, Pt and Au decorated $Mo_2CO_{2-\delta}$ monolayers.[197] After preliminary screening based on metal sintering, CO poisoning, and O_2 adsorption strength, Zn/$Mo_2CO_{2-\delta}$ was found to be the best among all. Upon further investigation, they found that Zn atoms reduce the O-O bond strength of the adsorbed oxygen molecule. They speculated that the Zn/$Mo_2CO_{2-\delta}$ catalyst is thermally stable and resistant to oxidation and CO poisoning. Zhang *et al.* modelled the CO oxidation reaction activity of single Pd-atom confined within an oxygen vacancy of Nb_2CO_2 MXene nanosheets.[198] It was found that the oxygen vacancy sites can stably anchor the Pd atoms. They modelled several possible CO oxidation mechanisms on this catalyst and found that a tri-molecular Eley-Rideal (TER) mechanism is preferential for CO oxidation. The TER mechanism demonstrated the lowest activation energy, 0.42 eV (Fig. 16(c)). These computation-based results provide key insights into the possible CO oxidation activities of doped MXene systems and can guide experimental catalyst design.

This section illustrates the promise of doped-MXene as a catalyst for CO_2 reduction and CO oxidation reaction. MXenes by themselves have very low or no affinity towards these reactions. However, theoretical findings show that MXenes have the potential to be excellent support matrix for single atom catalysts (Pt, Cu, Pd) and can also promote suitable pathways for the adsorption of reaction intermediates. Moreover, doping MXenes with heteroatoms (e.g. nitrogen) can further enhance the activities, through suitable modulation of the electronic band structure between the single atom catalyst and doped MXene matrix. Again, relying on the theoretical studies, it is important to find suitable doped MXenes that have lower selectivity towards the competing hydrogen evolution reaction. Moving ahead the success of MXenes towards carbon fixation would depend on the combined effect of low HER selectivity, defect sites which act as the anchoring point for single atom catalysts and surface terminal groups.

4.2. Energy storage

In the last few decades, the main challenges to modern society have been to tackleever-increasing global warming and expediate the search for clean and sustainable energy resources. As energy has become the lifeblood of modern civilization, electrochemical energy storage devices constitute supreme power sources for a cleaner energy economy. Devices such as fuel cells, batteries, supercapacitors and hybrid systems (e.g., based on both redox and capacitive activities) aim to fulfil the demand for sustainable clean energy storage and conversion. These devices have a great potential for commercialization owing to their capability to store and covnert energy at reasonable specific capacity, power density and long cycle life. A great challenge for electrochemical energy storage devices is supporting large energy exchange with renewable energy resources like solar fields and wind turbines. In essence, their charge storage capability depends on the choice of both cathode and anode active materials.

In recent years we see intensive efforts, devoting to develop innovative active materials for energy storage devices. Focusing on 2D structures, several families of such materials were explored in connection to energy storage applications including graphene species and their derivatives, transition metal dichalcogenides, boron nitrides, silicenes, metal–organic frameworks, and phosphorenes. [199]

These materials display astonishing physical and chemical properties. Among 2D materials, intensive research has been conducted on novel families such as MXene composites and doped MXenes. These materials are very attractive for energy storage devices owing to their outstanding properties including excellent compatibility, high electrical conductivity, rich surface chemistry, large interlayer spacing, high surface area, and tuneble bandgap.[126,200,201].

Recent investigations of energy storage devices with doped MXenes, which exhibit enhanced electrochemical performance, including Li-ion, Na-ion and metal sulfur (Li-S and Na-S) batteries, supercapacitors, and their hybrid systems, are detailed in the following sections. The introduction of heteroatoms enhances the interlayer spacing, increasing the c-lattice parameter and endowing the MXene moieties with a large surface area. The electronic conductivity is increased, defects are formed in the lattice, a porous nature is provided, and transportation of electrolyte ions to the MXene layers is facilitated.[27,202].

4.2.1. Li-ion batteries (LIBs)

Global transportation is usually responsible for a key share of energy consumption (roughly 75%). Transportation energy comes mainly from oil-based fuels. To minimize the use of fossil fuels in this sector, alternative sources are developed for sustainable energy.

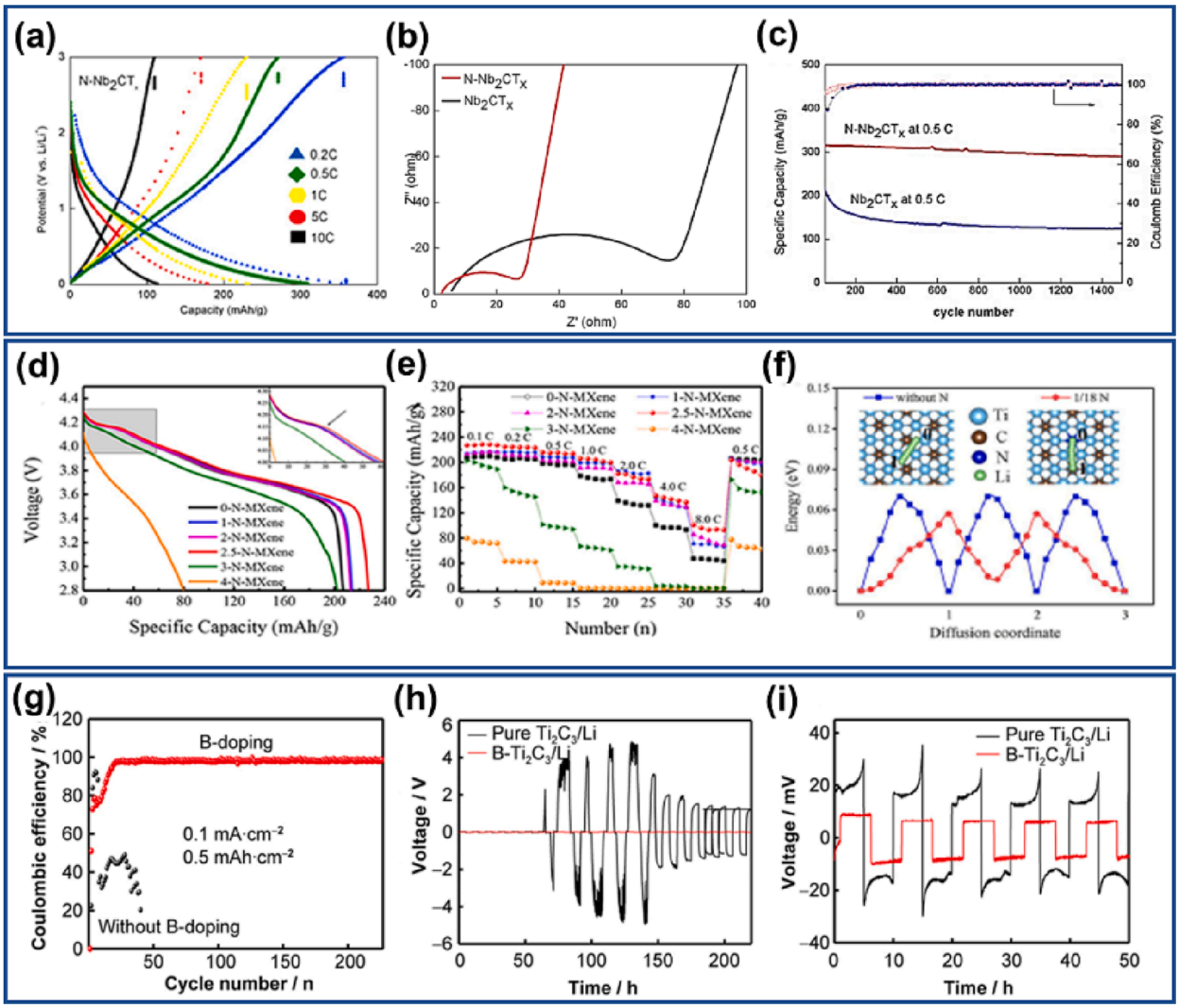

Fig. 17. Results on doped MXene as electrodes for Lithium ion batteries. (a) Charge and discharge profiles of N-Nb_2CT_x electrodes at 0.2, 0.5, 1, 5 and 10 C, respectively. (b) Electrochemical impedance performance of pristine and doped MXene. (c) Cycling performance of N-Nb_2CT_x electrode at 0.5C for 1500cycles. [217] (d) First discharge profiles of cells with different N-MXene additive at a current density of 0.1C (20 mA/g) between a voltage of 2.8~4.3 V. (e) Specific capacity of cells with different N-MXene additive under 0.1~8.0C current densities. (f) Diffusion pathway and corresponding energy profiles of Li-ion diffused on monolayer pure MXene and N-MXene. [51] (g) Coulombic efficiency comparison between B-doped $Ti_3C_2T_x$ and pure $Ti_3C_2T_x$ at 0.1 and 0.5 mAh/cm^2; (h) voltage stability measurements of Li metal plating/stripping of 0.5 mAh/cm^2 · at 0.1 mA/cm^2 · in B-doped $Ti_3C_2T_x$@Li and pure $Ti_3C_2T_x$@Li symmetric cells; (i) detailed voltage profiles in (h) from 0 to 50 h. [218]. Reproduced from [217,51,218] with permission from Elsevier and Springer.

LIBs are a prime target of technological innovation to promote the electromobility revolution by an intensive use of electric vehicles. In parallel, rechargeable batteries are becoming very important also in the field of grid-scale stationary energy storage. LIBs are very attractive for these applications as well. In the last few decades, LIBs for consumer devices, mainly mobile phones, laptops and digital cameras, were successfully commercialized and conquered the markets of power sources for portable electronic devices. Research LIBs for mobile electronics applications has focused on improving cyclability, high-rate performance, and safety. Good cyclability (~1500 cycles), high specific energy (150–200 Wh/kg) and low self-discharge were obtained.[203–207].

The worldwide success of commercial LIBs powering mobile electronic devices at nearly zero-fault levels, increases the self-confidence regarding their promotion to much more demanding applications like long-running EVs. In 1976, Whittingham developed the first rechargeable intercalation LIBs, consisting of metallic lithium as the anode and titanium disulfide (TiS_2) cathode. Li_xTiS_2 ($0 \leq x \leq 1$) maintain a voltage of 2 V. More dendrite formation at the Li anode results in battery failure and restricts the development of commercial applications [208,209]. Further research was motivated towards cathode materials. In 1981, Goodenough developed a cathode material with a similar structure as dichalcogenides. $LiCoO_2$ was coupled with metallic lithium, and the performance of $LiCoO_2$/Li systems in non-aqueous electrolyte solutions was studied. Initial $LiCoO_2$/Li systems had an open circuit voltage around 4 V, consistent with the Co^{+4}/Co^{+3} couple. In 1983 Yoshino invented a polyacetylene-based anode for LIBs. The limitations of these materials are low density, chemical stability, and capacity. Research has focused on carbonaceous materials, which are suitable anode candidates for LIBs, alleviating detrimental lithium dendrites formation upon charging. In 1991 the Sony Corporation of Japan successfully commercialized a rechargeable battery using a $LiCoO_2$ cathode and a carbon anode. [209,210].

Contemporary LIBs comprise an anode, a cathode, and a separator soaked in dissociated Li salt (e.g., $LiPF_6$) containing a non-aqueous electrolyte solution (e.g., ethylene carbonate (EC) and/or dimethyl carbonate (DMC), EMC, DEC). The anode is composed of layered structured graphite, which accommodates the intercalated Li-ions between the layers, whereas the cathode is made up of a layered transition metal oxide (e.g., $LiCoO_2$). The separator prevents short-circuiting, allowing an exchange of lithium ions between the anode and the cathode as the only charge transfer process between the electrodes in the cells. During charging, Li ions are de-intercalated from the cathode material, migrate through the non-aqueous electrolyte, and intercalate into the layered graphite anode material. The process is reversed during discharge.[206,211] A major challenge of LIBs is the thermodynamic instability of all relevant electrodes materials with the non-aqueous solutions that can be used in them. Thereby, their operation depends on development of electrodes' passivation phenomena by protecting surface films. Hence LIBs always work only at *meta*-stable conditions (thus limiting their cycle life and safety features). Other issues may be dangerous dendrite formation upon fast charging (due to Li metal deposition on the graphite anodes), huge volume variations of some electrodes' materials during the reversible intercalation processes with Li ions, and poor electrical conductivity of most of relevant cathode materials.[212–214].

Considering the unique structure, electrons and ions transport properties of MXene species, there is an incentive to explore and accommodate them as alternative anode materials for graphite, especially for fast charging applications. Also, MXenes can be considered desirable additives that increase the integration and electronic conductivity of composite LIBs electrodes (both anodes and cathodes).Similar to graphite, MXenes accommodate Li ion storage in the sheets due to the interlayer spacing (0.7 to 1.1 nm). [201,214–216] Nitrogen-doped two-dimensional Nb_2CT_x MXene synthesized via hydrothermal route – at 150 °C for 8 h – and used as the anode active material. [217] The 4.5 at.% of nitrogen in N-doped Nb_2CT_x MXene increases the c-lattice parameter from 22.32 to 34.78 Å. The N-Nb_2CT_x MXene voltage profile (Fig. 17 (a)) reflects the C-rate progress, subsequently decreasing the specific capacity of the cells due to the greater polarization and increasing the internal resistance and limited Li-ion transport kinetics. At 0.2C rate, the reversible capacity is 360 $mAhg^{-1}$, close to that of commercial graphite (372 mAh/g). The specific capacity of N-Nb_2CT_x is 300, 170 and 120 at 0.5C, 5C and 10C, respectively. Typical electrochemical impedance spectra of Nb_2CT_x and N-Nb_2CT_x electrodes studied before cycling is shown in Fig. 17 (b). The Nyquist plots show that N-Nb_2CT_x has a lower equivalent series resistance (2.2 Ohms) in comparison to Nb_2CT_x (6.1 Ohms) indicating good electrode conductivity and relatively low electrode/electrolyte interfacial impedance. The charge transfer resistance of the N-Nb_2CT_x electrode is lower compared to Nb_2CT_x, leading to stable long-term cycling of 1500 cycles with 92% capacity retention (Fig. 17(c)). The enhanced performance is due to the introduction of nitrogen in the MXene lattice, which improves the conductivity, modifies the electronic structure of the active materials and increases the interlayer spacing.

Another study revealed that using 2.5 wt% of N-MXene (wrinkled, flexible, and layered nitrogen-doped $Ti_3C_2T_x$) as a conductive additive for NCM811 ($LiNi_{0.8}Co_{0.1}Mn_{0.1}O_2$) based cathodes in high energy density LIBs improved considerably their performance. Cyanamide was used as a nitrogen source for doping of few-layered MXenes. [51] The chemical synthesis involves a freeze-drying process for 24 h, followed by calcination at 550 °C for 3 h. XPS confirms 1.6% and 0.8% of nitrogen present in nitrogen-doped and few-layered MXene lattices, affecting the surface morphology, interplanar distance, and electronic structure of the MXene species that were used as conductive additives that increased the integrity of the composite electrodes. The first discharge profiles of the NCM811 electrode consist of different amounts of N-MXenes such as 0,1, 2, 2.5, 3 and 4 % of conductive additive as shown in Fig. 17(d), studied at 0.1C current density with a voltage range of 2.8–4.3 V. N-MXene (2.5 wt%) delivers a specific capacity of 226.9 mAh/g, more than other compositions. At different C-rates, 2.5 wt% of N-MXene delivers an excellent performance in relation to the undoped material (Fig. 17(e)). Hence using doped MXenes as conductive additives in Ni-rich NCM cathodes for LIBs, can increase considerably their specific capacity. The enhanced electrochemical performance reported is due to the greater number of face-to-face contacts with NCM811. The wrinkled morphology contributes more lithium intercalation and deintercalation and subsequently enhances the conductivity and capacity, since these MXenes moieties easily adhere to the surface of the NCM811 particles, thus improving their electrical contact, reduce the resistance by maintaining good conductive network of the active mass. Density functional theory based calculations revealed that the N-doping not only weakens and decreases the MXene containing functional groups, but also increases the stability of lithium and transition metal ions in the NCM811 active mass. Doping improves the adsorption energy, surface charge distribution and diffusion of the lithium ions within the electrodes' composite structure. The diffusion pathway and barrier of undoped

and N-MXenes are shown in Fig. 17(f). The barrier values are 0.070 and 0.057 eV for undoped and N-MXenes, respectively. The lower barrier indicates improved Li^+ ions diffusion, which prevents the movement of oxidized transition metal ions to the anode side and reduces dendrite formation. [51].

Wu *et al.* developed 3D boron-doped multilayered $Ti_3C_2T_x$ (B-$Ti_3C_2T_x$) by one-pot hydrothermal route and studied their performance in LIBs. [218] The cycling stability of B-$Ti_3C_2T_x$ w.r.t lithium anode at different current densities of 0.1 and 0.5 mAh/cm2 is shown in Fig. 17(g). B-$Ti_3C_2T_x$ delivers a higher columbic efficiency compared to the pure $Ti_3C_2T_x$ electrodes. It seems that B-$Ti_3C_2T_x$ particles develop a more stable interface between the electrodes and the standard electrolyte solutions due to formation of effective solid electrolyte interphase (SEI) on the active mass . B-$Ti_3C_2T_x$@Li//B-$Ti_3C_2T_x$@Li symmetric cells show low dendrites formation during prolonged cycling (lithium stripping/plating) without short circuit as shown in Fig. 17 (h,i). The overall electrochemical performances are due to the using of 3D MXene with boron doping provides a uniform lithium distribution and fast lithium-ion kinetics interlayer spacing in the MXene lattice hinders lithium dendrites growth.[218].

4.2.2. *Sodium-ion batteries (SIBs)*

The limit of Li resources in the earth crust and the uneven geographical distribution of lithium may lead to a shortage in supply and hence push up the Li price. There are not enough Li resources on our planet to fulfill the needs of large-scale energy storage, if we want to move from fossil fuels to solar energy for mass electricity productions (a global energy storage needs in the order of hundreds of terawatts-hours per day). Hence, additional energy storage technologies, on top of LIBs are strongly required, in order to meet the needs for energy transition from fossil fuels to renewable "green" energy resources. SIBs could serve as potential complementary energy storage devices that meet global needs, thanks to the high sodium abundance in the earth crust (23,000 ppm Na compared to 20 ppm Li) and the low redox potential of the Na^+/Na couple, −2.71 V *vs.* standard hydrogen electrode (SHE), which promises also high energy density. Replacing Li^+ with Na^+ is an effective strategy to enhance electrochemical performances. Major sources such as earth crust and seawater consist of sodium at 28,400 mg/kg and 1000 mg/L, and lithium at 20 mg/kg and 0.18 mg/L, respectively, reflecting the low-cost viability of sodium in comparison to lithium.[219,220] The sodium intercalation mechanism was first investigated by

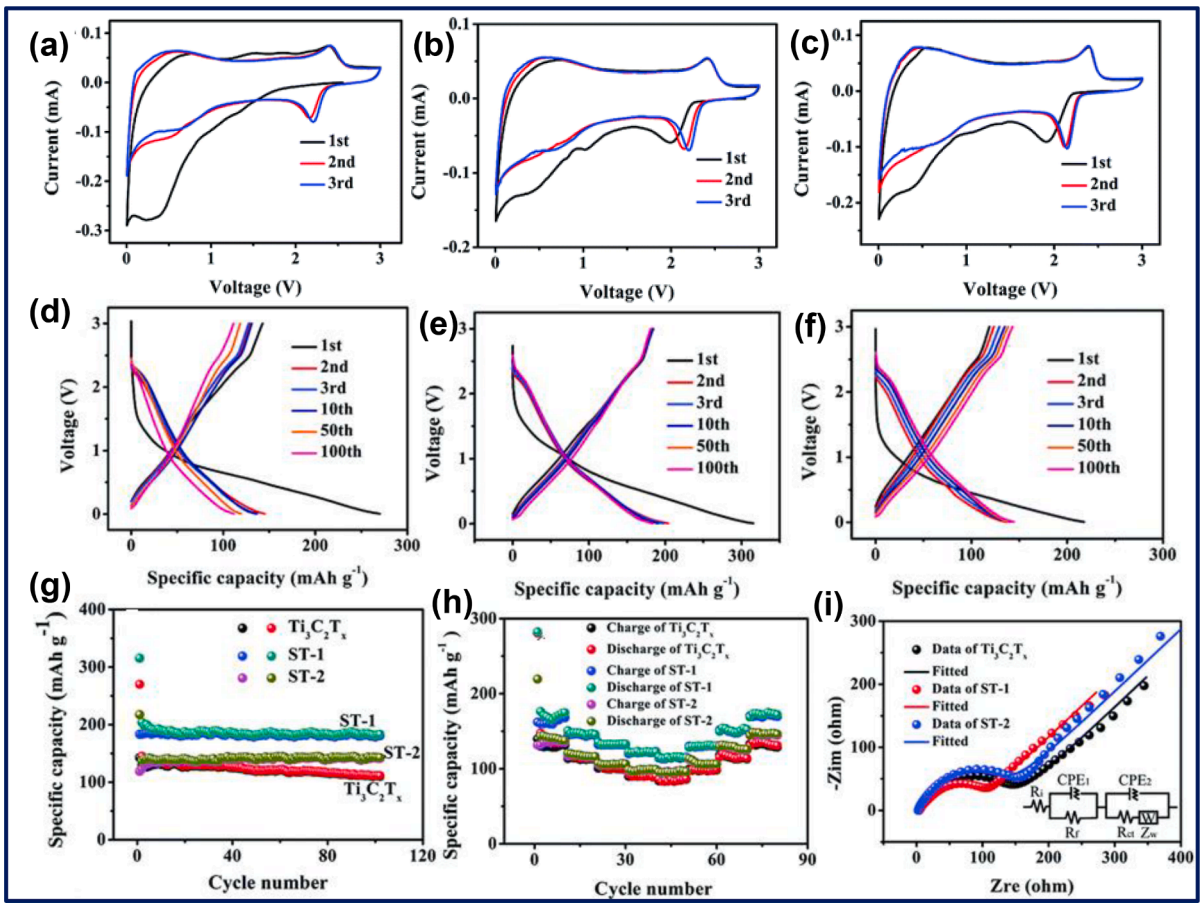

Fig. 18. Results on doped MXene as electrodes for Sodium ion batteries. S-doped MXene, CV curves from 3 to 0.005 V at 0.2 mV/s of (a) $Ti_3C_2T_x$, (b) S-$Ti_3C_2T_x$ (ST-1, 300 °C for 3 h), (c) S-$Ti_3C_2T_x$, charge–discharge profiles at 0.1 A/g of (d) $Ti_3C_2T_x$, (e) ST-1, (f) ST-2, (g) cycle life, (h) C-rate performance, and (i) EIS studies of three samples ($Ti_3C_2T_x$, ST-1/2). [61] Reproduced from [61] with permission from Royal Society of Chemistry.

Rouxel and his team, Silbernagel and Whittingham, in relation to sodium intercalation into TiS_2 host lattice; later SIBs research was a parallel continuation to LIBs. [221,222] However, LIB technologies were rapidly developed and dominate due to their high energy density factor. A Na-ion cell consists of a positive electrode (cathode) and a negative electrode (anode), non-aqueous-based organic electrolyte (1 M $NaClO_4$, and/or $NaPF_6$ salt dissolved in solvents like EC/DEC/PC, etc) soaked separator (glass-fibers GF) sandwiched between the two electrodes. Aluminum can be used as a current collector for both electrodes, at lower potentials; it does not alloying with sodium rather than like in Li. In general, cathode materials used as layered transition metal oxides, polyanionic materials, etc. for anode materials hard carbons, Ti-based oxides and phosphate compounds are used.[219,220,223–225].

During charging, Na-ions from the cathode material are inserted into the anode. This process is called sodiation. During discharge, Na-ions go back into the cathode from the anode, called de-sodiation. In charge–discharge, only Na-ions shuttle between the electrodes. In SIB systems, Na-ions from cathode material poorly intercalate into the commercial graphite anode. Na has a large ionic radius of 1.02 Å compared to Li with 0.76 Å, does not accommodate into the graphite layers, and delivers poor ions transport kinetics and cyclability. Theoretical studies reveal that the intercalation of sodium into graphite is accompanied by huge stress, forming unstable Na-graphite intercalation compounds.[225–227] Thereby, it is clear that graphite cannot serve as anode material for SIBs. Later, Stevens and Dahn revealed that sodium ions easily intercalate into the hard carbon anode in aprotic solvents and deliver the reversible capacity of 300 mAh/g, such carbons are most suitable for the anode materials to enhance the electrochemical activities.[228,229] Due to their high theoretical capacity, alloy compounds and pre metals can be considered as anodes for SIBs, but unfortunately suffer from pulverization. For large-scale energy applications research has been devoted to developing innovative cathode and anode materials for the SIBs to understand the sodium ion storage. [230–233].

Jiababo *et al.* developed the sulfur-doped $Ti_3C_2T_x$ MXene anode material for SIBs.[61] A thiourea precursor was used for doping into the multilayered MXene sheets. Sulfur doping enhances the electronic conductivity and the interlayer spacing, increases the atomic charge density, endows the surface area, simultaneously provides good transport for the electrons and ions, and improves sodium ion storage. CV curves of $Ti_3C_2T_x$ (undoped), S-$Ti_3C_2T_x$ (ST-1, 300 °C for 3 h), S-$Ti_3C_2T_x$ (ST-2, 400 °C for 3 h) are shown in Fig. 18. CV curves were studied from 3 to 0.005 V at a scan rate of 0.2 mV/s.. Undoped MXene CV (Fig. 18a) at the voltage range between 0.005 and 1 V reflects the sodium ion intercalation (sodiation) to the MXene, accompanied by electrolyte decomposition and surface films formation. A pair of peaks at 0.7 and 2.3 V reflects the sodium ion deintercalation (de-sodiation). Fig. 18(b) displays a ST-1 CV curve cathodic scan (around 2 and 1 V) showing that the sodiation at 0.5 V involves the irreversible formation of surface films by reduction of solution species. The anodic peak at 2.3 V corresponds to deintercalation of sodium ions from the MXene lattice. ST-2 CV curves shown in Fig. 18(c) display a similar electrochemical performance. Galvanostatic charge–discharge voltage profiles of undoped MXene, ST-1 and ST-2 MXenes electrodes are shown in Fig. 18(d–f). Three samples display similar charge–discharge voltage profiles. The columbic efficiencies of the three samples are 52.8%, 58.1% and 54.6%, respectively. As the cycle number increases, ST-1 and ST-2 have stable performance compared to the undoped MXene. The stability accounts for improved electrochemical performance due to sulfur doping. The cycle life performance of the three materials (Fig. 18(g)) studied at 0.1 A/g shows that the ST-1 MXenes electrodes are more stable and their specific capacity is higher than that of the undoped MXenes electrodes during 100 cycles, demonstrating good structure stability. At all current densities, ST-1 MXenes electrodes delivers excellent specific capacity in comparison to the other MXene electrodes explored in these studies. (Fig. 18(h)). Electrochemical impedance spectroscopic (EIS) studies of all three types of electrodes are shown in Fig. 18(i). ST-1 MXene electrodes (48.4 O) shows less resistance in comparison to undoped MXene electrodes (117 O) and ST-2 MXenes (94.9 O). In summary, the sulfur doped MXene electrodes demonstrate very good performance as potential anodes for SIBs.[61].

4.2.3. Alkali metal-sulphur (metal–S) batteries

For next-generation energy storage devices, rechargeable metal-sulfur batteries such as lithium-sulfur (Li–S) and room temperature sodium-sulfur (RT/Na–S) attracted considerable attention owing to their high theoretical capacity and volumetric energy densities. In a non-aqueous electrolyte media, sulfur cathodes (conversion reaction mechanism) provide up to ten times greater theoretical specific capacity than conventional metal oxide-based cathodes (intercalation mechanism) in Li-ion batteries. Furthermore, sulfur has overwhelming advantages as a low-cost and readily accessible abundant element and environmental compatibility. These factors fulfill the demands for advanced applications, where high energy density is very important (e.g., unmanned aviation).[234–238] However, scientific and technical issues greatly limit the practical application of Li–S and RT/Na–S batteries. For example, the insulating property of sulfur ($\sim 10^{-30}$ S/cm) and polysulfides (Li_2S_n / Na_2S_n) result in poor active material utilization, inhibiting the movement of electrons and ions. Volume expansion of sulfur occurs during the lithiation process (~80% in Li–S, ~160% in Na–S) through multi-electron conversion mechanism such as sulfur (S_8)–polysulfides (Li_2S_n/Na_2S_n)–sulfide (Li_2S/Na_2S). It results in structural damage and pulverization. Active material losses and low coulombic efficiency occur at both cathode and anode sides due to lithium polysulfides dissolved into the ether-based electrolytes. Highly reactive lithium/sodium metal anodes develop non-uniform surface films due to side reactions with the electrolyte solutions. This surface non-uniformity promote formation of lithium/sodium dendrites resulting in a low coulombic efficiency and internal short circuits, respectively. [238,239].

Principles of metal-S batteries

Conventional metal-S batteries are composed of sulfur composite cathodes, non–aqueous based electrolyte solutions, and metallic lithium or sodium anodes (denoted as Li-S or Na-S systems). Sulfur has a strong tendency to form the octahedral sulfur i.e. cyclo–S_8, the more stable allotrope at room temperature. However, during discharge mode *cyclo*-S_8 rings open and couple with lithium to form higher order soluble Li-polysulfides, as Li_2S_8–Li_2S_6–Li_2S_4. At upper voltage plateau, these intermediate products deliver 25% of the theoretical capacity (418 mAh/g). The discharge process further progresses, it forms lower order insoluble polysulfides such as Li_2S_4–Li_2S_2–Li_2S. At the lower voltage plateau, short chain Li-sulfides contributes to the 75% of the capacity (1255 mAh/g). The

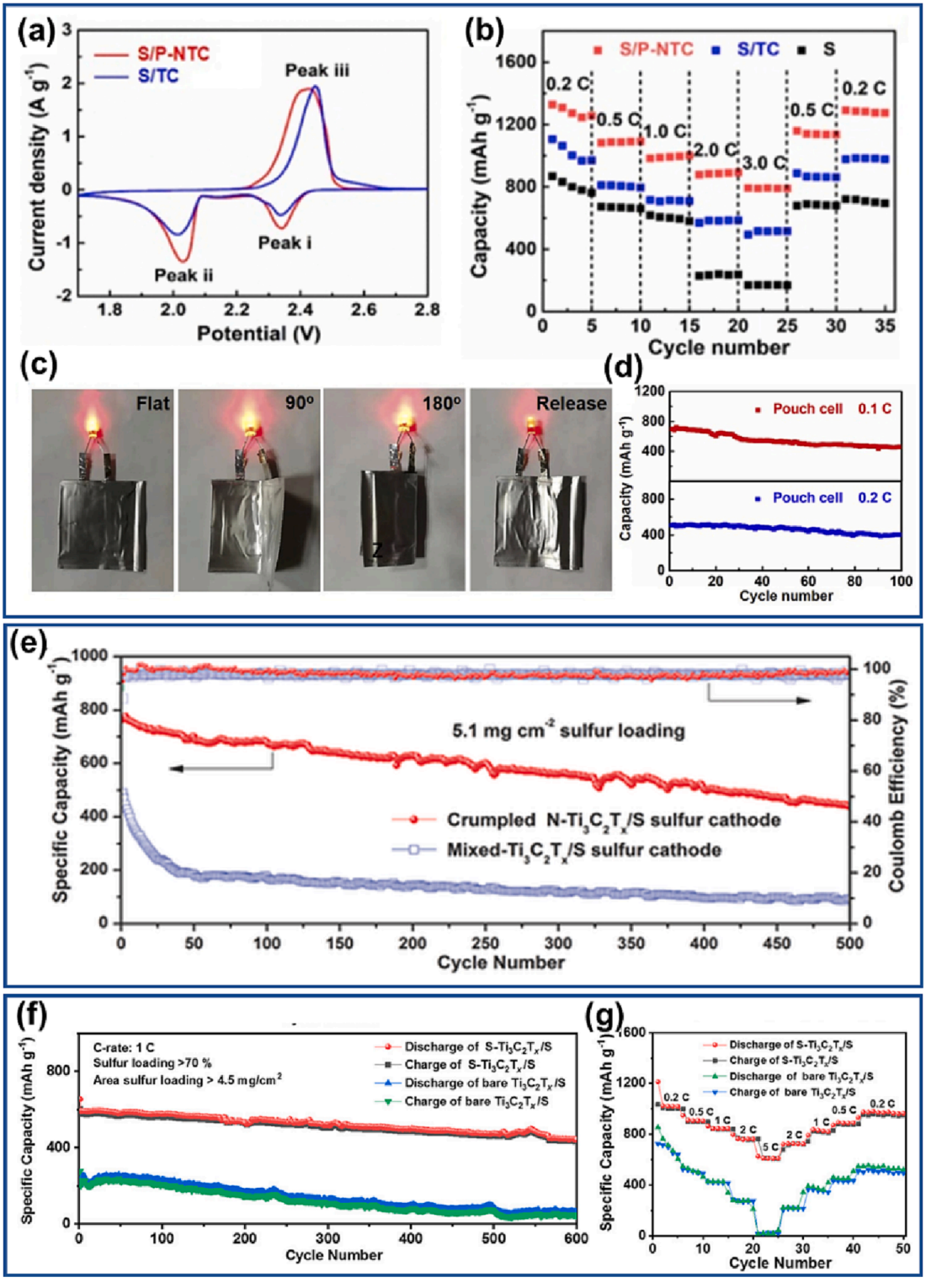

(caption on next page)

Fig. 19. Electrochemical performances of various doped MXene electrodes (a) CV profiles of porous nitrogen-doped Ti_3C_2 (S/P-NTC) and Ti_3C_2 (S/TC)at a scan rate of 0.05 mV s^{-1} in Li–S cell, (b) Rate performances of S/P-NTC, S/TC and bare S cathodes, (c) a flexible Li–S pouch cell with S/P-NTC cathode under various bending states to continuously power a red LED indicator, (d) Cycling performances of flexible Li–S pouch cells at 0.1 C and 0.2 C [244]; (e) Cycling performances of crumpled N-$Ti_3C_2T_x$/S electrodes and mixed-$Ti_3C_2T_x$/S electrodes with 5.1 mg cm^{-2} sulfur loadings at 0.2C for 500 cycles (1 C = 1673 mA g^{-1}); [119] (f) Cycling performances of sulfur doped–$Ti_3C_2T_x$/S and bare $Ti_3C_2T_x$ cells with a high sulfur loading of 4.5 mg/cm^2 at 1 C for 600 cycles, (g) Rate capability of S-$Ti_3C_2T_x$/S cathode and bare $Ti_3C_2T_x$/S cathode at current rates from 0.2 to 5 C.[58] Reproduced from [244,119,58]with permission from Elsevier, Wiley and American Chemical Society. (For interpretation of the references to color in this figure legend, the reader is referred to the web version of this article.)

conversion products formed at 2.3 V (S_8 to Li_2S_4), 2.1 V (Li_2S_4 to Li_2S) in ether-based electrolyte systems, Li_2S is the final discharge product in this process . The subsequent charging of the battery converts the Li_2S to *cyclo*-S_8 through the intermediate Li-polysulfides (Li_2S–Li_2S_2–Li_2S_4–Li_2S_6–Li_2S_8–S_8). Li-S battery charge storage greatly depends on the redox reaction between S_8 and Li_2S liquid–solid transition [234–236,238,240,241].

For Na-S batteries, the discharge voltage profile explains about, where *cyclo*-S_8 reacts with sodium to form Na_2S_8 at high voltage of 2.2 V, clearly reflecting a solid–liquid transition. The Na_2S_8 further reacts with sodium to form Na-polysulfides (Na_2S_6, Na_2S_5 and Na_2S_4) in the voltage range of 2.2 to 1.65 V. This is the most complex region and defines the liquid–liquid reaction between long chain Li-polysulfides. As discharge continues, Na_2S_4 converts to insoluble products as Na_2S_3 and Na_2S_2 at ~ 1.65 V. The discharge products depend on the electrochemical reaction between the Na-polysulfides in a liquid–solid transition. Where further reaction continuous formation of Na_2S as final product, at voltage range of 1.65 to 1.2 V, corresponds to the solid–solid transition. This region is non-conductive and hence reflect a slow kinetics. [230,237,239,242,243] A major problem of M−S batteries is a shuttle mechanism that avoids the possibility to fully oxidize the M−polysulfide moieties back to molecular sulfur, thus realizing the full capacity of these systems, because the active metal anodes in the M−S cells continuously reduce the soluble M−polysulfide species in solution phase (during the charging process). Using MXene species in the composite sulfur cathodes may avoid (at least partially) the problematic shuttle mechanism, thanks to possible strong adsorption of the M−polysulfide moieties formed upon discharge to the surface of the MXene particles in the composite electrodes.

Song *et al.*[244] employed a template-derived porous N-doped Ti_3C_2 (P-NTC) as an electrocatalyst in Li-S batteries. P-NTC was developed by following steps; chemical synthesis, exfoliation, and self-assembly followed by the thermal annealing at 500 °C for 150 min. P-NTC has a large surface area, highly porous and rich electrical conductivity, subsequently, reduces the Li-polysulfides shuttle in Li-S systems. The electrochemical performances of cathodes comprising sulfur / P-NTC composites and sulfur/exfoliated MXene layers (S/TC), with sulfur loading of 1.4–1.6 mg/cm^2 as explored. Their voltametric studies confirm the fully reversible two stages reduction of sulfur to Li_2S and its oxidation back of to S_8 at 2.5–2.2 V as shown in Fig. 19 (a). The synergetic effect of nitrogen and the MXene matrix greatly enhances precipitation and decomposition of Li_2S during cycling. The P-NTC matrix acts as a template, providing the active sites used for adsorption as well as conversion for lithium polysulfides. Faster sulfur reactions kinetics due to the lower dissociation barrier of Li_2S and nitrogen doping, which enhances the overall electrochemical performances, as shown in Fig. 19(b). Flexible pouch cells tested with the various bending angles deliver continuous power with light emitting diodes, demonstrated with a sulfur loading of 1.5 mg.cm^2 and size of 2.5 cm*2.5 cm (Fig. 19(c,d)). [244].

Another study revealed that lithium polysulfides are trapped by crumpled N-doped MXene (N-$Ti_3C_2T_x$), these are synthesized by one step thermal annealing process at 550 °C for 4 h. [119] Melamine's are positively charged; it can be easily electrostatically adsorbed onto the negatively charged MXene flakes. The nitrogen was successfully doped into $Ti_3C_2T_x$, with a precursor of melamine. N-$Ti_3C_2T_x$/S composites were prepared by the melting diffusion method. N_2 adsorption–desorption measurements reveal that these materials contain meso and micropores in their structure. The provision of a high surface area (385 m^2/g), and porous nature of these nanosheets offer high sulfur loading. N-doping confers a strong affinity between the titanium and sulfur atoms which appears to slow down the polysulfide formation and enhances cycling stability. The crumpled N-$Ti_3C_2T_x$/S composites could deliver 588 mAh/g specific capacity retention for ~ 500 cycles at 0.2 C rate (Fig. 19 (e)), an excellent electrochemical performance that can be attributed to the doping of N-atom, high surface area, and conductivity of the as-synthesized material. Ultraviolet spectra and XPS show that the nitrogen doping subsequently improves hydrophilic properties and Lewis acid adsorption with lithium polysulfides and sulfur. N-$Ti_3C_2T_x$/S composite electrodes delivered enhanced electrochemical performances in compared to the $Ti_3C_2T_x$/S.

Bao *et al.* synthesized sulfur-doped MXene (S-$Ti_3C_2T_x$) via the vacuum freeze-drying method, which does not affect the lattice structure. [58] was doped into the MXene lattice before etching as well as to remove the aluminum. S-$Ti_3C_2T_x$/S composite was obtained by annealing at 155 °C for 20 h. As synthesized material had a wrinkled morphology consisting of meso and micro-pores. Regarding Na-S systems, Sulfur doping in MXene enhances the redox activity and subsequently restricts Na polysulfide formation in sodium-sulfur batteries. DFT calculations reveal the strong adsorption capacity of S-$Ti_3C_2T_x$. DFT results confirmed that the polysulfides are potentially bind with the as synthesized S-$Ti_3C_2T_x$. Formation of strong adsorption tendency with S- $Ti_3C_2T_x$ compared to the other functional groups (F, OH) is revealed with the doped MXene. S-$Ti_3C_2T_x$ and the Na_2S_2, Na_2S_4 and Na_2S_6 binding energies are −1.887,-2.880 and −4.772 respectively. In a typical CV curves of S-$Ti_3C_2T_x$ /S and $Ti_3C_2T_x$ /S electrodes the reduction peak at 1.5 V reflects the conversion of S_8 to high order sodium polysulfides. The peak at 1.0 V corresponds to reduction of high order Na-polysulfides to low order Na-polysulfides (Na_2S/Na_2S_2). The oxidation peak at 2.1 V reflects the reversible oxidation of the Na_2S/Na_2S_2 moieties to higher order Na-polysulfides upon charging. The studied S-$Ti_3C_2T_x$/S cathodes demonstrated good reversibility with lower potential polarization, and could deliver an initial discharge capacity around of 820 mAh/g at 2C rate and around 580 mAh/g at the 500th cycle. With high sulfur loading of 4.5 mg/cm^2 at 1C rate for 600 cycles these electrodes exhibited a relatively low degradation per cycle (<0.12% per cycle in average), shown in Fig. 19(f). Also, the enhanced reversible stability of S-$Ti_3C_2T_x$ /S with respect

to $Ti_3C_2T_x$ /S can be seen form their rate capability plots (Fig. 19 (g)) at current rates from 0.2 to 5C. The longer cycle life and higher discharge capacity of these electrodes is attributed to the effective sulfur incorporation, which subsequently enhances the redox activity thanks to unique adsorption interactions of the sulfide moieties with the doped S-$Ti_3C_2T_x$ substrates in the composite electrodes, which is especially important at high sulfur loading.

4.2.4. Supercapacitors (SCs)

Supercapacitors (SCs) are emerging as another electrochemical energy storage technology that reaches practical applications. SCs utilize very high surface area electrodes (even thousands of square meters per gram), which charge storage mechanism is mostly capacitive. Since SCs are based on capacitive electrodes (surface activity), while batteries are based on redox electrodes (bulk activity), SCs have much lower energy density than batteries (in one or two orders of magnitude), but have much higher power density than batteries. Another great advantage of SCs is prolonged cycle life and durability, since the capacitive electrodes degrade much more slowly compared to redox (batteries) electrodes. The area of SCs and their applications develops very fast in recent years.[245–248].

In general, SCs are classified into three categories: (a) electrochemical double layer (EDL) supercapacitors (EDLCs), (b) pseudocapacitors, and (c) hybrid capacitors. EDLC capacitor electrodes are typically composed of activated carbon materials having high surface area and porosity is in the nanometer range where charge is stored at or near the interface of these electrodes (within their pores) and electrolyte solution. Their impedance depends on the resistivity of the electrolyte solution and the ease of ions diffusion within the micro/mesopores of the porous electrode material. The charge storage mechanism mainly depends on the adsorption phenomenon. Carbon-based materials such as activated carbons, graphene, carbon nanotubes, bio-derived carbons, and carbon

Table 3
Highlighted works on doped MXene for electrocatalysis.

MXene	Dopant	Synthesis method	Application	Improved property after doping	Ref
$Ti_3C_2T_x$	N	Heating in ammonia flow (200 ml min^{-1}) in quartz pipe furnace for 3 h	HER	~400 mV decreases in HER onset potential in 0.5 M H_2SO_4. overpotential 198 mV *vs.* RHE) at 10 mA/cm^2	[44]
$Ti_3C_2T_x$	N	lower temperature (35 °C) ultrasonication in ammonia, $NaBH_4$ solution for 3 h	HER	overpotentials 160 mV at 10 mA/cm^2 in N_2-saturated 0.5 M H_2SO_4. Pristine MXene (578 mV *vs.* RHE)	[57]
Mo_2CT_x	P	Phosphorization in a tube furnace at to 550 °C under Ar flow	HER	overpotential at 10 mA cm^{-2}: Mo_2CT_x (300 mV *vs.* RHE) and P–Mo_2CT_x (186 mV *vs.* RHE) in N_2-saturated 0.5 M H_2SO_4	[37]
V_2CT_x	P	treatment in triphenylphosphine (TPP) at 300–500 °C under Ar atmosphere	HER	V_2CT_x exhibits an overpotential of −760 mV(@10 mA cm^{-2}) and P–V_2CT_x exhibits -163 mV at 10 mA cm^{-2} in N_2-saturated 0.5 m H_2SO_4	[100]
$Mo_2TiC_2T_x$	Pt	M H_2SO_4	HER	Overpotential to reach 10 $mAcm^{-2}$ in 0.5 M H_2SO_4 decreased from 287 mV to 30 mV after Pt_{SA} doping	[95]
V_2CT_x	Pt	stirred at room temperature for 6 h in H_2PtCl_6 (10 mg/ml) solution	HER	V_2CT_x overpotential of 743 mV (@10 mA cm^{-2}) against Pt–V_2CT_x 27 mV (@10 mA cm^{-2}) in 0.5 M H_2SO_4	[136]
$Ti_3C_2T_x$	Pt	electrochemical deposition form pt foil in 0.5 M H_2SO_4	HER	Overpotential of 12 mV at a current density of 10 mA cm^{-2} 0.5 M H_2SO_4	[137]
$Ti_3C_2T_x$	Ru with the N and S	ultrasonicated for 30 min in thiourea and 15 mM $RuCl_3{\cdot}xH_2O$ solution	HER	Overpotentials @10 mA cm^{-2} for $Ti_3C_2T_x$, N-S-$Ti_3C_2T_x$, Ru_{SA}-$Ti_3C_2T_x$ and Ru_{SA}-N-S-$Ti_3C_2T_x$ 673, 453, 215 and 76 mV respectively. (Vs RHE in 0.5 m H_2SO_4)	[97]
$Ti_3C_2T_x$	Ir with the N and S	melamine, H_2IrCl_6, and thiourea solution added to $Ti_3C_2T_x$ followed by heating at 550 °C for 2 h under Argon atmosphere	HER	57.7 mV overpotential at a current density of 10 mA cm^{-2} for Ir_{SA}-2NS-$Ti_3C_2T_x$ in 0.5 M H_2SO_4	[69]
$Ti_3C_2T_x$	Ru with the B	$Ti_3C_2T_x$ mixed with H_3BO_3 and $RuCl_3{\cdot}xH_2O$ followed by heating at 600 °C for 3 h under Argon atmosphere	HER	Overpotential of 843 mV @10 mA cm^{-2} for $Ti_3C_2T_x$ while 16.9 mV for Ru@B–$Ti_3C_2T_x$ in 0.5 m H_2SO_4	[140]
Mo_2CT_x	Ru	HCl-LiF-$RuCl_3$ etching of Mo_2Ga_2C. in situ reduction of $RuCl_3$	HER	overpotential of 73 mV @ −10 mA cm^{-2} in (1.0 M phosphate buffer (pH 7.0)	[143]
Ti_3C_2	N	Ball milling TiN:TiC:Al:Ti followed by LiF/HCL etching	OER	Respective onset overpotentials (η_{onset}) are 449.0, 418.7, and 245.8 mV for Ti_3C_2, $Ti_3C_{1.8}N_{0.2}$, and $Ti_3C_{1.6}N_{0.4}$ in 1 M KOH	[117]
$Ti_3C_2T_x$	Pt	Ultrasonication in H_2PtCl_6 and $NaBH_4$ solution	ORR	limit-current of 6.5 mA cm^{-2} in O_2-saturated KOH (0.1 mol L^{-1})	[165]
Ti_3C_2	Au	Sequential stirring in $HAuCl_4$ and $NaBH_4$ solution.	NRR	Au/Ti_3C_2 exhibits NH_3 yield of 30.06 μg h^{-1} mg^{-1} for with Faraday efficiency of 18.34% at −0.2 V. Ti_3C_2 exhibits 1.78 μg h^{-1} mg^{-1}	[176]
Mo_2CT_x	Ru	$_2CT_X$ delaminated solution at room temperature for 10 h	NRR	Increased NH_3 yield: 40.57 μg h^{-1} mg^{-1}, with FE of 25.77% with respect to Pristine Mo_2CT_X (NH_3 yield: 10.43 μg $h^{-1}mg^{-1}$, FE: 7.73%)	[89]
$Ti_3C_2Cl_x$	Cu	Ball milling Ti, Al, Cu and graphite powders. followed by $ZnCl_2$/HCL etching	CO_2RR	CH_3OH faradaic efficiency of 59.1% compared to FE < 2% for $Ti_3C_2Cl_x$	[192]
Ti_3C_2	N	NH_3-etching pyrolysis approach	CO_2RR	CO_2RR in seawater with FE of 92%; −18.3 mA/cm^2 at −0.8 V *vs.* RHE for N-Ti_3C_2 against −3.4 mA/cm^2 for Ti_3C_2.	[188]

aerogels have been used successfully. Carbon-based substances are coated on the current collectors including graphite sheets, carbon fibers, nickel foam, aluminum foil and titanium sheets.[247,249,250].

In contrast to EDLCs which store charge electrostatically, the mechanism of pseudocapacitors involves surface redox reactions with ions inserted into active sites on the electrodes' surface. Hence pseudocapacitive electrodes involve both capacitive and surface redox charge transfer interactions. The extra-faradaic (surface) processes deliver high specific capacitance and maintain relatively power density and durability due to the combination of the charge storage mechanisms. Possible species that can contribute to pseudocapacitive/surface-redox are electronically conducting polymers and transition metal oxide nano-particles (attached to the high surface area electrodes). Conducting polymers have high conductivity (10^2–10^4 S/cm) and capacitance (70–200 F/g), in particular a low equivalent series resistance (ESR), which allows access to a much higher power density than carbon-based materials. Other materials besides conducting polymers, which also offer advantages such as metal oxides with relatively low cost, have a high theoretical capacitance and are also environmentally benign. Their CV and charge–discharge profiles are similar to those of battery electrodes. Pseudo-capacitors exhibit three types of mechanisms – underpotential deposition, redox, and intercalation pseudo-capacitance.[246,250–253] Whilst EDLCs have good cycling stability and high-power density, pseudo-capacitors have high specific capacitance. Hybrid SCs combine two electrodes, where one is the source of high-power density and the other provides energy density. With the appropriate combination of electrode active materials and electrolyte solutions, an increase in the cells voltage can result in higher energy and power density as well. Current research mainly focuses on three different types of pseudo-capacitors – electrode material-composite based, asymmetric, and battery-like. The development of new active materials for high-power SCs can be achieved by controlling the morphology and composition of the active electrode material.

MXenes can be ideal electrodes' materials for high performance pseudo-capacitors. They can serve only as negative electrodes for these devices, since they cannot interact well with anionic species due to repulsion interactions. MXene and MXene-based composite materials are being extensively studied as electrode materials in supercapacitors. MXene derived electrodes have been reported to deliver excellent performances. Comparison between the supercapacitor performance of MXene with other inorganic and 2D materials is presented in Table 4. Incorporation of heteroatoms such as nitrogen dramatically enhances their specific capacitance as anode materials. Wen *et al.* synthesized nitrogen doped MXene (N-$Ti_3C_2T_x$) by annealing in ammonia at various temperatures from 200 to

Table 4
Comparison of super capacitive performance of MXene with other materials.

Materials	Capacitance (F-g/cm^2/cm^3)	Cycle life	Electrolyte	Ref.
Ti_3C_2Tx	350 F/Cm^3	10,000 cycles at 1 A/g	1 M KOH	[254]
Ti_3C_2Tx	215 F/g	10,000 cycles at 5 A/g	1 M H_2SO_4	[255]
Ti_3C_2Tx	415 F/g	10,000 cycles at 5 A/g	1 M H_2SO_4	[256]
Ti_3C_2Tx	900 F/cm^3	10,000 cycles at 10 A/g	1 M H_2SO_4	[257]
Ti_3C_2Tx	33 F/cm^2	10,000 cycles at 1 A/cm^3	PVA/H_3PO_4	[258]
Ti_3C_2Tx/PPy	416 F/g	25,000 cycles at 100 mV/s	1 M H_2SO_4	[259]
Ti_3C_2Tx/ZnO	120 F/g	10,000 cycles at 5 A/g	1 M KOH	[260]
Ti_3C_2Tx/MnO_2	380 mF/cm^2	5,000 cycles at 5 A/g	6 M KOH	[261]
Ti_3C_2Tx/LDH	1061 F/g	4,000 cycles at 4 A/g	6 M KOH	[262]
Ti_3C_2Tx/SCNT	390 F/cm^3	10,000 cycles at 5 A/g	1 M $MgSO_4$	[263]
Ti_3C_2Tx/rGO	154.3 F/g	6,000 cycles at 4 A/g	2 M KOH	[264]
Ti_3C_2Tx/rGO	1040 F/cm^3	20,000 cycles at 100 mV/s	3 M H_2SO_4	[265]
Ti_3C_2Tx/ZIF-67/CoV_2O_6	285 F/g	4,000 cycles at 4 A/g	3 M KOH	[266]
Ti_3C_2-Cu	290 F/g	10,000 cycles at 2 A/g	1 M H_2SO_4	[267]
[Ni(thiophene-2,5-dicarboxylate)(4,4'-bipyridine)]$_n$	102 mF/cm^2	5,000 cycles at 3 mA/cm^2	3 M KOH	[268]
$Ni_2P_2O_7$	428 mA/cm^2	2,500 cycles at 50 mV/s	1 M KOH	[269]
$Co_2P_2O_7$	580 F/g	5,000 cycles at 10 A/g	3 M KOH	[270]
$Zn_2P_2O_7$	103 F/g	1,000 cycles at 1 A/g	3 M KOH	[271]
$Mn_2P_2O_7$@PPy	658 F/g	10,000 cycles at 1 A/g	2 M KOH	[272]
$Co_2P_2O_7$/MWCNT	207 F/g	5,000 cycles at 3.5 A/g	1 M KOH	[273]
GO/MnO_2	211 F/g	1,000 cycles at 0.2 A/g	1 M Na_2SO_4	[274]
CNTs/MnO_2	331 F/g	5,000 cycles at 1 A/g	0.5 M Na_2SO_4	[275]
C/MnO_2	679 F/g	5,000 cycles at 1 A/g	0.5 M Na_2SO_4	[276]
N,S doped graphene nano ribbons	328 F/g	10,000 cycles at 7 A/g	1 M Na_2SO_4	[277]
N doped Few layered graphene	227 F/g	1,000 cycles at 1 A/g	6 M NaOH	[278]
S doped graphene	320 F/g	1,500 cycles at 5 A/g	3 M KOH	[279]
N,S-doped graphene	298 F/g	10,000 cycles at 1 A/g	6 M NaOH	[280]
h-BN/RGO	824 F/g	4,000 cycles at 15 A/g	6 M KOH	[281]
MoS_2@hollow carbon nano bowl	560 F/g	5,000 cycles at 5 A/g	6 M KOH	[282]
NiCo-MOF	1109 F/g	10,000 cycles at 5 A/g	2 M KOH	[283]
Zn_2SnO_4/SnO_2/CNT	702 F/g	15,000 cycles at 10 A/g	6 M KOH	[284]
NiO/PANI/CNT	356 F/g	1,000 cycles at 5 A/g	10 M KCl in Aceto nitrile	[285]
MoS_2 nanosheets	129 F/g	500 cycles at 1 A/g	1 M Na_2SO_4	[286]
Porous tubular C/MoS_2	210 F/g	1,000 cycles at 4 A/g	3 M KOH	[287]
Graphene oxide	189 F/g	5,000 cycles at 0.45 A/g	6 M KOH	[288]
RGO	129 F/g	3,000 cycles at 10 mV/s	1 M H_2SO_4	[289]
RGO	232 F/g	1,000 cycles at 1 A/g	6 M KOH	[290]

700 °C with 1.7–20.7% nitrogen incorporated into the MXene lattice. [48] The thermal treatment enhances the structural change in the MXene sheets, facilitating the incorporation of nitrogen. Doping subsequently increases the c-lattice parameter from 1.92 to 2.46 nm. Specific capacitance of N-$Ti_3C_2T_x$ in 1 M H_2SO_4 exhibited 192 F/g, while pristine MXene delivered 34 F/g as shown in Fig. 20 (a). In 1 M $MgSO_4$, the solution delivered a specific capacitance of 82 F/g in N-$Ti_3C_2T_x$ and 52 F/g in $Ti_3C_2T_x$, see Fig. 20(b). Doped MXenes in sulfuric acid enabled enhanced redox activity which subsequently delivered a higher specific capacitance than in $MgSO_4$ (neutral) solutions. N-$Ti_3C_2T_x$-200 °C delivers excellent electrochemical properties, as compared to samples annealed at other different temperatures. Impedance studies reflect the lower charge transfer resistance of N-$Ti_3C_2T_x$-200 °C compared to bare $Ti_3C_2T_x$ in both sulfuric acid and magnesium sulfate solutions (Fig. 20(c,d)). DFT calculations found that the N-doping increases the electronic concentration and electrical conductivity. Overall, the specific capacitance is enhanced due to doping, which tunes the electrical conductivity and active surface area and increases interlayer spacing.

Yang *et al.* developed nitrogen-doped delaminated titanium carbides (N-d-Ti_3C_2) for high-performance supercapacitors via a liquid exfoliation of Ti_3C_2 with urea followed by annealing. [116] Delamination and subsequent heating improves the specific surface area of the material to 23.5 m^2/g (N-d-Ti_3C_2) of 5 m^2/g (Ti_3C_2) and offers thinner layers and more structural defects. XRD shows that the d-spacing increases from 1.01 to 1.30 nm for N-d-Ti_3C_2; the (0 0 2) peak shifts from 8.8° to 6.8°. Excellent electrochemical performance was revealed by assessment of the N-d-Ti_3C_2 cycle life in 6 M KOH solution, which exhibits 86.4% capacitance retention for 2,000 cycles at 2 A/g (Fig. 20 (e)). This observed performance can be attributed to the doping, the layered structure, and the high specific surface area, which allows the electrolyte ions (K^+, 0.138 nm) to intercalate/de-intercalate into the N-d-Ti_3C_2 interlayer (1.27 nm) of the electrode active material during cycling. Tang *et al.* [47] synthesized two-dimensional N-doped Ti_3C_2 by a one-step hydrothermal route at 60 °C for 3 h using urea as a nitrogen source. Raman spectra of Ti_3C_2 and N-Ti_3C_2 consist of D and G bands of graphitic carbon at circa 1350 and 1590 cm^{-1} with an I_D/I_G ratio of 0.85 and 0.88 for Ti_3C_2 and N-Ti_3C_2, respectively. These results are evident that N-Ti_3C_2 has more graphitic domains in comparison to the bare material. CV curves of Ti_3C_2 and N-Ti_3C_2 (Fig. 20 (f,g)) studied at scan

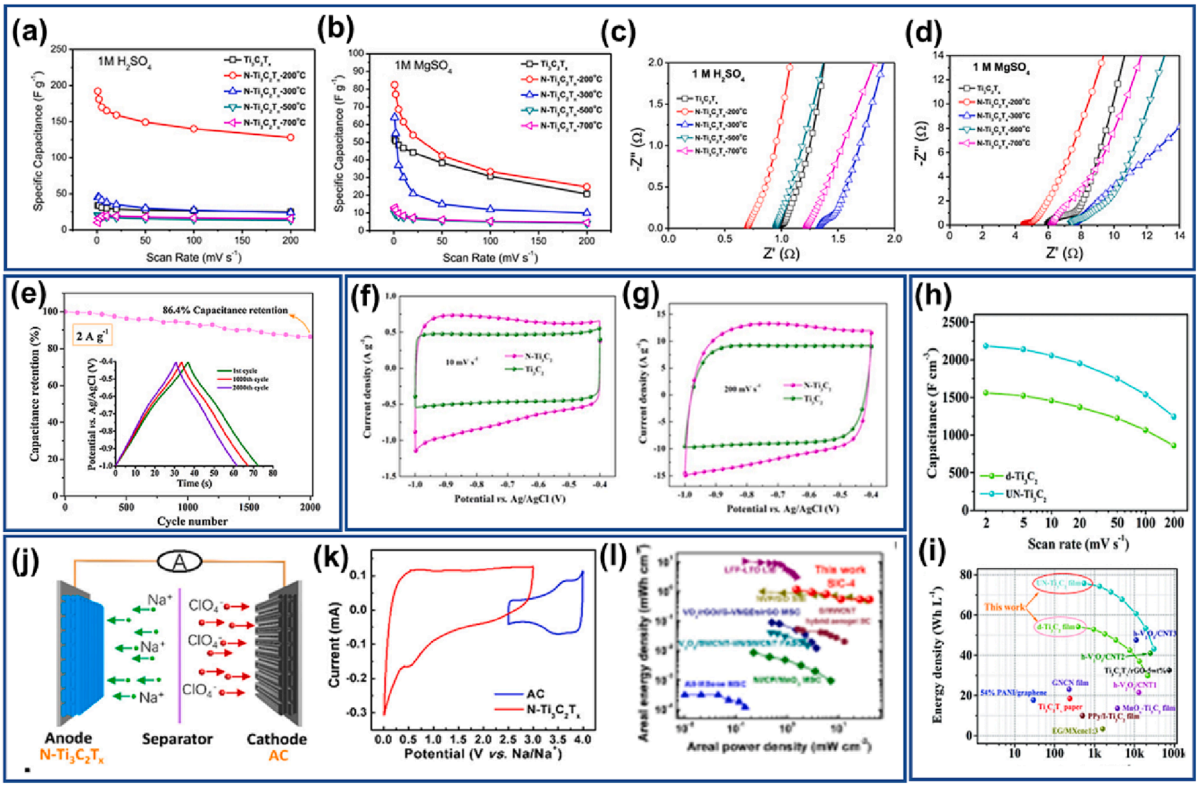

Fig. 20. Nitrogen-doped MXenes used for High-Performance Supercapacitors. Specific capacitances at different scan rates of $Ti_3C_2T_x$ and N-$Ti_3C_2T_x$ in (a) 1 M H_2SO_4,(b) 1 M $MgSO_4$,corresponding Nyquist plots of $Ti_3C_2T_x$ and N- $Ti_3C_2T_x$ MXene based supercapacitors in, (c) 1 M H_2SO_4 (d) 1 M $MgSO_4$ [48]; (e) galvanostatic charge discharge cycles showing capacitance retention of nitrogen-doped delaminated titanium carbide (N-d-Ti_3C_2) at 2 A/g for 2000 cycles [67]; (f,g) CV curves of Ti_3C_2 and N-Ti_3C_2 at 10 and 200 mV/S showing improved capacitive performance with nitrogen doping comparing other MXene based systems [47]; Performance comparison between urea-assisted nitrogen doped -Ti_3C_2 MXene (UN-Ti_3C_2) and freestanding MXene (d-Ti_3C_2) in symmetric capacitors and hybrid capacitors. (h) volumetric capacitance values w.r.t. scan rate (i) Ragone plots of volumetric energy density and power density [116]; (j) Schematic diagram of Na-ion hybrid capacitor (SIC) system, (k) CV of nitrogen-doped MXene (N-Ti_3C_2Tx) anode and activated carbon cathode in half-cells (l) Ragone plot of the 3D-printed N-$Ti_3C_2T_x$//AC SICs in comparison with other reported energy storage devices [93]. Reproduced from [48,92,47,116,93] with permission from American Chemical Society, Wiley, Wiley-VCH and The Electrochemical Society.

rates of 10 and 200 mV/s follow nearly rectangular shaped curves, which reflects ideal capacitive behavior. The area under the curve of N-Ti_3C_2 is higher compared to bare Ti_3C_2, reflecting that the greater specific capacitance of the doped material even at high scan rate of 200 mV/s. This enhancement is attributed to additional sites for charge storage provided by the nitrogen, which increase the electronic conductivity, delivering extra pseudo-capacitance, in addition to the two-dimensional layered structure of N-Ti_3C_2 with a greater extent of intercalation and deintercalation for K^+ ions from the electrolyte.

Nitrogen doped delaminated MXenes (N-Ti_3C_2) was synthesized using ex situ urea and monoethanolamine (MEA) assisted solvothermal method. [92] Flexible and freestanding N-Ti_3C_2 synthesized by Yang *et al.* had a face-to-face layered lattice structure with structural defects, high specific surface area, and conductive mesopores. An *ex-situ* solvothermal method of N-Ti_3C_2 delivered a high volumetric capacitance in relation to *in-situ* doping. N-doping increases the d-spacing from 1.15 to 1.24 nm. Urea-assisted N-Ti_3C_2 delivered enhanced volumetric capacitance over pristine MXene (Fig. 20 (h)). Due to the abundant pores structure and greater number of nitrogen-containing sites, urea-assisted N-Ti_3C_2 exhibits excellent volumetric capacitance of 2836 F/cm^3 in 3 M aqueous sulfuric acid at 5 mV/s. Besides, a symmetric capacitor delivers an impressive volumetric energy density of 76 Wh/L with a power density of >31000 W/L as shown in Fig. 20 (i). The electrochemical performance is due to the adequate amount of elemental N-doping, cation intercalation, proton diffusion, and high utilization of N-Ti_3C_2 film. Both N-Ti and N-O bonds contribute to enhanced performance. [92].

Current research aims to increase both energy and power by single devices called hybrid capacitors, which consists of a SC (capacitive) based cathode and a battery (redox) based anode. Fan *et al.* used a 3D printed N-doped MXene (N-$Ti_3C_2T_x$) as anode, activated carbon as cathode, with no current collector, for sodium ion capacitors (SICs) as shown in Fig. 20(j). [93] SEM presents the uniform and well-defined interconnected porous structure, while TEM reveals the few-layered structure with an interlayer spacing of 1.02 nm. N-$Ti_3C_2T_x$ half-cell configurations show a strong stability in cycle life at high rates of 5C (nearly 285 mAh/g after 1000 cycles) and 25C (165.5 mAh/g after 3000 cycles) with less charge transfer resistance. Full cells fabricated using charge balance theory with an optimized mass ratio of 1:3.5 showed an operating voltage of 0–4 V (Fig. 20(k)). The charge storage behavior depends mainly on the number of layers (2/3/4). SIC delivers around 1.2 mWh/cm^2 and around 40 mW/cm^2 (Fig. 20(l)). Na ions are reversibly inserted/extracted at the anode, and ClO_4^- ions are involved in adsorption/desorption during charge–discharge at the capacitive cathode side The interlayer expansion provides more charge sites for the sodium ions. Superior electrochemical performance was obtained due to the open pore structure and high electronic conductivity; N-$Ti_3C_2T_x$ consists of uniform N-doping, which enables fast kinetics. In summary, doped MXenes, especially with nitrogen, can be considered as excellent anode materials for pseudo-capacitors. The capability of these materials to insert various types of cations, within their layered structure, upon cathodic polarization, ensure high specific capacity values. Fortunately, ion exchange interactions with MXenes are fast, which enables to obtain high rate capabilities as well as highlighted in Table 5. There are many relevant MXenes materials, thereby, further optimization that will produce superb electrodes' materials for energy storage and conversion applications. One plausible approach to improve the capacity of electrodes is to create MXene based 3D composite structures or introducing bimetallic hybrid compounds onto MXene structure. [266,267].

4.3. Photovoltaics

Theoretical studies based on density functional theory (DFT) [294,295] investigated the effect of doping MXenes on band gaps to realise materials suitable for photon-electron conversion devices. Sc_2CF_2 MXene monolayers doped through C atom substitution with Si, Ge, Sn, F, S, N, B, and B + N were found to be either conductors or semiconductors. Semiconductors are generally indirect and with a band gap too small for photon-electron conversion, i.e. on the order of 1 eV.[295] On the other hand, the ideal 1.4 eV band gap was predicted for Sc_2CO_2 by doping with Nb ($ScNbCO_2$) and applying strain as shown in Fig. 21 (a).[294] The use of doped MXenes in real

Table 5
Highlighted works on Doped MXene for energy storage.

Application	Doped Mxene	Synthetic method	Electrochemical performances	References
LIBs	N-Nb_2CTx	Hydrothermal	1500 cycles at 0.5C, 92 % capacity retention	[217]
LIBs	N,S-V_2CTx	Calcination	100 cycles at 0.1 A/g	[68]
NIBs	S-Ti_3C_2Tx	Annealing	2000 cycles at 0.5 A/g	[61]
Li-S batteries	N-Ti_3C_2	Annealing	1200 cycles at 2C rate	[244]
Li-S batteries	N-$Ti_3C_2T_x$	Annealing	500 cycles at 0.2C rate	[119]
Na-S batteries	S-Ti_3C_2Tx	In-situ doping	500 cycles at 2C rate	[58]
Supercapacitors	N-$Ti_3C_2T_x$	Annealing	10,000 cycles at 50 mV S^{-1} 92 % capacitance retention	[48]
Supercapacitors	N-d-Ti_3C_2	Annealing	2,000 cycles at 2 A/g, 86.4 % capacitance retention	[92]
Supercapacitors	N-Ti_3C_2	Hydrothermal	5,000 cycles at 5 A/g, no measurable capacitance retention	[47]
Supercapacitors	N,S-Ti_3C_2	Annealing	5,000 cycles at 2 A/g, 90.1 % capacitance retention	[291]
Supercapacitors	N-Ti_3C_2	Annealing	5,000 cycles at 5 A/g, 96.2% capacitance retention	[292]
Supercapacitors	N-$V_4C_3T_x$	Annealing	10,000 cycles at 10 A/g, 96.3% capacitance retention	[293]
Symmetric supercapacitors	N-Ti_3C_2	Ex-situ Solvothermal	20,000 cycles at 10 A/g, 81.7% capacitance retention	[116]
Sodium-ion capacitors	N-Ti_3C_2	Chemical synthesis followed by freeze-drying	3,500 cycles at 2 A/g, 75 % capacitance retention	[93]

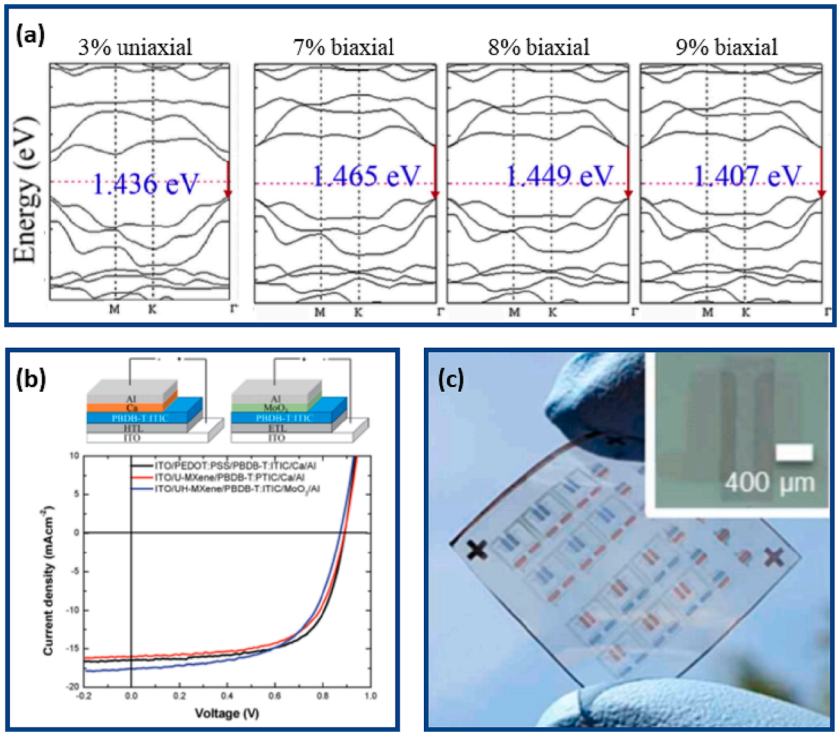

Fig. 21. Doped MXene for photovoltaics and electronics applications. (a) Ideal band gap for photovoltaics predicted for $ScNbCO_2$ under different strain as specified above the graphs.[294] (b) Upper diagrams: device architecture of the conventional device: indium tin oxide (ITO)/Hole Transport Layer (HLT)/active layer(PBDB-T:ITIC)/Ca/Al and the inverted device: ITO/Electron Transport Layer (ETL)/active layer(PBDB-T:ITIC)/MoO_3/Al. Main graph: J–V curves of PBDB-T:ITIC organic solar cells (OSCs) with the normal and inverted architecture. UVO-treated MXene (U-MXene) is used for hole collection in the normal OSC, and the UVO-then-N2H4 treated MXene (UH-MXene) is for electron collection in the inverted OSC. The J–V curve of a control OSC with PEDOT:PSS used as the HTL and Ca as the ETL was also generated for comparison.[111] (c) Photographic image of MXene-electrode-based organic field-effect transistors (OFETs) and logic gates fabricated on a plastic substrate. The inset shows an optical microscopy image of a single OFET.[299] Reproduced from [294,111,299]with permission from American Chemical Society and Royal Society of Chemistry.

photovoltaic devices is still embryonic but extended to different kinds of devices: MXene-silicon heterojunctions,[296] MXene-GaAs heterojunctions,[297] organic solar cells [111] and perovskite solar cell. [298].

Yu *et al.* developed a novel type of solar cell based on charge separation at the heterojunction formed by a transparent conducting MXene electrode and an n-type silicon (n-Si) wafer. [296] The $Ti_3C_2T_x$ electrode serves not only as a transparent conducting film for charge transport, but also contributes to the built-in potential and thus the separation of electron-hole pairs. Remarkably, the power conversion efficiency of the device produced with pristine MXenes (about 5%) could be improved to above 9% by employing two-step chemical treatments (2% HCl and $AuCl_3$). The HCl treatment introduces a doping effect on the MXene leading to improved conductivity, while AuCl3 treatment significantly improves the charge transfer properties of the devices. The HCl treatment has been proven to be effective also in MXene/GaAs heterojunction solar cells. The produced devices featured a high initial efficiency of 9.69% and demonstrated to be stable under air exposure.[297].

In the work on organic solar cells[111], $Ti_3C_2T_x$ was treated by UV-Ozone exposure or with N_2H_4 vapour in a sealed petri-dish. These treatments, respectively, increased and decreased the work function due to either the oxidation or reduction of the C element of $Ti_3C_2T_x$. By tuning the work function, it was possible to use the doped MXene layers as hole or electron transport layers in non-fullerene organic solar cells with power conversion efficiency comparable to those obtained using conventional charge-collection buffer materials (Fig. 21(b)). Bati *et al.* [298] doped $Ti_3C_2T_x$ MXene nanosheets with cesium and introduced them into a lead iodide (PbI_2) precursor solution for perovskite solar cells. According to their theoretical and experimental analysis, Cs plays an important role in improving the perovskite crystallization and thus leading to enlarged crystal grains, long-lived carrier lifetimes, and reduced charge recombination as compared to the devices fabricated without and with undoped $Ti_3C_2T_x$ MXene. Solar cells integrated with Cs doped $Ti_3C_2T_x$ MXene delivered a power conversion efficiency of up to 21.57%, exceeding by >2% the efficiency of MXene-free solar cells (19.03%) or solar cells integrated with pristine MXenes (19.19%).

4.4. Electronics

The feasibility of electronic nano-devices based on doped MXene has been computationally investigated through first-principles

density functional calculations[300] or non-equilibrium Green's function in combination with DFT.[301,302] Feng *et al.* investigated the incorporation of neighbouring elements (Sc, V, B and N) in the indirect semiconductor Ti_2CO_2.[300] According to their simulations, it is more convenient to realise a p-type semiconductor by substituting Ti with Sc rather than replacing C with B. In addition, both a high alloying with N in place of C, and a light V substitution of Ti, are capable of generating n-type semiconductors. Furthermore, Zhou *et al.*[301] analysed the effect of V or Sc doping on the electronic transport properties of pure 2D Ti_2CO_2 electrodes. Doping of V (Sc) atoms introduces an impurity band near the Fermi level and shifts the Fermi level up (down) changing the MXene layer from semiconductor to conductor. More recently, the same group extended the study to p-type doped, undoped, and n-type doped MXene heterojunctions, M_2CT_x–M_2CO_2 (where M = Ti, Zr, or Hf; T = F, OH; x = 0 or 2).[302] This work identifies n-type doping as a promising route to improve device performance and offers new insight for guiding the design of novel MXene nano electronic devices such as nano-memristive devices.

The utility of MXene doping has been demonstrated in large-area electrode arrays for high-performance organic field-effect transistors (OFETs) on flexible substrates shown in Fig. 21(c).[299] The work function of $Ti_3C_2T_x$ MXene electrodes was engineered via chemical doping with NH_3. The doping mechanism was explained as Ti–O···H–N hydrogen bonding between MXene and ammonia, which modulated the dipolarity of the MXene surface and decreased the work function. This modification drastically improved the performance of n-type OFETs with respect to pristine MXene electrodes. Furthermore, doped MXene electrodes featured better electron injection properties than standard Al electrodes.

MXenes are also promising candidates for optoelectronic devices as demonstrated in an interesting work by Chen *et al.*. [303] In this work, the work function of Ti_3C_2 MXenes was tuned by surface modification with LiF, Se and polyethylenimine ethoxylated to realise

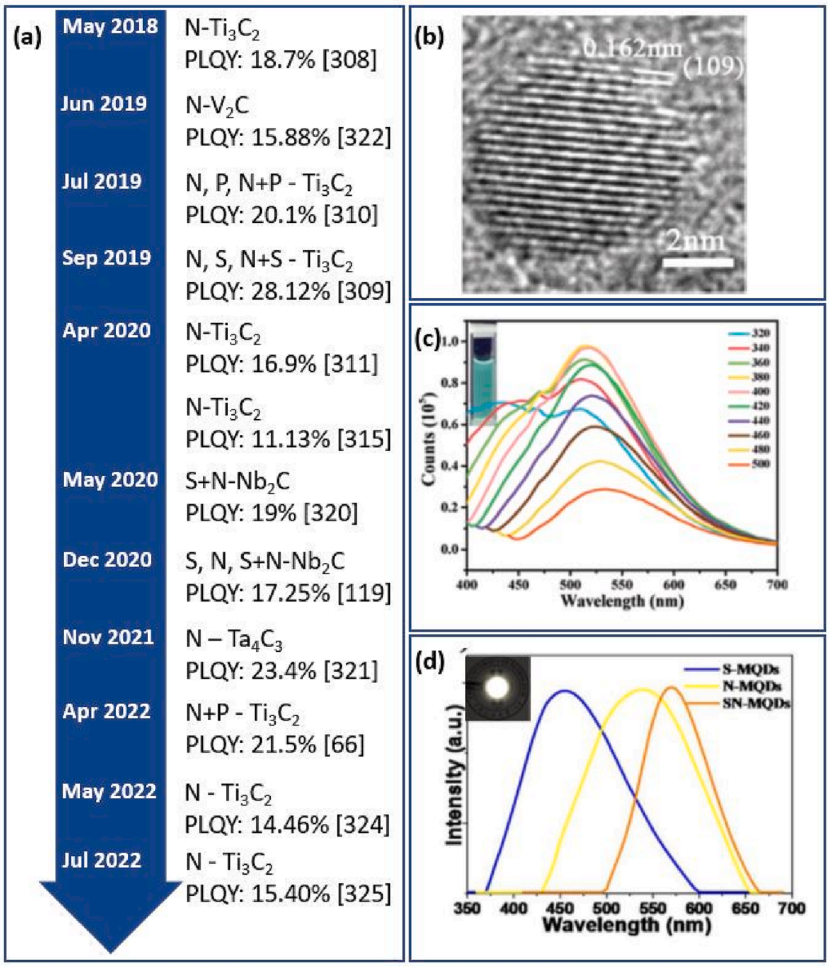

Fig. 22. Doped MXene quantum dots. (a) timeline of publications about doped MXenes quantum dots that reported PLQY values; (b) High Resolution TEM image of a N-MQDs (160 °C).[306] (c) Fluorescence emission spectra of the S,N-MQDs (160 °C) at different excitation wavelengths. Inset (top-left): Photograph under UV light (365 nm).[318] (d) Photoluminescence spectra of visible-light-emitting MQDs under 360 nm emission. Inset: Fluorescence images of the W-MQDs/PVP composite under 365 emissive chips.[307] Reproduced from [306,318,307] with permission from Springer Science + Business Media, Elsevier and Royal Society of Chemistry.

electrodes for photodetectors and functional "AND" and "OR" optoelectronic logic gates.

4.5. Photonics

The main application of doped MXenes in the field of photonics is in the realisation of quantum dots (QDs) [304,305] (Fig. 22(a) and Table 6). Ti_3C_2 MXene QDs have been doped with nitrogen [306–315], sulfur [307], phosphorus[308], europium[316]and co-doped with sulfur/nitrogen[307], phosphorus/nitrogen [65,308] or Chlorine/nitrogen [317] by hydrothermal method [232–234,237,240] solvothermal method [309,310,312,313] or potential static method [317]. Furthermore, sulfur and nitrogen co-doped Nb_2C QDs were produced by hydrothermal treatment.[118,318] N-doped Ta_4C_3 quantum dots have been produced in acid reflux by using Ta_4C_3 MXenes as precursors and ethylenediamine as nitrogen source.[319] V_2C and V_4C_3MXenes have been doped with nitrogen through hydrothermal and solvothermal processes respectively.[320,321].

In comparison to pristine MXene QDs, doped MXene QDs exhibit a smaller lateral size (2–6 nm)[118,306,308–311,313,317,318] (Fig. 22(b)) and significantly enhanced photoluminescence quantum yield (PLQY) of 19–23.4% [65,306,308,318,319] (Fig. 22(c)) against ~ 10% from non-doped QDs. Furthermore, heteroatom doping increases the QD lifetime and PLQY with respect to single atom

Table 6
Highlighted works on Doped MXene for photonics.

Year	MXene	Dopant	Synthetic method	Size (nm)	PLQY (%)	Application	Reference
2018	Ti_3C_2	N	hydrothermal	3.4	18.7	biosensor for the detection of $Fe3^+$	[306]
2019	V_2C	N	hydrothermal	4.13	15.88	White laser	[320]
2019	Ti_3C_2	N, P, N + P	top–bottomhydrothermal treatment	2.93	20.1	macrophage labeling and Cu_2^+ion sensing	[308]
2019	Ti_3C_2	S, N, S + N	hydrothermal	From 9 to 50 nm	up to 28.12%, 8.33% and 7.78% for SN-MQDs, N-MQDs, and S-MQDs, respectively	White light emitting diodes	[307]
2020	Nb_2C	S + N	hydrothermal	2.93	19	3D brain organoid labeling	[318]
2020	Nb_2C	S, N, S + N	hydrothermal	3.8	17.25	Cu_2^+ ion sensing and cell imaging	[118]
2020	Ti_3C_2	N	solvothermal	3.4	11.13% in reference to quinine sulfate whose quantum yield is 54% in 0.1 M H_2SO_4 solution	detection of H_2O_2 and Xanthine by single emission fluorescence or ratiometric fluorescence	[313]
2020	Ti_3C_2	N	Amine-assisted solvothermal	6	16.9	selective Cu_2^+ detection	[309]
2021	Ti_3C_2	N	solvothermal method to cut Ti_3C_2 MXenenanosheets in the presence of N, N-dimethylformamide and ammonium	3.09	–	"on–off-on" nanoprobe for chrominum (VI) and ascorbic acid based oninner filter effect	[310]
2021	Ti_3C_2	N	hydrothermal method using ammonium hydroxide as anitrogen source	–	–	Free-Radical Scavenging and H_2O_2 Detection	[314]
2021	Ti_3C_2	N	solvothermal method usingo-phenylenediamine as the nitrogen source	7.5	5.42	detection of alizarin red based on inner filter effect	[312]
2021	Ti_3C_2	Cl + N	potential static methodin a two-electrode system	3.45	–	scavenging activity towards •OH based on both dye protection and fluorescence tests	[317]
2021	Ta_4C_3	N	hydrothermal method using ethylenediamine as anitrogen source	2.60	23.4	heavy ion detection and stress monitoring of fluorescent hydrogels	[319]
2022	Ti_3C_2	N	hydrothermal method using ethylenediamine asthe nitrogen source	2–5	–	mucin 1 detection	[311]
2022	Ti_3C_2	N and Eu	hydrothermal	2.81	–	visual and quantitative point-of-care testing of tetracyclinederivatives	[316]
2022	Ti_3C_2	N + P	Microwave-assisted method	3.11	21.50	colorimetric/fluorometric dual-modal nitrite assay with aportable smartphone platform	[65]
2022	Ti_3C_2	N	inorganicbase stripping and solvothermal approach	2.3	14.46	nanoprobe for the simultaneous detection of Cu_2^+ and Ag^+ ions	[322]
2022	Ti_3C_2	N	hydrothermal	8.63	15.40	Fluorescent Cu_2^+ Ion Sensor	[323]
2022	V_4C_3	N	solvothermal	5–10	–	White light emitting diodes	[321]
2023	Ti_3C_2	N	solvothermal	5.5	–	ratiometric fluorescence probefor ascorbic acid and acid phosphatase	[324]

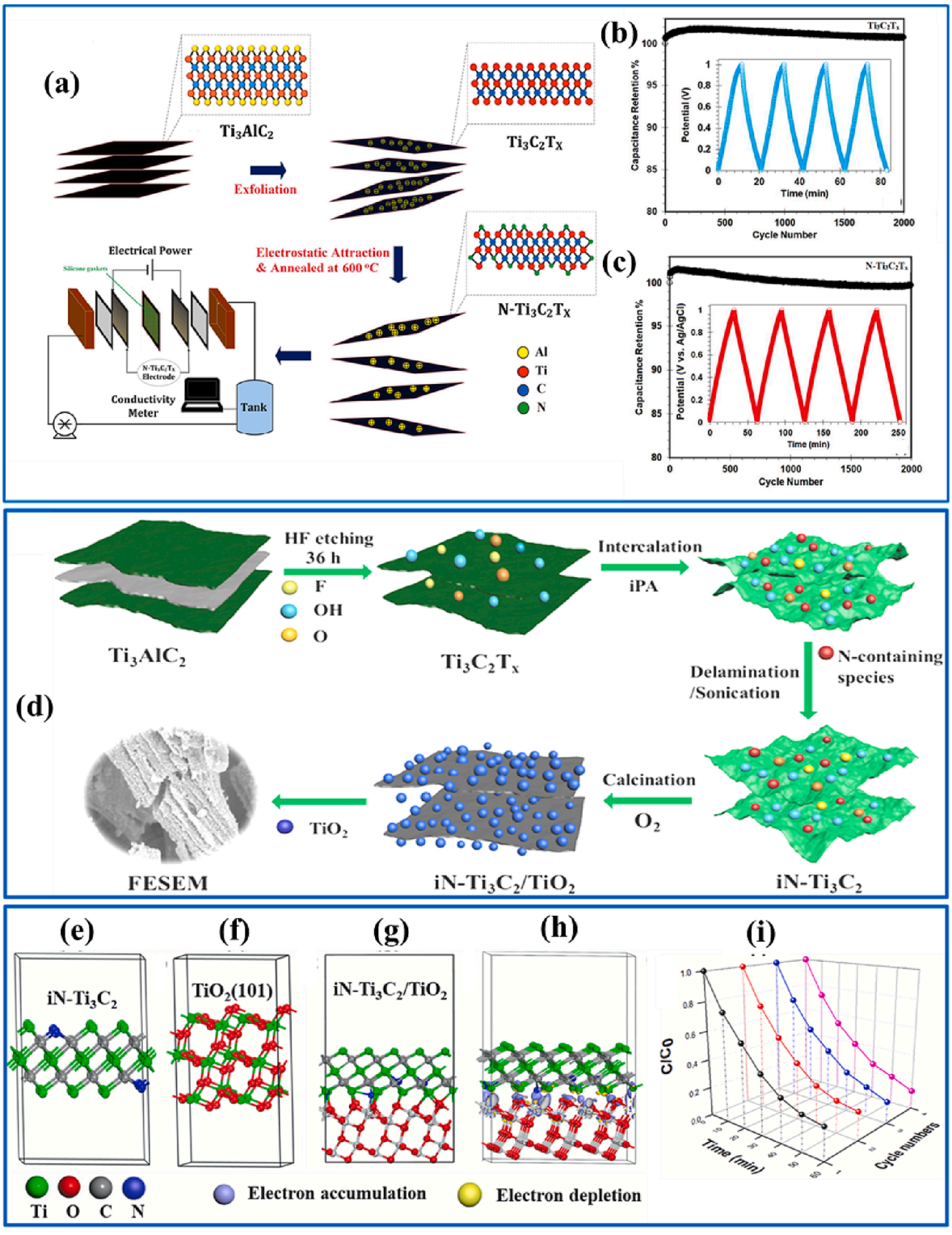

(caption on next page)

Fig. 23. Schematic illustration of doped MXene in environmental applications. (a) Schematic illustration for the synthesis of N–$Ti_3C_2T_x$ MXene sheets and their application as capacitive deionization electrodes, (b) $Ti_3C_2T_x$ sheets and (c) N–$Ti_3C_2T_x$ sheets after 2000 cycles at a current density of 0.5 A/g.[52] Insets of panels (b) and (c) are 4 charge–discharge cycles of the $Ti_3C_2T_x$ and N–$Ti_3C_2T_x$ electrodes, respectively.[52] (d) Schematic illustration for the in situ synthesis of nitrogen-doped Ti_3C_2/TiO_2.[328] Schematic illustration of electronic structures of (e) nitrogen-doped Ti_3C_2, (f) (1 0 1) facets of anatase TiO_2, and (g) nitrogen-doped Ti_3C_2/TiO_2; (h) calculated charge difference of nitrogen-doped Ti_3C_2/TiO_2; (i) recycle stability test of nitrogen-doped Ti_3C_2/TiO_2 in the MB degradation under UV light irradiation.[328] Reproduced from [52,328] with permission from Elsevier and American Chemical Society.

doping.[308] Besides exceptional fluorescence properties, MXene QDs exhibit low toxicity and maintain robust performance over a broad pH range, storage conditions and length of time. These properties make them optimal candidates for chemical and biological sensors. Doped MXene QDs have also been applied for ion sensing through fluorescence quenching and was found to be selective for either Cu^{2+} [118,308,309] or Fe^{3+} [306,319]. These and other MXene QDs applications in chemical and biological sensors are described in a next section. MXene QDs were applied also for bio-imaging, as detailed in section "Biomedical applications".

Another important application that is possible only by doping the MXenes, is in white light-emitting diodes (LEDs) [307] and white lasers. [320] In the first work (LED) in this field, Ti_3C_2 MXenes were doped with either sodium thiosulfate and ammonia or a combination of, to realise three types of QDs, i.e. S-doped, N-doped, and S/N co-doped. Interestingly, these QDs had a blue, yellow and orange fluorescence only when dispersed in an aqueous solution (Fig. 22(d)), whilst their photoluminescence emissions in the solid state were similar. In an aqueous solution hydrogen bonding between the respective doped-QDs created agglomerations of different sizes leading to the differences in peak photoluminescence emission. The white LED constructed from these QDs operated under 365 nm irradiation and a voltage of 3.0 V with a good stability over 30 days. More recently, machine learning was used to guide the production and optimisation of a white LED based on N-V_4C_3 MXenes.[321] The MXene QDs exhibit excellent blue, yellow and red fluorescence and machine learning was exploited to find their optimal combination in terms of LED colour coordinates. In another pioneering work, the photoluminescence of V_2C MXenes QDs was enhanced by N doping.[320] The resulting QDs emitted blue, green yellow and red light that was amplified and simultaneously lased to produce a white laser.

Interestingly, doped MXene QDs have been proven to be applicable in the field of mechanical sensing for measurement of forces and stresses.[319] For this purpose, doped MXene QDs have been loaded into a hydrogel whose volume changes when an external force compresses the hydrogel. As consequence, the volume concentration of the fluorescent quantum dots increases, causing the fluorescence emission intensity of the fluorescent hydrogel to increase. The intensity of the external force can be evinced from the variation in fluorescence intensity of the hydrogel.[319].

4.6. Environmental applications

Modified Ti_3C_2 MXenes have awakened tremendous attention because of their unique properties and as such are viewed as promising materials for the degradation of pollutants (e.g. by active electro-adsorption processes) and water splitting [20,325–327]. Some of the properties exhibited by modified MXenes include high elemental abundance in earth, prominent electrical conductivity, abundant surface functional groups, a unique layered microstructure and good optical properties [325]. To the best of our knowledge, despite the great potential for environmental applications, to date only two publications considered the use of doped MXenes in this field. Amiri et al. [52], proposed a facile and novel method (Fig. 23(a)) for preparing nitrogen-doped MXene sheets (N-$Ti_3C_2T_x$) which were highly porous, hindered restacking of MXene layers, possessed enhanced electrical conductivity, showed promising volumetric capacitance (514 Fcm^{-3}), and exhibited excellent electrochemical stability by maintaining 99.75% of the initial volumetric capacitance after 2000 cycles (Fig. 23 (b,c)). This enhanced electrochemical performance was attributed to expansion of the stacked N-$Ti_3C_2T_x$ layers during cycling by Na^+ ion intercalation from the electrolyte solution. Nitrogen doping into MXenes such as pyridinic nitrogen, improves the electrical conductivity by 10.1% in comparison with the bare MXene. N-$Ti_3C_2T_x$ was found to be the best performing high-potential electrode material (in terms of electro-adsorption rate and capacitance), hitherto fabricated, for capacitive deionization application in the desalination of seawater. In another publication, Ke Tao and colleagues [328] successfully prepared highly photocatalytic nitrogen-doped Ti_3C_2 via a facile in situ approach, which upon further calcination in O_2 atmosphere transformed in nitrogen-doped Ti_3C_2/TiO_2 nanohybrid (Fig. 23(d)). The electronic structures of the materials employed in the study are displayed in Fig. 23 (e-h). The optimized nitrogen doped Ti_3C_2/TiO_2 possessed a superb and stable photocatalytic performance in Methylene Blue (MB) degradation (Fig. 23 (i)).

Furthermore, Yan et al.[312] synthesized nitrogen doped MXene quantum dots for the detection of alizarin red (ARS), an anthraquinone compound that is commonly used as a dyeing agent for textiles. Nitrogen-doped were produced by a solvothermal method using Ti_3C_2 MXene as precursors and o-phenylenediamine (oPD) as the nitrogen source. The obtained N-MQDs were dispersed quasi-spherical nanoparticles, mainly composed of carbon, oxygen and nitrogen, with yellow fluorescence at 580 nm and quantum yield of 5.42 %. These QDs could detect ARS based on inner filter effect (IFE) with linear range and detection limit of 0–80 and 1.21 μM, respectively. Interestingly, ARS detection was possible also in real water samples, and these doped-MXenes QDs are expected to have further applications in the fields of environmental monitoring and biosensing.

More recently, Cao and co-workers successfully confined different metal ions of different valency's in a quasi-microcube shaped cobalt benzimidazole framework (CoZIF9) using space-confined synthesis. The presence of metal ions gave the material double-layer and pseudo capacitance properties, as well as creating new phases which accelerated Na^+ insertion/extraction, thus increased electrochemical adsorption. The study showed Ti-containing CoZIF9 materials to have an impeccable desalination capacity of 62.8 mg g^{-1} and an excellent cycling stability in capacitive deionization applications'. [329].

4.7. Sensors

Sensors play a pivotal role in our day-to-day lifestyle and are being used in a wide range of applications including wearable electronics [330,331] The sensing material used in the system influences the performance. Among other potential candidates, layered nanostructured materials with 2D structures possess superior properties as compared to their bulk counterparts. In this regard, undoubtedly, MXenes stand out as a promising 2D material and created new paradigms in the field of sensing applications owing to their distinctive merits and versatile properties. [332] Some of the highlighting features of MXenes concerning their applications in sensing include large surface area, spacious matrix for nanoparticles loading, intrinsic functional groups, metallic conductivity, rapid transduction of signals, adequate sites for biomolecule binding, etc. [333] MXenes can be widely used as sensing materials in a range of applications including gas sensors [334–338], force sensors [339–342], humidity sensors [343–346], strain/stress sensors [347], electrochemical biosensors [348–353], and optical sensors [332,354–358] and piezoresistive sensors [359,360] (Table 7). The compressive sensors based on MXenes can detect a broad range of compressions with a high Gauge Factor (GF ~ 180.1) and exhibit

Table 7
MXenes, MXene composites for sensor applications.

Sensing material/ Modified electrode	Probing strategy	Target/ Analyte	LOD/ Sensitivity	Detection limit	Reference
$Ti_3C_2T_x$	Electrochemical	H_2O_2	$0.7*10^{-9}$ m/79.27 μA μM^{-1}	$0.5*10^{-9}$ m	[364]
$Ti_3C_2T_x$	Calorimetric	Ag ions	$0.61*10^{-6}$ m/ 0.402 μAM^{-1}	$50*10^{-6}$ m	[365]
$Ti_3C_2T_x$	Capacitive	Humidity	NA/1003 pF/RH%	11 to 97 RH%	[366]
$Ti_3C_2T_x$	Electro-chemiluminescent	Exosomes	125 particles μL^{-1} /91.1461/ log (particles μL^{-1}	500–5 000 000 particles μL^{-1}	[367]
$Ti_3C_2T_x$	Electrochemical	PbCdZn	0.2 μgL^{-1}/0.98 μA (μg $L^{-1})^{-1}$ 0.4 μgL^{-1}/0.84 μA (μg $L^{-1})^{-1}$ 0.6 μgL^{-1}/0.60 μA (μg $L^{-1})^{-1}$	$0.0978*10^{-6}$ m $0.180*10^{-6}$ m $0.31*10^{-6}$ m	[368]
$Ti_3C_2T_x$	Electrochemical	Inosine monophosphate	0.224 ng mL^{-1}/ 4.54 μA μM^{-1} cm^{-2}	0.2–210 ng mL^{-1}	[369]
$Ti_3C_2T_x$	Electrochemical	Exosomes	37 particles μL^{-1} /2250.78/ log (particles μL^{-1}	110–11 000 000 particle μL^{-1}	. [370]
$Ti_3C_2T_x$	Electrochemical	BrO_3^-	$41*10^{-9}$ m/31.91 μA log $(M)^{-1}$	$5*10^{-6}$ *m*	[371]
$Ti_3C_2T_x$	Capacitive	Humidity	NA/ 280 pF/RH%	7 to 97 RH%	[346]
$V_4C_3T_x$	Chemiresistive	C_3H_6O	1 ppm/5%/ppm	200 ppm	[372]
$Ti_3C_2T_x$/Pt	Electrochemical	H_2O_2	$448*10^{-9}$ m/ 1.26 nA μM^{-1}	$5*10^{-3}$ m	[373]
$CsPbBr_3$–$Ti_3C_2T_x$	Photo-luminescent	Cd ions	$99*10^{-6}$ m/0.15% μM^{-1}	35×10^{-5} m	[374]
PANI/$Ti_3C_2T_x$	In-situ polymerisation	Ethanol	200 ppm (41.1%)	NA	[375]
$Ti_3C_2T_x$	Photo-luminescent	Uric acid	125×10^{-9} m/ 0.658 μM^{-1}	$1.2–75 \times 10^{-6}$ m	[376]
$Ti_3C_2T_x$	Photo-luminescent	Cu^{2+} ions	$2*10^{-6}$ m/60 μM^{-1}	5000×10^{-6} m	[377]
$Ti_3C_2T_x$/WSe_2	Chemiresistive	Ethanol	40	NA	[378]
V_2CT_x	Chemiresistive	CH_4	9.39 ppm/0.0167%/ppm	6–200 ppm	[334]
V_2CT_x	Chemiresistive	H_2	1.375 ppm/0.2435%/ppm	25–400 ppm	[334]
$W_{18}O_{49}$/$Ti_3C_2T_x$	Chemiresistive	C_3H_6O	170 ppb/ 0.58/ppm	0.17 to 500 ppm	[379]
$Ti_3C_2T_x$ /WSe_2	Chemiresistive	C_2H_5OH	1 ppm/ 0.231%/ppm	NA	[378]
$Ti_3C_2T_x$/Graphene	Chemiresistive	NH_3	10 ppm/ 0.135%/ppm	NA	[380]
$Ti_3C_2T_x$ /PEDOT:PSS	Chemiresistive	CH_3OH	NA/0.00331/ppm	NA	[381]
$Ti_3C_2T_x$	Chemiresistive	C_3H_6O	50 ppb/ 0.1%/ppm	0 to 100 ppm	[382]
MB-MXene/SPE	Electrochemical	Creatinine	1.2 μM/NA	10 to 400 μM	[383]
Nafion/Hb/TiO_2-Ti_3C_2/GCE	Electrochemical	H_2O_2	14 nM/NA	0.1 to 380 μm	[384]
Tyr/MXene/Chi/GCE	Electrochemical	Phenol	12 nM	0.05 to 15.5 μm	[385]
$Ti_3C_2T_x$ /Pt	Electrochemical	Ascorbic acid	0.25×10^{-6}/ 1.41 μA mM^{-1}	$0–750 \times 10^{-6}$ m	[373]
$Ti_3C_2T_x$	Electrochemical	Piroxicam	0.05×10^{-6} m/ 0.0272 μM^{-1}	$0.1–80 \times 10^{-6}$ m	[386]
$Ti_3C_2T_x$	Electrochemical	Paraoxon	6.36×10^{-12} m/23% /log (μg L^{-1})	$0.36–3634 \times 10^{-9}$ m	[387]
$Nb_4C_3T_x$/GCE	Electrochemical	Dopamine	29 nM	50 nM^{-1} μM	[371]
PEDOT-CH_2OH-MIP/MXene/ CNHs/GCE	Electrochemical	Adrenaline	0.3 nM/-	1 nm–60 μm	[388]
NS-Nb_2C/Nafion/GCE	Electrochemical	Dopamine	0.12 μM	0.4–90 μM	[389]
Sm_2O_3/2D TiC/GCE	Electrochemical	Nimodipine	4.2 nM/ 1.5 μA μM^{-1} cm^{-2}	0.001–950 μM	[390]
Ti_3C_2/PtNPs/GCE	Electrochemical	Dopamine	0.48 μM	5–180 μM	[391]
Fe-SACs/Ti_3C_2Tx/LSGE	Electrochemical	Dopamine	1.0 nM	10 nM–200 μM	[392]
SnO_2 QDs@Ti_3C_2/GCE	Electrochemical	Dopamine	2.0 nM	0.004 –8.0 μM	[393]
Ti_3C_2Tx/GCE	Electrochemical	Hydrogen sulfide	16.0 nM	100 nM–300 μM	[394]
Ti_3C_2Tx-rGO/GCE	Electrochemical	Serotonin	10 nM	0.025–147 μM	[395]
MoS_2@$Ti_3C_2T_x$	Electrochemical	Thyroxine	0.39 pg mL^{-1}	7.8 × 108 pg mL^{-1}	[396]
MOF@V_2CT_x/SPE	Electrochemical	Nitric oxide	NA	1–13 μM	[397]
MQDs@3DE	Electrochemical	Dopamine	0.003 μM	0.01–20 μM	[398]
Ti_3C_2Tx/CNTs/CuMOF/GCE	Electrochemical	Tyrosine	0.19 μM	0.53 μM–232.46 μM	[399]

excellent mechanical reversibility (over 4,000 times) and rapid response (<30 ms). In some recent studies, they used such sensors to observe and differentiate delicate human activities, such as swallowing, coughing, joint bending, and others. [359] However, only in the recent few years, doped MXenes are gaining momentum for their potential prospects in a broad range of sensing applications (energy, environmental, and health). This section describes the application of doped MXenes in sensors for metal ions [118,306,309], organic molecules [310,314,361], gases [60,362], radicals [314,315,317], biomolecules [311,363] and molecules important for biomedical applications [49,306,313,314] as highlighted in Table 7.

4.7.1. Chemical sensors

Feng *et al.* [309] presented a strategic synthetic procedure for the preparation of amine-assisted solvothermal route of N doped (in-situ) Ti_3C_2 MXene fluorescent quantum dots (QDs) (size: 6.2 nm and thickness: ~ 1 nm) toward selective and sensitive detection of various metal cations. Few layer MXenes were obtained through liquid exfoliation of pristine MXenes. As mentioned in section "Photonics", it was identified that N-doping reduces the particle size and distribution of QDs. Among the investigated cations, Cu^{2+} exhibited high sensitivity with a detection limit of 0.032×10^{-6}.[309] Xu *et al.* demonstrated that hydrothermally prepared N-doped Ti_3C_2 MXene QDs show high selectivity (Fenton reaction based mechanism) to Fe^{3+} ions with a detection limit of 100 mM. Ethylenediamine was used as a source of N.[306] In a similar way, highly fluorescent Ti_3C_2 MXene QDs were utilized for the detection of Cu^{2+} sensing by Guan *et al* [308] and Yan *et al.*[118]. In the latter, S and N co-doped Nb carbide MXene QDs (average size: 3.4 nm) were appropriately synthesized through the hydrothermal method with excellent photostability, high quantum yield (17.25%, 520 nm), and successfully evaluated for Cu^{2+} detection (2 mM/L).[118] In another study, a team of researchers developed a new type of electrochemical sensor comprising nitrogen-doped carbon-coated Ti_3C_2-MXene (Ti_3C_2@N-C) carbon heterostructure for selective and simultaneous detection of heavy metal ions (Cd and Pb) using square wave anode stripping voltammetry with low LOD (Pb^{2+} for 1.10 nM and Cd^{2+} for 2.55 nM) and remarkable high sensitivities (Pb^{2+} 0.05–2.00 μM and Cd^{2+} 0.1–4.00 μM) in water samples (seawater and tap water).[400] In addition, several possible interfering ions and molecules are also investigated. Several material/thin-film

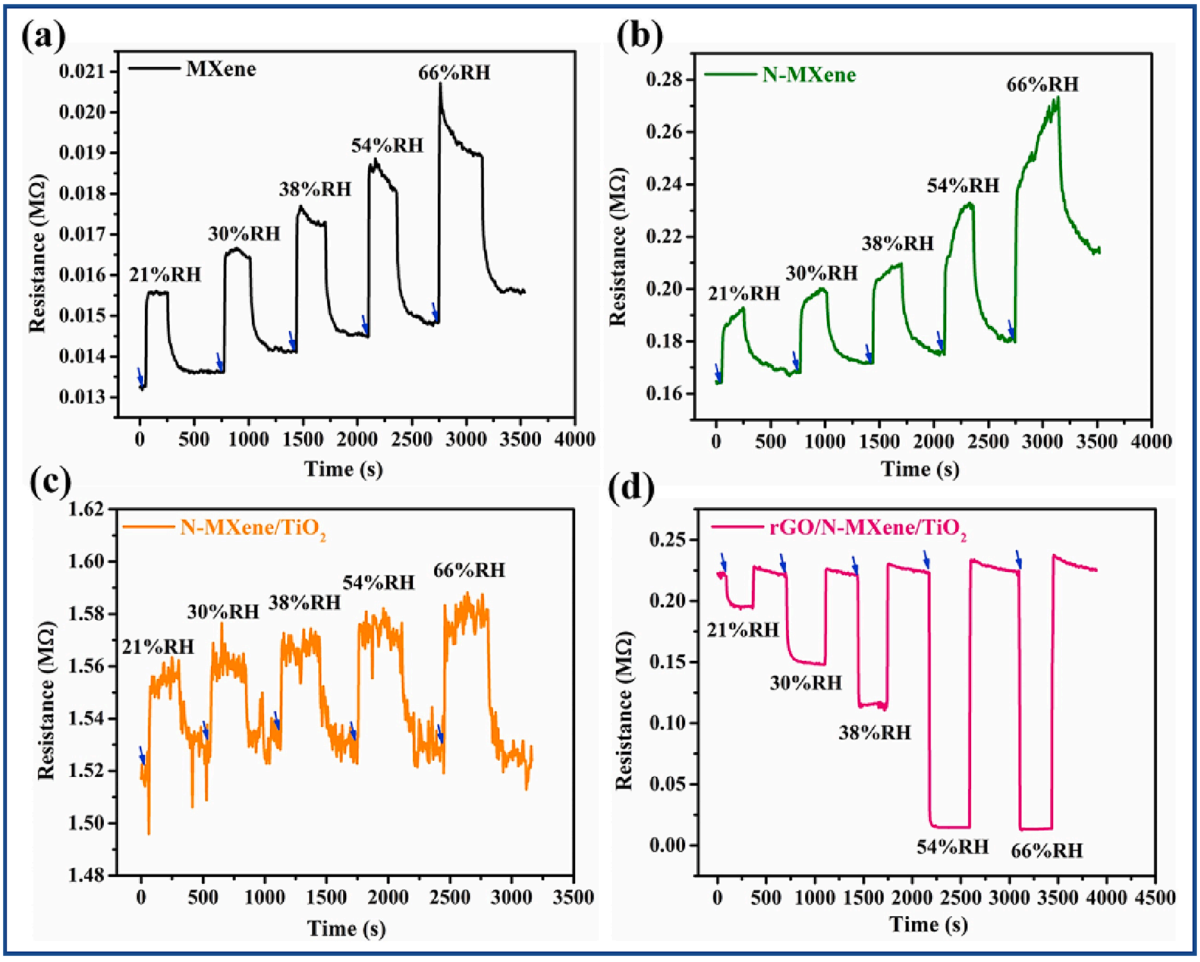

Fig. 24. The resistance transients for modulating RH conditions for studied sensing materials. (a) MXene, (b) N-MXene, (c) N-MXene/TiO_2, and (d) rGO/N-MXene/TiO_2 sensors at 20 °C. [401] Reproduced from [401] with permission from Elsevier.

characterization tools and adsorption experiments were employed to ascertain the various properties of the as-fabricated composites. The material system in the composite film synergistically contributes to the improved conductivity, rapid charge transfer and hence the detection capability.

Another valuable contribution makes use of the newly designed cost-effective molecularly imprinted (MIP) quartz crystal microbalance (QCM) sensor based on delaminated S doped MXene for chlorpyrifos (CHL) detection and compared the results with bare MXenes, wrinkled S doped MXenes, and others.[361] The as-developed MIP/d-S-$Ti_3C_2T_x$ MXene/QCM sensor possessed high conductivity and sensitivity with a limit of detection (LOD) of 3×10^{13} M and satisfy the key requirements of 3R's (repeatability, reusability, and reproducibility). The authors envisage that the developed sensor can find potential prospects in real-time therapeutic analysis.

Similarly, the composite film comprising of N-doped MXene/titanium dioxide incorporated reduced graphene oxide (rGO) ternary sensor (rGO/N-MXene/TiO_2) has been designed toward a ppm level (4 to 40 ppm) room temperature (20 °C) humidity activated ionic conduction for formaldehyde (HCHO) sensing under dynamic relative humidity (RH) conditions with high repeatability and long-term stability.[401] The resistance transients of as-fabricated ternary sensor performance (rGO/N-MXene/TiO_2) have been compared with their counterparts, single (MXene) and binary (N-MXene) and N-MXene/TiO_2 components (Fig. 24 (a-d)).[401] No noticeable response was recorded under dry conditions. Ternary sensor (rGO/N-MXene/TiO_2) displayed a mean response of 26% and 132% toward 4 and 20 ppm, respectively at 54% RH. The sensitivity, repeatability, and extended stability of the optimized condition were investigated. Besides, the authors propose an ionic conduction mechanism to ascertain and compare the analytical performance of the different sensing platforms.

Huang et al. found fluorescent nitrogen-doped Ti_3C_2 MXene quantum dots to be a unique "on–off-on" nanoprobe for chromium (VI) and ascorbic acid (AA). [310] Nitrogen doped Ti_3C_2 MXene QDs were synthesized by solvothermal method to cut Ti_3C_2 MXene nanosheets in the presence of N, N-dimethylformamide, and ammonium hydroxide. The resulting QDs exhibited their excellent blue photoluminescence at 440 nm and outstanding stability. The fluorescence of N-Ti_3C_2 MXene QDs was strongly inhibited by Cr(VI) resulting from the inner filter effect (IFE) and static quenching in the absence of AA; while the signal can be greatly restored upon the addition of AA since the redox between Cr(VI) and AA makes the effect from IFE to be weakened. The limits of detection (LOD) for Cr

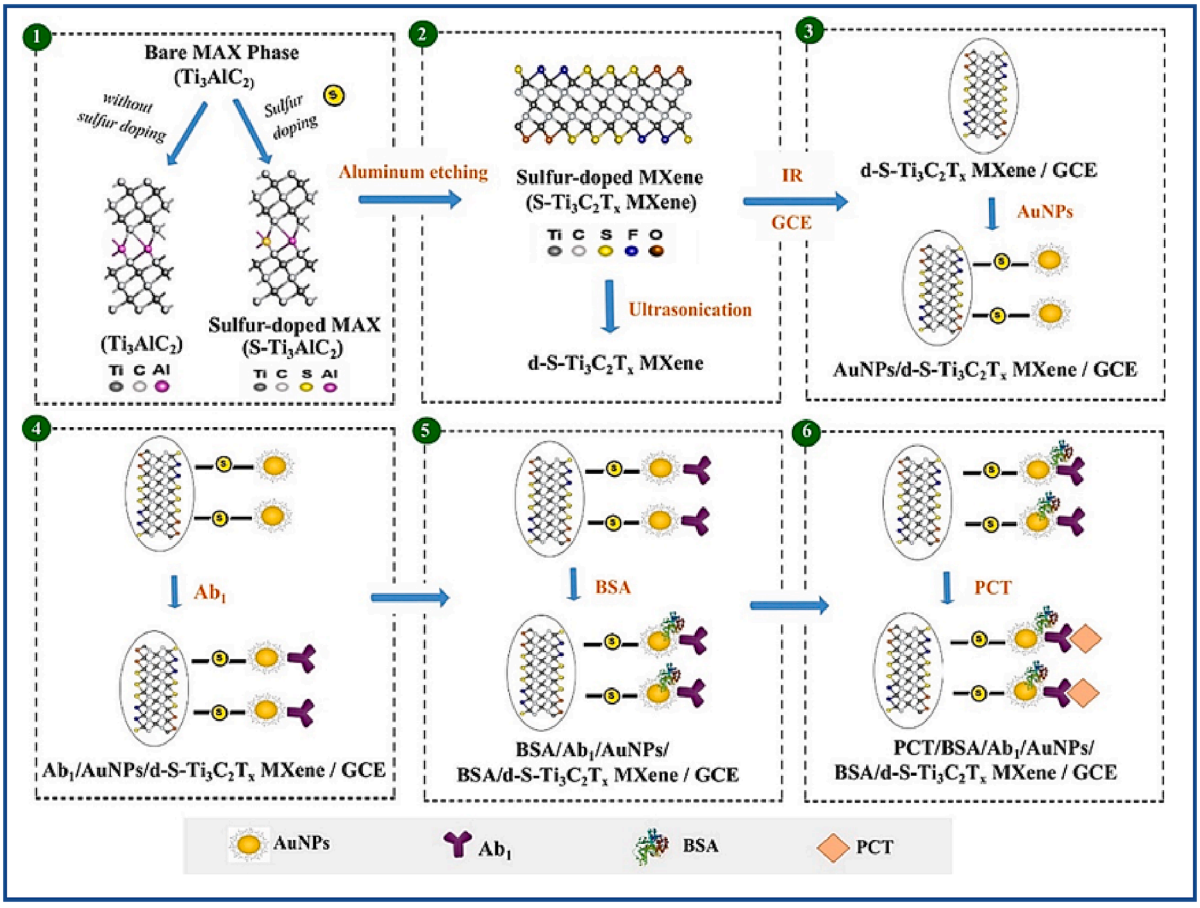

Fig. 25. The steps involved in the preparation route of PCT/BSA/Ab1/AuNPs/d-S-$Ti_3C_2T_x$ MXene/GCE. (AuNPs, Ab1, BSA, and PCT denote gold NPs, primary antibodies, bovine serum albumin, and procalcitonin, respectively). Reproduced from [363] with permission from Elsevier.

(VI) and AA are as low as 12 and 20 nM, respectively.

In an interesting study by Yong Zhou *et al.*, a humidity-induced CO_2 novel chemo-resistive sensing system was designed (for low concentration detection, ppm-level under controlled relative humidity (62%) at room temperature (20 °C) through employing ternary nanocomposite films comprising nitrogen (source: urea) (N) doped $Ti_3C_2T_x$ (N-MXene)/polyethyleneimine (PEI) embedded with reduced graphene oxide (rGO) nanosheets (rGO/N-MXene/PEI) and further evaluated the sensing performance.[362] In a similar way, Shuvo *et al.* investigated various VOC using sulfur (S) (source: thiourea) doped titanium carbide MXenes which are of high relevance for environmental remediation.[60] Exfoliation method was used to prepare MXenes and introduced in the conductometric gas sensor. The as-prepared materials were appropriately synthesized, characterized, and evaluated as electrode materials for a range of VOCs (toluene, hexane, ethanol, etc.). Doping S dramatically increased the interlayer spacing of the nanoflakes leading to enhanced electrical conductivity. It was found that the as-prepared S-doped counterparts showed high sensitivity (500 ppb which is 34 times higher) towards toluene than their undoped variants with remarkable stability. The authors envisage that the as-developed method can be extended potentially for its use in flexible (wearable) sensors.

Doped MXenes QDs exhibit outstanding radical scavenging properties.[314,317] Zhao et al.[317] produced chlorine and nitrogen co-doped MXene QDs by a potential static method in a two-electrode system. N and Cl were successfully introduced to carbon skeleton and Ti boundaries in the etching process by electrochemical reactions between selected electrolytes and Ti_3C_2 skeleton, respectively. The obtained Cl, N-Ti_3C_2 MQDs show a large surface-to-volume ratio due to small particle size (ca. 3.45 nm) and excellent scavenging activity towards •OH (93.3%) based on both dye protection and fluorescence tests. The underlying mechanism of scavenging activity was also studied based on the reduction experiment with potassium permanganate ($KMnO_4$). The reducing ability of the intrinsic Ti_3C_2 structure and electron donation of double dopants are the main contributors to the outstanding scavenging activity.

In another work, Wang *et al.* examined the mechanism of N-Doped Ti_3C_2 QDs for free-radical scavenging. [314] The authors fabricated the doped MXene QDs by hydrothermal method using ammonium hydroxide as a nitrogen source. The doped nitrogen atoms promote the electrochemical interaction between N-Ti_3C_2 QDs and free radicals and thus enhance their antioxidant performance. Density functional theory (DFT) simulations revealed the hydroxyl radical quenching process and confirmed that the doped N element promotes the free-radical absorption ability, especially for –F and –O functional groups in N-Ti_3C_2 QDs [314]. N-Ti_3C_2 QDs have been found to possess high scavenging activity toward •OH radicals also by Gou et al., with a scavenging ratio of 97.44%.[315].

4.7.2. Biosensors

What makes 2D MXenes quite fascinating biosensors compared to traditional nanoparticle-based biosensors is that MXenes have excellent conductivity and a high surface-to-volume ratio providing a high density of active surface sites for immobilization of the sensing target.[402] Also, due to its layered structure, MXenes demonstrated promising light absorption capability in terms of the maximum reflection loss and absorber thickness.[403] To the best of our knowledge, so far only a few publications explored the use of doped MXenes to detect molecules important for bio-sensing applications. [49,306,311,313,314].

In an exciting work, an electrochemical immunosensor for stable and ultra-sensitive quantification of procalcitonin (also known as PCT, an important biomarker of septicemia) was fabricated.[363] A self-assembly approach was utilized to fabricate thin films on glassy carbon electrode (GCE) modified with gold nanoparticles functionalized S-doped MXene as sensing medium and carboxylated graphitic carbon nitride (g-CN) as a signal amplification for PCT (Fig. 25). S-doped MXene was prepared by mixing a 1:3 mass ratio of Ti_3AlC_2 powder and elemental sulfur and sintered at 170 °C (3 h) and subsequently milled.[363] The morphology, microstructure, and analytical performance have been appropriately characterized using relevant instrumentations. The as-prepared immunosensor exhibited excellent stability, repeatability, reproducibility, and reusability with linear range and LOD of 0.01 to 1.0 pg/mL and 2 fg/mL, respectively. [363].

As mentioned in the section "Photonics", doped MXenes QDs represent ideal candidates for biosensing applications. So far, N-doped MXene QDs have been proven to detect H_2O_2 in the presence of Fe^{2+} by fluorescence quenching [306] or H_2O_2 and Xanthine through a dual-emission reverse change ratiometric sensor [313]. Furthermore, N-Ti_3C_2 QDs showed rapid, accurate, and remarkable sensitivity to hydrogen peroxide in the range of 5 nM–5.5 μM with a limit of detection of 1.2 nM within 15s, which is the lowest detection limit of the existing fluorescent probes up to now. [314] Similarly, Lu *et al.* assembled a dual-emission ratiometric photoluminescence sensor based on N-doped Ti_3C_2 QDs (donor) and 2,3-diaminophenazine (acceptor) toward the sensitive detection of H_2O_2 and xanthine. [313] More specifically, MXenes can facilitate photogenerated charge carriers (electrons and holes) due to enhanced light absorption and provide ultrafast electron transfer due to the aforementioned features. [404] Till now, many photoactive materials that can serve as a sensing platform have been systematically designed and developed including metal oxides [405–407], semiconductors [408–411], etc. In this regard, MXenes (Ti_3C_2) are the most widely studied 2D layered photoactive material in photoelectrochemical (PEC) sensing due to their desirable beneficial properties that include excellent electronic conductivity, electron transport capability having ample hydrophilic functionalities.[412–416] In addition to high photoluminescence quantum yield, MXenes QDs can show high electrochemiluminescence (ECL) quantum efficiency.[311] This property has been exploited for the detection of mucin 1 (MUC1), a protein that is closely associated with the development of malignancy. Jiang et al. obtained N-doped MXene QDs by a simple hydrothermal method using Ti_3C_2 as the precursor and ethylenediamine as the nitrogen source. [311] The doped MXene QDs not only exhibited ECL characteristics but also possessed higher ECL quantum efficiency than Ti_3C_2 QDs. The ECL quantum efficiency of doped QDs relative to undoped QDs was 1.58. Furthermore, the ECL signal of the immunosensor could be further enhanced using the co-reactant $S_2O_8^{2-}$. According to the authors, the prepared N-Ti_3C_2 QDs can promote the reduction of the co-reactant $S_2O_8^{2-}$ to generate abundant sulfate radicals causing the acceleration of the ECL reaction of N-Ti_3C_2 QDs. The ECL immunosensor based on the N-Ti_3C_2 QDs/ $S_2O_8^{2-}$- system can achieve sensitive MUC1 detection with a low detection limit of 0.31 fg/mL. Another composite found to be an efficient ECL sensing system was ZnO quantum dots/N-doped Ti_3C_2 MXene.[49] In this case, the Ti_3C_2 MXene matrix acted an important role to confine the

nucleation and growth of ZnO QDs, thus resulting in the well-dispersed ZnO QDs of 2 ~ 5 nm on the surface of MXene. The N doping of Ti_3C_2 MXene was realized due to the *in-situ* release of NOx and NH_3 from the decomposition of glycine-nitrate combustion. The N-doping level of Ti_3C_2 MXene in the composites could be simply tuned from 1.52 to 5.43 wt% by adjusting the amount of glycine. Electrochemical measurements demonstrated that the increasing doping contents in Ti_3C_2 MXene could boost the electrochemiluminescence (ECL) performance. The authors suggest that higher nitrogen contents were beneficial for accelerating electron transfer and decreasing the barrier of ZnO QDs reduction. By using the resultant ZnO/N-Ti_3C_2 nanocomposites, a novel ECL sensor was constructed for sensitive and selective detection of chloramphenicol, an antibiotic mainly used to treat eye infections and sometimes ear infections. This sensor displayed a wide linear range (0.1 ~ 100 ng/mL), a low detection limit (0.019 ng/mL) and high stability.Bai *et al.* produced nitrogen, phosphorus-doped Ti_3C_2 MQDs (N, P- Ti_3C_2 MQDs) through a facile microwave-assisted method. [65] The as-prepared N, P- Ti_3C_2 MQDs exhibited excitation-dependent photoluminescence, anti-photobleaching, and favorable dispersibility. The green fluorescence of N, P-Ti_3C_2 MQDs was found to be quenched by 1,10-phenanthroline-Fe (II) complex (Phen-Fe^{2+}) via inner filter effect (IFE), accompanied by the increased orange colour. After introduction of nitrite (NO^{2-}), owing to the redox reaction between NO^{2-} and Fe^{2+}, the fluorescence is recovered, and the colour varies from orange to colourless gradually. Therefore, a colorimetric/fluorometric dual-modal recognition of NO^{2-} was fabricated based on N, P-Ti_3C_2 MQDs and Phen-Fe^{2+} complex. Nitrite is a substance widely used in food industry as food preservative and fertilizer which might become a serious threat to the public health if present in high levels. The authors developed a novel dual-channel method for real-time visual assay of $NO^{2-}$with the use of a smartphone and paper-based test strips made by dropping a solution of N, P-Ti_3C_2 MQDs and Phen onto filter strips. [65] On close perusal of the literature on properly doped MXenes for electrochemical biosensing applications, the research is in its early stage and requires more intensive and extensive research strategies for the construction of these types of efficient sensing platforms by exploiting their inherent intriguing material properties to further take forward the research in this thriving field.

4.8. Biomedical applications

Given the favourable physiochemical properties and unique structure of 2D MXenes, extensive multidisciplinary research has been focused on their potential biomedical applications. So far, in this review, we have discussed syntheses, properties and applications of doped MXene systems. In this section, we describe the biomedical applications of pristine and doped 2D MXenes focusing on the antimicrobial activity, diagnostic imaging, therapeutic modalities, and biosafety evaluation with its recent developments, followed by a review of the current and future prospects of biocompatibility of doped MXenes.

4.8.1. Antimicrobial activity

MXenes exhibit important antimicrobial activity against both Gram-negative and Gram-positive bacterial strains. For example, 2D $Ti_3C_2T_x$ MXenes (the most studied MXenes) revealed significant antimicrobial properties through direct contact with the bacterial cell wall, releasing lactate dehydrogenase causing cellular damage to the bacteria and eventual death.[417] $Ti_3C_2T_x$ species showed greater growth inhibition (99%) compared with graphene oxide (GO, 90%) displaying more effective and higher antimicrobial efficiency against both Gram-negative *E. coli* and Gram-positive *B. subtili*.[418] As a result of these studies, MXene was introduced as a new family of 2D antimicrobial nanomaterials in areas of health and environmental protection in 2016.

4.8.2. Bioimaging

Another rapid development in biomedical applications of MXenes which has attracted much attention focuses on various bio-imaging techniques, including photoacoustic imaging and luminescence imaging, to enhance the diagnostic imaging performance. [419] In contrast to most optical imaging techniques, photoacoustic imaging has the ability to overcome the penetration limits, allowing deeper tissues to be imaged based on its low tissue attenuation coefficient.[402].

Luminescent properties of MXene QDs such as high photostability, tuneable wavelength and great quantum yields, have

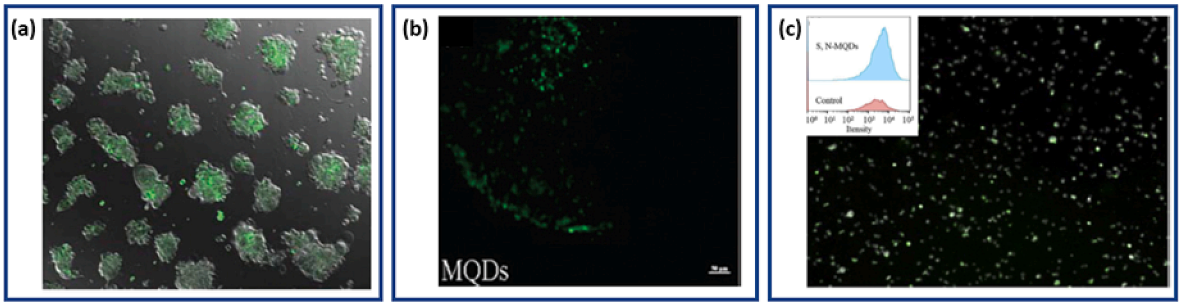

Fig. 26. Doped MXene quantum dots for bio-imaging. (a) Merged images of bright-field and confocal images (Ex = 488 nm) of the THP-1 monocytes incubated with N,P-MQDs.[308] (b) Counterstaining of 3D brain organoids by S,N doped Nb_2C MQDs.[318] (c) Caco-2 cells stained by S, N doped Nb_2C MQDs. Inset: The changes of S, N-MQDs intensity (top-blue) with respect to unstained control cells (bottom-pink).[118] Reproduced from [308,318,118] with permission from Royal Society of Chemistry and Elsevier. (For interpretation of the references to color in this figure legend, the reader is referred to the web version of this article.)

demonstrated desirable results for bioimaging due to small size and quantum confinement effect.[420] As mentioned in the section "Photonics", doping MXenes QDs enhances the photoluminescence quantum yield and reduces the lateral size with respect to pristine MXene QDs. Therefore, doping opens the door to the realization of more effective and more powerful bio-imaging systems. Guan *et al.* [308] produced N,P-Ti_3C_2 MQDs with highly fluorescent green emission and durable cell imaging potency at non-toxic concentrations (<25 mg mL^{-1}). Cellular uptake of the N,P-Ti_3C_2 MQDs by THP-1 macrophages occurred after 24 h exposure and these cells were imaged by bright-field and fluorescent confocal microscopy (Fig. 26(a)). Similarly, Xu et al.[318] stained 3D brain organoids with 5 mg mL^{-1} S,N- Nb_2C MQDs for 24 h to confer extensive green fluorescence for imaging under 488 nm excitation (Fig. 26(b)). Interestingly, S,N-Nb_2C MQDs effectively stained both the external and the internal layers of these cells, indicating that S,N-MQDs could effectively penetrate this multi-layered micro-tissue model. S,N-Nb_2C MQDs have been applied also for the fluorescent imaging of Caco-2 cells (Fig. 26 (c)). [118] Again, the doped MQDs were modest cytotoxic at low concentrations (<10 mg/mL) and capable of lasting cell imaging at nontoxic concentrations. Caco-2 cells exhibit a marked increase of green fluorescence after exposure to S,N-Nb_2C MQDs with respect to the low levels of auto-fluorescence in the control cells (inset in Fig. 26(c)).[118].

4.8.3. Therapeutic modalities

MXenes have also played a significant role in therapeutic modalities including photothermal effect for cell killing, cargo loading for synergistic therapy, and reactive oxygen species (ROS) generation for photodynamic cell killing. [421] The promising photothermal effect of MXenes is due to their wide ultraviolet (UV)/near-infrared (NIR) band, large specific surface area, and high photothermal conversion efficiency compared to conventional photothermal agents.[422] One of the two dimensional materials from the MXenes family which has demonstrated desirable photothermal properties and enzyme responsive biodegradability is 2D Nb_2C nanosheets. These nanosheets combined with microneedles (MNs) can be used as photothermal therapeutic agents achieving minimal invasion, responsive biodegradability towards tumour models and reducing toxicity.[423].

4.8.4. Biosafety

One of the main issues with clinical applications of nanomaterials is biosafety and long-term cytotoxicity. Numerous studies revealed that 2D MXenes have great potential for biomedical applications due to their excellent biocompatibility and low cytotoxicity toward cells. [420] Different biosafety studies on MXene based materials were completed including Ti_3C_2, Ta_4C_3, Nb_2C, MoC_2, V_2C and TiN, [424] which demonstrated insignificant cytotoxicity and reasonable *in vivo* biocompatibility. However, these studies are at an early stage, and whilst a short-term *in vivo* biocompatibility of MXenes was broadly shown, more systematic in-depth investigations and assessments are needed to ensure the biosafety of MXene-based materials.

5. Summary and outlook

The attractive chemical, electronic, and morphological properties of MXenes have made them promising candidates for use in multiple applications. Compared to other 2D systems where catalytic activity is constrained to the edge sites, theoretical and experimental studies have determined that in addition these sites, the basal planes of MXenes also show activity.[121–123] Even though these properties endow bare/pristine MXenes with more active sites, their performance is still far from ideal in the various applications.[11,16,120] Furthermore, it is well known that through material innovation, nanoscale structural design and hybrid manufacturing methods, the properties of materials can be enhanced for optimum performance in several applications. Consequently, in this review, we present a detailed overview of the recent progress made with doped MXenes and their applications in electrocatalysis, energy storage, photovoltaic, electronic, photonics, environmental, sensor, and biomedical fields. The doping strategies employed during synthesis have been reviewed and explained. In addition, the characterization techniques employed to probe the morphology, elemental and phase composition, chemical structure and stability of coordination compounds, surface area to volume ratio, pore size distribution, and thermal stability of doped MXenes have been presented. We have taken a step further to elucidate structure–activity relations of single and multiple elemental doping, and single atom supported MXenes in the various applications, as well as highlight the possibility of integrating MXenes with other materials and engineered at the atomic scale to yield hybrid heterostructures with multifunctionalities. Additionally, theoretical studies that explain the microstructure of doped MXenes, and the underlying doping mechanism have been highlighted.

Doping of MXenes with non-metals [44 101] and transition metals, [129,131] formation of single-atom immobilized MXene [95 135] and the combination of elemental doping with single atom immobilized systems [97] have been shown to be effective approaches to produce MXenes with superior catalytic properties compared with their pristine counterparts. In the various applications presented in this review, doped MXenes possessed superior properties and demonstrated enhanced activity, selectivity, and durability than pristine MXene and in some cases than commercially available catalysts. For instance in electrocatalytic applications, doping yielded MXenes with optimized electronic structures, increased metallic and conductive characteristics, increased number of catalytic sites, significantly reduced precious metal loadings, increased the stability of metals, lowered the Fermi level, weaken surface O–H bonds, suitably tuned the Gibbs free energies of hydrogen adsorption (ΔG_H^*), accelerated charge transfer during electrochemical reaction, improved the wettability, inhibited competitive reactions, and significantly reduced onset potentials for HER, OER, ORR, NRR and CO_2RR processes. [44 101 131 129 132–134 95 135 97,139144 145] For energy-related applications doping resulted in improved material conductivity, increased interlayer spacing in Li-ion Batteries; [217] facilitated sodiation-desodiation, excellent reversibility and high specific capacity for sodium battery systems; [228,425–428] retarded polysulfide formation, enhanced cycling stability, and improved specific capacity (up to 10 times greater than conventional metal oxide-based cathodes in Li-ion batteries) in Alkali metal sulfur batteries; [237,241,243,429] enhanced redox activity, restricted polysulfides formation and improved cycling stability in Na-S

batteries.[239 430 244] The great potential of doped MXenes for electronics and photovoltaic applications has been predicted theoretically although experimental research is still embryonic and surely represents a promising field to investigate. For environmental applications, modifications resulted in increased surface area, narrowed of bandgap and lowered charge recombination rate. [325,327,431,432] In the field of photonics, doped MXene quantum dots (QDs) possessed smaller lateral sizes (2–6 nm), significantly enhanced photoluminescence quantum yield, increased QD lifetime, low toxicity, and maintained robust performance over a broad pH range. [118,306,308–311,313,317,318 65,306,308,318,319] The upper limit of photoluminescence quantum yield seems to have been reached and recent research trends are focused on exploiting these quantum dots in chemical/biological sensing and imaging rather than further optimisation and fundamental research. Finally, for sensor applications, reduced particle size and size-distribution, excellent (photo)stability, reproducibility, reusability, selectivity, high quantum yield, and high scavenging properties have been reported for doped MXene. [306 308 118 310] The superior catalytic performance of doped MXenes has undoubtedly been linked to their improved microstructural, electronic and morphological properties. Table 3, 5 and 6 highlights some of the established strategies to achieve doped MXene and their corresponding applications. These doping routes can be extended to newly discovered MXenes as well.

Even though the versatile chemistry of MXenes renders their properties tuneable for a variety of applications, there still exist some bottlenecks and opportunities for future research in doped MXenes.

- Whilst the literature suggests that the dopant atoms are the active sites, we must not lose sight of the rich surface chemistry of MXenes which offers a variety of reaction and adsorption pathways necessary for the desired reactions. It is therefore prudent to suggest that the various cascade reactions result from the synergistic effect of the individual components making up the structure of the doped MXenes. Furthermore, with innovations in catalyst designs such as bifunctional and trifunctional catalysts, it is evident that the success of doped MXene systems must depend heavily on computational studies carried out to simulate their dynamic behaviour during catalysis and to predict the reaction mechanisms and intermediate products. Projections from such studies will guide experimentalists to synthesize new doped MXenes structures with enhanced activity.
- Secondly, considering that the synthesis techniques employed during preparation greatly influence the properties of doped MXenes, the development of new synthesis methods that yield high-quality MXenes with large lateral dimensions and controlled surface terminations is necessary.
- Thirdly, most characterization techniques employed so far, have enabled the study of as-prepared, calcined, modified, and/or deactivated catalysts measured under conventional conditions (e.g., room temperature). The development of quantitative structure–activity relationships and the gathering of fundamental insight into short-term and long-term deactivation mechanisms of these catalysts would require the incorporation of *in-situ* and/or operando characterization techniques (like SECM, STEM, XANES, EXAFS, XAS). This will further enhance our understanding of interfacial dynamics at the microscopic levels, which is known in electrochemistry to dictate the charge transfer kinetics and overall reaction mechanisms.
- MXenes research is limited to few members of the MXenes family due to the lack of precursor materials. Some MXenes such as Sc_2C, Hf_2C and W_2C were predicted to possess good stability, however starting materials for their synthesis were not determined. As such, the synthesis of new MAX phase precursors will further expand the exploitation of new members of MXene family.
- Finally, machine learning has been employed recently as a tool to predict the properties (e.g., band gap), activity (e.g., cytotoxicity), and enabled the discovery of new MXene compounds. As such, we suggest the use of machine learning in future research related to doped MXenes.

In the perspective of future applications, the practical implementation of doped MXene based devices is still in its infancy. With the increased need for multifunctional solutions for greener energy, efficient energy storage, faster and more reliable electronic devices it is extremely important that superior properties of these materials be truly exploited. Here we highlight some of the technology solutions that this unique material can provide. Over the past decade, interest in MXenes has seen exponential growth, with over 11,358 publications (Web of Science 20th June 2023) since the initial publication by Naguib *et al.* in 2011.[14] Novel chemistries have been exploited in MXenes discovery, whether through varying structural changes, multiple M−site chemistries or by tailoring surface chemistry, to enhance their versatility and applicability. Doping offers unique advantages in tuning the interlayer structure and surface area of MXenes.

- increase in electrochemical stability and performance.
- significant reduction in charge transfer resistance.
- increase in electrode conductivity.
- decrease in electrode/electrolyte interfacial impedance.

5.1. Wearable sensors

MXenes emergence as an amazing class of 2D layered materials have been widely explored as conductive electrodes for printed electronics, including electronic and optoelectronic devices, sensors, and energy storage systems. Here, the critical factors impacting device performance are comprehensively interpreted from the viewpoint of contact engineering, thereby giving a deep understanding of surface microstructures, contact defects, and energy level matching as well as their interaction principles. In addition, doping of Mxene will offer rich combination of elements in the MXene family, the spin–orbit coupling (SOC) effect, and dipole effect arising from

the surface termination also contribute to tuning the engineering of MXene contact. As a result, the ideal metal/semiconductor interface assembled with versatile printing techniques has allowed the development of MXene ink for applications in many technologies. One such game changing technology is wearable sensors, particularly non-invasive biosensing technologies with internet of things are of substantial interest for constant monitoring of substances in bodily fluids, for human health applications. For example, development of a wearable device to noninvasively monitor uric acid (UA) levels in sweat. Mxenes doped with the metalloid, Boron, provides a noble-metal-free electrocatalysts for the design of the enzyme-free wearable sensors for UA in human sweat. The B atoms strengthen the UA molecule adsorption and enhance electron transfer from the UA molecule to the B-doped Mxene sheet. This approach holds promise for development of other enzyme-free electrocatalysts with dependable and steady performance for wearable electronics. Such research for biomedical monitoring of human health holds open numerous avenues for MXene development and its related composites for wearable devices and Internet of Things (IoT) applications.

5.2. Batteries and supercapacitors

Lithium batteries are currently the most important power sources for mobile devices today, including small electronic devices or larger electric vehicles, because of their superior energy storage capacity, prolonged cycling life expectancy, and more environmentally benign compared to other substitutes. Doped MXenes will offer high competition with former 2D materials owing to wider tuneable structural and chemical properties. One of the massive advantages of doping MXene with other elements is the creation of a diversity of tuneable surfaces as well as the bulk chemistry of MXenes to afford valuable and distinctive properties, which can prove useful across many of the components of energy storage devices. Judiciously doped MXenes can offer diverse functions in batteries and supercapacitors, including double-layer and redox-type ion storage, ion transfer regulation, steric hindrance, ion redistribution, electrocatalysts, electrodeposition substrates and so on. The accommodation of variable-sized ions between 2D layers of $M_{n+1}X_nT_x$ also makes MXenes suitable to use beyond lithium-ion batteries (LiBs) as well as LiBs, where the electrode materials are limited.

5.3. Doped MXene can be superconductor!!

MXenes – M being a transition metal element and X either carbon or nitrogen – exhibit very versatile electronic properties, stemming from the interplay of charge, orbital and spin degrees of freedom. Spin orbit coupling can lead to significant changes in the band structures of MXenes, especially if the transition metal element has a high atomic number, as shown in this article.

Mxene when doped with elements like Sc, Ti, V,Cr, Zr, Nb, Mo, Hf, Ta, W, will offer six types of superconducting MXenes: three carbides (Mo_2C, W_2C and Sc_2C) and three nitrides (Mo_2N, W_2N and Ta_2N. One of the key aspects of W_2N is the possibility to present a novel case of competing superconducting and charge density wave phases. Recently, in our search, we identified other interesting quantum states that coexist or compete with superconductivity – such as magnetism in Cr_2C – resulting from the rich interplay between charge, orbital, spin, and structural degrees of freedom in MXenes. If any type of MXene will be proven to be a room temperature superconductor upon doping, such a discovery may revolutionise across a wide band of technological areas from telecommunications to medical diagnostics.

Declaration of Competing Interest

The authors declare that they have no known competing financial interests or personal relationships that could have appeared to influence the work reported in this paper.

Data availability

No data was used for the research described in the article.

Acknowledgements

S.K. acknowledges Recycling Lithium-ion batteries for a sustainable technological and economic development (ReListed) DSTUKIERI-2018-19-008, Royal Society IES\R2\170272 Royal Academy of Engineering Newton Fund and European commission Smart innovative system for recycling wastewater project id: 958491 and creating closed loops in textile manufacturing industrial processes, Global challenges research fund on cleaning systems for solar cells. The authors gratefully acknowledge Camila Silva Ribeiro for her support in providing some graphical images for this paper. They would also like to acknowledge Dr Suela Kellici and Dr Uthman Alli for providing useful inputs, texts, and references in this work.

References

[1] Caldwell JD, Aharonovich I, Cassabois G, Edgar JH, Gil B, Basov DN. Photonics with hexagonal boron nitride. Nat Rev Mater 2019;4:552–67. https://doi.org/10.1038/s41578-019-0124-1.

[2] Akhtar M, Anderson G, Zhao R, Alruqi A, Mroczkowska JE, Sumanasekera G, et al. Recent advances in synthesis, properties, and applications of phosphorene. NPJ 2D Mater Appl 2017;1:5. https://doi.org/10.1038/s41699-017-0007-5.

[3] Manzeli S, Ovchinnikov D, Pasquier D, Yazyev OV, Kis A. 2D transition metal dichalcogenides. Nat Rev Mater 2017;2:17033. https://doi.org/10.1038/natrevmats.2017.33.

[4] Kalantar-zadeh K, Ou JZ, Daeneke T, Mitchell A, Sasaki T, Fuhrer MS. Two dimensional and layered transition metal oxides. Appl Mater Today 2016;5:73–89. https://doi.org/10.1016/j.apmt.2016.09.012.

[5] Oughaddou H, Enriquez H, Tchalala MR, Yildirim H, Mayne AJ, Bendounan A, et al. Silicene, a promising new 2D material. Prog Surf Sci 2015;90:46–83. https://doi.org/10.1016/j.progsurf.2014.12.003.

[6] Liu N, Bo G, Liu Y, Xu X, Du Y, Dou SX. Recent progress on germanene and functionalized germanene: preparation, characterizations, applications, and challenges. Small 2019;15:1805147. https://doi.org/10.1002/smll.201805147.

[7] Sahoo SK, Wei K. A perspective on recent advances in 2D stanene nanosheets. Adv Mater Interfaces 2019;6:1900752. https://doi.org/10.1002/admi.201900752.

[8] Naguib M, Mochalin VN, Barsoum MW, Gogotsi Y. 25th anniversary article: MXenes: a new family of two-dimensional materials. Adv Mater 2014;26:992–1005. https://doi.org/10.1002/adma.201304138.

[9] Naguib M, Mashtalir O, Carle J, Presser V, Lu J, Hultman L, et al. Two-dimensional transition metal carbides. ACS Nano 2012;6:1322–31. https://doi.org/10.1021/nn204153h.

[10] Anasori B, Lukatskaya MR, Gogotsi Y. 2D metal carbides and nitrides (MXenes) for energy storage. Nat Rev Mater 2017;2. https://doi.org/10.1038/natrevmats.2016.98.

[11] Pang J, Mendes RG, Bachmatiuk A, Zhao L, Ta HQ, Gemming T, et al. Applications of 2D MXenes in energy conversion and storage systems. Chem Soc Rev 2019;48:72–133. https://doi.org/10.1039/c8cs00324f.

[12] Liu A, Liang X, Ren X, Guan W, Gao M, Yang Y, et al. Recent progress in MXene-based materials: potential high-performance electrocatalysts. Adv Funct Mater 2020;2003437. https://doi.org/10.1002/adfm.202003437.

[13] Verger L, Natu V, Carey M, Barsoum MW. MXenes: an introduction of their synthesis, select properties, and applications. Trends Chem 2019;1:656–69. https://doi.org/10.1016/j.trechm.2019.04.006.

[14] Naguib M, Kurtoglu M, Presser V, Lu J, Niu J, Heon M, et al. Two-dimensional nanocrystals produced by exfoliation of Ti 3AlC 2. Adv Mater 2011;23:4248–53. https://doi.org/10.1002/adma.201102306.

[15] Gogotsi Y, Anasori B. The Rise of MXenes. ACS Nano 2019;13:8491–4. https://doi.org/10.1021/acsnano.9b06394.

[16] Nguyen TP, Tuan Nguyen DM, Tran DL, Le HK, Vo DVN, Lam SS, et al. MXenes: Applications in electrocatalytic, photocatalytic hydrogen evolution reaction and CO2 reduction. Mol Catal 2020;486:110850. https://doi.org/10.1016/j.mcat.2020.110850.

[17] Jeon M, Jun BM, Kim S, Jang M, Park CM, Snyder SA, et al. A review on MXene-based nanomaterials as adsorbents in aqueous solution. Chemosphere 2020;261:127781. https://doi.org/10.1016/j.chemosphere.2020.127781.

[18] Bu F, Zagho MM, Ibrahim Y, Ma B, Elzatahry A, Zhao D. Porous MXenes: synthesis, structures, and applications. Nano Today 2020;30:100803. https://doi.org/10.1016/j.nantod.2019.100803.

[19] Al-Hamadani YAJ, Jun BM, Yoon M, Taheri-Qazvini N, Snyder SA, Jang M, et al. Applications of MXene-based membranes in water purification: a review. Chemosphere 2020;254:126821. https://doi.org/10.1016/j.chemosphere.2020.126821.

[20] Damptey L, Jaato BN, Ribeiro CS, Varagnolo S, Power NP, Selvaraj V, et al. Surface functionalized MXenes for Wastewater treatment—a comprehensive review. Global Chall 2022;6:2100120. https://doi.org/10.1002/gch2.202100120.

[21] Mashtalir O, Cook KM, Mochalin VN, Crowe M, Barsoum MW, Gogotsi Y. Dye adsorption and decomposition on two-dimensional titanium carbide in aqueous media. J Mater Chem A 2014;2:14334–8. https://doi.org/10.1039/C4TA02638A.

[22] Zhang CJ, Pinilla S, McEvoy N, Cullen CP, Anasori B, Long E, et al. Oxidation stability of colloidal two-dimensional titanium carbides (MXenes). Chem Mater 2017;29:4848–56. https://doi.org/10.1021/acs.chemmater.7b00745.

[23] Wu Z, Shang T, Deng Y, Tao Y, Yang Q. The assembly of MXenes from 2D to 3D. Adv Sci 2020;7:1903077. https://doi.org/10.1002/advs.201903077.

[24] Szuplewska A, Kulpińska D, Jakubczak M, Dybko A, Chudy M, Olszyna A, et al. The 10th anniversary of MXenes: challenges and prospects for their surface modification toward future biotechnological applications. Adv Drug Deliv Rev 2022;182:114099. https://doi.org/10.1016/j.addr.2021.114099.

[25] Wang H, Maiyalagan T, Wang X. Review on recent progress in nitrogen-doped graphene: synthesis, characterization, and its potential applications. ACS Catal 2012;2:781–94. https://doi.org/10.1021/cs200652y.

[26] Dey A, Chroneos A, Braithwaite NStJ, Gandhiraman RP, Krishnamurthy S. Plasma engineering of graphene. Appl Phys Rev 2016;3:021301. https://doi.org/10.1063/1.4947188.

[27] Wang X, Sun G, Routh P, Kim DH, Huang W, Chen P. Heteroatom-doped graphene materials: syntheses, properties and applications. Chem Soc Rev 2014;43:7067–98. https://doi.org/10.1039/c4cs00141a.

[28] Wang Y, Mao J, Meng X, Yu L, Deng D, Bao X. Catalysis with two-dimensional materials confining single atoms: concept, design, and applications. Chem Rev 2018. https://doi.org/10.1021/acs.chemrev.8b00501.

[29] Fu Z, Wang N, Legut D, Si C, Zhang Q, Du S, et al. Rational design of flexible two-dimensional MXenes with multiple functionalities. Chem Rev 2019;119:11980–2031. https://doi.org/10.1021/acs.chemrev.9b00348.

[30] Zhu J, Ha E, Zhao G, Zhou Y, Huang D, Yue G, et al. Recent advance in MXenes: a promising 2D material for catalysis, sensor and chemical adsorption. Coord Chem Rev 2017;352:306–27. https://doi.org/10.1016/j.ccr.2017.09.012.

[31] Gao Q, Zhang W, Shi Z, Yang L, Tang Y. Structural design and electronic modulation of transition-metal-carbide electrocatalysts toward efficient hydrogen evolution. Adv Mater 2019;31:1802880. https://doi.org/10.1002/adma.201802880.

[32] Peng J, Chen X, Ong WJ, Zhao X, Li N. Surface and heterointerface engineering of 2D MXenes and their nanocomposites: insights into electro- and photocatalysis. Chem 2019;5:18–50. https://doi.org/10.1016/j.chempr.2018.08.037.

[33] Wang H, Lee JM. Recent advances in structural engineering of MXene electrocatalysts. J Mater Chem A Mater 2020;8:10604–24. https://doi.org/10.1039/d0ta03271a.

[34] Gao L, Bao W, Kuklin AV, Mei S, Zhang H, Ågren H. Hetero-MXenes: theory, synthesis, and emerging applications. Adv Mater 2021;2004129:1–43. https://doi.org/10.1002/adma.202004129.

[35] Kim H, Anasori B, Gogotsi Y, Alshareef HN. Thermoelectric properties of two-dimensional molybdenum-based MXenes. Chem Mater 2017;29:6472–9. https://doi.org/10.1021/acs.chemmater.7b02056.

[36] Anasori B, Xie Y, Beidaghi M, Lu J, Hosler BC, Hultman L, et al. Two-dimensional, ordered, double transition metals carbides (MXenes). ACS Nano 2015;9:9507–16. https://doi.org/10.1021/acsnano.5b03591.

[37] Qu G, Zhou Y, Wu T, Zhao G, Li F, Kang Y, et al. Phosphorized MXene-phase molybdenum carbide as an earth-abundant hydrogen evolution electrocatalyst. ACS Appl Energy Mater 2018;1:7206–12. https://doi.org/10.1021/acsaem.8b01642.

[38] Khazaei M, Arai M, Sasaki T, Chung C-Y, Venkataramanan NS, Estili M, et al. Novel electronic and magnetic properties of two-dimensional transition metal carbides and nitrides. Adv Funct Mater 2013;23:2185–92. https://doi.org/10.1002/ADFM.201202502.

[39] Baragau I-A, Power NP, Morgan DJ, Heil T, Lobo RA, Roberts CS, et al. Continuous hydrothermal flow synthesis of blue-luminescent, excitation-independent nitrogen-doped carbon quantum dots as nanosensors. J Mater Chem A Mater 2020;8:3270–9. https://doi.org/10.1039/C9TA11781D.

[40] Chen Z, Chen Z, Higgins D. Nitrogen doped carbon nanotubes and their impact on the oxygen reduction reaction in fuel cells. Carbon N Y 2010;48:3057–65. https://doi.org/10.1016/J.CARBON.2010.04.038.

[41] Qasim M, Hou J, Qadeer MA, Butt S, Farooq MH, Farooq MQ, et al. Nitrogen-doped carbon nanosheets decorated with Mn2O3 nanoparticles for excellent oxygen reduction reaction. Front Chem 2019;7:741. https://doi.org/10.3389/FCHEM.2019.00741/BIBTEX.

[42] Zou Y, Kinloch IA, Dryfe RAW. Nitrogen-doped and crumpled graphene sheets with improved supercapacitance. J Mater Chem A Mater 2014;2:19495–9. https://doi.org/10.1039/C4TA04076G.

[43] Li Y, Chen M, Liu B, Zhang Y, Liang X, Xia X. Heteroatom doping: an effective way to boost sodium ion storage. Adv Energy Mater 2020;10:2000927. https://doi.org/10.1002/AENM.202000927.

[44] Le TA, Bui QV, Tran NQ, Cho Y, Hong Y, Kawazoe Y, et al. Synergistic effects of nitrogen doping on MXene for enhancement of hydrogen evolution reaction. ACS Sustain Chem Eng 2019;7:16879–88. https://doi.org/10.1021/acssuschemeng.9b04470.

[45] Cai L, Pan F, Zhu X, Dong Y, Shi Y, Xiang Z, et al. Etching engineering and electrostatic self-assembly of N-doped MXene/hollow Co-ZIF hybrids for high-performance microwave absorbers. Chem Eng J 2022;434. https://doi.org/10.1016/j.cej.2021.133865.

[46] Lu C, Yang L, Yan B, Sun L, Zhang P, Zhang W, et al. Nitrogen-doped Ti3C2 MXene: mechanism investigation and electrochemical analysis. Adv Funct Mater 2020;30:1–11. https://doi.org/10.1002/adfm.202000852.

[47] Tang Y, Zhu J, Wu W, Yang C, Lv W, Wang F. Synthesis of nitrogen-doped two-dimensional Ti 3 C 2 with enhanced electrochemical performance. J Electrochem Soc 2017;164:A923–9. https://doi.org/10.1149/2.0041706jes.

[48] Wen Y, Rufford TE, Chen X, Li N, Lyu M, Dai L, et al. Nitrogen-doped Ti3C2Tx MXene electrodes for high-performance supercapacitors. Nano Energy 2017;38:368–76. https://doi.org/10.1016/j.nanoen.2017.06.009.

[49] Jiang D, Wei M, Du X, Qin M, Shan X, Chen Z. One-pot synthesis of ZnO quantum dots/N-doped Ti3C2 MXene: tunable nitrogen-doping properties and efficient electrochemiluminescence sensing. Chem Eng J 2022;430:132771. https://doi.org/10.1016/J.CEJ.2021.132771.

[50] Bao W, Liu L, Wang C, Choi S, Wang D, Wang G. Facile synthesis of crumpled nitrogen-doped MXene nanosheets as a new sulfur host for lithium-sulfur batteries. Adv Energy Mater 2018;8. https://doi.org/10.1002/aenm.201702485.

[51] Liao SY, Cui SF, Li YZ, Cheng WX, Huang XW, Zhang J, et al. Wrinkled and flexible N-doped MXene additive for improving the mechanical and electrochemical properties of the nickel-rich LiNi0.8Co0.1Mn0.1O2 cathode. Electrochim Acta 2022:410. https://doi.org/10.1016/j.electacta.2022.139989.

[52] Amiri A, Chen Y, Bee Teng C, Naraghi M. Porous nitrogen-doped MXene-based electrodes for capacitive deionization. Energy Storage Mater 2020;25:731–9. https://doi.org/10.1016/j.ensm.2019.09.013.

[53] Yang F, Hegh D, Song D, Zhang J, Usman KAS, Liu C, et al. Synthesis of nitrogen-sulfur co-doped Ti3C2Tx MXene with enhanced electrochemical properties. Mater Reports: Energy 2022;2:100079. https://doi.org/10.1016/J.MATRE.2022.100079.

[54] Yu L, Fan Z, Shao Y, Tian Z, Sun J, Liu Z. Versatile N-doped MXene ink for printed electrochemical energy storage application. Adv Energy Mater 2019;9:1901839. https://doi.org/10.1002/AENM.201901839.

[55] Chen X, Zhai X, Hou J, Cao H, Yue X, Li M, et al. Tunable nitrogen-doped delaminated 2D MXene obtained by NH3/Ar plasma treatment as highly efficient hydrogen and oxygen evolution reaction electrocatalyst. Chem Eng J 2021;420:129832. https://doi.org/10.1016/J.CEJ.2021.129832.

[56] Alli U, McCarthy K, Baragau I-A, Power NP, Morgan DJ, Dunn S, et al. In-situ continuous hydrothermal synthesis of TiO2 nanoparticles on conductive N-doped MXene nanosheets for binder-free Li-ion battery anodes. Chem Eng J 2022;430:132976. https://doi.org/10.1016/j.cej.2021.132976.

[57] Han M, Yang J, Jiang J, Jing R, Ren S, Yan C. Efficient tuning the electronic structure of N-doped Ti-based MXene to enhance hydrogen evolution reaction. J Colloid Interface Sci 2021;582:1099–106. https://doi.org/10.1016/j.jcis.2020.09.001.

[58] Bao W, Shuck CE, Zhang W, Guo X, Gogotsi Y, Wang G. Boosting performance of Na-S batteries using sulfur-doped Ti3C2Tx MXene nanosheets with a strong affinity to sodium polysulfides. ACS Nano 2019;13:11500–9. https://doi.org/10.1021/acsnano.9b04977.

[59] An Y, Tian Y, Liu C, Xiong S, Feng J, Qian Y. Rational design of sulfur-doped three-dimensional Ti 3 C 2 T x MXene/ZnS heterostructure as multifunctional protective layer for dendrite-free zinc-ion batteries. ACS Nano 2021;15:15259–73. https://doi.org/10.1021/acsnano.1c05934.

[60] Shuvo SN, Ulloa Gomez AM, Mishra A, Chen WY, Dongare AM, Stanciu LA. Sulfur-doped titanium carbide MXenes for room-temperature gas sensing. ACS Sens 2020;5:2915–24. https://doi.org/10.1021/acssensors.0c01287.

[61] Li J, Yan D, Hou S, Li Y, Lu T, Yao Y, et al. Improved sodium-ion storage performance of Ti3C2TX MXenes by sulfur doping. J Mater Chem A Mater 2018;6:1234–43. https://doi.org/10.1039/c7ta08261d.

[62] Myagmarsereejid P, Bat-Erdene M, Bati ASR, Sainbileg B, Hayashi M, Shapter JG, et al. Sulfur-functionalized titanium carbide Ti3C2Tx(MXene) nanosheets modified light absorbers for ambient fabrication of Sb2S3 solar cells. ACS Appl Nano Mater 2022;5:12107–16. https://doi.org/10.1021/ACSANM.2C01520/ASSET/IMAGES/LARGE/AN2C01520_0007.JPEG.

[63] Wen Y, Li R, Liu J, Wei Z, Li S, Du L, et al. A temperature-dependent phosphorus doping on Ti3C2Tx MXene for enhanced supercapacitance. J Colloid Interface Sci 2021;604:239–47. https://doi.org/10.1016/j.jcis.2021.06.020.

[64] Gupta N, Sahu RK, Mishra T, Bhattacharya P. Microwave-assisted rapid synthesis of titanium phosphate free phosphorus doped Ti3C2 MXene with boosted pseudocapacitance. J Mater Chem A Mater 2022. https://doi.org/10.1039/D2TA04061A.

[65] Bai Y, He Y, Wang M, Song G. Microwave-assisted synthesis of nitrogen, phosphorus-doped Ti3C2 MXene quantum dots for colorimetric/fluorometric dual-modal nitrite assay with a portable smartphone platform. Sens Actuat B Chem 2022;357:131410. https://doi.org/10.1016/J.SNB.2022.131410.

[66] Xia Y, Zhao Y, Ai F, Yi Y, Liu T, Lin H, et al. N and P co-doped MXenes nanoribbons for electrodeposition-free stripping analysis of Cu(II) and Hg(II). J Hazard Mater 2022;425:127974. https://doi.org/10.1016/J.JHAZMAT.2021.127974.

[67] Chen D, Shao S, Zhang W, Zhao J, Lian M. Nitrogen and sulfur co-doping strategy to trigger the peroxidase-like and electrochemical activity of Ti3C2 nanosheets for sensitive uric acid detection. Anal Chim Acta 2022;1197:339520. https://doi.org/10.1016/J.ACA.2022.339520.

[68] Zhang Y, Li J, Gong Z, Xie J, Lu T, Pan L. Nitrogen and sulfur co-doped vanadium carbide MXene for highly reversible lithium-ion storage. J Colloid Interface Sci 2021;587:489–98. https://doi.org/10.1016/J.JCIS.2020.12.044.

[69] Lin W, Lu Y-R, Peng W, Luo M, Chan T-S, Tan Y. Atomic bridging modulation of Ir–N, S co-doped MXene for accelerating hydrogen evolution. J Mater Chem A Mater 2022;10:9878–85. https://doi.org/10.1039/d2ta00550f.

[70] Li M, Lu J, Luo K, Li Y, Chang K, Chen K, et al. Element replacement approach by reaction with lewis acidic molten salts to synthesize nanolaminated MAX phases and MXenes. J Am Chem Soc 2019;141:4730–7. https://doi.org/10.1021/JACS.9B00574/ASSET/IMAGES/MEDIUM/JA-2019-00574Q_M008.GIF.

[71] Li Y, Shao H, Lin Z, Lu J, Liu L, Duployer B, et al. A general Lewis acidic etching route for preparing MXenes with enhanced electrochemical performance in non-aqueous electrolyte. Nat Mater 2020 19:8 2020;19:894–9. https://doi.org/10.1038/s41563-020-0657-0.

[72] Kamysbayev V, Filatov AS, Hu H, Rui X, Lagunas F, Wang D, et al. Covalent surface modifications and superconductivity of two-dimensional metal carbide MXenes. Science 1979;2020(369):979–83. https://doi.org/10.1126/SCIENCE.ABA8311/SUPPL_FILE/ABA8311_KAMYSBAYEV_SM.PDF.

[73] Sarfraz B, Mehran MT, Baig MM, Naqvi SR, Khoja AH, Shahzad F. <scp>HF</scp> free greener <scp>Cl</scp> -terminated <scp>MXene</scp> as novel electrocatalyst for overall water splitting in alkaline media. Int J Energy Res 2022;46:10942–54. https://doi.org/10.1002/er.7895.

[74] Zhu L, Ji J, Yin H, Zhao H. Pseudocapacitance of Cl-terminated MXene nanosheets for efficient chloride-ion hybrid capacitors. Energy Fuel 2023;37:5607–12. https://doi.org/10.1021/acs.energyfuels.3c00248.

[75] Gong S, Zhao F, Xu H, Li M, Qi J, Wang H, et al. Iodine-functionalized titanium carbide MXene with ultra-stable pseudocapacitor performance. J Colloid Interface Sci 2022;615:643–9. https://doi.org/10.1016/J.JCIS.2022.02.013.

[76] Yu W, Ma S, He M, Li R, Yang H, Li Y, et al. Immobilization and kinetic acceleration of lithium polysulfides by iodine-doped mxene nanosheets in lithium-sulfur batteries. J Phys Chem C 2022;126:10986–94. https://doi.org/10.1021/ACS.JPCC.2C02689/ASSET/IMAGES/LARGE/JP2C02689_0006.JPEG.

[77] Persson I, Halim J, Hansen TW, Wagner JB, Darakchieva V, Palisaitis J, et al. How much oxygen can a MXene surface take before it breaks? Adv Funct Mater 2020;30:1909005. https://doi.org/10.1002/adfm.201909005.

[78] Tian Y, Ju M, Luo Y, Bin X, Lou X, Que W. In situ oxygen doped Ti3C2T MXene flexible film as supercapacitor electrode. Chem Eng J 2022;446:137451. https://doi.org/10.1016/j.cej.2022.137451.

[79] Zha X-H, Luo K, Li Q, Huang Q, He J, Wen X, et al. Role of the surface effect on the structural, electronic and mechanical properties of the carbide MXenes. EPL (Europhysics Letters) 2015;111:26007. https://doi.org/10.1209/0295-5075/111/26007.

[80] Jiang Y, Sun T, Xie X, Jiang W, Li J, Tian B, et al. Oxygen-functionalized ultrathin Ti 3 C 2 T x MXene for enhanced electrocatalytic hydrogen evolution. ChemSusChem 2019;12:1368–73. https://doi.org/10.1002/cssc.201803032.

[81] Khan SA, Amin B, Gan L-Y, Ahmad I. Strain engineering of electronic structures and photocatalytic responses of MXenes functionalized by oxygen. PCCP 2017;19:14738–44. https://doi.org/10.1039/C7CP02513K.

[82] Tan J, Wang Y, Wang Z, He X, Liu Y, Wang B, et al. Large out-of-plane piezoelectricity of oxygen functionalized MXenes for ultrathin piezoelectric cantilevers and diaphragms. Nano Energy 2019;65:104058. https://doi.org/10.1016/j.nanoen.2019.104058.

[83] Weng H, Ranjbar A, Liang Y, Song Z, Khazaei M, Yunoki S, et al. Large-gap two-dimensional topological insulator in oxygen functionalized MXene. Phys Rev B 2015;92:075436. https://doi.org/10.1103/PhysRevB.92.075436.

[84] Junkaew A, Arróyave R. Enhancement of the selectivity of MXenes (M_2C, M = Ti, V, Nb, Mo) *via* oxygen-functionalization: promising materials for gas-sensing and -separation. PCCP 2018;20:6073–82. https://doi.org/10.1039/C7CP08622A.

[85] Imani Yengejeh S, Kazemi SA, Wen W, Wang Y. Oxygen-terminated M4X3 MXenes with superior mechanical strength. Mech Mater 2021;160:103957. https://doi.org/10.1016/j.mechmat.2021.103957.

[86] Mishra A, Srivastava P, Carreras A, Tanaka I, Mizuseki H, Lee K-R, et al. Atomistic origin of phase stability in oxygen-functionalized MXene: a comparative study. J Phys Chem C 2017;121:18947–53. https://doi.org/10.1021/acs.jpcc.7b06162.

[87] Hou T, Luo Q, Li Q, Zu H, Cui P, Chen S, et al. Modulating oxygen coverage of Ti3C2Tx MXenes to boost catalytic activity for HCOOH dehydrogenation. Nat Commun 2020;11:4251. https://doi.org/10.1038/s41467-020-18091-7.

[88] Hart JL, Hantanasirisakul K, Gogotsi Y, Taheri ML. Termination-property coupling via reversible oxygen functionalization of MXenes. ACS Nanoscience Au 2022;2:433–9. https://doi.org/10.1021/acsnanoscienceau.2c00024.

[89] Peng W, Luo M, Xu X, Jiang K, Peng M, Chen D, et al. Spontaneous atomic ruthenium doping in Mo2CTX MXene defects enhances electrocatalytic activity for the nitrogen reduction reaction. Adv Energy Mater 2020;10:1–9. https://doi.org/10.1002/aenm.202001364.

[90] Peng W, Han J, Lu Y-R, Luo M, Chan T-S, Peng M, et al. A general strategy for engineering single-metal sites on 3D porous N, P Co-doped Ti 3 C 2 T X MXene. ACS Nano 2022;16:4116–25. https://doi.org/10.1021/acsnano.1c09841.

[91] Alnoor H, Elsukova A, Palisaitis J, Persson I, Tseng EN, Lu J, et al. Exploring MXenes and their MAX phase precursors by electron microscopy. Mater Today Adv 2021:9. https://doi.org/10.1016/j.mtadv.2020.100123.

[92] Yang C, Que W, Yin X, Tian Y, Yang Y, Que M. Improved capacitance of nitrogen-doped delaminated two-dimensional titanium carbide by urea-assisted synthesis. Electrochim Acta 2017;225:416–24. https://doi.org/10.1016/j.electacta.2016.12.173.

[93] Fan Z, Wei C, Yu L, Xia Z, Cai J, Tian Z, et al. 3D printing of porous nitrogen-doped Ti3C2 MXene Scaffolds for high-performance sodium-ion hybrid capacitors. ACS Nano 2020;14:867–76. https://doi.org/10.1021/acsnano.9b08030.

[94] Li Z, Cui Y, Wu Z, Milligan C, Zhou L, Mitchell G, et al. Reactive metal-support interactions at moderate temperature in two-dimensional niobium-carbide-supported platinum catalysts. Nat Catal 2018;1:349–55. https://doi.org/10.1038/s41929-018-0067-8.

[95] Zhang J, Zhao Y, Guo X, Chen C, Dong CL, Liu RS, et al. Single platinum atoms immobilized on an MXene as an efficient catalyst for the hydrogen evolution reaction. Nat Catal 2018;1:985–92. https://doi.org/10.1038/s41929-018-0195-1.

[96] Zhao D, Chen Z, Yang W, Liu S, Zhang X, Yu Y, et al. MXene (Ti 3 C 2) vacancy-confined single-atom catalyst for efficient functionalization of CO 2. J Am Chem Soc 2019;141:4086–93. https://doi.org/10.1021/jacs.8b13579.

[97] Ramalingam V, Varadhan P, Fu HC, Kim H, Zhang D, Chen S, et al. Heteroatom-mediated interactions between ruthenium single atoms and an MXene support for efficient hydrogen evolution. Adv Mater 2019;31:1903841. https://doi.org/10.1002/adma.201903841.

[98] Bunaciu AA, Udriştioiu E gabriela, Aboul-Enein HY. X-Ray Diffraction: Instrumentation and Applications. Crit Rev Anal Chem 2015;45:289–99. https://doi.org/10.1080/10408347.2014.949616.

[99] Zhang J, Usman KAS, Judicpa MAN, Hegh D, Lynch PA, Razal JM. Applications of X-ray-based characterization in MXene research. Small Methods 2023:: 2201527. https://doi.org/10.1002/smtd.202201527.

[100] Yoon Y, Tiwari AP, Choi M, Novak TG, Song W, Chang H, et al. Precious-metal-free electrocatalysts for activation of hydrogen evolution with nonmetallic electron donor: chemical composition controllable phosphorous doped vanadium carbide MXene. Adv Funct Mater 2019;29:1903443. https://doi.org/10.1002/adfm.201903443.

[101] Yoon Y, Tiwari AP, Lee M, Choi M, Song W, Im J, et al. Enhanced electrocatalytic activity by chemical nitridation of two-dimensional titanium carbide MXene for hydrogen evolution. J Mater Chem A Mater 2018;6:20869–77. https://doi.org/10.1039/C8TA08197B.

[102] Kuznetsov DA, Chen Z, Kumar PV, Tsoukalou A, Kierzkowska A, Abdala PM, et al. Single site cobalt substitution in 2D molybdenum carbide (MXene) enhances catalytic activity in the hydrogen evolution reaction. J Am Chem Soc 2019;141:17809–16. https://doi.org/10.1021/jacs.9b08897.

[103] Fatima M, Fatheema J, Monir NB, Siddique AH, Khan B, Islam A, et al. Nb-doped MXene with enhanced energy storage capacity and stability. Front Chem 2020;8:168. https://doi.org/10.3389/fchem.2020.00168.

[104] Rafiq S, Ahmad H, Rani M, Rizwan S. Structural and morphological analysis for cerium (Ce +3) doped intercalated 2D MXene. Https://DoiOrg/101117/122574353 2020;11561:8–17. https://doi.org/10.1117/12.2574353.

[105] Deng J, Zhang Q, Lv X, Zhang D, Xu H, Ma D, et al. Understanding photoelectrochemical water oxidation with X-ray absorption spectroscopy. ACS Energy Lett 2020;5:975–93. https://doi.org/10.1021/acsenergylett.9b02757.

[106] Heber M, Grünert W. Application of ultraviolet photoelectron spectroscopy in the surface characterization of polycrystalline oxide catalysts. 2. Depth variation of the reduction degree in the surface region of partially reduced V_2O 5. J Phys Chem B 2000;104:5288–97. https://doi.org/10.1021/jp994188o.

[107] García-Romeral N, Keyhanian M, Morales-García Á, Illas F. Relating X-ray photoelectron spectroscopy data to chemical bonding in MXenes. Nanoscale Adv 2021;3:2793–801. https://doi.org/10.1039/D0NA01033B.

[108] Näslund L-Å, Persson POÅ, Rosen J. X-ray Photoelectron spectroscopy of Ti_3AlC_2, Ti 3 C 2 *T* z, and TiC provides evidence for the electrostatic interaction between laminated layers in MAX-phase materials. J Phys Chem C 2020;124:27732–42. https://doi.org/10.1021/acs.jpcc.0c07413.

[109] Yuen ACY, Chen TBY, Lin B, Yang W, Kabir II, De Cachinho Cordeiro IM, et al. Study of structure morphology and layer thickness of Ti3C2 MXene with small-angle neutron scattering (SANS). Compos Part C: Open Access 2021;5:100155. https://doi.org/10.1016/j.jcomc.2021.100155.

[110] Chava VSN, Chandrasekhar PS, Gomez A, Echegoyen L, Sreenivasan ST. MXene-based tailoring of carrier dynamics, defect passivation, and interfacial band alignment for efficient planar p–i–n perovskite solar Cells. ACS Appl Energy Mater 2021;4:12137–48. https://doi.org/10.1021/acsaem.1c01669.

[111] Yu Z, Feng W, Lu W, Li B, Yao H, Zeng K, et al. MXenes with tunable work functions and their application as electron- and hole-transport materials in non-fullerene organic solar cells. J Mater Chem A Mater 2019;7:11160–9. https://doi.org/10.1039/c9ta01195a.

[112] Zhao S, Wen Y, Peng X, Mi Y, Liu X, Liu Y, et al. Isolated single-atom Pt sites for highly selective electrocatalytic hydrogenation of formaldehyde to methanol. J Mater Chem A Mater 2020;8:8913–9. https://doi.org/10.1039/d0ta00190b.

[113] Sarycheva A, Gogotsi Y. Raman spectroscopy analysis of the structure and surface chemistry of Ti3C2T xMXene. Chem Mater 2020;32:3480–8. https://doi.org/10.1021/acs.chemmater.0c00359.

[114] Wang C, Chen S, Song L. Tuning 2D MXenes by surface controlling and interlayer engineering: methods, properties, and synchrotron radiation characterizations. Adv Funct Mater 2020::2000869. https://doi.org/10.1002/adfm.202000869.

[115] Gao ZW, Zheng W, Lee LYS. Highly enhanced pseudocapacitive performance of vanadium-doped MXenes in neutral electrolytes. Small 2019;15:1–9. https://doi.org/10.1002/smll.201902649.

[116] Yang C, Tang Y, Tian Y, Luo Y, Faraz Ud Din M, Yin X, et al. Flexible Nitrogen-Doped 2D Titanium Carbides (MXene) Films Constructed by an Ex Situ Solvothermal Method with Extraordinary Volumetric Capacitance. Adv Energy Mater 2018;8:1802087. https://doi.org/10.1002/aenm.201802087.

[117] Tang Y, Yang C, Tian Y, Luo Y, Yin X, Que W. The effect of: in situ nitrogen doping on the oxygen evolution reaction of MXenes. Nanoscale Adv 2020;2: 1187–94. https://doi.org/10.1039/c9na00706g.

[118] Yan X, Ma J, Yu K, Li J, Yang L, Liu J, et al. Highly green fluorescent Nb2C MXene quantum dots for Cu2+ ion sensing and cell imaging. Chin Chem Lett 2020. https://doi.org/10.1016/j.cclet.2020.05.020.

[119] Bao W, Liu L, Wang C, Choi S, Wang D, Wang G. Facile synthesis of crumpled nitrogen-doped MXene nanosheets as a new sulfur host for lithium-sulfur batteries. Adv Energy Mater 2018:8. https://doi.org/10.1002/aenm.201702485.

[120] Wang Y, Nian Y, Biswas AN, Li W, Han Y, Chen JG. Challenges and opportunities in utilizing MXenes of carbides and nitrides as electrocatalysts. Adv Energy Mater 2020::2002967. https://doi.org/10.1002/aenm.202002967.

[121] Seh ZW, Fredrickson KD, Anasori B, Kibsgaard J, Strickler AL, Lukatskaya MR, et al. Two-Dimensional molybdenum carbide (MXene) as an efficient electrocatalyst for hydrogen evolution. ACS Energy Lett 2016;1:589–94. https://doi.org/10.1021/acsenergylett.6b00247.

[122] Pan H. Ultra-high electrochemical catalytic activity of MXenes. Sci Rep 2016;6:1–10. https://doi.org/10.1038/srep32531.
[123] Gao G, O'Mullane AP, Du A. 2D MXenes: a new family of promising catalysts for the hydrogen evolution reaction. ACS Catal 2017;7:494–500. https://doi.org/10.1021/acscatal.6b02754.
[124] Jia J, Xiong T, Zhao L, Wang F, Liu H, Hu R, et al. Ultrathin N-doped Mo2C nanosheets with exposed active sites as efficient electrocatalyst for hydrogen evolution reactions. ACS Nano 2017;11:12509–18. https://doi.org/10.1021/acsnano.7b06607.
[125] Ang H, Tan HT, Luo ZM, Zhang Y, Guo YY, Guo G, et al. Hydrophilic nitrogen and sulfur Co-doped molybdenum carbide nanosheets for electrochemical hydrogen evolution. Small 2015;11:6278–84. https://doi.org/10.1002/smll.201502106.
[126] Zhang C (John), Ma Y, Zhang X, Abdolhosseinzadeh S, Sheng H, Lan W, et al. Two-Dimensional Transition Metal Carbides and Nitrides (MXenes): Synthesis, Properties, and Electrochemical Energy Storage Applications. Energy & Environmental Materials 2020;3:29–55. https://doi.org/10.1002/eem2.12058.
[127] Ding B, Ong WJ, Jiang J, Chen X, Li N. Uncovering the electrochemical mechanisms for hydrogen evolution reaction of heteroatom doped M2C MXene (M = Ti, Mo). Appl Surf Sci 2020;500:143987. https://doi.org/10.1016/j.apsusc.2019.143987.
[128] Nam H, Sim ES, Je M, Choi H, Chung YC. Theoretical approach toward optimum anion-doping on mxene catalysts for hydrogen evolution reaction: an ab initio thermodynamics study. ACS Appl Mater Interfaces 2021;13:37035–43. https://doi.org/10.1021/acsami.1c07476.
[129] Ling C, Shi L, Ouyang Y, Chen Q, Wang J. Transition metal-promoted V2CO2 (MXenes): a new and highly active catalyst for hydrogen evolution reaction. Adv Sci 2016;3:1600180. https://doi.org/10.1002/advs.201600180.
[130] Tahini HA, Tan X, Smith SC. Activating Inert MXenes for hydrogen evolution reaction via anchored metal centers. Adv Theory Simul 2022;5:1–5. https://doi.org/10.1002/adts.202100383.
[131] Li P, Zhu J, Handoko AD, Zhang R, Wang H, Legut D, et al. High-throughput theoretical optimization of the hydrogen evolution reaction on MXenes by transition metal modification. J Mater Chem A Mater 2018;6:4271–8. https://doi.org/10.1039/c8ta00173a.
[132] Gan J, Li F, Tang Y, Tang Q. Theoretical study of transition-metal-modified Mo2CO2 MXene as a catalyst for the hydrogen evolution reaction. ChemSusChem 2020;13:6005–15. https://doi.org/10.1002/cssc.202002163.
[133] Shen Z, Fan X, Ma S, An Y, Yang D, Guo N, et al. 3d transitional-metal single atom catalysis toward hydrogen evolution reaction on MXenes supports. Int J Hydrogen Energy 2020;45:14396–406. https://doi.org/10.1016/j.ijhydene.2020.03.174.
[134] Chen Z, Huang S, Huang B, Wan M, Zhou N. Transition metal atoms implanted into MXenes (M2CO2) for enhanced electrocatalytic hydrogen evolution reaction. Appl Surf Sci 2020;509:145319. https://doi.org/10.1016/j.apsusc.2020.145319.
[135] Jing T, Liang D, Hao J, Deng M, Cai S. Single Pt atoms stabilized on Mo2TiC2O2 for hydrogen evolution: a first-principles investigation. J Chem Phys 2019;151:024702. https://doi.org/10.1063/1.5099571.
[136] Park S, Lee YL, Yoon Y, Park SY, Yim S, Song W, et al. Reducing the high hydrogen binding strength of vanadium carbide MXene with atomic Pt confinement for high activity toward HER. Appl Catal B 2022;304:120989. https://doi.org/10.1016/j.apcatb.2021.120989.
[137] Jian X, Li T, Guo S, Gao L, Fu F, Tian Y, et al. Platinum nanoparticle-electrodeposited Ti3C2TxMXene as a binder-free electrocatalyst for improved hydrogen evolution. ACS Appl Energy Mater 2022;5:3092–9. https://doi.org/10.1021/acsaem.1c03708.
[138] Huang J, Feng M, Peng Y, Huang C, Yue X, Huang S. Encapsulating Ni nanoparticles into interlayers of nitrogen-doped Nb $_2$ CT $_x$ MXene to boost hydrogen evolution reaction in acid. Small 2023;19:2206098. https://doi.org/10.1002/smll.202206098.
[139] Liu H, Hu Z, Liu Q, Sun P, Wang Y, Chou S, et al. Single-atom Ru anchored in nitrogen-doped MXene (Ti3C2T: X) as an efficient catalyst for the hydrogen evolution reaction at all pH values. J Mater Chem A Mater 2020;8:24710–7. https://doi.org/10.1039/d0ta09538a.
[140] Bat-Erdene M, Batmunkh M, Sainbileg B, Hayashi M, Bati ASR, Qin J, et al. Highly dispersed Ru nanoparticles on boron-doped Ti3C2Tx (MXene) nanosheets for synergistic enhancement of electrocatalytic hydrogen evolution. Small 2021;17:1–10. https://doi.org/10.1002/smll.202102218.
[141] Du CF, Sun X, Yu H, Liang Q, Dinh KN, Zheng Y, et al. Synergy of Nb doping and surface alloy enhanced on water-alkali electrocatalytic hydrogen generation performance in Ti-based MXene. Adv Sci 2019;6:1900116. https://doi.org/10.1002/advs.201900116.
[142] Zou Y, Kazemi SA, Shi G, Liu J, Yang Y, Bedford NM, et al. Ruthenium <scp>single-atom</scp> modulated <scp> Ti 3 C 2 T x MXene </scp> for efficient alkaline electrocatalytic hydrogen production. EcoMat 2023:5. https://doi.org/10.1002/eom2.12274.
[143] Wu Y, Wang L, Bo T, Chai Z, Gibson JK, Shi W. Boosting hydrogen evolution in neutral medium by accelerating water dissociation with Ru clusters loaded on Mo $_2$ CTx MXene. Adv Funct Mater 2023:33. https://doi.org/10.1002/adfm.202214375.
[144] Dey A, Chandrabose G, Damptey LAO, Erakulan ES, Thapa R, Zhuk S, et al. Cu2O/CuO heterojunction catalysts through atmospheric pressure plasma induced defect passivation. Appl Surf Sci 2021;541:148571. https://doi.org/10.1016/j.apsusc.2020.148571.
[145] Si F, Zhang Y, Yan L, Zhu J, Xiao M, Liu C, et al. Electrochemical Oxygen Reduction Reaction. Rotating Electrode Methods and Oxygen Reduction Electrocatalysts, Elsevier B.V.; 2014. p. 133–70.
[146] Zhu Q, Cui Y, Zhang Y, Cao Z, Shi Y, Gu J, et al. Strategies for engineering the MXenes toward highly active catalysts. Mater Today Nano 2021;13:100104. https://doi.org/10.1016/j.mtnano.2020.100104.
[147] Peng Q, Zhou J, Chen J, Zhang T, Sun Z. Cu single atoms on Ti2CO2 as a highly efficient oxygen reduction catalyst in a proton exchange membrane fuel cell. J Mater Chem A Mater 2019;7:26062–70. https://doi.org/10.1039/c9ta08297b.
[148] Liu CY, Li EY. Termination effects of Pt/v-Ti n+1 C n T 2 MXene surfaces for oxygen reduction reaction catalysis. ACS Appl Mater Interfaces 2019;11:1638–44. https://doi.org/10.1021/acsami.8b17600.
[149] Zhang X, Zhang Y, Cheng C, Yang Z, Hermansson K. Tuning the ORR activity of Pt-based Ti2CO2 MXenes by varying the atomic cluster size and doping with metals. Nanoscale 2020;12:12497–507. https://doi.org/10.1039/d0nr00048e.
[150] Cheng YW, Dai JH, Zhang YM, Song Y. Two-dimensional, ordered, double transition metal carbides (MXenes): A new family of promising catalysts for the hydrogen evolution reaction. J Phys Chem C 2018;122:28113–22. https://doi.org/10.1021/acs.jpcc.8b08914.
[151] Zeng Z, Chen X, Weng K, Wu Y, Zhang P, Jiang J, et al. Computational screening study of double transition metal carbonitrides M′2M{\Prime}CNO2-MXene as catalysts for hydrogen evolution reaction. NPJ Comput Mater 2021;7:2–8. https://doi.org/10.1038/s41524-021-00550-4.
[152] Ma N, Wang Y, Zhang Y, Liang B, Zhao J, Fan J. First-principles screening of Pt doped Ti2CNL (N = O, S and Se, L = F, Cl, Br and I) as high-performance catalysts for ORR/OER. Appl Surf Sci 2022;596:153574. https://doi.org/10.1016/j.apsusc.2022.153574.
[153] Gao X, Zhou Y, Tan Y, Liu S, Cheng Z, Shen Z. Strain effects on Co, N co-decorated graphyne catalysts for overall water splitting electrocatalysis. PCCP 2020;22:2457–65. https://doi.org/10.1039/C9CP05548G.
[154] Huang H, Jia H, Liu Z, Gao P, Zhao J, Luo Z, et al. Understanding of strain effects in the electrochemical reduction of CO2: using pd nanostructures as an ideal platform. Angew Chem Int Ed 2017;56:3594–8. https://doi.org/10.1002/ANIE.201612617.
[155] Asano M, Kawamura R, Sasakawa R, Todoroki N, Wadayama T. Oxygen reduction reaction activity for strain-controlled Pt-based model alloy catalysts: surface strains and direct electronic effects induced by alloying elements. ACS Catal 2016;6:5285–9. https://doi.org/10.1021/ACSCATAL.6B01466/SUPPL_FILE/CS6B01466_SI_001.PDF.
[156] Hsu S-H, Hung S-F, Wang H-Y, Xiao F-X, Zhang L, Yang H, et al. Tuning the electronic spin state of catalysts by strain control for highly efficient water electrolysis. Small Methods 2018;2:1800001. https://doi.org/10.1002/SMTD.201800001.
[157] Ma N, Li N, Zhang Y, Wang T, Zhao J, Fan J. Strain adjustment Pt-doped Ti2CO2 as an efficient bifunctional catalyst for oxygen reduction reactions and oxygen evolution reactions by first-principles calculations. Appl Surf Sci 2022;590. https://doi.org/10.1016/j.apsusc.2022.153149.
[158] Ma N, Li N, Wang T, Ma X, Fan J. Strain engineering in the oxygen reduction reaction and oxygen evolution reaction catalyzed by Pt-doped Ti2CF2. J Mater Chem A Mater 2022;10:1390–401. https://doi.org/10.1039/d1ta07349d.
[159] Kan D, Lian R, Wang D, Zhang X, Xu J, Gao X, et al. Screening effective single-atom ORR and OER electrocatalysts from Pt decorated MXenes by first-principles calculations. J Mater Chem A Mater 2020;8:17065–77. https://doi.org/10.1039/d0ta04429f.
[160] Kan D, Wang D, Zhang X, Lian R, Xu J, Chen G, et al. Rational design of bifunctional ORR/OER catalysts based on Pt/Pd-doped Nb2CT2 MXene by first-principles calculations. J Mater Chem A Mater 2020;8:3097–108. https://doi.org/10.1039/c9ta12255a.

[161] Cheng Y, Dai J, Song Y, Zhang Y. Nanostructure of Cr2CO2 MXene supported single metal atom as an efficient bifunctional electrocatalyst for overall water splitting. ACS Appl Energy Mater 2019;2:6851–9. https://doi.org/10.1021/acsaem.9b01329.
[162] Shabana N, Arjun AM, Nubla K, Ankitha M, Rasheed PA. Platinum nanoparticles decorated Nb2CT MXene as an efficient dual functional catalyst for hydrogen evolution and oxygen reduction reaction. Int J Hydrogen Energy 2023;48:7698–707. https://doi.org/10.1016/j.ijhydene.2022.11.216.
[163] Sharma V, Dhiman R, Mahajan A. Ti2+ and Ti4+ species enriched MXene electrocatalyst for highly efficient hydrogen evolution and oxygen evolution reaction kinetics. Appl Surf Sci 2023;612:155883. https://doi.org/10.1016/j.apsusc.2022.155883.
[164] Fu Z, Ling C, Wang J. A Ti3C2O2 supported single atom, trifunctional catalyst for electrochemical reactions. J Mater Chem A Mater 2020;8:7801–7. https://doi.org/10.1039/d0ta01047b.
[165] Zhang C, Ma B, Zhou Y, Wang C. Highly active and durable Pt/MXene nanocatalysts for ORR in both alkaline and acidic conditions. J Electroanal Chem 2020;865:114142. https://doi.org/10.1016/j.jelechem.2020.114142.
[166] Cui X, Tang C, Zhang Q. A review of electrocatalytic reduction of dinitrogen to ammonia under ambient conditions. Adv Energy Mater 2018;8:1–25. https://doi.org/10.1002/aenm.201800369.
[167] Liu D, Chen M, Du X, Ai H, Lo KH, Wang S, et al. Development of Electrocatalysts for Efficient Nitrogen Reduction Reaction under Ambient Condition. Adv Funct Mater 2020:2008983. https://doi.org/10.1002/adfm.202008983.
[168] Luo Y, Chen GF, Ding L, Chen X, Ding LX, Wang H. Efficient electrocatalytic N 2 fixation with MXene under ambient conditions. Joule 2019;3:279–89. https://doi.org/10.1016/j.joule.2018.09.011.
[169] Li T, Yan X, Huang L, Li J, Yao L, Zhu Q, et al. Fluorine-free Ti3C2T: X (T = O, OH) nanosheets (~50-100 nm) for nitrogen fixation under ambient conditions. J Mater Chem A Mater 2019;7:14462–5. https://doi.org/10.1039/c9ta03254a.
[170] Zhao J, Zhang L, Xie XY, Li X, Ma Y, Liu Q, et al. Ti3C2Tx (T = F, OH) MXene nanosheets: conductive 2D catalysts for ambient electrohydrogenation of N2 to NH3. J Mater Chem A Mater 2018;6:24031–5. https://doi.org/10.1039/c8ta09840a.
[171] Johnson LR, Sridhar S, Zhang L, Fredrickson KD, Raman AS, Jang J, et al. MXene materials for the electrochemical nitrogen reduction-functionalized or not? ACS Catal 2020;10:253–64. https://doi.org/10.1021/acscatal.9b01925.
[172] Li L, Wang X, Guo H, Yao G, Yu H, Tian Z, et al. Theoretical screening of single transition metal atoms embedded in mxene defects as superior electrocatalyst of nitrogen reduction reaction. Small Methods 2019;3:1–7. https://doi.org/10.1002/smtd.201900337.
[173] Huang B, Li N, Ong WJ, Zhou N. Single atom-supported MXene: how single-atomic-site catalysts tune the high activity and selectivity of electrochemical nitrogen fixation. J Mater Chem A Mater 2019;7:27620–31. https://doi.org/10.1039/c9ta09776g.
[174] Gao Y, Zhuo H, Cao Y, Sun X, Zhuang G, Deng S, et al. A theoretical study of electrocatalytic ammonia synthesis on single metal atom/MXene. Cuihua Xuebao/Chinese Journal of Catalysis 2019;40:152–9. https://doi.org/10.1016/S1872-2067(18)63197-3.
[175] Zheng S, Li S, Mei Z, Hu Z, Chu M, Liu J, et al. Electrochemical nitrogen reduction reaction performance of single-boron catalysts tuned by MXene substrates. J Phys Chem Lett 2019:6984–9. https://doi.org/10.1021/acs.jpclett.9b02741.
[176] Liu D, Zhang G, Ji Q, Zhang Y, Li J. Synergistic electrocatalytic nitrogen reduction enabled by confinement of nanosized Au particles onto a two-dimensional Ti3C2 substrate. ACS Appl Mater Interfaces 2019;11:25758–65. https://doi.org/10.1021/acsami.9b02511.
[177] Liu A, Liang X, Yang Q, Ren X, Gao M, Yang Y, et al. Electrocatalytic synthesis of ammonia using a 2D Ti3C2 MXene loaded with copper nanoparticles. ChemPlusChem 2020;124221:166–70. https://doi.org/10.1002/cplu.202000702.
[178] Liu A, Yang Q, Ren X, Gao M, Yang Y, Gao L, et al. Two-dimensional CuAg/Ti3C2catalyst for electrochemical synthesis of ammonia under ambient conditions: a combined experimental and theoretical study. Sustain Energy Fuels 2020;4:5061–71. https://doi.org/10.1039/d0se00915f.
[179] Liu A, Gao M, Ren X, Meng F, Yang Y, Yang Q, et al. A two-dimensional Ru@MXene catalyst for highly selective ambient electrocatalytic nitrogen reduction. Nanoscale 2020;12:10933–8. https://doi.org/10.1039/d0nr00788a.
[180] Azofra LM, Li N, Macfarlane DR, Sun C. Promising prospects for 2D d2–d4 M3C2 transition metal carbides (MXenes) in N2 capture and conversion into ammonia. Energ Environ Sci 2016;9:2545–9. https://doi.org/10.1039/c6ee01800a.
[181] Zhang G, Xu H, Li Y, Xiang C, Ji Q, Liu H, et al. Interfacial engineering of SeO ligands on tellurium featuring synergistic functionalities of bond activation and chemical states buffering toward electrocatalytic conversion of nitrogen to ammonia. Adv Sci 2019;6:1901627. https://doi.org/10.1002/ADVS.201901627.
[182] Shi Y, Liu Y. Vacancy and N dopants facilitated Ti3+ sites activity in 3D Ti3-xC2Ty MXene for electrochemical nitrogen fixation. Appl Catal B 2021;297:120482. https://doi.org/10.1016/j.apcatb.2021.120482.
[183] Zhai X, Dong H, Li Y, Yang X, Li L, Yang J, et al. Termination effects of single-atom decorated v-Mo2CTx MXene for the electrochemical nitrogen reduction reaction. J Colloid Interface Sci 2022;605:897–905. https://doi.org/10.1016/j.jcis.2021.07.083.
[184] Xue ZH, Zhang SN, Lin YX, Su H, Zhai GY, Han JT, et al. Electrochemical reduction of N2 into NH3 by donor-acceptor couples of Ni and Au nanoparticles with a 67.8% faradaic efficiency. J Am Chem Soc 2019;141:14976–80. https://doi.org/10.1021/jacs.9b07963.
[185] Li N, Chen X, Ong WJ, Macfarlane DR, Zhao X, Cheetham AK, et al. Understanding of electrochemical mechanisms for CO2 capture and conversion into hydrocarbon fuels in transition-metal carbides (MXenes). ACS Nano 2017;11:10825–33. https://doi.org/10.1021/ACSNANO.7B03738/SUPPL_FILE/NN7B03738_SI_001.PDF.
[186] Handoko AD, Khoo KH, Tan TL, Jin H, Seh ZW. Establishing new scaling relations on two-dimensional MXenes for CO2 electroreduction. J Mater Chem A Mater 2018;6:21885–90. https://doi.org/10.1039/c8ta06567e.
[187] Handoko AD, Chen H, Lum Y, Zhang Q, Anasori B, Seh ZW. Two-dimensional titanium and molybdenum carbide MXenes as electrocatalysts for CO2 reduction. IScience 2020;23:101181. https://doi.org/10.1016/j.isci.2020.101181.
[188] Qu D, Peng X, Mi Y, Bao H, Zhao S, Liu X, et al. Nitrogen doping and titanium vacancies synergistically promote CO2fixation in seawater. Nanoscale 2020;12:17191–5. https://doi.org/10.1039/d0nr03775c.
[189] Peterson AA, Nørskov JK. Activity descriptors for CO 2 electroreduction to methane on transition-metal catalysts. J Phys Chem Lett 2012;3:251–8. https://doi.org/10.1021/jz201461p.
[190] Baturina OA, Lu Q, Padilla MA, Xin L, Li W, Serov A, et al. CO2 electroreduction to hydrocarbons on carbon-supported Cu nanoparticles. ACS Catal 2014;4:3682–95. https://doi.org/10.1021/cs500537y.
[191] Eid K, Lu Q, Abdel-Azeim S, Soliman A, Abdullah AM, Abdelgwad AM, et al. Highly exfoliated Ti3C2T: XMXene nanosheets atomically doped with Cu for efficient electrochemical CO2reduction: An experimental and theoretical study. J Mater Chem A Mater 2022;10:1965–75. https://doi.org/10.1039/d1ta09471h.
[192] Zhao Q, Zhang C, Hu R, Du Z, Gu J, Cui Y, et al. Selective etching quaternary MAX phase toward single atom copper immobilized MXene (Ti3C2Clx) for efficient CO2 electroreduction to methanol. ACS Nano 2021;15:4927–36. https://doi.org/10.1021/acsnano.0c09755.
[193] Handoko AD, Fredrickson KD, Anasori B, Convey KW, Johnson LR, Gogotsi Y, et al. Tuning the basal plane functionalization of two-dimensional metal carbides (MXenes) to control hydrogen evolution activity. ACS Appl Energy Mater 2018;1:173–80. https://doi.org/10.1021/acsaem.7b00054.
[194] Cheng Y, Xu X, Li Y, Zhang Y, Song Y. CO2 reduction mechanism on the Nb2CO2 MXene surface: effect of nonmetal and metal modification. Comput Mater Sci 2022;202:110971. https://doi.org/10.1016/j.commatsci.2021.110971.
[195] Freund HJ, Meijer G, Scheffler M, Schlögl R, Wolf M. CO oxidation as a prototypical reaction for heterogeneous processes. Angewandte Chemie - International Edition 2011;50:10064–94. https://doi.org/10.1002/anie.201101378.
[196] Cheng C, Zhang X, Yang Z, Zhou Z. Cu3-cluster-doped monolayer Mo2CO2 (MXene) as an electron reservoir for catalyzing a CO oxidation reaction. ACS Appl Mater Interfaces 2018;10:32903–12. https://doi.org/10.1021/acsami.8b12318.
[197] Cheng C, Zhang X, Yang Z, Hermansson K. Identification of high-performance single-atom MXenes catalysts for low-temperature CO oxidation. Adv Theory Simul 2019;2:1900006. https://doi.org/10.1002/adts.201900006.
[198] Zhang X, Xu C, Zhang Y, Cheng C, Yang Z, Hermansson K. Regulation of CO oxidation with Pd additives on Nb2CO2 MXene. Int J Hydrogen Energy 2020;46:8477–85. https://doi.org/10.1016/j.ijhydene.2020.11.278.

[199] Glavin NR, Rao R, Varshney V, Bianco E, Apte A, Roy A, et al. Emerging applications of elemental 2D materials. Adv Mater 2020;32. https://doi.org/10.1002/adma.201904302.
[200] Kshetri T, Tran DT, Le HT, Nguyen DC, Hoa H van, Kim NH, et al. Recent advances in MXene-based nanocomposites for electrochemical energy storage applications. Prog Mater Sci 2021;117. https://doi.org/10.1016/j.pmatsci.2020.100733.
[201] Yang J, Bao W, Jaumaux P, Zhang S, Wang C, Wang G. MXene-Based Composites: Synthesis and Applications in Rechargeable Batteries and Supercapacitors. Adv Mater Interfaces 2019;6. https://doi.org/10.1002/admi.201802004.
[202] Kumar R, Sahoo S, Joanni E, Singh RK, Maegawa K, Tan WK, et al. Heteroatom doped graphene engineering for energy storage and conversion. Mater Today 2020;39:47–65. https://doi.org/10.1016/j.mattod.2020.04.010.
[203] Etacheri V, Marom R, Elazari R, Salitra G, Aurbach D. Challenges in the development of advanced Li-ion batteries: a review. Energ Environ Sci 2011;4:3243–62. https://doi.org/10.1039/c1ee01598b.
[204] Li M, Lu J, Chen Z, Amine K. 30 years of lithium-ion batteries. Adv Mater 2018;30. https://doi.org/10.1002/adma.201800561.
[205] Haregewoin AM, Wotango AS, Hwang BJ. Electrolyte additives for lithium ion battery electrodes: progress and perspectives. Energ Environ Sci 2016;9:1955–88. https://doi.org/10.1039/c6ee00123h.
[206] Li W, Song B, Manthiram A. High-voltage positive electrode materials for lithium-ion batteries. Chem Soc Rev 2017;46:3006–59. https://doi.org/10.1039/c6cs00875e.
[207] Bauer D, Ashton TE, Groves AR, Dey A, Krishnamurthy S, Matsumi N, et al. Continuous hydrothermal synthesis of metal germanates (M_2 GeO_4; M = Co, Mn, Zn) for high-capacity negative electrodes in Li-ion batteries. Energ Technol 2020;8:1900692. https://doi.org/10.1002/ente.201900692.
[208] Whittingham MS. Lithium batteries and cathode materials. Chem Rev 2004;104:4271–301. https://doi.org/10.1021/cr020731c.
[209] Whittingham MS. Electrical energy storage and intercalation chemistry. Science 1979;1976(192):1126–7. https://doi.org/10.1126/science.192.4244.1126.
[210] Ozawa K. Lithium-ion rechargeable batteries with LiCoO2 and carbon electrodes: the LiCoO2/C system. vol. 69. 1994.
[211] Bruce PG, Scrosati B, Tarascon JM. Nanomaterials for rechargeable lithium batteries. Angewandte Chemie - International Edition 2008;47:2930–46. https://doi.org/10.1002/anie.200702505.
[212] Marom R, Amalraj SF, Leifer N, Jacob D, Aurbach D. A review of advanced and practical lithium battery materials. J Mater Chem 2011;21:9938–54. https://doi.org/10.1039/c0jm04225k.
[213] Schipper F, Erickson EM, Erk C, Shin J-Y, Chesneau FF, Aurbach D. Review—recent advances and remaining challenges for lithium ion battery cathodes. J Electrochem Soc 2017;164:A6220–8. https://doi.org/10.1149/2.0351701jes.
[214] Kumar P, Abuhimd H, Wahyudi W, Li M, Ming J, Li L-J. Review—two-dimensional layered materials for energy storage applications. ECS J Solid State Sci Technol 2016;5:Q3021–5. https://doi.org/10.1149/2.0051611jss.
[215] Garg R, Agarwal A, Agarwal M. A Review on MXene for energy storage application: effect of interlayer distance. Mater Res Express 2020;7. https://doi.org/10.1088/2053-1591/ab750d.
[216] Hong Ng VM, Huang H, Zhou K, Lee PS, Que W, Xu JZ, et al. Recent progress in layered transition metal carbides and/or nitrides (MXenes) and their composites: synthesis and applications. J Mater Chem A Mater 2017;5:3039–68. https://doi.org/10.1039/c6ta06772g.
[217] Liu R, Cao W, Han D, Mo Y, Zeng H, Yang H, et al. Nitrogen-doped Nb2CTx MXene as anode materials for lithium ion batteries. J Alloy Compd 2019;793:505–11. https://doi.org/10.1016/j.jallcom.2019.03.209.
[218] Wu N, Zhang Q-Y, Guo Y-J, Zhou L, Zhang L-J, Wu M-X, et al. Boron-doped three-dimensional MXene host for durable lithium-metal anode RARE METALS. Rare Met 1944;41:2217–22. https://doi.org/10.1007/s12598.
[219] Ponrouch A, Marchante E, Courty M, Tarascon JM, Palacín MR. In search of an optimized electrolyte for Na-ion batteries. Energ Environ Sci 2012;5:8572–83. https://doi.org/10.1039/c2ee22258b.
[220] Xiang X, Zhang K, Chen J. Recent advances and prospects of cathode materials for sodium-ion batteries. Adv Mater 2015;27:5343–64. https://doi.org/10.1002/adma.201501527.
[221] Whittingham MS. Chemistry of intercalation compounds: metal guests in chalcogenide hosts. Prog Solid State Chem 1978;12:41–99. https://doi.org/10.1016/0079-6786(78)90003-1.
[222] Newman GH, Klemann LP. Ambient temperature cycling of an Na - TiS2 cell. J Electrochem Soc 1980;127:2097–9. https://doi.org/10.1149/1.2129353/XML.
[223] Yabuuchi N, Kubota K, Dahbi M, Komaba S. Research development on sodium-ion batteries. Chem Rev 2014;114:11636–82. https://doi.org/10.1021/cr500192f.
[224] Pan H, Hu YS, Chen L. Room-temperature stationary sodium-ion batteries for large-scale electric energy storage. Energ Environ Sci 2013;6:2338–60. https://doi.org/10.1039/c3ee40847g.
[225] Hwang JY, Myung ST, Sun YK. Sodium-ion batteries: present and future. Chem Soc Rev 2017;46:3529–614. https://doi.org/10.1039/c6cs00776g.
[226] Okamoto Y. Density functional theory calculations of alkali metal (Li, Na, and K) graphite intercalation compounds. J Phys Chem C 2014;118:16–9. https://doi.org/10.1021/jp4063753.
[227] Nobuhara K, Nakayama H, Nose M, Nakanishi S, Iba H. First-principles study of alkali metal-graphite intercalation compounds. J Power Sources 2013;243:585–7. https://doi.org/10.1016/j.jpowsour.2013.06.057.
[228] Stevens DA, Dahn JR. High capacity anode materials for rechargeable sodium-ion batteries. J Electrochem Soc 2000;147:1271. https://doi.org/10.1149/1.1393348.
[229] Fong R, von Sacken U, Dahn JR. Studies of lithium intercalation into carbons using nonaqueous electrochemical cells. J Electrochem Soc 1990;137:2009–13. https://doi.org/10.1149/1.2086855.
[230] Lei YJ, Yan ZC, Lai WH, Chou SL, Wang YX, Liu HK, et al. Tailoring MXene-based materials for sodium-ion storage: synthesis, mechanisms, and applications. Electrochem Energy Rev 2020;3:766–92. https://doi.org/10.1007/s41918-020-00079-y.
[231] Hou H, Qiu X, Wei W, Zhang Y, Ji X. Carbon anode materials for advanced sodium-ion batteries. Adv Energy Mater 2017;7. https://doi.org/10.1002/aenm.201602898.
[232] Perveen T, Siddiq M, Shahzad N, Ihsan R, Ahmad A, Shahzad MI. Prospects in anode materials for sodium ion batteries - a review. Renew Sustain Energy Rev 2020;119. https://doi.org/10.1016/j.rser.2019.109549.
[233] Zheng X, Bommier C, Luo W, Jiang L, Hao Y, Huang Y. Sodium metal anodes for room-temperature sodium-ion batteries: Applications, challenges and solutions. Energy Storage Mater 2019;16:6–23. https://doi.org/10.1016/j.ensm.2018.04.014.
[234] Manthiram A, Fu Y, Chung SH, Zu C, Su YS. Rechargeable lithium-sulfur batteries. Chem Rev 2014;114:11751–87. https://doi.org/10.1021/cr500062v.
[235] Liu Y, Elias Y, Meng J, Aurbach D, Zou R, Xia D, et al. Electrolyte solutions design for lithium-sulfur batteries. Joule 2021;5:2323–64. https://doi.org/10.1016/j.joule.2021.06.009.
[236] Manthiram A, Chung SH, Zu C. Lithium-sulfur batteries: progress and prospects. Adv Mater 2015;27:1980–2006. https://doi.org/10.1002/adma.201405115.
[237] Syali MS, Kumar D, Mishra K, Kanchan DK. Recent advances in electrolytes for room-temperature sodium-sulfur batteries: a review. Energy Storage Mater 2020;31:352–72. https://doi.org/10.1016/j.ensm.2020.06.023.
[238] Chung SH, Chang CH, Manthiram A. Progress on the Critical Parameters for Lithium–Sulfur Batteries to be Practically Viable. Adv Funct Mater 2018;28. https://doi.org/10.1002/adfm.201801188.
[239] Wang YX, Zhang B, Lai W, Xu Y, Chou SL, Liu HK, et al. Room-temperature sodium-sulfur batteries: a comprehensive review on research progress and cell chemistry. Adv Energy Mater 2017;7. https://doi.org/10.1002/aenm.201602829.
[240] Seh ZW, Sun Y, Zhang Q, Cui Y. Designing high-energy lithium-sulfur batteries. Chem Soc Rev 2016;45:5605–34. https://doi.org/10.1039/c5cs00410a.
[241] Ma L, Hendrickson KE, Wei S, Archer LA. Nanomaterials: science and applications in the lithium-sulfur battery. Nano Today 2015;10:315–38. https://doi.org/10.1016/j.nantod.2015.04.011.
[242] Wen Z, Cao J, Gu Z, Xu X, Zhang F, Lin Z. Research on sodium sulfur battery for energy storage. Solid State Ion 2008;179:1697–701. https://doi.org/10.1016/j.ssi.2008.01.070.

[243] Wei S, Xu S, Agrawral A, Choudhury S, Lu Y, Tu Z, et al. A stable room-temperature sodium-sulfur battery. Nat Commun 2016;7:1–10. https://doi.org/10.1038/ncomms11722.
[244] Song Y, Sun Z, Fan Z, Cai W, Shao Y, Sheng G, et al. Rational design of porous nitrogen-doped Ti3C2 MXene as a multifunctional electrocatalyst for Li–S chemistry. Nano Energy 2020;70:1–10. https://doi.org/10.1016/j.nanoen.2020.104555.
[245] Wang C, Zhang L, Zhang Z, Zhao R, Zhao D, Ma R, et al. Layered materials for supercapacitors and batteries: Applications and challenges. Prog Mater Sci 2021; 118. https://doi.org/10.1016/j.pmatsci.2020.100763.
[246] Fleischmann S, Mitchell JB, Wang R, Zhan C, Jiang DE, Presser V, et al. Pseudocapacitance: from fundamental understanding to high power energy storage materials. Chem Rev 2020;120:6738–82. https://doi.org/10.1021/acs.chemrev.0c00170.
[247] Wang Y, Song Y, Xia Y. Electrochemical capacitors: mechanism, materials, systems, characterization and applications. Chem Soc Rev 2016;45:5925–50. https://doi.org/10.1039/c5cs00580a.
[248] Chakrabarty N, Dey A, Krishnamurthy S, Chakraborty AK. CeO2/Ce2O3 quantum dot decorated reduced graphene oxide nanohybrid as electrode for supercapacitor. Appl Surf Sci 2021;536:147960. https://doi.org/10.1016/j.apsusc.2020.147960.
[249] Yu M, Lin D, Feng H, Zeng Y, Tong Y, Lu X. Boosting the energy density of carbon-based aqueous supercapacitors by optimizing the surface charge. Angewandte Chemie - International Edition 2017;56:5454–9. https://doi.org/10.1002/anie.201701737.
[250] Wang G, Zhang L, Zhang J. A review of electrode materials for electrochemical supercapacitors. Chem Soc Rev 2012;41:797–828. https://doi.org/10.1039/c1cs15060j.
[251] Augustyn V, Simon P, Dunn B. Pseudocapacitive oxide materials for high-rate electrochemical energy storage. Energ Environ Sci 2014;7:1597–614. https://doi.org/10.1039/c3ee44164d.
[252] Zhi M, Xiang C, Li J, Li M, Wu N. Nanostructured carbon-metal oxide composite electrodes for supercapacitors: a review. Nanoscale 2013;5:72–88. https://doi.org/10.1039/c2nr32040a.
[253] Meng Q, Cai K, Chen Y, Chen L. Research progress on conducting polymer based supercapacitor electrode materials. Nano Energy 2017;36:268–85. https://doi.org/10.1016/j.nanoen.2017.04.040.
[254] Lukatskaya MR, Mashtalir O, Ren CE, Dall'Agnese Y, Rozier P, Taberna PL, et al. Cation Intercalation and High Volumetric Capacitance of Two-Dimensional Titanium Carbide. Science (1979) 2013;341:1502–5. https://doi.org/10.1126/science.1241488.
[255] Mashtalir O, Lukatskaya MR, Kolesnikov AI, Raymundo-Piñero E, Naguib M, Barsoum MW, et al. The effect of hydrazine intercalation on the structure and capacitance of 2D titanium carbide (MXene). Nanoscale 2016;8:9128–33. https://doi.org/10.1039/C6NR01462C.
[256] Dall'Agnese Y, Lukatskaya MR, Cook KM, Taberna P-L, Gogotsi Y, Simon P. High capacitance of surface-modified 2D titanium carbide in acidic electrolyte. Electrochem Commun 2014;48:118–22. https://doi.org/10.1016/j.elecom.2014.09.002.
[257] Ghidiu M, Lukatskaya MR, Zhao M-Q, Gogotsi Y, Barsoum MW. Conductive two-dimensional titanium carbide 'clay' with high volumetric capacitance. Nature 2014;516:78–81. https://doi.org/10.1038/nature13970.
[258] Li H, Hou Y, Wang F, Lohe MR, Zhuang X, Niu L, et al. Flexible all-solid-state supercapacitors with high volumetric capacitances boosted by solution processable MXene and electrochemically exfoliated graphene. Adv Energy Mater 2017;7:1601847. https://doi.org/10.1002/aenm.201601847.
[259] Boota M, Anasori B, Voigt C, Zhao M-Q, Barsoum MW, Gogotsi Y. Pseudocapacitive electrodes produced by oxidant-free polymerization of pyrrole between the layers of 2D titanium carbide (MXene). Adv Mater 2016;28:1517–22. https://doi.org/10.1002/adma.201504705.
[260] Wang F, Cao M, Qin Y, Zhu J, Wang L, Tang Y. ZnO nanoparticle-decorated two-dimensional titanium carbide with enhanced supercapacitive performance. RSC Adv 2016;6:88934–42. https://doi.org/10.1039/C6RA15384D.
[261] Tang Y, Zhu J, Yang C, Wang F. Enhanced supercapacitive performance of manganese oxides doped two-dimensional titanium carbide nanocomposite in alkaline electrolyte. J Alloy Compd 2016;685:194–201. https://doi.org/10.1016/j.jallcom.2016.05.221.
[262] Wang Y, Dou H, Wang J, Ding B, Xu Y, Chang Z, et al. Three-dimensional porous MXene/layered double hydroxide composite for high performance supercapacitors. J Power Sources 2016;327:221–8. https://doi.org/10.1016/j.jpowsour.2016.07.062.
[263] Zhao M-Q, Ren CE, Ling Z, Lukatskaya MR, Zhang C, Van Aken KL, et al. Flexible MXene/carbon nanotube composite paper with high volumetric capacitance. Adv Mater 2015;27:339–45. https://doi.org/10.1002/adma.201404140.
[264] Zhao C, Wang Q, Zhang H, Passerini S, Qian X. Two-dimensional titanium carbide/RGO composite for high-performance supercapacitors. ACS Appl Mater Interfaces 2016;8:15661–7. https://doi.org/10.1021/acsami.6b04767.
[265] Yan J, Ren CE, Maleski K, Hatter CB, Anasori B, Urbankowski P, et al. Flexible MXene/graphene films for ultrafast supercapacitors with outstanding volumetric capacitance. Adv Funct Mater 2017;27:1701264. https://doi.org/10.1002/adfm.201701264.
[266] Liu C, Bai Y, Li W, Yang F, Zhang G, Pang H. In situ growth of three-dimensional MXene/metal–organic framework composites for high-performance supercapacitors. Angew Chem 2022;134. https://doi.org/10.1002/ange.202116282.
[267] Bai Y, Liu C, Chen T, Li W, Zheng S, Pi Y, et al. MXene-copper/cobalt hybrids via lewis acidic molten salts etching for high performance symmetric supercapacitors. Angew Chem 2021;133:25522–6. https://doi.org/10.1002/ange.202112381.
[268] Zheng S, Sun Y, Xue H, Braunstein P, Huang W, Pang H. Dual-ligand and hard-soft-acid-base strategies to optimize metal-organic framework nanocrystals for stable electrochemical cycling performance. Natl Sci Rev 2022;9. https://doi.org/10.1093/nsr/nwab197.
[269] Marje SJ, Katkar PK, Pujari SS, Khalate SA, Lokhande AC, Patil UM. Regulated micro-leaf like nickel pyrophosphate as a cathode electrode for asymmetric supercapacitor. Synth Met 2020;259:116224. https://doi.org/10.1016/j.synthmet.2019.116224.
[270] Khan Z, Senthilkumar B, Lim S, Shanker R, Kim Y, Ko H. Redox-additive-enhanced high capacitance supercapacitors based on Co 2 P 2 O 7 nanosheets. Adv Mater Interfaces 2017;4:1700059. https://doi.org/10.1002/admi.201700059.
[271] Karaphun A, Sawadsitang S, Duangchuen T, Chirawatkul P, Putjuso T, Kumnorkaew P, et al. Influence of calcination temperature on structural, morphological, and electrochemical properties of Zn2P2O7 nanostructure. Surf Interfaces 2021;23:100961. https://doi.org/10.1016/j.surfin.2021.100961.
[272] BoopathiRaja R, Vadivel S, Parthibavarman M, Prabhu S, Ramesh R. Effect of polypyrrole incorporated sun flower like Mn2P2O7 with lab waste tissue paper derived activated carbon for asymmetric supercapacitor applications. Surf Interfaces 2021;26:101409. https://doi.org/10.1016/j.surfin.2021.101409.
[273] Agarwal A, Majumder S, Sankapal BR. Carbon nanotube-functionalized surface-assisted growth of cobalt phosphate nanodots: a highly stable and bendable all-solid-state symmetric supercapacitor. Energy Fuel 2022;36:5953–64. https://doi.org/10.1021/acs.energyfuels.2c00600.
[274] Chen S, Zhu J, Wu X, Han Q, Wang X. Graphene oxide−MnO_2 nanocomposites for supercapacitors. ACS Nano 2010;4:2822–30. https://doi.org/10.1021/nn901311t.
[275] Wang J-W, Chen Y, Chen B-Z. Synthesis and control of high-performance MnO2/carbon nanotubes nanocomposites for supercapacitors. J Alloy Compd 2016; 688:184–97. https://doi.org/10.1016/j.jallcom.2016.07.005.
[276] Vangapally N, V. KK, Kumar A, Martha SK. Charge storage behavior of sugar derived carbon/MnO2 composite electrode material for high-performance supercapacitors. J Alloys Compd 2022;893:162232. https://doi.org/10.1016/j.jallcom.2021.162232.
[277] Gopalsamy K, Balamurugan J, Thanh TD, Kim NH, Lee JH. Fabrication of nitrogen and sulfur co-doped graphene nanoribbons with porous architecture for high-performance supercapacitors. Chem Eng J 2017;312:180–90. https://doi.org/10.1016/j.cej.2016.11.130.
[278] Xiao N, Lau D, Shi W, Zhu J, Dong X, Hng HH, et al. A simple process to prepare nitrogen-modified few-layer graphene for a supercapacitor electrode. Carbon N Y 2013;57:184–90. https://doi.org/10.1016/j.carbon.2013.01.062.
[279] Parveen N, Ansari MO, Ansari SA, Cho MH. Simultaneous sulfur doping and exfoliation of graphene from graphite using an electrochemical method for supercapacitor electrode materials. J Mater Chem A Mater 2016;4:233–40. https://doi.org/10.1039/C5TA07963B.
[280] Rotte NK, Naresh V, Muduli S, Reddy V, Srikanth VVS, Martha SK. Microwave aided scalable synthesis of sulfur, nitrogen co-doped few-layered graphene material for high-performance supercapacitors. Electrochim Acta 2020;363:137209. https://doi.org/10.1016/j.electacta.2020.137209.
[281] Saha S, Jana M, Khanra P, Samanta P, Koo H, Murmu NC, et al. Band gap engineering of boron nitride by graphene and its application as positive electrode material in asymmetric supercapacitor device. ACS Appl Mater Interfaces 2015;7:14211–22. https://doi.org/10.1021/acsami.5b03562.

[282] Wang L, Liu F, Zhao B, Ning Y, Zhang L, Bradley R, et al. Carbon nanobowls filled with MoS $_2$ nanosheets as electrode materials for supercapacitors. ACS Appl Nano Mater 2020;3:6448–59. https://doi.org/10.1021/acsanm.0c00924.

[283] Liu Y, Wang Y, Chen Y, Wang C, Guo L. NiCo-MOF nanosheets wrapping polypyrrole nanotubes for high-performance supercapacitors. Appl Surf Sci 2020;507:145089. https://doi.org/10.1016/j.apsusc.2019.145089.

[284] Samuel E, Kim T-G, Park C-W, Joshi B, Swihart MT, Yoon SS. Supersonically sprayed Zn $_2$ SnO $_4$ /SnO $_2$ /CNT nanocomposites for high-performance supercapacitor electrodes. ACS Sustain Chem Eng 2019;7:14031–40. https://doi.org/10.1021/acssuschemeng.9b02549.

[285] Das D, Borthakur LJ, Nath BC, Saikia BJ, Mohan KJ, Dolui SK. Designing hierarchical NiO/PAni-MWCNT core–shell nanocomposites for high performance super capacitor electrodes. RSC Adv 2016;6:44878–87. https://doi.org/10.1039/C6RA01777K.

[286] Huang K-J, Zhang J-Z, Shi G-W, Liu Y-M. Hydrothermal synthesis of molybdenum disulfide nanosheets as supercapacitors electrode material. Electrochim Acta 2014;132:397–403. https://doi.org/10.1016/j.electacta.2014.04.007.

[287] Hu B, Qin X, Asiri AM, Alamry KA, Al-Youbi AO, Sun X. Synthesis of porous tubular C/MoS2 nanocomposites and their application as a novel electrode material for supercapacitors with excellent cycling stability. Electrochim Acta 2013;100:24–8. https://doi.org/10.1016/j.electacta.2013.03.133.

[288] Xu B, Yue S, Sui Z, Zhang X, Hou S, Cao G, et al. What is the choice for supercapacitors: graphene or graphene oxide? Energ Environ Sci 2011;4:2826. https://doi.org/10.1039/c1ee01198g.

[289] Chen Y, Zhang X, Zhang D, Yu P, Ma Y. High performance supercapacitors based on reduced graphene oxide in aqueous and ionic liquid electrolytes. Carbon N Y 2011;49:573–80. https://doi.org/10.1016/j.carbon.2010.09.060.

[290] Krishnan P, Biju V. Effect of electrolyte concentration on the electrochemical performance of RGO–KOH supercapacitor. Bull Mater Sci 2021;44:288. https://doi.org/10.1007/s12034-021-02576-2.

[291] Yang C, Que W, Tang Y, Tian Y, Yin X. Nitrogen and sulfur Co-doped 2D titanium carbides for enhanced electrochemical performance. J Electrochem Soc 2017;164:A1939–45. https://doi.org/10.1149/2.1091709jes.

[292] Yoon Y, Lee M, Kim SK, Bae G, Song W, Myung S, et al. A strategy for synthesis of carbon nitride induced chemically doped 2D MXene for high-performance supercapacitor electrodes. Adv Energy Mater 2018;8:1703173. https://doi.org/10.1002/aenm.201703173.

[293] Li H, Wang X, Li H, Lin S, Zhao B, Dai J, et al. Capacitance improvements of V4C3T by NH3 annealing. J Alloy Compd 2019;784:923–30. https://doi.org/10.1016/j.jallcom.2019.01.111.

[294] Guo J, Sun Y, Liu B, Zhang Q, Peng Q. Two-dimensional scandium-based carbides (MXene): band gap modulation and optical properties. J Alloy Compd 2017;712:752–9. https://doi.org/10.1016/j.jallcom.2017.04.149.

[295] Balci E, Akkuş ÜÖ, Berber S. Band gap modification in doped MXene: Sc2CF2. J Mater Chem C Mater 2017;5:5956–61. https://doi.org/10.1039/c7tc01765k.

[296] Yu L, Bati ASR, Grace TSL, Batmunkh M, Shapter JG. Ti3C2Tx (MXene)-silicon heterojunction for efficient photovoltaic cells. Adv Energy Mater 2019;9:1901063. https://doi.org/10.1002/AENM.201901063.

[297] Zhang Z, Lin J, Sun P, Zeng Q, Deng X, Mo Y, et al. Air-stable MXene/GaAs heterojunction solar cells with a high initial efficiency of 9.69%. J Mater Chem A Mater 2021;9:16160–8. https://doi.org/10.1039/D1TA04194K.

[298] Bati ASR, Sutanto AA, Hao M, Batmunkh M, Yamauchi Y, Wang L, et al. Cesium-doped Ti3C2Tx MXene for efficient and thermally stable perovskite solar cells. Cell Rep Phys Sci 2021;100598. https://doi.org/10.1016/J.XCRP.2021.100598.

[299] Lyu B, Kim M, Jing H, Kang J, Qian C, Lee S, et al. Large-area MXene electrode array for flexible electronics. ACS Nano 2019;13:11392–400. https://doi.org/10.1021/acsnano.9b04731.

[300] Feng L, Zha XH, Luo K, Huang Q, He J, Liu Y, et al. Structures and mechanical and electronic properties of the Ti2CO2 MXene incorporated with neighboring elements (Sc, V, B and N). J Electron Mater 2017;46:2460–6. https://doi.org/10.1007/s11664-017-5311-5.

[301] Zhou Y, Zhai G, Yan T, Huang Q, Guo Z, Te LC, et al. Current rectification induced by V-doped and Sc-doped in Ti2CO2 devices. Comput Mater Sci 2017;138:175–82. https://doi.org/10.1016/j.commatsci.2017.06.017.

[302] Zhou Y, Zhai G, Yan T, Francisco JS, Tian H, Huang Q, et al. Effects of different surface functionalization and doping on the electronic transport properties of M2CT x–M2CO2 heterojunction devices. J Phys Chem C 2018;122:14908–17. https://doi.org/10.1021/acs.jpcc.8b02026.

[303] Chen J, Liu X, Li Z, Cao F, Lu X, Fang X. Work-function-tunable MXenes electrodes to optimize p-CsCu $_{2\,I}$ 3 /n-C$_a$ 2 N$_b$ 3_x Ta $x_{\,O}$ 10 junction photodetectors for image sensing and logic electronics. Adv Funct Mater 2022;32:2201066. https://doi.org/10.1002/adfm.202201066.

[304] Shao B, Liu Z, Zeng G, Wang H, Liang Q, He Q, et al. Two-dimensional transition metal carbide and nitride (MXene) derived quantum dots (QDs): Synthesis, properties, applications and prospects. J Mater Chem A Mater 2020;8:7508–35. https://doi.org/10.1039/d0ta01552k.

[305] Safaei M, Shishehbore MR. Energy conversion and optical applications of MXene quantum dots. Journal of Materials Science 2021 56:32 2021;56:17942–78. https://doi.org/10.1007/S10853-021-06428-6.

[306] Xu Q, Ding L, Wen Y, Yang W, Zhou H, Chen X, et al. High photoluminescence quantum yield of 18.7% by using nitrogen-doped Ti3C2 MXene quantum dots. J Mater Chem C Mater 2018;6:6360–9. https://doi.org/10.1039/c8tc02156b.

[307] Xu Q, Yang W, Wen Y, Liu S, Liu Z, Ong WJ, et al. Hydrochromic full-color MXene quantum dots through hydrogen bonding toward ultrahigh-efficiency white light-emitting diodes. Appl Mater Today 2019;16:90–101. https://doi.org/10.1016/j.apmt.2019.05.001.

[308] Guan Q, Ma J, Yang W, Zhang R, Zhang X, Dong X, et al. Highly fluorescent Ti3C2 MXene quantum dots for macrophage labeling and Cu2+ ion sensing. Nanoscale 2019;11:14123–33. https://doi.org/10.1039/c9nr04421c.

[309] Feng Y, Zhou F, Deng Q, Peng C. Solvothermal synthesis of in situ nitrogen-doped Ti3C2 MXene fluorescent quantum dots for selective Cu2+ detection. Ceram Int 2020;46:8320–7. https://doi.org/10.1016/j.ceramint.2019.12.063.

[310] Huang D, Wu Y, Ai F, Zhou X, Zhu G. Fluorescent nitrogen-doped Ti3C2 MXene quantum dots as a unique "on-off-on" nanoprobe for chrominum (VI) and ascorbic acid based on inner filter effect. Sens Actuat B Chem 2021;342:130074. https://doi.org/10.1016/J.SNB.2021.130074.

[311] Jiang X, Wang H, Shen Y, Hu N, Shi W. Nitrogen-doped Ti3C2 MXene quantum dots as novel high-efficiency electrochemiluminescent emitters for sensitive mucin 1 detection. Sens Actuators B Chem 2022;350:130891. https://doi.org/10.1016/J.SNB.2021.130891.

[312] Yan F, Sun J, Zang Y, Sun Z, Zhang H, Xu J, et al. Solvothermal synthesis of nitrogen-doped MXene quantum dots for the detection of alizarin red based on inner filter effect. Dyes Pigm 2021;195:109720. https://doi.org/10.1016/J.DYEPIG.2021.109720.

[313] Lu Q, Wang J, Li B, Weng C, Li X, Yang W, et al. Dual-emission reverse change ratio photoluminescence sensor based on a probe of nitrogen-doped Ti 3 C 2 quantum dots@DAP to detect H 2 O 2 and xanthine. Anal Chem 2020;92:7770–7. https://doi.org/10.1021/acs.analchem.0c00895.

[314] Wang L, Zhang N, Li Y, Kong W, Gou J, Zhang Y, et al. Mechanism of nitrogen-doped Ti3C2 quantum dots for free-radical scavenging and the ultrasensitive H2O2 detection performance. ACS Appl Mater Interfaces 2021;13:42442–50. https://doi.org/10.1021/acsami.1c11242.

[315] Gou J, Zhao L, Li Y, Zhang J. Nitrogen-doped Ti $_2$ C MXene quantum dots as antioxidants. ACS Appl Nano Mater 2021;4:12308–15. https://doi.org/10.1021/acsanm.1c02783.

[316] Fu C, Ai F, Huang J, Shi Z, Yan X, Zheng X. Eu doped Ti3C2 quantum dots to form a ratiometric fluorescence platform for visual and quantitative point-of-care testing of tetracycline derivatives. Spectrochim Acta A Mol Biomol Spectrosc 2022;272:120956. https://doi.org/10.1016/j.saa.2022.120956.

[317] Zhao L, Wang Z, Li Y, Wang S, Wang L, Qi Z, et al. Designed synthesis of chlorine and nitrogen co-doped Ti3C2 MXene quantum dots and their outstanding hydroxyl radical scavenging properties. J Mater Sci Technol 2021;78:30–7. https://doi.org/10.1016/J.JMST.2020.10.048.

[318] Xu Q, Ma J, Khan W, Zeng X, Li N, Cao Y, et al. Highly green fluorescent Nb2C MXene quantum dots. Chem Commun 2020;56:6648–51. https://doi.org/10.1039/d0cc02131h.

[319] Li S, Ma J, Zhao X, Zhu P, Xu M, Niu Y, et al. Highly fluorescence Ta4C3 MXene quantum dots as fluorescent nanoprobe for heavy ion detection and stress monitoring of fluorescent hydrogels. Chin Chem Lett 2022;33:1850–4. https://doi.org/10.1016/j.cclet.2021.11.020.

[320] Huang D, Xie Y, Lu D, Wang Z, Wang J, Yu H, et al. Demonstration of a white laser with V $_2$ C MXene-based quantum dots. Adv Mater 2019::1901117. https://doi.org/10.1002/adma.201901117.

[321] Li S, Zheng H, Ding L, Xiao X, Niu Y, Tang Y, et al. Machine learning guided full-color V $_{4\,C}$ 3 MXene quantum dots for building WLEDs. J Mater Chem C Mater 2022;10:14282–7. https://doi.org/10.1039/D2TC02969C.

[322] Wang X, Zhang X, Cao H, Huang Y. An inorganic base stripping approach to synthesize N-doped Ti3C2 quantum dots as fluorescence nanoprobe for the simultaneous detection of Co2+ and Ag+ ions. Microchem J 2022;180:107629. https://doi.org/10.1016/j.microc.2022.107629.
[323] Wan M, Zhou J, Yang H, Dai X, Zheng Y, Xia Z, et al. Covalently N-doped MXene quantum dots for highly stable fluorescent Cu $^{2+}$ ion sensor. ACS Appl Nano Mater 2022;5:11715–22. https://doi.org/10.1021/acsanm.2c02699.
[324] Ren D, Cheng X, Chen Q, Xu G, Wei F, Yang J, et al. MXene-derived Ti3C2 quantum dots-based ratiometric fluorescence probe for ascorbic acid and acid phosphatase determination. Microchem J 2023;187:108397. https://doi.org/10.1016/j.microc.2023.108397.
[325] Kuang P, Low J, Cheng B, Yu J, Fan J. MXene-based photocatalysts. J Mater Sci Technol 2020;56:18–44. https://doi.org/10.1016/j.jmst.2020.02.037.
[326] Zhao Y, Que M, Chen J, Yang C. MXenes as co-catalysts for the solar-driven photocatalytic reduction of CO2. J Mater Chem C Mater 2020;8:16258–81. https://doi.org/10.1039/d0tc02979c.
[327] Tariq A, Ali SI, Akinwande D, Rizwan S. Efficient visible-light photocatalysis of 2D-MXene nanohybrids with Gd3+- and Sn4+-codoped bismuth ferrite. ACS Omega 2018;3:13828–36. https://doi.org/10.1021/acsomega.8b01951.
[328] Ke T, Shen S, Rajavel K, Yang K, Lin D. In situ growth of TiO2 nanoparticles on nitrogen-doped Ti3C2 with isopropyl amine toward enhanced photocatalytic activity. J Hazard Mater 2021;402:124066. https://doi.org/10.1016/j.jhazmat.2020.124066.
[329] Cao S, Li Y, Tang Y, Sun Y, Li W, Guo X, et al. Space-confined metal ion strategy for carbon materials derived from cobalt benzimidazole frameworks with high desalination performance in simulated seawater. Adv Mater 2023. https://doi.org/10.1002/adma.202301011.
[330] Pei Y, Zhang X, Hui Z, Zhou J, Huang X, Sun G, et al. Ti 3 C 2 T X MXene for sensing applications: recent progress, design principles, and future perspectives. ACS Nano 2021;15:3996–4017. https://doi.org/10.1021/acsnano.1c00248.
[331] Sun Y, Wang S, Du X, Du Z, Wang H, Cheng X. Skin-conformal MXene-doped wearable sensors with self-adhesive, dual-mode sensing, and high sensitivity for human motions and wireless monitoring. J Mater Chem B 2021;9:8667–75. https://doi.org/10.1039/D1TB01769A.
[332] Bhardwaj SK, Singh H, Khatri M, Kim KH, Bhardwaj N. Advances in MXenes-based optical biosensors: a review. Biosens Bioelectron 2022;202:113995. https://doi.org/10.1016/J.BIOS.2022.113995.
[333] Ud Din Babar Z, Bartolomeo Della Ventura ab, Velotta R, Iannotti V. Advances and emerging challenges in MXenes and their nanocomposites for biosensing applications. RSC Adv 2022;12:19590–610. https://doi.org/10.1039/D2RA02985E.
[334] Lee E, VahidMohammadi A, Yoon YS, Beidaghi M, Kim D-J. Two-dimensional vanadium carbide MXene for gas sensors with ultrahigh sensitivity toward nonpolar gases. ACS Sens 2019;4:1603–11. https://doi.org/10.1021/acssensors.9b00303.
[335] Koh H-J, Kim SJ, Maleski K, Cho S-Y, Kim Y-J, Ahn CW, et al. Enhanced Selectivity of MXene Gas Sensors through Metal Ion Intercalation: In Situ X-ray Diffraction Study. ACS Sens 2019;4:1365–72. https://doi.org/10.1021/acssensors.9b00310.
[336] Wu M, He M, Hu Q, Wu Q, Sun G, Xie L, et al. Ti $_{3\ C}$ 2 MXene-based sensors with high selectivity for N_H 3 detection at room temperature. ACS Sens 2019;4:2763–70. https://doi.org/10.1021/acssensors.9b01308.
[337] Khakbaz P, Moshayedi M, Hajian S, Soleimani M, Narakathu BB, Bazuin BJ, et al. Titanium carbide MXene as NH $_3$ sensor: realistic first-principles study. J Phys Chem C 2019;123:29794–803. https://doi.org/10.1021/acs.jpcc.9b09823.
[338] Xiao B, Li YC, Yu XF, Cheng JB. MXenes: reusable materials for NH3 sensor or capturer by controlling the charge injection. Sens Actuat B Chem 2016;235:103–9. https://doi.org/10.1016/J.SNB.2016.05.062.
[339] Ma Y, Liu N, Li L, Hu X, Zou Z, Wang J, et al. A highly flexible and sensitive piezoresistive sensor based on MXene with greatly changed interlayer distances. Nature Communications 2017 8:1 2017;8:1–8. https://doi.org/10.1038/s41467-017-01136-9.
[340] Li L, Fu X, Chen S, Uzun S, Levitt AS, Shuck CE, et al. Hydrophobic and stable MXene–polymer pressure sensors for wearable electronics. ACS Appl Mater Interfaces 2020;12:15362–9. https://doi.org/10.1021/acsami.0c00255.
[341] Cheng Y, Ma Y, Li L, Zhu M, Yue Y, Liu W, et al. Bioinspired microspines for a high-performance spray Ti 3 C 2 T x MXene-based piezoresistive sensor. ACS Nano 2020;14:2145–55. https://doi.org/10.1021/acsnano.9b08952.
[342] Yue Y, Liu N, Liu W, Li M, Ma Y, Luo C, et al. 3D hybrid porous Mxene-sponge network and its application in piezoresistive sensor. Nano Energy 2018;50:79–87. https://doi.org/10.1016/J.NANOEN.2018.05.020.
[343] Osti NC, Naguib M, Ostadhossein A, Xie Y, Kent PRC, Dyatkin B, et al. Effect of metal ion intercalation on the structure of MXene and water dynamics on its internal surfaces. ACS Appl Mater Interfaces 2016;8:8859–63. https://doi.org/10.1021/acsami.6b01490.
[344] Célérier S, Hurand S, Garnero C, Morisset S, Benchakar M, Habrioux A, et al. Hydration of Ti 3 C 2 T x MXene: an interstratification process with major implications on physical properties. Chem Mater 2019;31:454–61. https://doi.org/10.1021/acs.chemmater.8b03976.
[345] Muckley ES, Naguib M, Ivanov IN. Multi-modal, ultrasensitive, wide-range humidity sensing with Ti3C2 film. Nanoscale 2018;10:21689–95. https://doi.org/10.1039/C8NR05170D.
[346] Li N, Jiang Y, Zhou C, Xiao Y, Meng B, Wang Z, et al. High-performance humidity sensor based on urchin-like composite of Ti $_{3\ C}$ 2 MXene-derived Ti_O 2 nanowires. ACS Appl Mater Interfaces 2019;11:38116–25. https://doi.org/10.1021/acsami.9b12168.
[347] Zhang J, Wan L, Gao Y, Fang X, Lu T, Pan L, et al. Highly stretchable and self-healable MXene/polyvinyl alcohol hydrogel electrode for wearable capacitive electronic skin. Adv Electron Mater 2019;5:1900285. https://doi.org/10.1002/AELM.201900285.
[348] Yao B, Yao J, Fan Z, Zhao J, Zhang K, Huang W. Rapid advances of versatile MXenes for electrochemical enzyme-based biosensors, immunosensors, and nucleic acid-based biosensors. ChemElectroChem 2022;9:e202200103.
[349] Rhouati A, Berkani M, Vasseghian Y, Golzadeh N. MXene-based electrochemical sensors for detection of environmental pollutants: a comprehensive review. Chemosphere 2022;291:132921. https://doi.org/10.1016/J.CHEMOSPHERE.2021.132921.
[350] Scheibe B, Wychowaniec JK, Scheibe M, Peplińska B, Jarek M, Nowaczyk G, et al. Cytotoxicity assessment of Ti–Al–C based MAX phases and Ti 3 C 2 T x MXenes on human fibroblasts and cervical cancer cells. ACS Biomater Sci Eng 2019;5:6557–69. https://doi.org/10.1021/acsbiomaterials.9b01476.
[351] Shahzad F, Iqbal A, Zaidi SA, Hwang SW, Koo CM. Nafion-stabilized two-dimensional transition metal carbide (Ti3C2Tx MXene) as a high-performance electrochemical sensor for neurotransmitter. J Ind Eng Chem 2019;79:338–44. https://doi.org/10.1016/J.JIEC.2019.03.061.
[352] Wang H, Li H, Huang Y, Xiong M, Wang F, Li C. A label-free electrochemical biosensor for highly sensitive detection of gliotoxin based on DNA nanostructure/MXene nanocomplexes. Biosens Bioelectron 2019;142:111531. https://doi.org/10.1016/J.BIOS.2019.111531.
[353] Kalambate PK, Gadhari NS, Li X, Rao Z, Navale ST, Shen Y, et al. Recent advances in MXene–based electrochemical sensors and biosensors. TrAC Trends Anal Chem 2019;120:115643. https://doi.org/10.1016/J.TRAC.2019.115643.
[354] In Jhon Y, Koo J, Anasori B, Seo M, Han Lee J, Gogotsi Y, et al. Metallic MXene saturable absorber for femtosecond mode-locked lasers. Adv Mater 2017;29:1702496. https://doi.org/10.1002/ADMA.201702496.
[355] Chen Y, Ge Y, Huang W, Li Z, Wu L, Zhang H, et al. Refractive index sensors based on Ti 3 C 2 T x MXene fibers. ACS Appl Nano Mater 2020;3:303–11. https://doi.org/10.1021/acsanm.9b01889.
[356] Chertopalov S, Mochalin VN. Environment-sensitive photoresponse of spontaneously partially oxidized Ti $_{3\ C}$ 2 MXene thin films. ACS Nano 2018;12:6109–16. https://doi.org/10.1021/acsnano.8b02379.
[357] Deng W, Huang H, Jin H, Li W, Chu X, Xiong D, et al. All-sprayed-processable, large-area, and flexible perovskite/MXene-based photodetector arrays for photocommunication. Adv Opt Mater 2019;7:1801521. https://doi.org/10.1002/ADOM.201801521.
[358] Mohammadniaei M, Koyappayil A, Sun Y, Min J, Lee MH. Gold nanoparticle/MXene for multiple and sensitive detection of oncomiRs based on synergetic signal amplification. Biosens Bioelectron 2020;159:112208. https://doi.org/10.1016/J.BIOS.2020.112208.
[359] Ma Y, Liu N, Li L, Hu X, Zou Z, Wang J, et al. A highly flexible and sensitive piezoresistive sensor based on MXene with greatly changed interlayer distances. Nat Commun 2017;8:1207. https://doi.org/10.1038/s41467-017-01136-9.
[360] Lei D, Liu N, Su T, Zhang Q, Wang L, Ren Z, et al. Roles of MXene in pressure sensing: preparation, composite structure design, and mechanism. Adv Mater 2022;34:2110608. https://doi.org/10.1002/adma.202110608.
[361] Kadirsoy S, Atar N, Yola ML. Molecularly imprinted QCM sensor based on delaminated MXene for chlorpyrifos detection and QCM sensor validation. New J Chem 2020;44:6524–32. https://doi.org/10.1039/d0nj00951b.

[362] Zhou Y, Wang Y, Wang Y, Li X. Humidity-enabled ionic conductive trace carbon dioxide sensing of nitrogen-doped Ti3C2TxMXene/polyethyleneimine composite films decorated with reduced graphene oxide nanosheets. Anal Chem 2020;92:16033–42. https://doi.org/10.1021/acs.analchem.0c03664.

[363] Medetalibeyoglu H, Beytur M, Akyıldırım O, Atar N, Yola ML. Validated electrochemical immunosensor for ultra-sensitive procalcitonin detection: Carbon electrode modified with gold nanoparticles functionalized sulfur doped MXene as sensor platform and carboxylated graphitic carbon nitride as signal amplification. Sens Actuat B Chem 2020;319:128195. https://doi.org/10.1016/j.snb.2020.128195.

[364] Lorencova L, Bertok T, Dosekova E, Holazova A, Paprckova D, Vikartovska A, et al. Electrochemical performance of Ti3C2Tx MXene in aqueous media: towards ultrasensitive H2O2 sensing. Electrochim Acta 2017;235:471–9. https://doi.org/10.1016/j.electacta.2017.03.073.

[365] Wang Y, Wang S, Dong N, Kang W, Li K, Nie Z. Titanium carbide MXenes mediated *in situ* reduction allows label-free and visualized nanoplasmonic sensing of silver ions. Anal Chem 2020;92:4623–9. https://doi.org/10.1021/acs.analchem.0c00164.

[366] Ho DH, Choi YY, Jo SB, Myoung J, Cho JH. Sensing with MXenes: progress and prospects. Adv Mater 2021;33:2005846. https://doi.org/10.1002/adma.202005846.

[367] Cao Y, Li L, Han B, Wang Y, Dai Y, Zhao J. A catalytic molecule machine-driven biosensing method for amplified electrochemical detection of exosomes. Biosens Bioelectron 2019;141:111397. https://doi.org/10.1016/j.bios.2019.111397.

[368] WU Q, BI H-M, HAN X-J. Research Progress of Electrochemical Detection of Heavy Metal Ions. Chinese Journal of Analytical Chemistry 2021;49:330–40. https://doi.org/10.1016/S1872-2040(21)60083-X.

[369] Wang G, Sun J, Yao Y, An X, Zhang H, Chu G, et al. Detection of inosine monophosphate (IMP) in meat using double-enzyme sensor. Food Anal Methods 2020;13:420–32. https://doi.org/10.1007/s12161-019-01652-y.

[370] Fang D, Zhao D, Zhang S, Huang Y, Dai H, Lin Y. Black phosphorus quantum dots functionalized MXenes as the enhanced dual-mode probe for exosomes sensing. Sens Actuat B Chem 2020;305:127544. https://doi.org/10.1016/j.snb.2019.127544.

[371] Abdul Rasheed P, Pandey RP, Gomez T, Jabbar KA, Prenger K, Naguib M, et al. Nb-based MXenes for efficient electrochemical sensing of small biomolecules in the anodic potential. Electrochem Commun 2020;119:106811. https://doi.org/10.1016/j.elecom.2020.106811.

[372] Zhao W-N, Yun N, Dai Z-H, Li Y-F. A high-performance trace level acetone sensor using an indispensable V 4 C 3 T x MXene. RSC Adv 2020;10:1261–70. https://doi.org/10.1039/C9RA09069J.

[373] Lorencova L, Bertok T, Filip J, Jerigova M, Velic D, Kasak P, et al. Highly stable Ti3C2Tx (MXene)/Pt nanoparticles-modified glassy carbon electrode for H2O2 and small molecules sensing applications. Sens Actuat B Chem 2018;263:360–8. https://doi.org/10.1016/j.snb.2018.02.124.

[374] Pandey P, Sengupta A, Parmar S, Bansode U, Gosavi S, Swarnkar A, et al. CsPbBr 3 –Ti 3 C 2 T x MXene QD/QD heterojunction: photoluminescence quenching, charge transfer, and Cd ion sensing application. ACS Appl Nano Mater 2020;3:3305–14. https://doi.org/10.1021/acsanm.0c00051.

[375] Zhao L, Wang K, Wei W, Wang L, Han W. High-performance flexible sensing devices based on polyaniline/MXene nanocomposites. InfoMat 2019;1:407–16. https://doi.org/10.1002/inf2.12032.

[376] Liu M, He Y, Zhou J, Ge Y, Zhou J, Song G. A ''naked-eye'' colorimetric and ratiometric fluorescence probe for uric acid based on Ti3C2 MXene quantum dots. Anal Chim Acta 2020;1103:134–42. https://doi.org/10.1016/j.aca.2019.12.069.

[377] Guan Q, Ma J, Yang W, Zhang R, Zhang X, Dong X, et al. Highly fluorescent Ti $_{3\ C}$ 2 MXene quantum dots for macrophage labeling and C^{u} 2+ ion sensing. Nanoscale 2019;11:14123–33. https://doi.org/10.1039/C9NR04421C.

[378] Chen WY, Jiang X, Lai S-N, Peroulis D, Stanciu L. Nanohybrids of a MXene and transition metal dichalcogenide for selective detection of volatile organic compounds. Nat Commun 2020;11:1302. https://doi.org/10.1038/s41467-020-15092-4.

[379] Sun S, Wang M, Chang X, Jiang Y, Zhang D, Wang D, et al. W18O49/Ti3C2Tx Mxene nanocomposites for highly sensitive acetone gas sensor with low detection limit. Sens Actuators B Chem 2020;304:127274. https://doi.org/10.1016/j.snb.2019.127274.

[380] Lee SH, Eom W, Shin H, Ambade RB, Bang JH, Kim HW, et al. Room-temperature, highly durable Ti 3 C 2 T x MXene/graphene hybrid fibers for NH 3 gas sensing. ACS Appl Mater Interfaces 2020;12:10434–42. https://doi.org/10.1021/acsami.9b21765.

[381] Wang X, Sun K, Li K, Li X, Gogotsi Y. Ti3C2T /PEDOT:PSS hybrid materials for room-temperature methanol sensor. Chin Chem Lett 2020;31:1018–21. https://doi.org/10.1016/j.cclet.2019.11.031.

[382] Yuan W, Yang K, Peng H, Li F, Yin F. A flexible VOCs sensor based on a 3D Mxene framework with a high sensing performance. J Mater Chem A Mater 2018;6:18116–24. https://doi.org/10.1039/C8TA06928J.

[383] Liu J, Jiang X, Zhang R, Zhang Y, Wu L, Lu W, et al. MXene-Enabled Electrochemical Microfluidic Biosensor: Applications toward Multicomponent Continuous Monitoring in Whole Blood. Adv Funct Mater 2019;29:1807326. https://doi.org/10.1002/adfm.201807326.

[384] Wang F, Yang C, Duan M, Tang Y, Zhu J. TiO2 nanoparticle modified organ-like Ti3C2 MXene nanocomposite encapsulating hemoglobin for a mediator-free biosensor with excellent performances. Biosens Bioelectron 2015;74:1022–8. https://doi.org/10.1016/j.bios.2015.08.004.

[385] Wu L, Lu X, Dhanjai W-S, Dong Y, Wang X, et al. 2D transition metal carbide MXene as a robust biosensing platform for enzyme immobilization and ultrasensitive detection of phenol. Biosens Bioelectron 2018;107:69–75. https://doi.org/10.1016/j.bios.2018.02.021.

[386] Zhang R, Liu J, Li Y. MXene with great adsorption ability toward organic dye: an excellent material for constructing a ratiometric electrochemical sensing platform. ACS Sens 2019;4:2058–64. https://doi.org/10.1021/acssensors.9b00654.

[387] Zhao F, Yao Y, Jiang C, Shao Y, Barceló D, Ying Y, et al. Self-reduction bimetallic nanoparticles on ultrathin MXene nanosheets as functional platform for pesticide sensing. J Hazard Mater 2020;384:121358. https://doi.org/10.1016/j.jhazmat.2019.121358.

[388] Chen S, Shi M, Yang J, Yu Y, Xu Q, Xu J, et al. MXene/carbon nanohorns decorated with conductive molecularly imprinted poly(hydroxymethyl-3,4-ethylenedioxythiophene) for voltammetric detection of adrenaline. Microchim Acta 2021;188:420. https://doi.org/10.1007/s00604-021-05079-3.

[389] Lian M, Shi Y, Zhang W, Zhao J, Chen D. Nitrogen and sulfur co-doped Nb2C-MXene nanosheets for the ultrasensitive electrochemical detection dopamine under acidic conditions in gastric juice. J Electroanal Chem 2022;904:115849. https://doi.org/10.1016/j.jelechem.2021.115849.

[390] Anupriya J, Senthilkumar T, Chen SM. A precise electrochemical sensor based on Sm2O3/2D TiC hybrid for highly sensitive and selective detection of antihypertensive drug nimodipine. Colloids Surf A Physicochem Eng Asp 2022;641:128531. https://doi.org/10.1016/j.colsurfa.2022.128531.

[391] Xue Y, Zheng Y, Wang E, Yang T, Wang H, Hou X. Ti 3 C 2 T x (MXene)/Pt nanoparticle electrode for the accurate detection of DA coexisting with AA and UA. Dalton Trans 2022;51:4549–59. https://doi.org/10.1039/D2DT00110A.

[392] Shetty SS, El-Demellawi JK, Khan Y, Hedhili MN, Arul P, Mani V, et al. Iron single-atom catalysts on MXenes for ultrasensitive monitoring of adrenal tumor markers and cellular dopamine. Adv Mater Technol 2023;8:2202069. https://doi.org/10.1002/admt.202202069.

[393] Shi Y, Hu K, Mei L, Yang X, Shi Y, Wu X, et al. SnO2 quantum dots-functionalized Ti3C2 MXene nanosheets for electrochemical determination of dopamine in body fluids. Microchim Acta 2022;189:451. https://doi.org/10.1007/s00604-022-05555-4.

[394] Liu X, He L, Li P, Li X, Zhang P. A direct electrochemical H 2 S sensor based on Ti 3 C 2 T x MXene. ChemElectroChem 2021;8:3658–65. https://doi.org/10.1002/celc.202100964.

[395] Su M, Lan H, Tian L, Jiang M, Cao X, Zhu C, et al. Ti3C2Tx-reduced graphene oxide nanocomposite-based electrochemical sensor for serotonin in human biofluids. Sens Actuat B Chem 2022;367:132019. https://doi.org/10.1016/j.snb.2022.132019.

[396] Kashefi-Kheyrabadi L, Koyappayil A, Kim T, Cheon Y-P, Lee M-H. A MoS2@Ti3C2Tx MXene hybrid-based electrochemical aptasensor (MEA) for sensitive and rapid detection of Thyroxine. Bioelectrochemistry 2021;137:107674. https://doi.org/10.1016/j.bioelechem.2020.107674.

[397] Tan Y, Yang L, Zhai D, Sun L, Zhai S, Zhou W, et al. MXene-derived metal-organic framework@MXene heterostructures toward electrochemical NO sensing. Small 2022;18:2204942. https://doi.org/10.1002/smll.202204942.

[398] Wan M, Jimu A, Yang H, Zhou J, Dai X, Zheng Y, et al. MXene quantum dots enhanced 3D-printed electrochemical sensor for the highly sensitive detection of dopamine. Microchem J 2023;184:108180. https://doi.org/10.1016/j.microc.2022.108180.

[399] Chen J, Chen Y, Li S, Yang J, Dong J, Lu X. MXene/CNTs/Cu-MOF electrochemical probe for detecting tyrosine. Carbon N Y 2022;199:110–8. https://doi.org/10.1016/j.carbon.2022.07.021.

[400] Zhang X, An D, Bi Z, Shan W, Zhu B, Zhou L, et al. Ti3C2-MXene@N-doped carbon heterostructure-based electrochemical sensor for simultaneous detection of heavy metals. J Electroanal Chem 2022;911:116239. https://doi.org/10.1016/J.JELECHEM.2022.116239.

[401] Wang Y, Zhou Y, Wang Y. Humidity activated ionic-conduction formaldehyde sensing of reduced graphene oxide decorated nitrogen-doped MXene/titanium dioxide composite film. Sens Actuat B Chem 2020;323:128695. https://doi.org/10.1016/j.snb.2020.128695.
[402] Lin H, Chen Y, Shi J. Insights into 2D MXenes for Versatile Biomedical Applications: Current Advances and Challenges Ahead. Advanced Science 2018;5. https://doi.org/10.1002/advs.201800518.
[403] Liu P, Yao Z, Ng VMH, Zhou J, Kong LB, Yue K. Facile synthesis of ultrasmall Fe3O4 nanoparticles on MXenes for high microwave absorption performance. Compos A Appl Sci Manuf 2018;115:371–82. https://doi.org/10.1016/j.compositesa.2018.10.014.
[404] Long M, Wang P, Fang H, Hu W. Progress, challenges, and opportunities for 2D material based photodetectors. Adv Funct Mater 2019;29:1803807. https://doi.org/10.1002/adfm.201803807.
[405] Fan D, Liu X, Bao C, Feng J, Wang H, Ma H, et al. A novel sandwich-type photoelectrochemical immunosensor based on Ru(bpy) 32+ and Ce-CdS co-sensitized hierarchical ZnO matrix and dual-inhibited polystyrene@CuS-Ab 2 composites. Biosens Bioelectron 2019;129:124–31. https://doi.org/10.1016/j.bios.2019.01.029.
[406] Nallal M, Anantha Iyengar G, Pill-Lee K. New titanium dioxide-based heterojunction nanohybrid for highly selective photoelectrochemical-electrochemical dual-mode sensors. ACS Appl Mater Interfaces 2017;9:37166–83. https://doi.org/10.1021/acsami.7b10519.
[407] Muthuchamy N, Lee KP, Gopalan AI. Enhanced photoelectrochemical biosensing performances for graphene (2D) – Titanium dioxide nanowire (1D) heterojunction polymer conductive nanosponges. Biosens Bioelectron 2017;89:390–9. https://doi.org/10.1016/j.bios.2016.06.005.
[408] Wang J, Long J, Liu Z, Wu W, Hu C. Label-free and high-throughput biosensing of multiple tumor markers on a single light-addressable photoelectrochemical sensor. Biosens Bioelectron 2017;91:53–9. https://doi.org/10.1016/j.bios.2016.12.029.
[409] Gopalan AI, Muthuchamy N, Lee KP. A novel bismuth oxychloride-graphene hybrid nanosheets based non-enzymatic photoelectrochemical glucose sensing platform for high performances. Biosens Bioelectron 2017;89:352–60. https://doi.org/10.1016/j.bios.2016.07.017.
[410] Liu Y, Zeng H, Chai Y, Yuan R, Liu H. Ti3C2/BiVO4 Schottky junction as a signal indicator for ultrasensitive photoelectrochemical detection of VEGF165. Chem Commun 2019;55:13729–32. https://doi.org/10.1039/c9cc07108c.
[411] Zhu YC, Xu YT, Xue Y, Fan GC, Zhang PK, Zhao WW, et al. Three-dimensional CdS@carbon fiber networks: innovative synthesis and application as a general platform for photoelectrochemical bioanalysis. Anal Chem 2019;91:25. https://doi.org/10.1021/acs.analchem.9b01186.
[412] Liu S-T, Liu X-P, Chen J-S, Mao C, Jin B-K. Highly sensitive photoelectrochemical biosensor for microRNA159c detection based on a Ti3C2:CdS nanocomposite of breast cancer. Biosens Bioelectron 2020;165:112416. https://doi.org/10.1016/j.bios.2020.112416.
[413] Soomro RA, Jawaid S, Kalawar NH, Tunesi M, Karakuş S, Kilislioğlu A, et al. In-situ engineered MXene-TiO2/ BiVO4 hybrid as an efficient photoelectrochemical platform for sensitive detection of soluble CD44 proteins. Biosens Bioelectron 2020;166:112439. https://doi.org/10.1016/j.bios.2020.112439.
[414] Hemanth NR, Kandasubramanian B. Recent advances in 2D MXenes for enhanced cation intercalation in energy harvesting applications: a review. Chem Eng J 2020;392:123678. https://doi.org/10.1016/j.cej.2019.123678.
[415] Zhang C, Xu S, Cai D, Cao J, Wang L, Han W. Planar supercapacitor with high areal capacitance based on Ti3C2/Polypyrrole composite film. Electrochim Acta 2020;330:135277. https://doi.org/10.1016/j.electacta.2019.135277.
[416] Zhang K, Lv S, Zhou Q, Tang D. CoOOH nanosheets-coated g-C3N4/CuInS2 nanohybrids for photoelectrochemical biosensor of carcinoembryonic antigen coupling hybridization chain reaction with etching reaction. Sens Actuat B Chem 2020;307:127631. https://doi.org/10.1016/j.snb.2019.127631.
[417] Khazaei M, Mishra A, Venkataramanan NS, Singh AK, Yunoki S. Recent advances in MXenes: from fundamentals to applications. Curr Opin Solid State Mater Sci 2019;23:164–78. https://doi.org/10.1016/j.cossms.2019.01.002.
[418] Rasool K, Helal M, Ali A, Ren CE, Gogotsi Y, Mahmoud KA. Antibacterial activity of Ti3C2Tx MXene. ACS Nano 2016;10:3674–84. https://doi.org/10.1021/acsnano.6b00181.
[419] Yang K, Feng L, Shi X, Liu Z. Nano-graphene in biomedicine: theranostic applications. Chem Soc Rev 2013;42:530–47. https://doi.org/10.1039/c2cs35342c.
[420] Huang Z, Cui X, Li S, Wei J, Li P, Wang Y, et al. Two-dimensional MXene-based materials for photothermal therapy. Nanophotonics 2020;9:2233–49. https://doi.org/10.1515/nanoph-2019-0571.
[421] Huang K, Li Z, Lin J, Han G, Huang P. Two-dimensional transition metal carbides and nitrides (MXenes) for biomedical applications. Chem Soc Rev 2018;47:5109–24. https://doi.org/10.1039/c7cs00838d.
[422] Dong LM, Ye C, Zheng LL, Gao ZF, Xia F. Two-dimensional metal carbides and nitrides (MXenes): preparation, property, and applications in cancer therapy. Nanophotonics 2020;9:2125–45. https://doi.org/10.1515/nanoph-2019-0550.
[423] Lin S, Lin H, Yang M, Ge M, Chen Y, Zhu Y. A two-dimensional MXene potentiates a therapeutic microneedle patch for photonic implantable medicine in the second NIR biowindow. Nanoscale 2020;12:10265–76. https://doi.org/10.1039/d0nr01444c.
[424] Wang Y, Feng W, Chen Y. Chemistry of two-dimensional MXene nanosheets in theranostic nanomedicine. Chin Chem Lett 2020;31:937–46. https://doi.org/10.1016/j.cclet.2019.11.016.
[425] Zhang W, Zhang F, Ming F, Alshareef HN. Sodium-ion battery anodes: status and future trends. EnergyChem 2019;1:100012. https://doi.org/10.1016/j.enchem.2019.100012.
[426] Balogun MS, Luo Y, Qiu W, Liu P, Tong Y. A review of carbon materials and their composites with alloy metals for sodium ion battery anodes. Carbon N Y 2016;98:162–78. https://doi.org/10.1016/j.carbon.2015.09.091.
[427] Asher RC, Wilson SA. Lamellar compound of sodium with graphite [10]. Nature 1958;181:409–10. https://doi.org/10.1038/181409a0.
[428] Tan H, Chen D, Rui X, Yu Y. Peering into alloy anodes for sodium-ion batteries: current trends, challenges, and opportunities. Adv Funct Mater 2019;29:1808745. https://doi.org/10.1002/adfm.201808745.
[429] Bruce PG, Freunberger SA, Hardwick LJ, Tarascon JM. LigO2 and LigS batteries with high energy storage. Nat Mater 2012;11:19–29. https://doi.org/10.1038/nmat3191.
[430] Yu X, Manthiram A. Capacity enhancement and discharge mechanisms of room-temperature sodium-sulfur batteries. ChemElectroChem 2014;1:1275–80. https://doi.org/10.1002/celc.201402112.
[431] Lin P, Shen J, Yu X, Liu Q, Li D, Tang H. Construction of Ti3C2 MXene/O-doped g-C3N4 2D–2D Schottky-junction for enhanced photocatalytic hydrogen evolution. Ceram Int 2019;45:24656–63. https://doi.org/10.1016/j.ceramint.2019.08.203.
[432] Iqbal MA, Ali SI, Amin F, Tariq A, Iqbal MZ, Rizwan S. La- and Mn-codoped bismuth ferrite/Ti $_{3\,C}$ 2 MXene composites for efficient photocatalytic degradation of congo red dye. ACS Omega 2019;4:8661–8. https://doi.org/10.1021/acsomega.9b00493.